Compensating Microphonics in SRF Cavities to Ensure Beam Stability for Future Free-Electron-Lasers

Mikrophoniekompensation in supraleitenden Hohlraumresonatoren zur Gewährkeistung der Strahlstabilität für zukünftige Freie Elektronen Laser

DISSERTATION

zur Erlangung des akademischen Grades
doctor rerum naturalium
(Dr. rer. nat.)
im Fach Physik

eingereicht an der
Mathematisch-Naturwissenschaftlichen Fakultät I
Humboldt-Universität zu Berlin

von
Herr Dipl.-Phys. Axel Neumann
geboren am 31.01.1975 in Hansestadt Lübeck

Präsident der Humboldt-Universität zu Berlin:
Prof. Dr. Dr. h.c. Christoph Markschies

Dekan der Mathematisch-Naturwissenschaftlichen Fakultät I:
Prof. Dr. Lutz-Helmut Schön

Gutachter:

1. Prof. Dr. Eberhard Jaeschke
2. Prof. Dr. Hermann Kolanoski
3. Prof. Dr. Shaukat Khan

eingereicht am: 22. April 2008
Tag der mündlichen Prüfung: 21. Juli 2008

Abstract

In seeded High-Gain-Harmonic-Generation free electron lasers or energy recovery linear accelerators the requirements for the bunch-to-bunch timing and energy jitter of the beam are in the femtosecond and per mill regime. This implies the ability to control the cavity radio-frequency (RF) field to an accuracy of 0.02° in phase and up to $1{\cdot}10^{-4}$ in amplitude. For the planned BESSY-FEL it is envisaged to operate 144 superconducting 1.3 GHz cavities of the 2.3 GeV driver linac in continuous wave mode and at a low beam current. The cavity resonance comprises a very narrow bandwidth of the order of tens of Hertz. Such cavities have been characterized under accelerator like conditions in the HoBiCaT test facility. It was possible to measure the error sources affecting the field stability in continuous wave (CW) operation. Microphonics, the main error source for a mechanical detuning of the cavities, lead to an average fluctuation of the cavity resonance of 1-5 Hz rms. Furthermore, the static and dynamic Lorentz force detuning and the helium pressure dependance of the cavity resonance have been measured. Single cavity RF control and linac bunch-to-bunch longitudinal phase space modeling containing the measured properties showed, that it is advisable to find means to minimize the microphonics detuning by mechanical tuning. Thus, several fast tuning systems have been tested for CW operation. These tuners consist of a motor driven lever for slow and coarse tuning and a piezo that is integrated into the tuner support for fast and fine tuning. Regarding the analysis of the detuning spectrum an adaptive feedforward method based on the least-mean-square filter algorithm has been developed for fast cavity tuning. A detuning compensation between a factor of two and up to a factor of seven has been achieved. Modeling the complete system including the fast tuning scheme, showed that the requirements of the BESSY-FEL are attainable.

Keywords:
Superconducting Cavity, Microphonics, Fast mechanical tuner, Adaptive feedforward

Zusammenfassung

Laser-initiierte Freie Elektronen Laser (FEL)* und Energy Recovery Linearbeschleuniger (ERL)† erfordern höchste Stabilität der beschleunigten Elektronenpakete. Die zeitliche Streuung der Elektronenpakete und die mittlere Energieabweichung in den Undulatoren sollten in der Größenordnung von Femtosekunden bzw. im Promille Bereich liegen. Das erfordert eine Regelung der Hochfrequenz (HF) Beschleunigungsfelder in den supraleitenden Hohlraumresonatoren bis zu 0.02° Phasen- und $1{\cdot}10^{-4}$ Amplitudengenauigkeit. Die TESLA Resonatoren des 2.3 GeV Linearbeschleunigers des geplanten BESSY-FEL sollen im Dauerstrichbetrieb bei geringer Strahllast betrieben werden. Die HF Resonanzbreite ist folglich sehr schmalbandig und liegt im Bereich von 10 Hertz. Um die erreichbare Feldstabilität zu erfassen, wurden die Resonatoren einem umfangreichen Messprogramm in der HoBiCaT Testanlage unterzogen. Eine Charakterisierung der vollständigen Resonatoreinheit hinsichtlich der mechanischen Verstimmung durch Mikrophonie, statische -und dynamische Lorentzkraftverstimmung, ihrer mechanischen Eigenschaften und HF-System Rauschen erbrachte wichtige Daten, um die zu erwartende Feld -und somit Strahlstabilität im Linac zu simulieren. Die gemessene Mikrophonie betrug 1-5 Hz rms, ist somit eine dominante Fehlergröße und wirkt sich limitierend auf die Strahlstabilität im Linac aus. Um sie zu minimieren, wurden aktive Dämpfungsmethoden entwickelt. Dazu wurden unterschiedliche mechanische Abstimmungssysteme mit integrierten Piezoelementen getestet. Ein adaptiver, vorauskompensierender Regelungsalgorithmus wurde entwickelt, welcher die gemessene Transferfunktion der Abstimmvorrichtung beinhaltet. Damit wurde eine Kompensierung der Mikrophonie um einem Faktor von zwei bis sieben erreicht. Die Einbeziehung dieser Regelung in die Linacsimulationen zeigte, dass diese einen wichtigen Beitrag zur Erreichbarkeit der benötigten Strahlstabilität für zukünftige FELs und ERLs darstellt.

Schlagwörter:
Supraleitender Hohlraumresonator, Mikrophonie, Schnelle mechanische Abstimmer, Selbstanpassende Vorauskompensation

---

[*] Englisch: Seeded FEL, von to seed, säen

[†] Rezirkulierender Linearbeschleuniger mit Rückgewinnung der Strahlenergie

to Eberhard Neumann (*1941 - †2003)

Contents

1 Introduction and motivation **1**
1.1 The next generation of synchrotron light sources–FELs . . . 1
1.2 Outline of the thesis . . . 3

2 Stability requirements for the linear accelerator **5**
2.1 Beam quality for the HGHG-FEL process . . . 5
2.2 Required beam quality . . . 7
2.3 Acceleration of electrons . . . 8
  2.3.1 Linac layout of the BESSY-FEL . . . 10
2.4 Sources of cavity field errors . . . 13
  2.4.1 Field control . . . 13
  2.4.2 Mechanical detuning . . . 14
  2.4.3 RF control related effects . . . 15
  2.4.4 Beam related effects . . . 16
2.5 Error budget . . . 17
  2.5.1 Required field stability . . . 19

3 Modeling of SRF cavities **23**
3.1 Superconducting RF cavity: Figures of merit . . . 23
3.2 Modeling the cavity behavior . . . 25
3.3 Simulating RF control with the cavity model . . . 34
  3.3.1 System components and error sources . . . 34
3.4 Field stability versus bandwidth . . . 39
3.5 Linac calculations . . . 41

4 The cavity measurement setup **47**
4.1 TESLA technology for the BESSY-FEL . . . 47
4.2 The HoBiCaT test facility . . . 49
4.3 RF detuning measurements . . . 50
  4.3.1 Principle of an RF mixer . . . 51
  4.3.2 Measurement accuracy and calibration . . . 54

5 Microphonics in HoBiCaT **59**
5.1 Introduction . . . 59
  5.1.1 Sources of microphonics . . . 59
  5.1.2 Aim of the measurements . . . 60

5.2 Measurements with the phase detector . . . 61
5.2.1 Analysis of the detuning . . . 66
5.3 Lorentz-Force detuning . . . 73
5.3.1 Static detuning . . . 74
5.3.2 Dynamic Lorentz force detuning . . . 74
5.4 Conclusion: Cavity statistics at HoBiCaT . . . 78

6 Piezo based fast cavity tuning systems 81
6.1 Tuning systems for TESLA-type cavities . . . 81
6.1.1 The Saclay I and II tuning systems . . . 81
6.1.2 The piezo tuner . . . 83
6.2 Characterizing the tuning system . . . 84
6.2.1 The coarse tuners . . . 84
6.2.2 DC characteristics of the piezo tuner . . . 86
6.2.3 The transfer function: Mechanical properties of the cavity-piezo-tuner system . . . 88
6.2.4 Summary: Evaluating tuner performance for CW operation . . . 96

7 Compensating microphonics detuning and impact on beam stability 99
7.1 Potential feedback and feedforward concepts . . . 99
7.1.1 The piezo controller setup . . . 102
7.2 Feedback control . . . 103
7.3 LMS–based adaptive feedforward control . . . 106
7.3.1 LMS-Theory . . . 107
7.3.2 Implementation of the feedforward controller . . . 110
7.4 A combined controller: Achieved results . . . 111
7.4.1 Compensation of measured microphonics at 1.8 Kelvin . . . 112
7.4.2 Stability and robustness of the controller . . . 116
7.5 Impact of detuning control on cavity operation . . . 119
7.5.1 Cavity stability . . . 121
7.5.2 Summary . . . 124

8 Summary and future perspectives 125
8.1 Outlook . . . 127

A Timing jitter in the photoinjector and booster 129

B Ponderomotive effects 133

C Fit parameter for the electro-mechanical transfer function 137

Bibliography 143

List of Figures 149

List of Tables 153

Chapter 1

Introduction and motivation

1.1 The next generation of synchrotron light sources–FELs

Physics and material structure research with synchrotron radiation resolving down to the nanometer-scale and studying dynamic processes in the femtosecond regime push for ever shorter and more intense light pulses. To study, for example, short-lived chemical reactions or magnetization dynamics that proceed on a femtosecond time scale, the light-pulse duration has to be at least of this order of magnitude. Furthermore, there are strong demands for coherent, reproducible light pulses with freely selectable polarizations opening new possibilities for imaging processes, microscopy and holography [1] [2] [3]. To perform pump-probe experiments of, e.g. atomic clusters, a deterministic stable time delay between an external pumping radiation synchronized to the sampling by synchrotron radiation has to exist.

Third-generation synchrotron light sources, in operation since the 1990s, are hard-pushed to fulfill many of these requirements. Circular, accelerator-based, light sources have beam properties [4] that are given by an equilibrium condition determined by the balance of excitation and damping terms. Hence, the bunch length is limited to tens of ps and thus limits the minimum length of any light pulse emitted in the undulator or dipole sections. The achieved beam quality of present 3$^{\text{rd}}$ generation synchrotron light sources allows for a peak brightness[*] of about 10^{20}-10^{23} from infra-red to hard x-ray wavelengths[5].

To address the demands set by the physics to be explored, new linear accelerator (linac) based free-electron lasers (FELs) are being developed. In these single-pass accelerators the beam quality is determined by the source rather than being an equilibrium quantity and hence much less divergent beams with smaller beam sizes (emittance) can be accelerated. Beam manipulation along the linac allows for compression of the bunches down to the sub-ps scale. These beams can then be used to generate laser light using the free-electron laser process. To reach wavelengths from UV up to x-rays linac driven FEL light sources represent the most effective design, still allowing to tune the radiation outcome of the FEL process.

Currently, there are several FELs in operation or will be completed within the next years which are based on the SASE[†] principle (XFEL, LCLS, SCSS). This process amplifies spontaneous undulator radiation triggered by stochastic noise in the electron bunch. In rather long undulator sections (e.g. about 60 m for the LCLS), due to interaction with the

---

[*] in photons per second per mm^2 per mrad^2 per 0.1% relative bandwidth

[†] SASE stands for *Self-Amplified-Spontaneous-Emission*

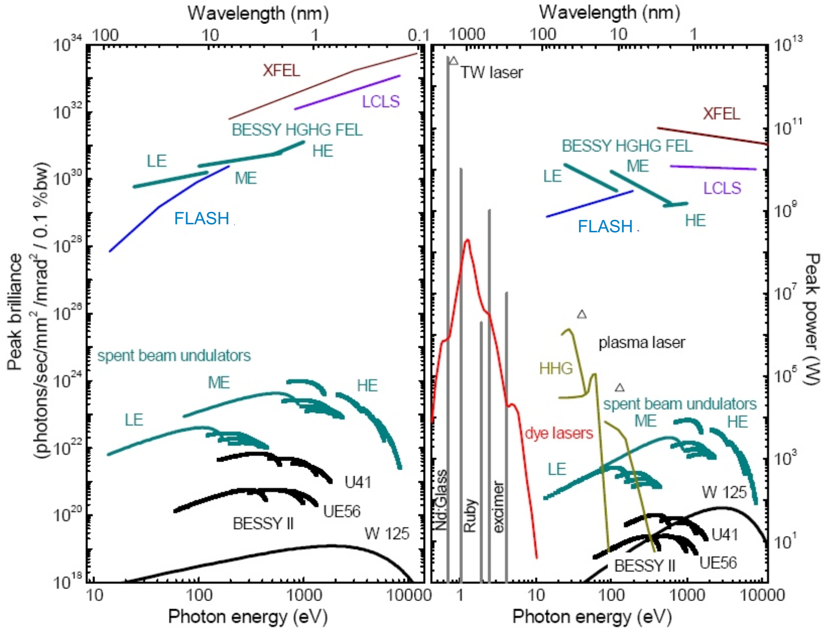

Figure 1.1: The expected performance in peak brilliance (left) and peak power (right) of the BESSY-FEL are shown. For a comparison the performance of other facilities as BESSY II in single-bunch mode, the DESY FLASH, the X-FEL and the Stanford LCLS project are given.

radiation field, the electrons are redistributed to so called microbunches which can radiate coherently. As this process is triggered by noise, shot-to-shot variations of the spectral content result.

Much more stable and reproducible radiation may be produced by seeded FELs. They form the second generation of FELs. An external seed laser in a short undulator imprints an energy modulation on the beam, which is transformed by a magnetic dipole chicane into an electron-density modulation. This bunch sub-structure allows an amplification of the FEL radiation in the high gain regime, even at higher harmonics.

The properties of the seed laser, pulse shape and duration, are generally retained by the synchrotron radiation. Since the FEL process is seeded by controllable lasers, the shot to shot uncertainty of the SASE process does not occur.

As seed lasers at wavelengths in the VUV and X-ray range presently do not exist, the High-Gain-Harmonics-Generation (HGHG) scheme as discussed in Section 2.1 is used [6]. It foresees a cascade of several undulator stages after the first undulator, where the higher harmonic content of one stage acts as the seed radiation for the next. This enables the up-conversion of the seed-laser radiation up to the XUV spectral range.

The BESSY HGHG-FEL

BESSY plans to build an FEL user facility with photon energies ranging from 24 eV to 1 keV [1]. The light pulses will have durations as short as 20 fs with a peak power from 1.5-14 GW and a peak brilliance in the 10^{30}-10^{31} regime. Figure 1.1 (Taken from [1]) shows a comparison of the peak brilliance and power of different FEL and storage ring based projects or facilities. The gain in peak brilliance alone is about nine orders of magnitude above present day storage ring performance.

Critical to all FELs, and especially so for the HGHG process is that a very high-quality electron beam that is nearly jitter free in time and energy is provided by the linac. As will be shown in Chapter 2, a beam jitter of 100 fs already reduces the BESSY FEL output power by 10% and shifts the radiation's relative wavelength by 1×10^{-3}.

The choice of a CW driven linac is partially driven by this fact. Because the linac's RF power "is always on", a greater field stability may be achieved as compared to a pulsed machine where different and more significant error sources for the stability occur. Furthermore, it grants the flexibility to more freely choose the possible bunch patterns. This allows to adopt the light pulse time pattern to the needs of the experiments.

1.2 Outline of the thesis

The key issue of this thesis is to characterize the TESLA superconducting cavity technology in CW operation to determine what RF field stability one may expect. As will be shown, microphonic detuning may limit the FEL performance. Hence, methods to compensate the microphonics detuning are developed. This turns out to be an important feature to achieve the field stability needed for the BESSY-FEL.

The thesis is organized as follows:

In Chapter 2 stable cavity operating conditions, that satisfy the strict boundary conditions set by the seeded FEL process for the electron beam stability, are defined.

In Chapter 3 a Matlab$^{\mathrm{TM}\ddagger}$-based cavity model is developed. It allows the incorporation of error sources and the mechanical properties of the cavity system, which affect the field stability in phase and amplitude. In particular the mechanics are given by the Lorentz-force detuning transfer function and the action of the cavity tuner including a fast piezo tuner. These inputs to the model are determined experimentally, the results being discussed in the subsequent chapters. This model was expanded to simulate the linac's beam's longitudinal phase space distribution. It takes into account all accelerating structures and manipulations of the longitudinal phase space with respect to beam bunch-to-bunch stability. Simulations of the linac performance allows one to determine the permissible limit for the cavity error sources.

In Chapter 4 the test facility **Ho**rizontal- **Bi**- **Ca**vity- **T**eststand (**HoBiCaT**) is introduced, where the cavities have been characterized under cryogenic conditions with respect to CW operation.

In Chapter 5 the measurement of the error sources of the field stability, mainly the microphonics detuning, is discussed. The analysis, in the time-frequency domain, showed, that the main contributions are given by excited mechanical eigenmodes of the cavity-tuner system and pressure variations of the helium system. To reduce their impact, a good understanding of the cavity tuner system is required.

This characterization is discussed in Chapter 6. A detailed analysis of the detuning data and tuner performance obtained under accelerator-like conditions provides the basis to develop tuner-based compensation strategies.

The developed system is presented in Chapter 7. An adaptive feedforward approach has been chosen and tested successfully. This permitted the reduction of microphonics detuning

---

[‡] Matlab$^{\mathrm{TM}}$is a trademark of the Mathworks company

by a factor from at least two up to seven. Thus the residual detuning limit was between 0.4-1 Hz rms.

Finally, the measured error sources, transfer functions and piezo control algorithm were incorporated in the cavity simulations first developed in Chapter 3. It was demonstrated, that the requirements of the FEL, determined in Chapter 2, can be met. However, the simulations also demonstrated, that the field control and piezo feedback loops should not be regarded independently. Rather, their operation parameters must be optimized together to avoid "interference" between both systems which may degrade the level of control or even lead to instabilities.

Chapter 2

Stability requirements for the linear accelerator

In the following Chapter the requirements for the beam quality and thus the acceleration process will be elaborated upon. Potential cavity field error sources will be discussed and the error budget for the total energy and time jitter at the linac exit will be derived.

For machines such as the BESSY FEL the maximum permitted beam jitter is, to a large extent, determined by the High Gain Harmonics Generation (HGHG) process and can be derived analytically. The required beam stability will determine the necessary level of cavity field control and thus also will set the boundary conditions for the cavity field error sources.

2.1 Beam quality for the HGHG-FEL process

Principle of High Gain Harmonic Generation

The HGHG principle [7] as proposed for the BESSY-FEL is depicted in Figure 2.1. In contrast to the Self-Amplified-Spontaneous-Emission (SASE) design the micro bunching of the electron beam is produced by the reproducible external radiation field of a laser. This is achieved by first imprinting an energy modulation onto the beam due to the interaction of the laser's electric field component and the transverse movement of the electrons in the first undulator, called modulator. The laser wavelength is thus chosen as the undulator's resonant wavelength

$$\lambda_{res} = \frac{\lambda_u}{2\gamma^2}\left(1 + \frac{K^2}{2}\right), \tag{2.1}$$

with λ_u the undulator period, γ the relativistic beam energy and K the dimensionless undulator parameter given by

$$K = \frac{eB_0\lambda_u}{2\pi mc^2\beta}. \tag{2.2}$$

Here, B_0 is the peak magnetic field. This longitudinal energy modulation is transferred into a density distribution by a magnetic chicane, such that the electron density maxima are spaced by λ_{res}.

The bunching at the resonant wavelength of the first undulator also contains higher harmonics. The second undulator makes use of this fact and is tuned to a higher harmonic λ_{res}/n and the bunched electron beam starts to radiate coherently at that wavelength. As

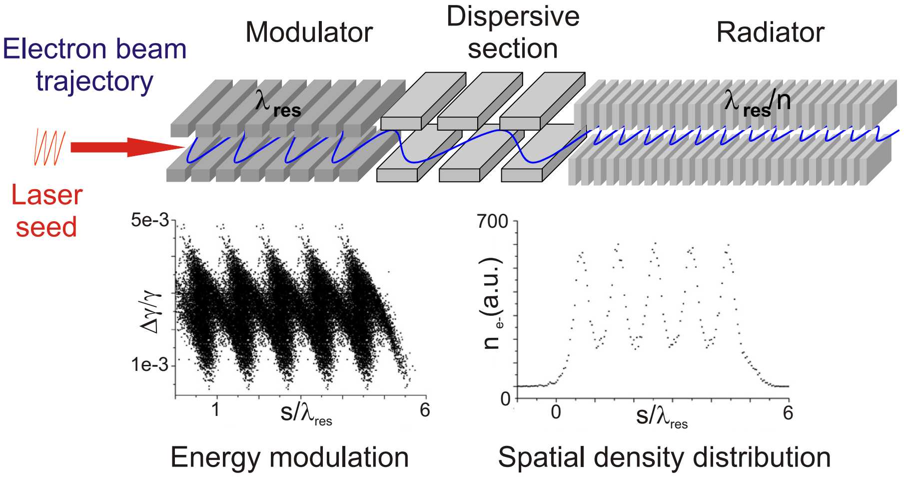

Figure 2.1: Overview of the high-gain-harmonic-generation principle for a single stage seeded FEL. An energy modulation is imprinted on the electron beam in a first undulator by interaction of the wiggling electron beam with the electric field of the seeding laser. A subsequent magnetic chicane converts the energy modulation to a density distribution in the longitudinal phase space to create micro-bunching of the electrons, which also contains higher harmonics of the fundamental modulation. This allows a coherent radiation of the electron bunch at a higher harmonic of the seed laser in the second undulator. The left plot shows the relative energy $\Delta\gamma/\gamma$ along the bunch length s in resonant wavelengths λ_{res}. The right plot depicts the number of electrons (n_{e-} (a.u.)) along the bunch after the chicane.

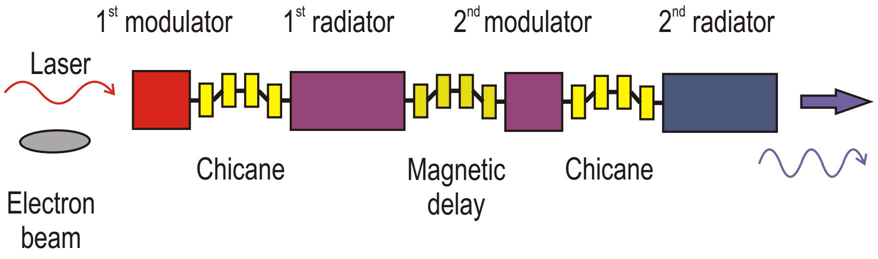

Figure 2.2: Several HGHG stages are cascaded to achieve shorter wavelengths. The seeding radiation of the preceding stage is used for energy modulation of the bunch in the successive stage. The magnetic chicane in between two stages delays the beam with respect to the radiation field for the ”fresh bunch” technique [7].

the laser pulse of the initial seeding radiation is very short, about 20-30 fs, only that part of the bunch is being rearranged in phase space.

In this way the properties of the initial laser beam (amplitude stability, pulse length),

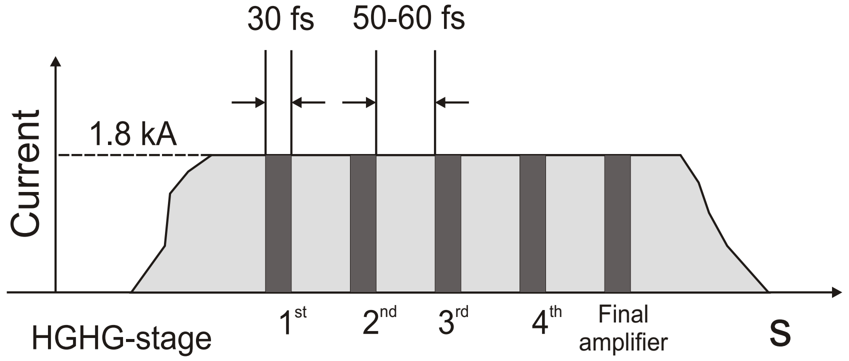

Figure 2.3: This scheme shows the parts of the electron bunch profile which interact in the HGHG stages with the radiation field to achieve energy modulation and thus radiation at the desired wavelength. The shifting of an nearly unperturbed part of the bunch to the interaction spot in the undulator requires a reproducibility of the bunch's timing below 150 fs.

referred to as the seeding radiation, are transferred to the FEL output radiation. Several HGHG stages can be cascaded, the output of one being used to seed the next stage. In that manner one can convert the initial wavelength of the first modulator to a shorter wavelength down to the soft x-ray regime. As the part of the bunch which interacted with the seed in the first stage is already perturbed by the energy modulation* a *fresh* part of the bunch is used for the next stage. This is achieved by delaying the beam with respect to the radiation field by another magnetic chicane. The scheme for a two stage system is given in Figure 2.2. The BESSY FEL design foresees an additional undulator after the last radiator which is optimized to deliver a maximum radiation output of the desired wavelength of the last stage. This undulator is called final amplifier.

2.2 Required beam quality

To allow stable operation of this principle there are stringent conditions for the stability of the electron beam. For the control of the acceleration process only the bunch-to-bunch beam stability is concerned, because intra-bunch feedback cannot be realized. Lack of RF field control impacts the HGHG process in several ways. The three most important effects are as follows:

1. For an n-stage cascade $n+1$ slices of the electron bunch are required for beam-radiation-field interaction, see Figure 2.3. The beam time jitter must be small enough, that all

---

*The whole bunch is also modulated in energy by spontaneous emission.

$n+1$ slices lie within the flat top part of the bunch. To avoid an overlap between slices, which already interacted resonantly in the preceding undulator sections, a time lag between these bunch regions is necessary. This requires the time jitter to be no more than 150 fs.

2. The peak current has to be high enough to have a reasonable saturation length of the FEL process in the final amplifier undulator and power efficiency for the radiation generation in the individual HGHG stages. According to tolerance studies of [8] a change in beam parameters affects the output radiation shot-to-shot stability in two ways:

    - A time jitter of the bunch would only lead for the first or last slice to a change of the peak current and so the amount of electrons to contribute to the FEL process in the according stages. A deviation of about 20% from the design current would alter the peak output power by about 25%.
    - Timing jitter results in energy jitter of the slices which affects the radiation output power. To illustrate the importance of a jitter-free beam for the HGHG process, Figure 2.4 depicts the simulated bunch phase space of the beam in the BESSY FEL as it arrives at the undulators. Both plots are taken from [9]. The nearly linear chirp is a result of the bunch compression scheme that was implemented to achieve peak currents of 1.8 kA[1].

      The longitudinal intra-bunch phase space is given in the left plot of Figure 2.4. The corresponding current is shown in the right plot. The relative energy jitter given by the energy chirp of the bunch is $8{\cdot}10^{-6}$/fs. According to the tolerance studies [8] a shift in the central bunch energy by $\Delta\gamma/\gamma{=}1{\cdot}10^{-3}$ already leads to a reduction of the output power by $\sim$10% and a shift of the central wavelength of about $\Delta\lambda/\lambda{=}1{\cdot}10^{-3}$. This is displayed in Figure 2.5. Therefore, it is important to keep the relative energy jitter well below $1{\cdot}10^{-3}$. Accounting for the relative energy chirp along the bunch, this corresponds to a time jitter of the electron bunch of less than 125 fs.

3. The energy spread $\Delta\gamma/\gamma$ of the electron beam should be less than the acceptance energy bandwidth of the undulator and as well be smaller than the energy modulation, which will be transferred by the seeding laser radiation in the modulator undulator.

In addition to the bunch jitter one has to consider the timing jitter of the seed laser, which is expected to be of the order of 110 fs[1]. This leaves 60 fs allowable timing jitter of the electron bunches to keep the output power and wavelength of the FEL radiation jitter within or below 10%.

2.3 Acceleration of electrons

In order to understand what causes the jitter, one has to examine the acceleration process in the linac. Any shift from the central design energy E_0 is caused by imperfections in the acceleration process starting from the photo injector RF cavity up to the final superconducting cavity of the driver linac. This also applies to deviations from the desired arrival time of the electron bunch with respect to the seed laser Δt.

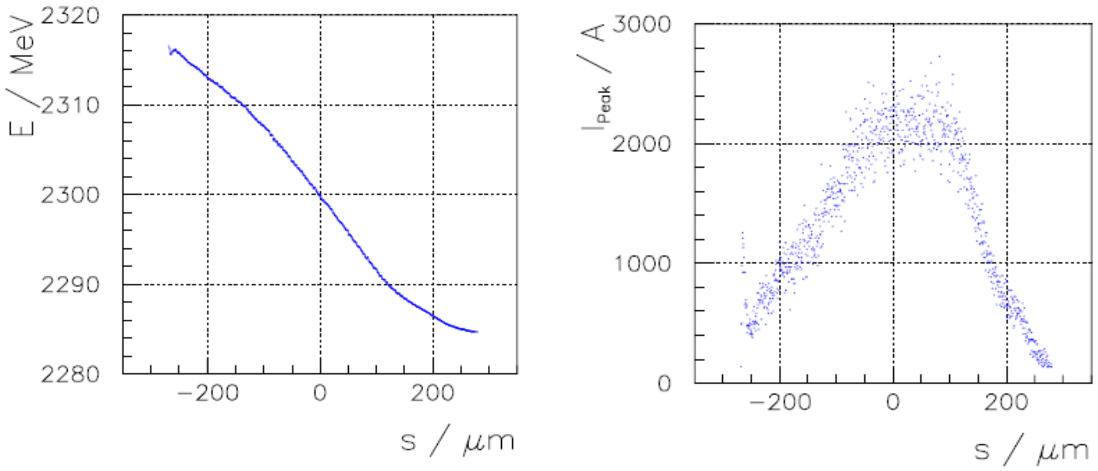

Figure 2.4: Left: Longitudinal phase space of the electron bunch at the linac exit showing the correlated energy chirp. Right: Current or electron distribution along the bunch at the linac exit.

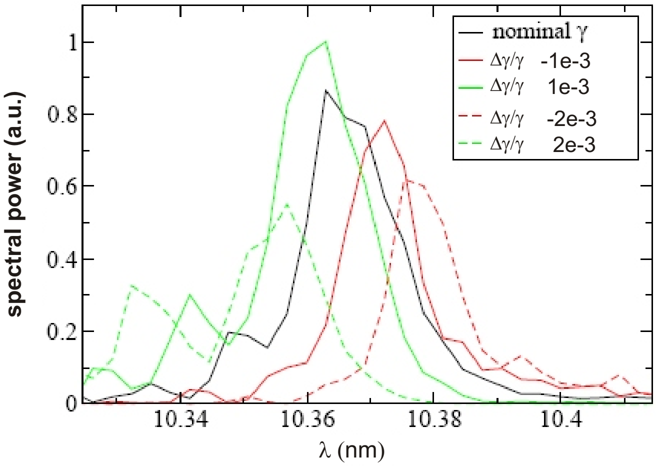

Figure 2.5: Spectra of the low energy FEL for varying offset energies taken from [8].

These two properties of the bunch form the longitudinal phase space of the bunch's center energy and the arrival time with respect to an unperturbed moving reference particle. The principle of electron acceleration by an RF field is displayed in Figure 2.6. The obtained energy of an electron bunch is given by the integral of the electric field component along the path of the bunch in the cavity:

$$\Delta E = q \cdot \Delta V_c = q \cdot \int_{-d/2}^{d/2} E_z(r=0,z,t)dz = q \cdot \int_{-d/2}^{d/2} E(0,z)\cos\left(\omega t(z) + \Phi_b\right). \tag{2.3}$$

Here, V_c denotes the cavity accelerating voltage, E_z the time varying electric field along the path of the particle ($r = 0$) and d the length of the accelerating gap. The particle achieves maximum energy gain, if it reaches the center of the cavity cell when the electrical field component is at maximum value. This is called *on-crest* acceleration ($\Phi_b = 0$). Using the

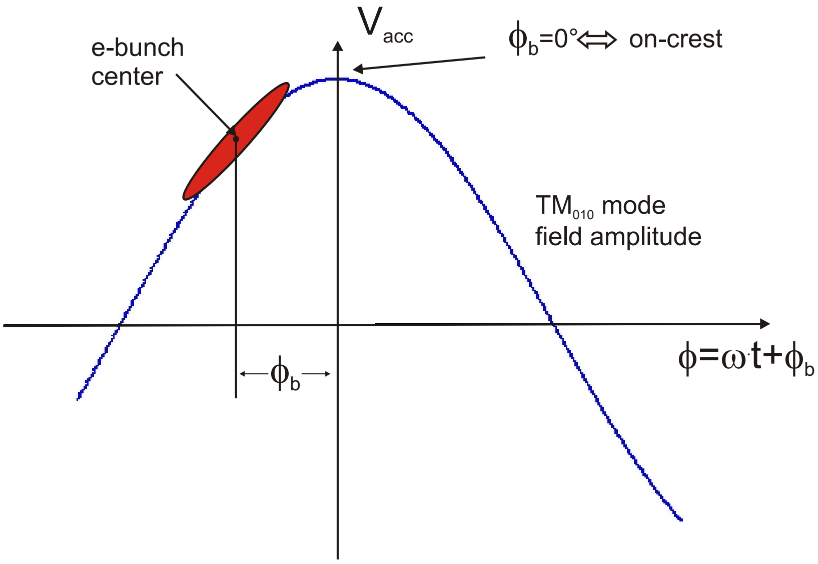

Figure 2.6: Scheme showing the acceleration of an electron bunch in a time varying RF field. The beam phase is defined with respect to the maximum voltage.

trigonometric identity

$$\cos(\alpha \pm \beta) = \cos(\alpha)\cos(\beta) \mp \sin(\alpha)\sin(\beta) \tag{2.4}$$

the energy gain of a particle is defined by

$$\Delta E = q \cdot V_0 T \cos(\Phi_b) \tag{2.5}$$

where $V_0 = \int_{-d/2}^{d/2} E(0,z)dz$ is the axial RF voltage and T the transit time factor, which takes into account the time varying RF field during passage of the cavity. Clearly, this is dependent on the velocity of the bunch. In all but the first cavity this is $v \simeq c$ or $\beta = v/c \simeq 1$.

Nevertheless the transit time factor has to be regarded deviating from the $\beta \simeq 1$ case, i.e. smaller for the first cavity with $v < c$, where there are still non-relativistic processes. Referring to Equation 2.5 any deviation in the beam's phase Φ_b, the accelerating voltage V_0 and the transit time factor T due to non-relativistic acceleration in the first cavity may lead to a shift of the particle or bunch's center position in the longitudinal phase space.

Hence, especially in the early linac section, where the bunch still is at $\beta<1$, any phase and amplitude error in the acceleration leads to an increase in the arrival time jitter, because in small drift sections between the photo injector's RF cavity and the first booster cavity an unwanted velocity bunching may occur. This has been analyzed in more detail in Appendix A.

2.3.1 Linac layout of the BESSY-FEL

The linac layout of the planned facility is shown in Figure 2.7. Initially, a laser driven photo-injector creates bunches with a peak current of 65 A. It is followed by one accelerating section, where a correlated energy chirp is imprinted on the beam by off-crest acceleration

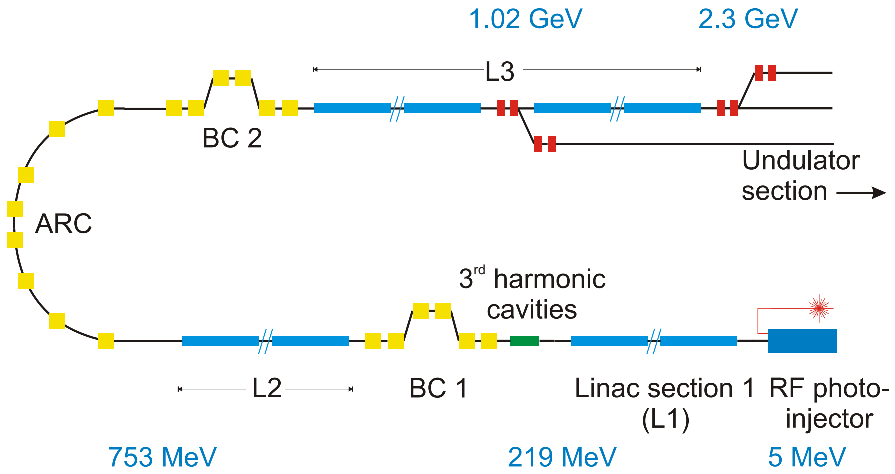

Figure 2.7: Overview of the driver linac of the BESSY-FEL. The operational parameters are given in Table 3.1. The linac sections L1-L3 consist of superconducting cavities. The sections denote where different acceleration phases apply. BC1 and BC2 are the first and second bunch compressor to achieve the 1.8 kA peak current of the beam.

at 13°. Producing electron bunches with the high peak charge needed for the FEL (1.8 kA) in the injector is not possible due to space charge driven inflation of the bunches [10]. Instead, two magnetic chicanes will compress the beam at higher energy to the required 1.8 kA by making use of the energy path-length dependency of the beam. After the first bunch compressor the acceleration takes place at 5°. In the last section the beam is accelerated to the final 2.3 GeV by on-crest operation.

Effect of bunch compression

Two dispersive sections consisting of dipole magnets manipulate the longitudinal intra-bunch phase space to increase the current from 65 A to 1.8 kA. This is achieved by first creating a correlated energy-position relation along the bunch due to off-crest acceleration in the sections before the bunch-compressors.

The energy dependent path length in the non-isochronous transport line (see Figure 2.8) [4] rearranges the electrons in a bunch according to their energy in the longitudinal phase space. The bunch compressor is a beam transport system of at least four dipole magnets with a finite momentum compaction factor

$$\alpha_c = \int_0^{L_0} \frac{\eta}{\rho} ds \tag{2.6}$$

where L_0 is the length of the beam transport system, ρ the bending radius of the dipole magnets and η the dispersion function describing the energy dependance of the particle trajectory with respect to a reference energy. The energy modulation or chirping of the bunch due to the off-crest acceleration may be linearly approximated by an energy ramp in

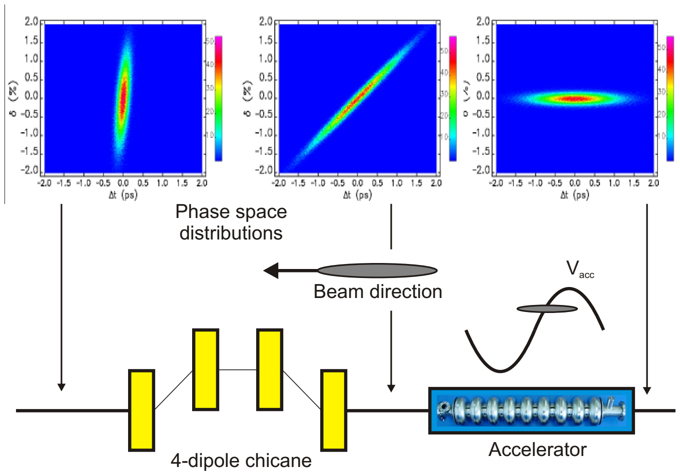

Figure 2.8: Layout of a bunch compressor magnetic chicane in combination with off-crest linac operation. Phase space distributions taken from [11].

the $E - z$ space:

$$dE(z) = e \cdot \frac{dV_c}{dz} \cdot z \tag{2.7}$$

with dE being the energy shift due to gradient of the local acceleration voltage V_c the particle experiences. The path length dependency resulting in the redistribution of the bunch is given by:

$$dL = \alpha_c \cdot \frac{dE}{E_0} \tag{2.8}$$

In linear accelerator bunch compression schemes the momentum compaction factor is often named after its transfer matrix element in six-dimensional phase space. The first order effect as given by Equation 2.8 is named R_{56}, the term $\propto (dE/E)^2$ is named T_{566}.

Neglecting higher-order effects the final longitudinal distribution along the z-axis is given by the initial distribution $\sigma_{z,initial}$ and the transformation of the energy spread $\sigma_{E,initial}$ by the momentum compaction factor as [1]

$$\sigma_{z,final} = \sqrt{\left(1 + kR_{56}\right)^2 \sigma_{z,initial} + R_{56}^2 \sigma_{E,initial}^2}. \tag{2.9}$$

Here, k is the linear correlation constant between particle energy and its longitudinal position z given by $k = \delta E/\delta z$. σ_z is the bunch length and σ_E the energy spread. If $-1/k$ equals exactly the momentum compaction factor R_{56} this simplifies to

$$\sigma_{z,final} = R_{56}\sigma_{E,initial} \tag{2.10}$$

Thus, it is obvious for a maximum bunch compression, that the RF acceleration process has to meet the given design correlation k very precisely, e.g. for the BESSY-FEL's first bunch compressor it is given by 1.44 MV/mm. Large variations from this design value lead to an "over-compression" of the bunch effectively lengthening the bunch, thereby impacting the current distribution.

The same longitudinal phase space description applies when regarding a bunch as a macro particle. Any jitter in the bunch's arrival phase leads to a change in the mean energy. Any starting time jitter occurring in the early acceleration stages or even during creation of the

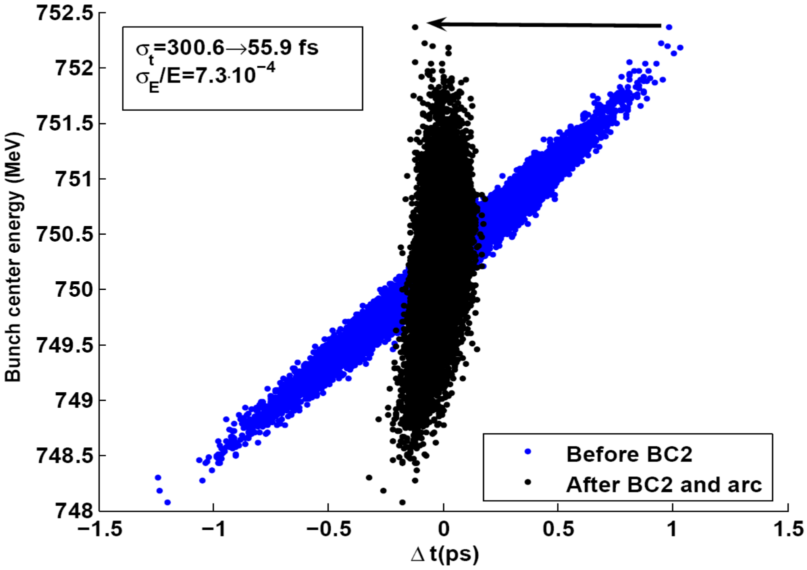

Figure 2.9: Simulated distribution of the electron bunches before (blue dots) and after the second bunch compressions and arc in the BESSY-FEL linac. Each dot represents the mean energy and time of a bunch with respect to a reference particle.

bunch at the photo injector cathode due to a time jitter of the laser will result in a correlated bunch-to-bunch energy jitter at the first bunch compressor which thus compresses the beam jitter. Any energy spread, that is not correlated with the longitudinal position of the bunch widens the energy distribution, thereby limiting the jitter compression. Figure 2.9 shows an example of the compression in the second bunch compressor of the BESSY-FEL. This result has been achieved by simulations described in Chapter 3. The correlated energy spread leads to a reduction of the distribution along the t-axis. The minor axis of the ellipse is dominated by individual uncorrelated errors from each cavity and thus defines a limit for the reduction of the total bunch-to-bunch timing jitter. Hence, the acceleration errors in the individual cavities have to be controlled to a small residual value. In principle, these mechanisms of acceleration and phase space manipulations and the variations in these processes due to different error sources in the linac cavities form the limit to the achievable bunch-to-bunch beam stability.

2.4 Sources of cavity field errors

The various error sources affecting the cavity field stability will be shortly introduced in the following sections. Especially the main error source, the mechanical detuning, will be described in more detail in the measurement related Chapter 5.

2.4.1 Field control

To control the RF field a cavity is equipped with an RF control system, which can be digital or analogue. Here the digital version planned for the BESSY-FEL is described, in principle comparable to systems as [12] or [13]. An overview of a typical RF control path including

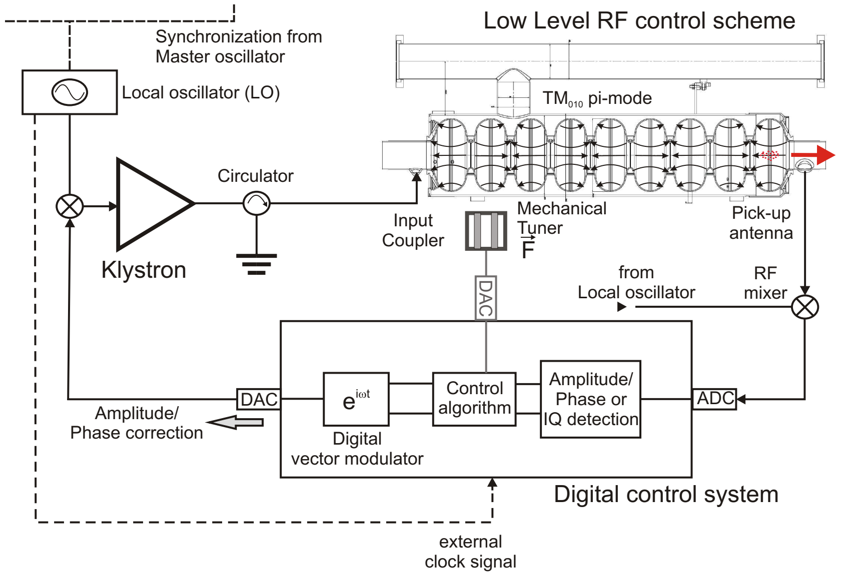

Figure 2.10: Layout of a generic single cavity RF control system in a generator driven setup. The amplitude and phase of the cavity field is measured with respect to the reference given by a master oscillator.

the cavity is given in Figure 2.10. The field in the cavity is detected by a weakly coupled pick-up antenna. The amplitude and phase of this signal are compared at an RF mixer with an external reference. The reference is derived from the master oscillator of the whole facility defining the overall stability of the machine. The measured difference is amplified and modulated on an outgoing wave, which is up-converted at another RF mixer to the cavity frequency. This low power wave drives a klystron, i.e. modulating the forward high power wave to the input coupler, which feeds the power into the cavity. Phase and amplitude shifts are thus corrected for. Additionally a mechanical tuning system may deform the cavity such, that the eigenfrequency is kept constant.

The error sources can be distinguished between those which are correlated over the whole linac and uncorrelated ones different for each cavity.The impact of uncorrelated errors on the beam is reduced by $1/\sqrt{N_{cav}}$, where N_{cav} is the number of cavities [12].

2.4.2 Mechanical detuning

The TESLA cavities are made of thin walled niobium (2.5 mm). There are stiffening rings between adjacent cells, but they were mainly intended to reduce the effect of the radiation pressure of the RF field onto the walls (Lorentz-force detuning). Because both, losses in the cavity and beam loading are small, the bandwidth of the RF mode is small and hence the cavity can be easily detuned by more than a bandwidth by deformations in the nm regime. Furthermore external forces may excite mechanical eigenmodes of the cavity body.

To control fast changes in the cavity mechanical dimension, presently superconducting cavities are equipped with fast tuning systems, based on piezoelectricity or magnetostrictive effects. These are often integrated in slower mechanical tuners using stepper motors to deform the cavity (See Chapter 6).

Microphonics

The term microphonics summarizes all types of external noise and mechanical vibrations, which may be transferred to the cavity via beam pipes or supporting structures. Also vibration caused by pumps in the helium-liquefaction plant can be transmitted by the liquid helium directly to the cavity structure. Thermo-acoustic fluctuations arising from enclosed volumes in the cryo-plant [14] trigger pressure waves. This will directly act as an isotropically distributed force onto the cavity via the helium transfer line.

Additionally, slow ground motions often act on the whole linear accelerator and have to be regarded as a correlated effect. Wavelengths up to several hundred meters occur with very low frequencies of ≤ 1.0 Hz [15]. The sources of this natural noise are e.g. given by seismic activities of the ground and ocean waves. As the BESSY-FEL facility will be rather short, most of these slow motions will affect the facility as a whole and should not impact the beam stability [16].

It can be expected, that the microphonics noise is dominated by man-made, i.e. machinery caused oscillations and motions. This has been demonstrated by the obtained microphonics detuning spectra in Chapter 5. They were found to be mostly different for different cavities, such as it will be very unlikely, that the microphonics are correlated between all cavities in the BESSY-FEL (See Section 5.1.2).

Lorentz force detuning

Another detuning source is given by residual fluctuations of the controlled field level in the cavity. The electric and magnetic field components of the standing wave interact with the currents in the cavity wall. Such forces mainly take effect at the cavity iris and equator section of a cell. These forces mainly disturb pulsed machines, where the field level changes from zero to values up to 30 MV/m. In a CW-driven machine, amplitude variations are mainly caused by external mechanical detuning sources, which trigger a change in the Lorentz forces. E.g., an amplitude jitter $\Delta A/A$ of $2{\cdot}10^{-4}$ will result in a Lorentz force detuning of 0.05 Hz at 16 MV/m. Mainly microphonics detuning triggers these amplitude fluctuations. Thus, in the case of uncorrelated microphonics this error source is assumed as being uncorrelated. In addition the mechanical responses of the cavities can be different for individual cavities.

2.4.3 RF control related effects

In general the RF control section will counteract shifts between a desired set point value and the actual field measurement by modulating the klystron's forward RF power. A proper design and characterization of this control system is mandatory, as many error sources may distort the measurement and hence the corrections.

- The measurement of the cavity field at the pick-up antenna may be falsified by measurement noise at the antenna and RF cabling (which still needs to be characterized) and non-linearities of the field detectors given by RF mixers (see Section 4.3). Calibration errors will only cause a systematic error which will be compensated by beam based feedback. For CW operation, where the field phase is kept constant the mixer will mostly work in the linear regime. This is reasonable as the phase errors by the microphonics detuning are rather small and even off-crest operation at a phase angle different from zero may be shifted by individual phase shifters to the mixer's linear regime.

- The field components are detected by referring the measured RF signal to an external reference oscillator. Noise, especially phase noise of such a device will modulate the measured signal and lead to noise driven corrections by the feedback system. This error source is correlated for all cavities as it is derived from one source. A time jitter due to phase noise of e.g. 70 fs corresponds to 0.03° phase error (see Figure 4.9).

- The klystron gain curve shows a non-linear gradient with respect to the input driving current and has a saturation level. Depending on the level of control therefore the actual total feedback gain will vary. As both, the gain curve and also the phase shift by the klystron are characteristic depending on the input power, they can be compensated by feedforward look-up tables or an additional feedback loop [17].

- Fast fluctuations in the power supply for the klystron cathode and the RF cavity of the klystron drift section for velocity bunching cause a ripple in the output power. This is effectively phase and amplitude noise modulated on the output power within the bandwidth of the klystron (usually of the order of some MHz).

2.4.4 Beam related effects

Depending on the bunch length, the charge distribution along the bunch and the distance of the bunch to the beam pipes and cavity walls the beam induces short and long range wakefields. For the case of short range longitudinal fields the wake potential caused by the bunch head interacts with the bunch tail thus leading to an increase of the single bunch energy spread [18] [19]. When a sequence of bunches with a given repetition rate passes through a cavity, wakefields caused by the leading bunches affect the following bunches. This is an even more severe effect, when higher order modes of the cavity are excited, given the mode is a multiple of the bunch repetition rate. This increases the bunch-to-bunch energy jitter [20].

Two further effects caused by imperfections of the photo-injector cause energy jitter of the beam:

1. An electron bunch passing through the cavity extracts energy proportional to its charge from the RF field, observable as a transient dip in the field amplitude. The charge jitter, resulting from laser shot-to-shot intensity variations at the photo-cathode of the injector, will increase the energy spread linearly. It depends on the field decay time constant, the gain of the RF feedback loop and the spacing between two bunches how much this effect increases the energy jitter.

2. Phase errors in the acceleration due to time jitter of the beam is mainly caused by the injector laser's time stability. Additional errors are caused by non-relativistic velocity spread given by phase errors in the first accelerating cavity cells. This error has to be regarded as correlated along the whole linac.

2.5 Error budget

The following results show the influence of each individual error source on the cavity field stability and thus the final energy jitter of a single cavity. These values depend on the bandwidth of the cavity's RF resonance, which is linearly proportional to the quality factor of the resonance and the feedback gain of the RF controller. In principle, assuming small, correlated, gaussian distributed phase and amplitude errors of the cavity field, the expected energy jitter is given by the following equation:

$$\frac{\sigma_E}{E} \approx \sqrt{\frac{1}{2}(1+\cos(2\Phi_b))\left(\frac{\sigma_A}{A}\right)^2 + \frac{1}{2}(1-\cos(2\Phi_b))\sigma_\Phi^2 + \frac{1}{4}(3\cos(2\Phi_b)-1)\sigma_\Phi^4} \qquad (2.11)$$

Here the quantity σ_A/A is the relative cavity field amplitude rms jitter while σ_Φ describes the rms phase error. In short, this relationship has been derived by considering the following distributed RF voltage:

$$V_{acc} = V_0(1+\sigma_A/A)\cos(\Phi_b+\sigma_\Phi). \qquad (2.12)$$

σ_A and σ_Φ are random variables characterized by their distribution functions, which are assumed to being Gaussian. This is also shown by the detuning measurements in Section 5.1.2. Equation 2.11 can then be determined by summing 2.12 over all linac cavities and taking the square root of the rms relative energy spread squared given by the quadratic average and the average squared as $(\langle V_{acc}^2\rangle - \langle V_{acc}\rangle^2)/\langle V_{acc}\rangle^2$. The complete derivation is given in [21].

For on-crest operation, where Φ_b=0° this simplifies to

$$\frac{\sigma_E}{E} = \sqrt{\left(\frac{\sigma_A}{A}\right)^2 + \frac{\sigma_\Phi^4}{2}} \qquad (2.13)$$

In the case of completely uncorrelated errors among the cavities this error is reduced by $\sqrt{N}$, with N the number of cavities. To use this analytical expression for the whole BESSY-FEL linac, it may only be used between the bunch compression stages, as the correlated phase errors for the subsequent acceleration after the compression changes there. The total energy jitter will be given by the quadratic sum of the uncorrelated and correlated errors for each linac section as:

$$\left(\frac{\sigma_E}{E}\right) = \sqrt{\left(\frac{\sigma_E}{E}\right)^2_{\text{uncorr.}} + \left(\frac{\sigma_E}{E}\right)^2_{\text{corr.}}}. \qquad (2.14)$$

The cavity simulation, which will be introduced in Chapter 3 showed similar results as this analytical expression. To calculate the influence of measured error sources which showed sometimes non-Gaussian distributions , the simulations were used instead of the expression above. The details of the simulations are described in Section 3.3. Here, just the salient results are presented to extract the required field stability.

Figure 2.11 shows the influence of the individual error sources on the bunch energy jitter after one cavity. For these calculations the loaded quality factor Q_L has been set to $3{\cdot}10^7$, the feedback gain to K_P =200 and the cavity field amplitude to 16.0 MV/m (see Chapter 3). It is obvious, that off-crest acceleration is more susceptible to phase errors with respect to energy jitter than on-crest operation. The influence of klystron noise† and charge jitter of the bunches seems negligible, as they are 2-3 orders of magnitude smaller than the contributions

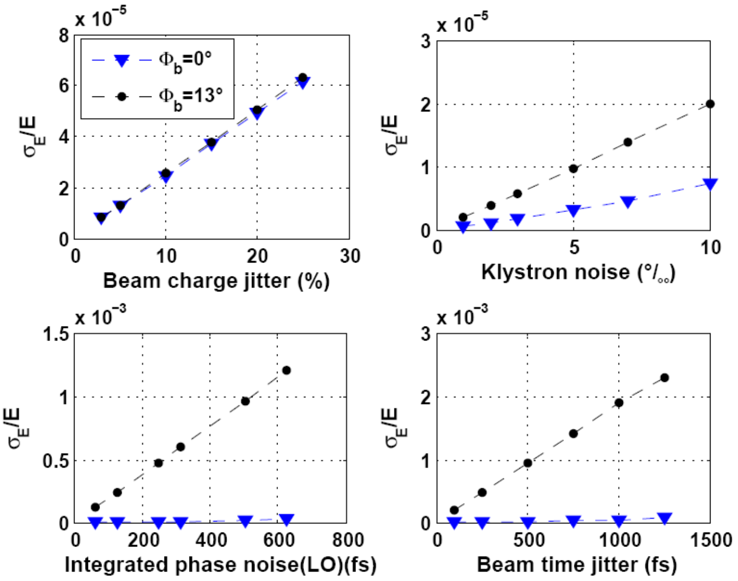

Figure 2.11: Bunch energy jitter after one cavity with a feedback gain K_P of 200 and a quality factor of $3{\cdot}10^7$ in dependance of the individual error sources for on-crest and off-crest ($\Phi_b = 13°$) operation. The phase noise of the LO has been derived by scaling the phase noise given in Figure 4.9 (Bandwidth:10Hz -10 MHz).

by phase noise from the master oscillator or time jitter of the bunches. Figure 2.12 displays the dependance of the energy jitter on the level of microphonics detuning. The lower plot also shows the dependance on detuning (for off-crest operation) including the other error sources set to realistic values for different RF feedback gains.

Before a discussion of these results one should consider the following about the influence of the different error sources.

- Microphonic detuning is very likely an error which is in a statistical sense uncorrelated between the cavities. The mean field error of the cavity by this effect will be reduced by $1/\sqrt{N}$. Nevertheless this amount of energy jitter is not correlated with respect to the longitudinal time axis in the phase space, thus not compressed at the bunch compressor. It determines the lower limit of the final time jitter at the linac exit.

- Beam related effects like injection time jitter and charge jitter are correlated among the cavities. But the influence of charge jitter is a small effect. The injection time jitter of the bunches lead to a correlation of bunch phase and energy and thus allows a compression of this jitter in the bunch compressor section. The energy jitter caused by this effect is still below the level set by stability reasoning.

- Phase noise by the master oscillator is an error which is correlated for all cavities. If the phase error induced by this effect is too large, it alters the correlated energy jitter by the injection time jitter. That means, that an effective compression of that jitter is reduced.

The following may be extracted from these calculations: To achieve a low time jitter at the linac exit the uncorrelated jitter has to be kept small to have a good compression of

---

[†] Band-limited white noise is assumed for phase and amplitude noise.

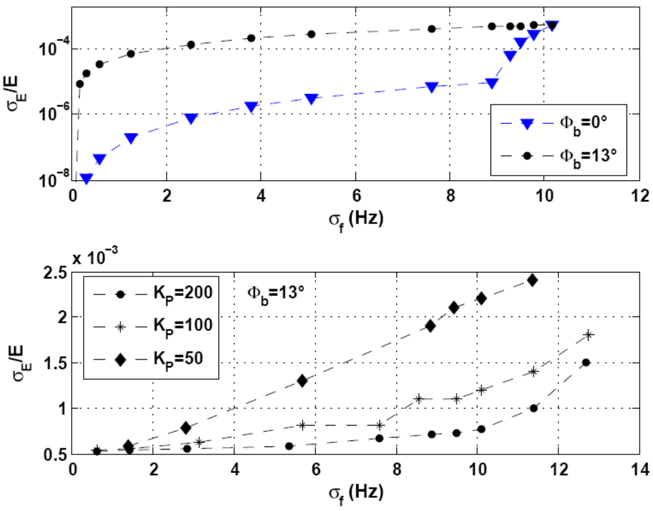

Figure 2.12: Bunch energy jitter after one cavity for different detuning values σ_f (Hz) (upper plot). The cavity parameters are the same as in Figure 2.11. The lower plot shows the energy jitter with detuning including the other typical error sources for different RF feedback gains K_P at Φ_b=13°.

the bunch-to-bunch distribution. This uncorrelated jitter is mainly given by the detuning. There are two possibilities to achieve a reduction of this error source. First to drive the cavity with a feedback gain as high as possible. This option may be limited by stability issues of high gain feedback systems and be further restricted by measurement noise in the control loop. An alternative method would be to reduce the effect of this error source by external means. To allow the effective time jitter compression further unwanted correlation by the master oscillator's phase noise have to be minimized, especially in the bandwidth of the complete cavity-controller setup (mainly the noise components between 10-10k Hz).

2.5.1 Required field stability

To give an upper limit for the required field stability and hence the detuning error sources, Figure 2.13 shows the final time and energy jitter of the electron bunches at the linac exit (upper plot). In this case the microphonics detuning is the only error source. The time jitter before the first bunch compressor is zero, so that only the uncorrelated energy jitter is translated into time jitter by BC1 and hence phase error for the next cavity sections (lower plot). The time jitter after the first bunch compressor is only slightly increased in the following linac section including the second compression.

The final time jitter should be below 60 fs for the fresh bunch technique and to guarantee stable FEL radiation (see Section 2.2). For the single cavity one may derive the following stability requirements:

The final time jitter is given by the correlated error sources of the injection time jitter[‡] and the uncorrelated single cavity field jitter, which are transferred by the bunch compressor to a time jitter.

Assuming a starting time jitter of 750 fs in the first section due to correlated error sources by beam time jitter from the photoinjector, a compression down to ~40 fs is possible

---

[‡] Assuming here an RF reference and synchronization system, which fulfills the phase noise requirements.

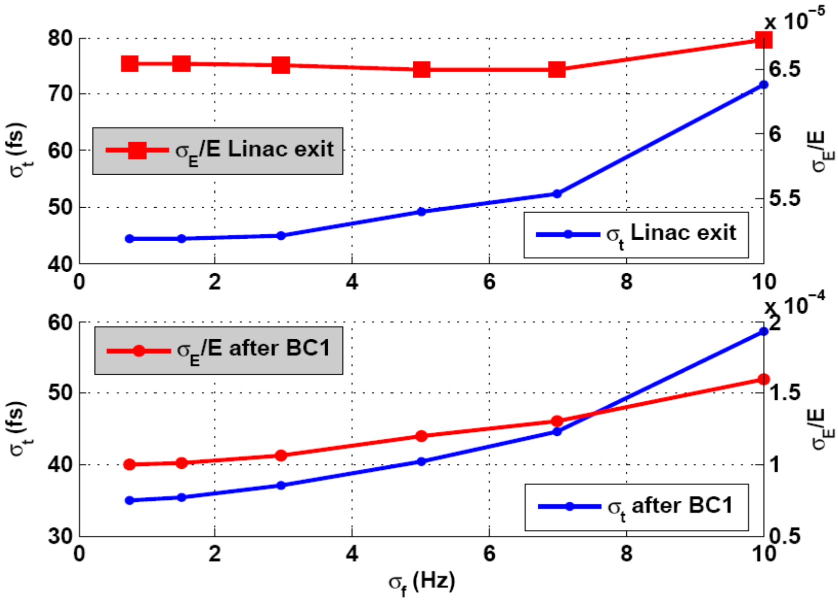

Figure 2.13: Dependance of linac exit (after L3) time and energy jitter of the electron bunches for different cavity detuning levels. Here microphonics is the only error source (upper plot). The lower plot shows the values after the first bunch compressor. The feedback gain in the first linac section before compression has been set to 250. Note, that for $\sigma_f \to 0$ the residual jitter are larger than 0 as an energy jitter from the gun (20 keV) is still included. The linac parameters are given in Table 3.1.

according to the simulations shown in Chapter 3. Here photoinjector means the combination of the photoinjector's RF cavity and the first accelerating TESLA cavity including a drift space in between. The jitter is made up of time jitter of the injector's laser, which releases the electrons from the photo-cathode. This jitter is further increased by non-relativistic effects, which lead to a velocity bunching depending on the phase of the bunches to the RF fields. A simulation of this effect is given in Appendix A. Given field stabilities achieved in present photoinjector RF cavities [22], an injector induced time jitter of 750 fs of the bunches seems realistic.

The jitter caused by microphonics and the injection jitter are stochastically independent. The total jitter is given by the quadratic sum. The allowable residual time jitter given by the total linac cavity energy jitter is thus

$$\sigma_{t,\Delta f} = \sqrt{\sigma^2_{t,final} - \sigma^2_{t,\mathrm{corr.}}} = \sqrt{60\mathrm{fs}^2 - 40\mathrm{fs}^2} = 45\mathrm{fs} \tag{2.15}$$

at the linac exit. According to the results in Figure 2.13 this corresponds to a maximum allowable detuning of 1.5-2 Hz rms. This is related to a phase stability of 0.016-0.02° for the feedback gain of 250 for these simulations.

The complete linac RF stability simulations in Chapter 3 will display similar results when including all further error sources. The critical error sources affecting the beam's stability are on the one hand the cavity detuning and on the other the injection time jitter. As shown in Appendix A this depends critically on the RF field stability of the photoinjector's cavity. In a second phase the BESSY-FEL will be equipped with an injector which is based on SRF technology. There again the stability of this SRF cavity's field in context of microphonics becomes an important issue.

Chapter 3

Modeling of SRF cavities

To be able to predict the achievable beam stability for a machine such as the BESSY-FEL models must be developed for the components involved in the beam acceleration. This includes the cavity, their mechanics, the tuning system and external noise sources, in particular microphonics. Later, for a refinement of the calculations measured values replaced the models.

In the following Chapter there will be given a short introduction to the physics of radio-frequency (RF) superconducting cavities. The description of the fundamental accelerating mode by an LCR equivalent circuit will be introduced and serves as a basis for the modeling of the cavity performance in continuous-wave driven mode. This model includes the cavity transient behavior, the RF and detuning feedback system, the cavity mechanics and their excitation, the klystron, beam-loading-related effects and noise from the RF reference system.

The model has been used to understand and analyze the expected impact of the error sources on the field stability. Including the detuning measurement results, the characterization of the tuning system and the detuning compensation presented in Chapters 5, 6 and 7, one can derive an estimate for the expected performance of the cavities.

To estimate the bunch-to-bunch beam stability with respect to energy -and timing jitter, the single cavity model has been used as an element of a whole linac RF model. The linac model incorporates the 144 accelerating cavities, the 3^{rd} harmonic cavity, the two bunch compressors with the accompanying arc and timing jitter due to the photo-injector and non-relativistic acceleration in the first cavities. It allows a calculation of the bunch-to-bunch distribution in the longitudinal phase space (energy, phase) to evaluate the influence of the various noise sources on the final stability. Furthermore upper bounds for the allowable detuning error can be formulated which demonstrates the importance of compensating microphonics which is discussed in Chapter 7.

3.1 Superconducting RF cavity: Figures of merit

Superconducting RF technology makes use of the effect, that the microwave resistance (R_s) drops theoretically down to the BCS-limit (Bardeen-Cooper-Schrieffer) when cooling the superconductor to T→0 K. Due to imperfections during the production and assembly of the superconducting cavity and trapped magnetic flux the BCS-limit is never reached but the residual RF-resistance for Niobium can be as low as a nΩ at 1.3 GHz [23]. It has a temperature independent and a temperature dependent term*:

$$R_s = R_{\mathrm{BCS}}(T) + R_{\mathrm{res}} \tag{3.1}$$

There are tangential magnetic fields at the cavity wall due to the field distribution of the TM$_{010}$ monopole mode. Following Maxwell's equation $\nabla \times \boldsymbol{B} = \mu \boldsymbol{J} + \mu\epsilon\partial\boldsymbol{E}/\partial t$ current must flow which results in power dissipation P_{diss} because of the surface resistance:

$$P_{\mathrm{diss}} = \frac{1}{2}\int\int \boldsymbol{H}^2 R_s ds. \tag{3.2}$$

For each mode one may define an intrinsic quality factor by

$$Q_0 = \frac{\omega_0 U}{P_{\mathrm{diss}}} \tag{3.3}$$

and ω_0 is the mode's frequency. U is the stored energy of the RF field inside the cavity. The *intrinsic* quality factor Q_0 describes the number of RF cycles a free running cavity disconnected from its power source would oscillate until damping down to $1/e$ of the initial stored energy times 2π.

The shunt impedance can be defined by

$$P_{\mathrm{diss}} = \frac{V_{\mathrm{cav}}^2}{R_{\mathrm{sh}}}. \tag{3.4}$$

R_{sh} is a measure for the time average power dissipation of a cavity. It measures the effectiveness of producing an axial accelerating voltage V_{cav} for a given power dissipation. When modeling the cavity resonance by an LCR circuit model, where the resistance is given by R_{sh}, the relation between these parameters is given by:

$$R_s = \frac{1}{2}\cdot R_{\mathrm{sh}} = \frac{1}{2}\cdot\left(\frac{R_s}{Q}\right)\cdot Q_0 \tag{3.5}$$

Here the term $\frac{R_s}{Q}$ describes the efficiency of acceleration per stored energy and can be obtained by combining Equation 3.5 with the definition of Q_0:

$$\frac{R_s}{Q} = \frac{V_{\mathrm{cav}}^2}{\omega_0 U}. \tag{3.6}$$

It only depends on the cavity geometry.

There are more processes included in the loss mechanisms of a cavity. The coupling by the input power coupler (see Figure 3.1) determines the amount of power leaking back into the cavity transmission line. These losses may be described by a quality factor, the *external* quality factor Q_{ext}:

$$Q_{\mathrm{ext}} = \frac{\omega_0 U}{P_{\mathrm{ext}}} \tag{3.7}$$

where P_{ext} incorporates all external power losses.

---

* In principal the BCS-resistance R_{BCS} is also a function of the RF frequency, but for this work only the value at f=1.3 GHz applies. In general: $R_{\mathrm{BCS}}(f) \simeq 2\cdot 10^{-4}\left(\frac{f}{1.5\cdot 10^9}\right)^2 \frac{e^{-17.67/T}}{T}$

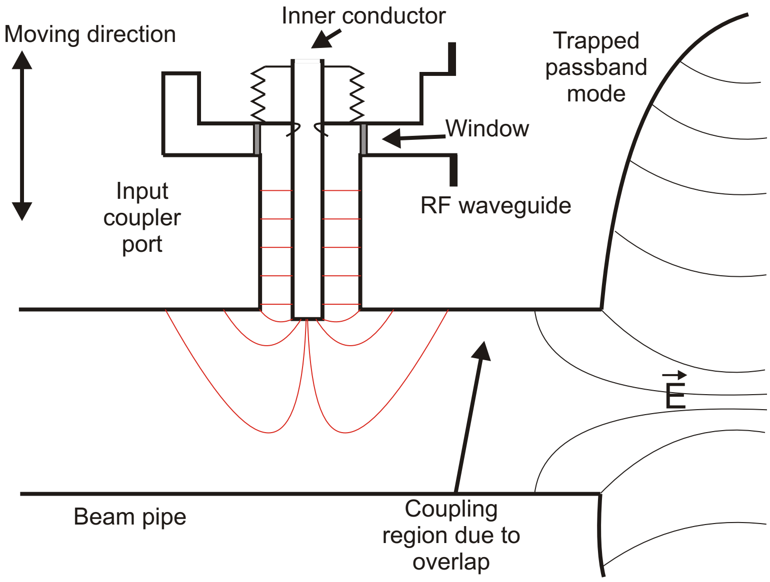

Figure 3.1: Scheme of an adjustable power coupler. The penetration depths of the coupler into the beam pipe defines the power transfer to the trapped passband mode in the first cavity cell.

As a result of the interaction of the particle beam with the cavity field a part of the stored energy is transferred to the beam, being the gained energy due to the acceleration. Therefore also a quality factor for this beam loading effect may be introduced by:

$$Q_{\mathrm{b}} = \frac{\omega_0 U}{P_{\mathrm{b}}}. \tag{3.8}$$

P_{b} represents the power lost due to the beam loading effect. This is only of importance for high beam current accelerators.

All loss effects may be summarized by a general quantity describing the quality factor of a cavity resonance diminished by the external effects, the *loaded* quality factor. This quantity as shown in the following determines the bandwidth of the RF resonance and will be the key parameter for characterizing CW driven RF cavities. It is given by:

$$\frac{1}{Q_{\mathrm{L}}} = \frac{1}{Q_0} + \frac{1}{Q_{\mathrm{ext}}} + \frac{1}{Q_{\mathrm{b}}}, \quad \text{and is derived from:} \quad P_{\mathrm{tot}} = P_{\mathrm{diss}} + P_{\mathrm{ext}} + P_{\mathrm{b}} \tag{3.9}$$

The BESSY-FEL will have a very low beam loading, such that it may be neglected and the loaded quality factor Q_{L} will be in the following regarded without the beam loading term.

While the possible RF eigenmodes of a cavity can be calculated from Maxwell's equations (see [24] or [25]) by incorporating the given boundary conditions, a base to model the dynamics and transient behavior of a cavity field is given by the LCR model described in the next section. The correspondences of the above given quantities to the impedance, inductance and capacitance will be shown.

3.2 Modeling the cavity behavior

The model presented in the following is based on the common LCR description of a cavity's RF passband modes as can be found in [4], [12] or [26]. This general model has been adapted

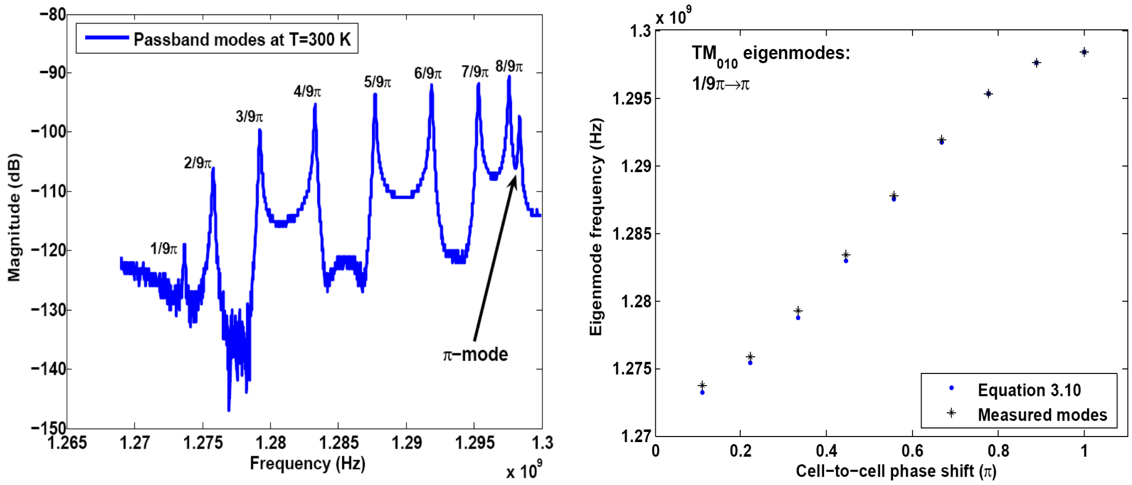

Figure 3.2: Passband modes of a TESLA cavity at room temperature (left plot) and the theoretical distribution of these modes.

to the parameters and the dominant error sources for CW operation.

The passband and its circuit model

A multi-cell type cavity consists of several cells (e.g. nine for TESLA-type) connected to the neighboring one via an iris. Each cell can be described as a single cavity.

The cells couple weakly to each other allowing only a set of eigenmodes which has specific phase shifts between the standing waves in each cell. The set of modes is given by:

$$\omega_q = \frac{\omega_{\pi/2}}{\sqrt{1 + k\cos\left(\pi q/N\right)}} \tag{3.10}$$

with N being the number of cells, q=1,2,...,N the mode's number and k the intra-cell coupling constant. Figure 3.2 shows the theoretical distribution for the TM_{010} passband modes of the nine-cell TESLA cavity and a measured spectrum by a network analyzer at room temperature.

The assembly of nine electrically or magnetically coupled cells may be described by nine single LCR circuits coupling inductively or capacitively. Figure 3.3 shows an equivalent circuit diagram of a nine-cell cavity with magnetic coupling. Of the nine passband modes the π-mode is used for acceleration as this phase shift allows for maximum energy gain of the particles when moving in a synchronized way through the nine cells. Next to the π mode is the $8/9\pi$-mode, which is only shifted by $\approx$ 800 kHz from the fundamental accelerating mode. Any control system of the RF field has to suppress this mode accordingly to allow stable acceleration. In principle the sum of all passband modes may be modeled by nine parallel acting LCR circuits, where the parameters L,C and R are the same for all nine cells with the exception of the end cells, which account for the openings for the beam pipe. According to field flatness measurements by [27] the relative variation of the LCR parameters on a cell-to-cell base are of the order of $3{\cdot}10^{-4}$.

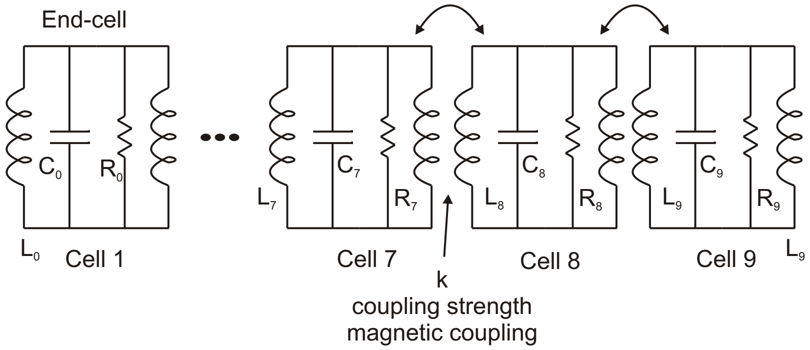

Figure 3.3: The equivalent circuit representation of a nine cell cavity with magnetically coupled cells.

The LCR circuit

Figure 3.4 shows a complete description of a cavity connected via a coupler and a waveguide to an RF power source. The excitation by the RF source can be modeled by a current source, which is matched to the waveguide connecting the source to the input coupler antenna. The impedance of the transmission line Z_0 is a real quantity and generally the characteristic impedance of a coaxial waveguide is 50 or 75 Ω. Any mismatch between the cavity and source impedances leads to a reflection of a part of the forward power wave at the coupler. As this reflected wave may destroy the RF source, the back traveling wave is redirected by a circulator into a matched load.

The coupling factor of the antenna's field with the standing wave of the cavity is described by an ideal transformer with a winding ratio 1:n. The input coupler connects the waveguide side and cavity side currents and voltages by the transformation equations:

$$V' = n \cdot V, \qquad I' = \frac{1}{n} \cdot I \tag{3.11}$$

which provides the following relationship between impedances of the waveguide side seen from the cavity side:

$$Z' = n^2 \cdot Z. \tag{3.12}$$

All primed quantities are given for the cavity side. The beam, extracting energy from the RF field, is represented by a current source shifted by the some phase with respect to the cavity voltage V_{cav}. A bunched beam can be seen as a pulsed current in time domain given by a series of Gaussian spaced peaks. The beam current seen by the RF field is given by the Fourier component of the beam at the RF frequency (see [4]). As will be shown, the bandwidth of CW SRF cavities is very small and hence only one spectral line of the bunched-beam spectrum couples to the RF field.

For this simplified view of the particle beam it is assumed, that the particles are already at the speed of light ($v = c$), that the velocity change is negligible during the passage of

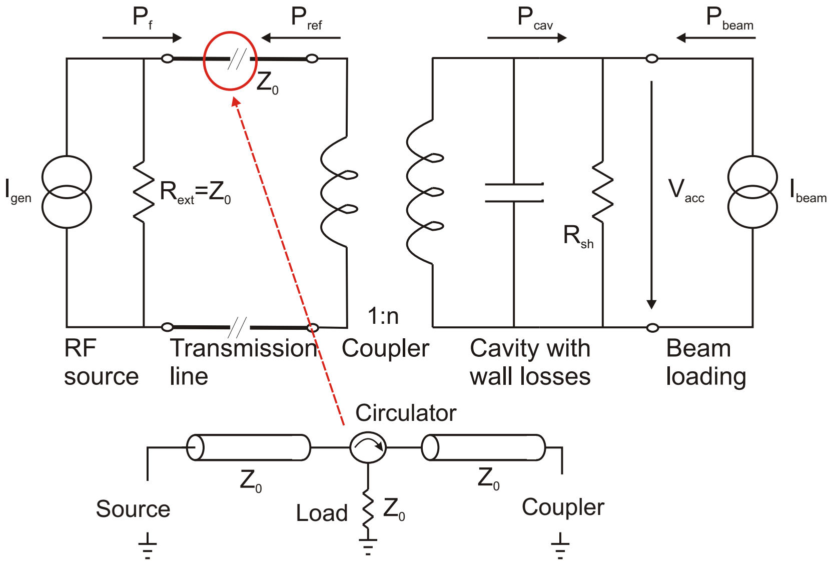

Figure 3.4: Equivalent circuit model for a cavity connected via a coupler antenna to an RF power source and accelerating a particle beam. The coupler is given by a transformer, the RF source is matched to the waveguide connecting to the coupler and is modeled by a current source. The beam, extracting energy from the cavity, is thus given by a current sink.

the cavity, so that the current is constant. Any excitation of higher-order modes by higher frequency components of the beam are not included in the simulation at this point. They may be regarded as sufficiently damped by special higher-order-mode (HOM) couplers.

To simplify the description, all impedances of the RF source side are transformed to the cavity side of the coupler. The input circuit has thus an impedance of $n^2 \cdot Z_0$ and the power dissipated in the waveguide and the cavity are given by:

$$P_{\text{ext}} = \frac{V_{\text{cav}}^2}{2n^2 Z_0} \tag{3.13}$$

$$P_{\text{diss}} = \frac{V_{\text{cav}}^2}{R_{\text{sh}}} \tag{3.14}$$

The coupling β_c between the RF forward wave and the field excited in the cavity may be defined by the ratio of emitted and dissipated power. If it is one, the coupler is perfectly matched and no power is reflected (no beam loading).

$$\beta_\text{c} = \frac{P_{\text{ext}}}{P_{\text{diss}}} = \frac{R_{\text{sh}}}{n^2 Z_0} \tag{3.15}$$

The circuit parameters can be related as follows to the cavity quantities:

$$V_{\text{cav}} = \quad \text{Voltage of the accelerating mode} \tag{3.16}$$

$$\omega_0 = \frac{1}{\sqrt{LC}} \tag{3.17}$$

$$Q_0 = \omega_0 R_{\text{sh}} C = \frac{R_{\text{sh}}}{L\omega_0} \tag{3.18}$$

$$Q_{\text{ext}} = \frac{Q_0}{\beta_\text{c}} = \sqrt{\frac{C}{L}} \frac{R_{\text{sh}}}{\beta_\text{c}} \tag{3.19}$$

A loaded impedance R_L related to the loaded quality factor Q_L is given by replacing the individual resistors $n^2 Z_0$ and R_sh by

$$\frac{1}{R_\mathrm{L}} = \frac{1}{R_\mathrm{sh}} + \frac{1}{n^2 Z_0} \Longleftrightarrow \tag{3.20}$$

$$\frac{1}{Q_\mathrm{L}} = \frac{1}{Q_0} + \frac{1}{Q_\mathrm{ext}} \quad \text{and following} \tag{3.21}$$

$$R_\mathrm{L} = \frac{R_\mathrm{sh}}{1+\beta_\mathrm{c}}, \qquad Q_\mathrm{L} = \frac{Q_0}{1+\beta_\mathrm{c}} \tag{3.22}$$

The intrinsic quality factor is a measure of the residual resistance and thus the heat load due to RF losses, which have to be handled by the cryogenic system, the loaded quality factor, as will be shown, defines the overall bandwidth of the RF mode. It is therefore a figure specifying the sensitivity of the accelerating mode to any frequency shifts of the resonance by detuning effects.

The envelope description

We are not interested in the cavity behavior on the time scale of the RF cycle but rather on the time scales of e.g. the detuning error sources or the beam repetition rate. Thus a description of the RF envelope suffices. A model for describing the behavior of the RF field envelope with time can now directly be derived from the circuit model with the cavity related parameters by applying Kirchhoff's loop rule. Taking the derivative with time a second order differential equation for the cavity voltage is obtained:

$$\ddot{V}(t) + \frac{\omega_0}{Q_\mathrm{L}}\dot{V}(t) + \omega_0^2 V(t) = \frac{\omega_0 R_\mathrm{L}}{Q_\mathrm{L}}\dot{I}(t) \tag{3.23}$$

This is the general form of a damped externally driven harmonic oscillator. Assuming an harmonic current applied to the right side of the equation, the solution of the differential equation is given by the stationary solution for $t \to \infty$, which is the particular solution [28]. The cavity will oscillate with the driving terms frequency as:

$$V(t) = \hat{V} \cdot \sin(\omega t + \psi) \quad \text{with } \hat{V} \text{ and } \psi \text{ given by} \tag{3.24}$$

$$\hat{V} = \frac{R_\mathrm{L} I_0}{\sqrt{1+\tan^2(\psi)}} \tag{3.25}$$

$$\tan(\psi) = Q_\mathrm{L}\left(\frac{\omega_0}{\omega} - \frac{\omega}{\omega_0}\right) \tag{3.26}$$

The difference between the driving frequency ω and the RF eigenmode frequency ω_0 can be expected to be small compared to the radio frequency of 1.3 GHz. With $\Delta\omega = \omega_0 - \omega$ as the cavity detuning Equations 3.25 and 3.26 can be rewritten to obtain the frequency dependence of the cavity field amplitude and phase, which is known as the Lorentz curve or Breit-Wigner distribution.

$$\tan(\psi) \approx 2 Q_\mathrm{L} \frac{\Delta\omega}{\omega_0} \tag{3.27}$$

$$\hat{V}(\Delta\omega) \approx \frac{R_\mathrm{L} I_0}{\sqrt{1+\tan^2(\psi)}} \tag{3.28}$$

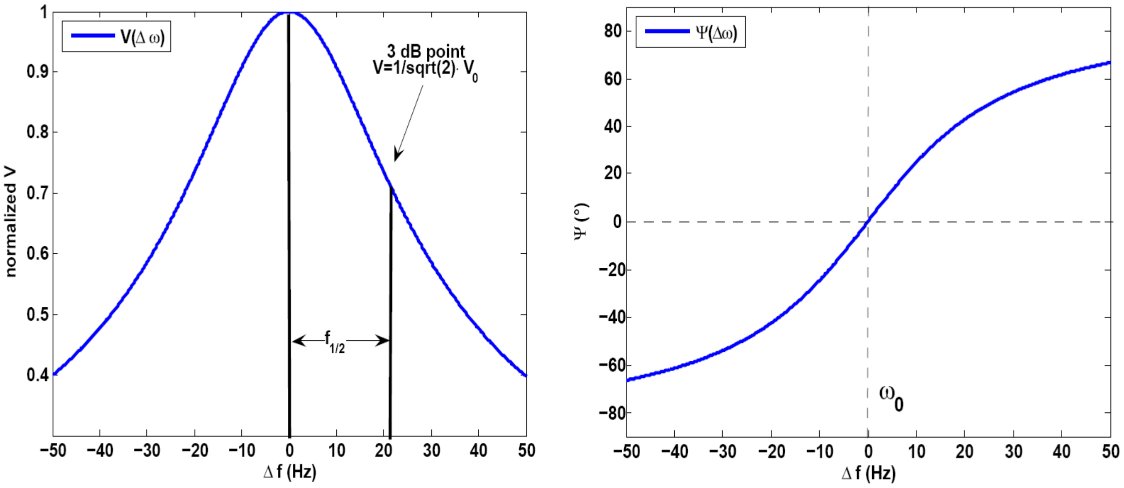

Figure 3.5: Amplitude and phase of a cavity resonance plotted against frequency. The 3dB point marks the bandwidth or half-bandwidth $f_{1/2}$ of the resonance.

This distribution is shown in Figure 3.5 for a loaded quality factor of Q_{L}=3·10^7. The half-bandwidth of a cavity resonance is defined as the point where the power($\propto V^2$) drops by -3 dB. The half-bandwidth can be expressed by

$$\omega_{1/2} = \frac{\omega_0}{2Q_{\mathrm{L}}}, \text{ where } \psi = \pm\tfrac{\pi}{4} \tag{3.29}$$

In the following, equations describing the transient behavior of the (TESLA)[†] cavity in CW mode will be derived. These equations will only simulate the evolution of the field envelope vector with time, as the time scale on which the error sources affect the field stability is rather long compared to the RF period. The starting point is given by Equation 3.23, describing the driven LCR circuit model. The cavity is assumed to be in steady state with respect to be constantly driven by the RF power source apart from small perturbations. Time varying contributions will be given by beam loading, klystron noise and cavity detuning related error sources.

The solution for the cavity field is given, as well as the current driving the cavity, by a harmonic behavior with an $e^{i\omega t}$ time dependence.

$$\begin{aligned} \boldsymbol{V}(t) &= (V_{\mathrm{re}}(t) + iV_{\mathrm{im}}(t)) \cdot e^{i\omega t} \\ \boldsymbol{I}(t) &= (I_{\mathrm{re}}(t) + iI_{\mathrm{im}}(t)) \cdot e^{i\omega t} \end{aligned} \tag{3.30}$$

The envelope field vector is thus described by its real and imaginary components or phasor representation. In RF control theory these parameters are called *in-phase* (I) and *in-quadrature* (Q). Figure 3.6 displays the relationship of V_{re} and V_{im} or I and Q with the field vectors amplitude and phase.

The field vector rotates with 1.3 GHz around the center of the unity circle. Any change of the vector components by slow variations as cavity detuning leads to a further modulation of the field's amplitude and phase. The time varying behavior of a CW-driven cavity is sufficiently described by the field's vector envelope $V_{\mathrm{re}}(t)$ and $V_{\mathrm{im}}(t)$.

[†] In principle this model may be used for any cavity by adapting the parameters, such as $\frac{R_s}{Q}$.

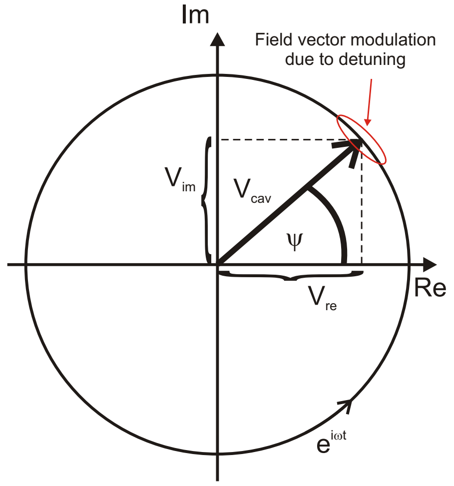

Figure 3.6: Phasor representation of the RF field vector. The field vector circles with $\omega/(2\pi)$=1.3 GHz. A slower disturbance due to detuning errors leads to an additional modulation of the vectors amplitude and phase.

A separationansatz can be made as given by Equations 3.30 by only inserting the slow field variations into Equation 3.23. This represents also the usage of a LLRF control system. As it is impractical to sample a field at its radio frequency of 1.3 GHz with the needed accuracy, the signal is down-converted to an intermediate frequency (IF) signal still containing the sideband information of the cavity detuning error sources. This IF signal is used to detect the I and Q components of the field vector.

Neglecting all terms with the second derivative in time as they are small compared to the lower order terms and linearizing the equations around the resonance frequency ω_0 one obtains the first-order differential equations for the field envelope (The whole derivation starting from Maxwell's equations is given in [20]).

$$\begin{aligned} \dot{V}_{\mathrm{re}} + \omega_{1/2} V_{\mathrm{re}} + \Delta\omega V_{\mathrm{im}} &= R_{\mathrm{L}} \omega_{1/2} I_{\mathrm{re}} \\ \dot{V}_{\mathrm{im}} + \omega_{1/2} V_{\mathrm{im}} - \Delta\omega V_{\mathrm{re}} &= R_{\mathrm{L}} \omega_{1/2} I_{\mathrm{im}} \end{aligned}$$

This equation can be rewritten in the matrix form of the state space formalism as

$$\frac{d}{dt}\begin{pmatrix} V_{\mathrm{re}} \\ V_{\mathrm{im}} \end{pmatrix} = \begin{pmatrix} -\omega_{1/2} & -\Delta\omega \\ \Delta\omega & -\omega_{1/2} \end{pmatrix} \cdot \begin{pmatrix} V_{\mathrm{re}} \\ V_{\mathrm{im}} \end{pmatrix} + \begin{pmatrix} R_{\mathrm{L}}\omega_{1/2} & 0 \\ 0 & R_{\mathrm{L}}\omega_{1/2} \end{pmatrix} \cdot \begin{pmatrix} I_{\mathrm{re}} \\ I_{\mathrm{im}} \end{pmatrix} \tag{3.31}$$

with the following matrixes:

$$\boldsymbol{A} = \begin{pmatrix} -\omega_{1/2} & -\Delta\omega \\ \Delta\omega & -\omega_{1/2} \end{pmatrix}$$

$$\boldsymbol{B} = \begin{pmatrix} R_{\mathrm{L}}\omega_{1/2} & 0 \\ 0 & R_{\mathrm{L}}\omega_{1/2} \end{pmatrix}$$

$$\vec{x}(t) = \begin{pmatrix} V_{\mathrm{re}}(t) \\ V_{\mathrm{im}}(t) \end{pmatrix}$$

$$\vec{u}(t) = \begin{pmatrix} I_{\mathrm{re}}(t) \\ I_{\mathrm{im}}(t) \end{pmatrix}$$

The driving term given by the current vector consists of the transformed contribution from the klystron and the beam current

$$\vec{u}(t) = \begin{pmatrix} \frac{1}{n} I_{\mathrm{kly,re}} + I_{\mathrm{b,r}} \\ \frac{1}{n} I_{\mathrm{kly,im}} + I_{\mathrm{b,im}} \end{pmatrix} \tag{3.32}$$

The matrix $\boldsymbol{A}$ describes the transition of the cavity state, given by the two field vector components, in time by incorporating the cavity bandwidth and detuning. For each finite time step the detuning may be regarded as constant, so that this system of equations can be assumed to be linear and time invariant for short times. Regarding the timescale of detuning in the ms regime and the simulation time constant of 1 μs, the system may be regarded as being time invariant for t<100 μs. The half-bandwidth is a constant parameter. Each change of the detuning will lead to a different steady state response of the cavity. In the case of the detuning with time the system will oscillate about the mean steady state.

The matrix $\boldsymbol{B}$ represents the driving term including the coupling of the klystron forward power to the cavity mode and the beam loading term. With a given starting condition of $\vec{x}(t_0) = \begin{pmatrix} V_{\mathrm{re}}(t_0) \\ V_{\mathrm{im}}(t_0) \end{pmatrix}$ the general solution of a state space system of differential equations is [29]

$$\vec{x}(t) = \left. \underbrace{e^{\boldsymbol{A}\cdot t}}_{\boldsymbol{\Phi}(t_0)} \cdot \vec{x}(t_0) + \int_{t_0}^{t} \underbrace{e^{\boldsymbol{A}\cdot(t-t')}}_{\boldsymbol{\Phi}(t-t')} \cdot \boldsymbol{B} \cdot \vec{u}(t')dt' \right|_{t_0=0} \tag{3.33}$$

The state transition matrix $\boldsymbol{\Phi}(t)$ given by the matrix exponential of the system matrix $\boldsymbol{A}$ can be derived in the Laplace frequency domain [29] by:

$$\boldsymbol{\Phi}(t) = \mathcal{L}^{-1} \left. \left\{ \left(s \begin{bmatrix} 1 & 0 \\ 0 & 1 \end{bmatrix} - \boldsymbol{A} \right)^{-1} \right\} \right|_{t} \tag{3.34}$$

Here $\mathcal{L}^{-1}$ is the inverse Laplace transformation [28] and s is the Laplace space variable $s = \sigma + i\omega$ (σ is a real damping term). Transforming $\boldsymbol{A}$ into Laplace space variable representation and forming $(s\boldsymbol{I} - \boldsymbol{A})^{-1}$ and doing a back transformation yields the transition matrix $\boldsymbol{\Phi}(t)$:

$$\boldsymbol{\Phi}(t) = e^{-\omega_{1/2} t} \begin{pmatrix} \cos(\Delta\omega t) & \sin(\Delta\omega t) \\ \sin(\Delta\omega t) & \cos(\Delta\omega t) \end{pmatrix} \tag{3.35}$$

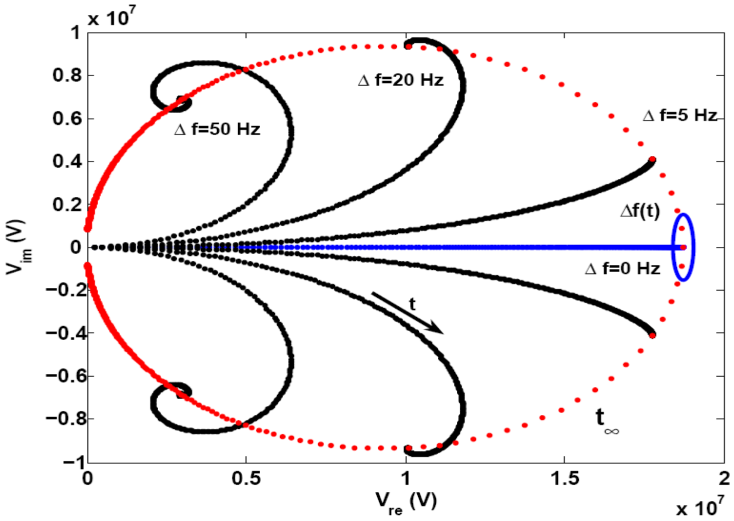

Figure 3.7: Transient behavior of the cavity field components for several detuning values when constant power is coupled to the cavity. The detuning defines the final position on the circle given by the steady state solution. The following parameters were used: $Z_0 = 50\Omega$, $Q_L = 3 \cdot 10^7$, $\frac{R_s}{Q} = 1040\Omega$, $f_{1/2}$=21.7 Hz. The small blue circle shows the rotation around the mean steady state solution due to time varying detuning.

For a constant input power only containing a real component, i.e. $\boldsymbol{I} = \begin{pmatrix} I_{\mathrm{g}} \\ 0 \end{pmatrix}$, Equation 3.33 may be solved in Laplace domain and transformed back into time domain to obtain the following solution:

$$\begin{pmatrix} V_{re} \\ V_{im} \end{pmatrix} = \frac{R_{\mathrm{L}} \cdot I_{\mathrm{g}} \cdot \omega_{1/2}}{\left(\omega_{1/2}^2 + \Delta\omega^2\right)} \cdot \left[e^{-\omega_{1/2} t} \begin{pmatrix} -\omega_{1/2} \cos(\Delta\omega t) + \Delta\omega \sin(\Delta\omega t) \\ -\omega_{1/2} \sin(\Delta\omega t) - \Delta\omega \sin(\Delta\omega t) \end{pmatrix} + \begin{pmatrix} \omega_{1/2} \\ \Delta\omega \end{pmatrix} \right]. \tag{3.36}$$

For t→ ∞ the exponential term vanishes and the steady state solution is expressed by

$$\begin{pmatrix} V_{\mathrm{re}} \\ V_{\mathrm{im}} \end{pmatrix} = \frac{R_{\mathrm{L}} \cdot I_{\mathrm{g}} \cdot \omega_{1/2}}{\left(\omega_{1/2}^2 + \Delta\omega^2\right)} \begin{pmatrix} \omega_{1/2} \\ \Delta\omega \end{pmatrix} \Bigg|_{t \to \infty} \tag{3.37}$$

In the case of time varying detuning $\Delta\omega(t)$ the obtained field vector circulates with the modulating frequency around this steady state solution. The steady state solutions for several detuning offset values are depicted in Figure 3.7. The steady state solution forms in dependance of the detuning and the constant input power a circle in the complex plane. The transient behavior for several detuned cases are given by the black dotted lines.

Rewriting Equation 3.36 in complex notation the complex field vector envelope is given by

$$\boldsymbol{V}(t, \Delta\omega, \boldsymbol{I}) = \frac{R_{\mathrm{L}} \boldsymbol{I}}{1 - i \frac{\Delta\omega}{\omega_{1/2}}} \left(1 - e^{-(\omega_{1/2} - i\Delta\omega)t}\right). \tag{3.38}$$

The detuning angle of the steady state solution again is given by

$$\tan\psi := \frac{\Delta\omega}{\omega_{1/2}}. \tag{3.39}$$

Taking the magnitude of the steady state response of Equation 3.38 $V_{cav,stat}$ and using the detuning angle definition again gives the Lorentz curve of the cavity field resonance

$$V_{\mathrm{cav,stat}} = |\boldsymbol{V}|_{t\to\infty} = \frac{R_{\mathrm{L}}\,|\boldsymbol{I}|}{\sqrt{1+\frac{\Delta\omega^2}{\omega_{1/2}}}} = \frac{R_{\mathrm{L}}\,|\boldsymbol{I}|}{\sqrt{1+\tan^2(\psi)}}. \qquad (3.40)$$

3.3 Simulating RF control with the cavity model

Based on the derived field envelope description of the LCR circuit cavity model a simulation tool has been developed.

The continuous state space model (Equation 3.31) of the π-mode forms the central part of the cavity model. For different aspects of simulations the continuous model is solved by Runge-Kutta or Euler integration methods [30] or can be transferred directly to a time-discrete description. The latter is useful for introducing time-discrete systems like digital controllers and time delays formed by system latencies. This is mainly of importance to test the stability limits of LLRF controllers based on digital systems in simulation.

For the characterization of the cavity driven in CW-mode and being exposed to different error sources a hybrid model of continuous and time discrete subsystems has been used. In general the accuracy of this model and the continuous components are dependent on the sampling time of the integration methods used. Mostly this time constant has been chosen as T_{sim}=$1{\cdot}10^{-6}$ seconds.

The measurement results, as given in Chapters 3-7, have been included to allow a more realistic simulation of the expected field stability for the BESSY-FEL.

Figure 3.8 shows an overview of the model programmed in Matlab-Simulink$^{\mathrm{TM}}$. It includes the cavity state space model and a number of noise sources: Microphonics, Lorentz-force detuning, noise from the master oscillator, klystron noise and saturation and beam related effects. The subsystems of the model, as given by the Figure, will be presented in the following.

3.3.1 System components and error sources

Klystron or inductive output tube

The klystron or IOT (inductive output tube, see [31]) is modeled as an amplifier with a bandpass wider than the highest frequency which may occur due to the error sources. Both systems usually have a bandwidth of several MHz. A typical gain curve for an IOT, being considered for the BESSY-FEL [1], with a saturation level of 13-17 kW is given by a look-up table (Figure 3.9) [32]. To account for the noise an IOT has, some amplitude and phase noise contributions being of the order of 5 ‰ have been introduced. The frequencies of this noise has been assumed as a band-limited white noise contributions. A thorough analysis of all phase noise sources, including all amplifiers of the RF setup, still needs to be done.

The Low-level RF controller

The LLRF controller is given by the discretized version of a proportional-integral-derivative controller (PID). A digital lowpass filter is included, which serves in a typical LLRF system to damp the next passband mode given by the $8/9\pi$-mode. The cutoff frequency of this

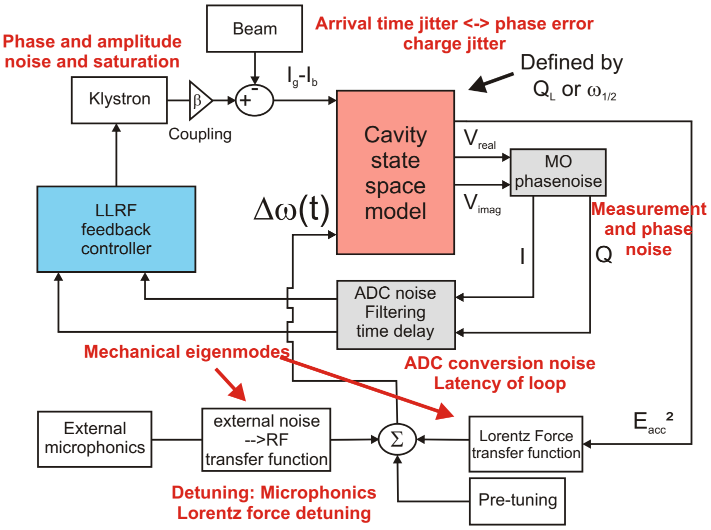

Figure 3.8: Overview of the cavity modeling in Matlab-Simulink^{TM}including the cavity state space description, a mechanical model with the different detuning sources contributing to the total detuning $\Delta\omega$, a model for the klystron with saturation and noise effects, measurement noise, phase noise from the master oscillator, beam loading effects and time delay in the feedback path.

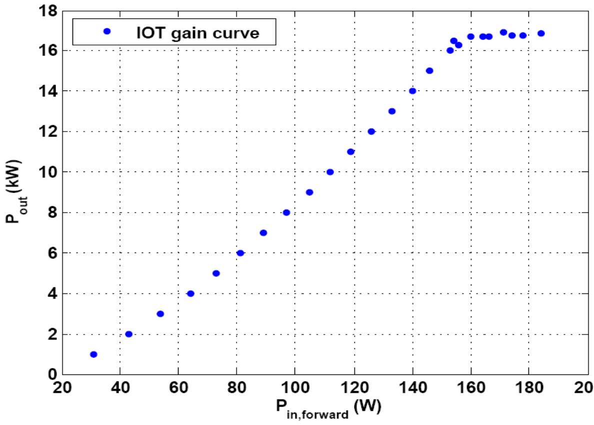

Figure 3.9: Measured IOT gain curve with saturation at high input levels.

filter depends on the sampling time of the digital system. For the planned system it will lie between 100-500 kHz. Additionally there is a time delay which can be set in multiples of the simulation sampling time $T_{\rm sim}$ and is usually about 1-2 μs. Present day digital LLRF feedback systems can perform better, achieving latencies of order of several hundred nanoseconds.

The analogue-to-digital conversion is modeled by a sample and hold block assuming 14 bit resolution. Thus least-significant-bit noise is also implemented.

The measurement process of the field vector is based on down-converting the RF from 1.3 GHz to some intermediate frequency to measure the field envelope components. The process of down-conversion at an RF mixer, as explained in Chapter 4, is diluted by measurement noise. Non-linearities of the RF mixer and noise contributions from the sideband phase noise of the master oscillator will falsify the measurement. The phase noise leads to an unwanted phase modulation of the measured signal, which the feedback will compensate for and hence the feedback signal. Time domain phase noise signals can be modeled by a Fourier series of the individual sideband phase noise contributions extracted from the measured spectrum (as in Figure 4.9) as:

$$\theta(k \cdot T_\mathrm{s}) = \sum_{i=1}^{n} \sqrt{2} \cdot (10^{P_\mathrm{i}[dBc/Hz]/20}) \cdot \sin(p_\mathrm{i} \cdot 2 \cdot \pi \cdot kT_\mathrm{s} + \psi_\mathrm{i}), \tag{3.41}$$

with $k \cdot T_\mathrm{s}$ the discrete time step of the simulation, p_i the offset frequency of the sideband, ψ gaussian distributed phase between 0 and 2π and P_i the power contribution at the offset frequency in a 1 Hz bandwidth. A more detailed description about phase noise can be found in [33], about the modeling see [34]. The phase noise used for modeling encompasses integrated timing jitters between 50 fs and 1 ps in a sideband between 1.0 Hz-1.0 MHz. The integrated time jitter is thereby given by:

$$\Delta T = \frac{1}{2\pi f_0} \cdot \sqrt{2 \int \frac{(\Delta\Theta)^2}{B} \cdot df}, \tag{3.42}$$

where f_0 is the RF carrier frequency and $\Delta\Theta$ the phase noise contribution of each sideband in radian. The LLRF feedback gains used for the calculations is about ten times higher as given by [12] for two reasons. The pulsed TESLA system becomes unstable at a gain of 210, given a cavity bandwidth of 430 Hz. The cavity bandwidth will be approximately ten times smaller for the BESSY-FEL. The transfer function of the cavity drops by 20 dB per decade in magnitude allowing a higher critical gain for the narrow bandwidth CW-operated cavities.

The limiting factor for the gain is mainly given by all parameters increasing the phase shift between the measured cavity error and the output of the controller to the IOT. The critical gain at 2 μs time delay and the loaded quality factor of $3{\cdot}10^7$ is about 2000 allowing theoretically a stable operation at a gain of 1000 [35]. Regarding the amplification of all noise sources the gain has been limited to 200-400.

Mechanical detuning model

The detuning of the cavity model consists of three different sources. A tuner pre-detunes the cavity such that any kind of static Lorentz force detuning is compensated. The dynamic Lorentz-force detuning as well as the coupling of the cavity to external mechanical oscillations are modeled by second order systems incorporating about 20 mechanical eigenmodes of the cavity system. The model, derived by [36], is given by a set of parallel acting eigenmodes which couple differently to external oscillations. In principal the transfer characteristic of mechanical noise acting on the cavity body from the outside is unknown and cannot be measured directly. Instead, the detuning response excited by the fast piezo tuner (Chapter 6) sweeping the frequency range of microphonics detuning has been used.

The time domain description of the mechanical system is given by:

$$\begin{aligned} \Delta\ddot{\omega}_\mathrm{cav,i}(t) + 2\xi\omega_\mathrm{m,i} \cdot \Delta\dot{\omega}_\mathrm{cav,i}(t) + \omega_\mathrm{m,i}^2 \cdot \Delta\omega_\mathrm{cav,i} &= -k_i 2\pi\omega_\mathrm{m,i}^2 F(t) \\ \Delta\omega_\mathrm{cav}(t) &= \sum_i \Delta\omega_\mathrm{cav,i}(t) \end{aligned} \tag{3.43}$$

Here $\omega_\mathrm{m,i}$ is the frequency of the i^th mechanical eigenmode , ξ the damping constant, $\Delta\omega_\mathrm{cav}$ the detuning contribution by this mechanical mode, k some coupling constant between the

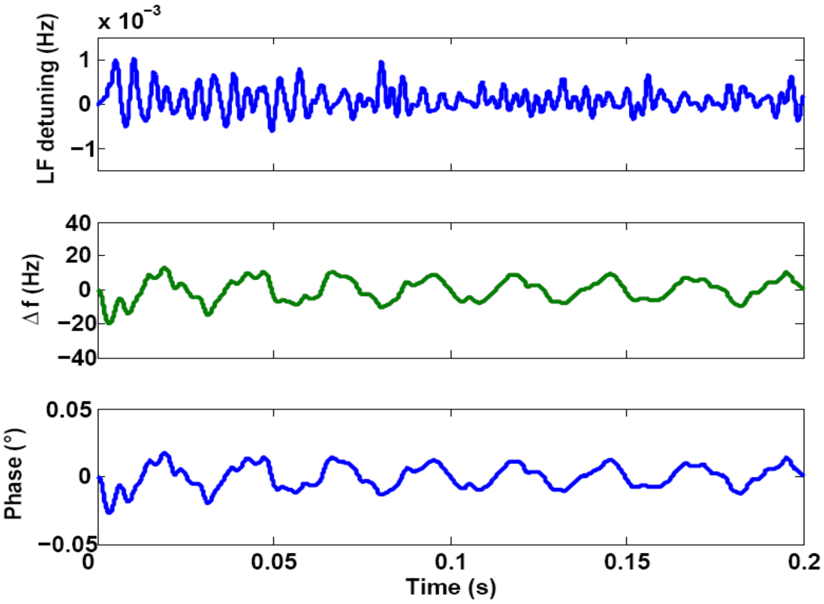

Figure 3.10: Simulated Lorentz force detuning, microphonic detuning and phase for a cavity with Q_{L}=3·10^7. The rms detuning is 6.6 Hz. The phase follows the detuning, as expected by $\tan(\Phi) = \Delta f/f_{1/2}$. The feedback (gain 200) suppresses any field amplitude modulation, thus very little Lorentz-force detuning occurs.

external time varying forces and this mode. The damping time constant of each mode is $\tau_{\mathrm{m}} = 1/\xi\omega_{\mathrm{m}}$.

The total detuning is given by the sum of all components. The driving term for the Lorentz force detuning is given by the square of the field vector, whereas the driving term for the microphonics detuning are those measured in HoBiCaT.

The detuning is updated each simulation time step. The Lorentz force detuning and microphonics may be saved separately to analyze their individual contributions.

Making use of the advanced matrix handling capabilities of Matlab$^{\mathrm{TM}}$, the mechanical models have also been transformed to a state space notation, here e.g. for the Lorentz force detuning:

$$\begin{bmatrix} \Delta\dot{\omega}_1 \\ \Delta\ddot{\omega}_1 \\ \cdot \\ \cdot \\ \Delta\dot{\omega}_{\mathrm{n}} \\ \Delta\ddot{\omega}_{\mathrm{n}} \end{bmatrix} = \begin{bmatrix} 0 & 1 & \cdots\, 0\; 0 \\ -\omega_1^2 & -\frac{1}{\tau_1} & \cdots\, 0\; 0 \\ & \cdots & \\ & \cdots & \\ 0\; 0 \cdots & 0 & 1 \\ 0\; 0 \cdots & -\omega_{\mathrm{n}}^2 & -\frac{1}{\tau_{\mathrm{n}}} \end{bmatrix} \cdot \begin{bmatrix} \Delta\omega_1 \\ \Delta\dot{\omega}_1 \\ \cdot \\ \cdot \\ \Delta\omega_{\mathrm{n}} \\ \Delta\dot{\omega}_{\mathrm{n}} \end{bmatrix} + 2\pi \begin{bmatrix} 0 \\ -k_{\mathrm{LF},1}\omega_1^2 \\ \cdot \\ \cdot \\ 0 \\ -k_{\mathrm{LF,n}}\omega_{\mathrm{n}}^2 \end{bmatrix} \cdot V_{\mathrm{acc}}^2 \qquad (3.44)$$

Here n means the total number of modes simulated. The static Lorentz force detuning is about k_{LF}=1.4 Hz/(MV/m)^2, as shown in Section 5.3 and is the DC component of the sum over all modes.

As an example the simulated detuning and its influence on the cavity's phase stability is depicted in Figure 3.10 for a measured microphonics spectrum. All other error sources have been set to zero, the LLRF feedback gain was 200. The phase stability is mainly given by the microphonics detuning. Given these settings the amplitude modulations are too small to lead to any significant Lorentz force detuning.

Beam loading

If the beam is distributed in trains of bunches, there may be not enough power available to replenish the energy lost to a bunch before the next one follows then the second will be accelerated at a reduced field level. This will in total widen the expected energy spread of the bunches. In the BESSY-FEL the bunch repetition rate will be more relaxed. But nevertheless any variations in the bunch charge will only partly be compensated, that a charge jitter induced increase of the energy jitter will be observed. The total cavity voltage after bunch passage is given in complex notation by:

$$\begin{aligned} \boldsymbol{V}(t) &= \boldsymbol{V}_{\mathrm{kly}}(t) + \boldsymbol{V}_{\mathrm{beam}}(t) && (3.45) \\ &= \frac{R_{\mathrm{L}}\frac{2}{n}\boldsymbol{I}_{\mathrm{kly}}(t)}{1 - i\frac{\Delta\omega}{\omega_{1/2}}}\left(1 - e^{-(\omega_{1/2} - i\Delta\omega)t}\right) + \frac{R_{\mathrm{L}}2\boldsymbol{I}_{\mathrm{b},0}(t)\Theta(t - t_{bunch})}{1 - i\frac{\Delta\omega}{\omega_{1/2}}} && (3.46) \\ &\times \left(1 - e^{-(\omega_{1/2} - i\Delta\omega)(t - t_{bunch})}\right) \end{aligned}$$

If there is no detuning ($\Delta\omega = 0$) this equation becomes

$$\boldsymbol{V} = R_{\mathrm{L}}\left(\frac{2}{n}\boldsymbol{I}_{\mathrm{kly}}(t)\left(1 - e^{-\omega_{1/2}t}\right) + 2\boldsymbol{I}_{\mathrm{b},0}(t)\Theta(t - t_{bunch})\left(1 - e^{-\omega_{1/2}(t - t_{bunch})}\right)\right)$$

Assuming, that the cavity has already reached its CW steady state prior to the bunch passage, the first exponential term will vanish. The time t_{bunch} is the general injection time of the electron bunch, the complex quantity of the beam current $\hat{I}_{\mathrm{b},0}$ incorporates the injection phase and any injection phase errors.

The beam loading includes two error sources: The bunch charge fluctuates with the laser amplitude of the photo-injector. It is assumed to be between 5-10 % [37]. The laser pulse will also jitter in time, thus leading to shifted arrival times of the electron bunch in the cavity. This alters the injection phase and thus the energy gained by the bunch. This is particulary important at the beginning of the acceleration process in the RF cavity of the photo-injector and the first booster cavity. This section includes drift spaces, where different velocities lead to a rearrangement of the bunches in the longitudinal phase space. This problem is shortly addressed in Appendix A.

The beam energy transferred by one cavity may also expressed by the phasor components, where the cavity amplitude, phase and the beam phase errors are included:

$$E_b = \Re\left(\frac{\boldsymbol{V}_{\mathrm{cav}} \cdot \boldsymbol{I}_{\mathrm{b}}}{|\boldsymbol{I}_{\mathrm{b}}|}\right) e. \ [E_b] = \mathrm{eV} \tag{3.47}$$

Figure 3.11 displays the cavity field amplitude being distorted by the jitter in the beam loading. The variations in the induced voltage by the beam is given by a 5 % charge jitter and a 250 fs arrival time jitter. The bunch charge is 2.5 nC. In this case the bunch repetition rate is 25 kHz, leading to a beam loading current of 125 μA. In general this effect can be neglected as small, because the beam loading itself is small and thus a small influence on the final energy jitter, which has already be shown in Section 2.5.

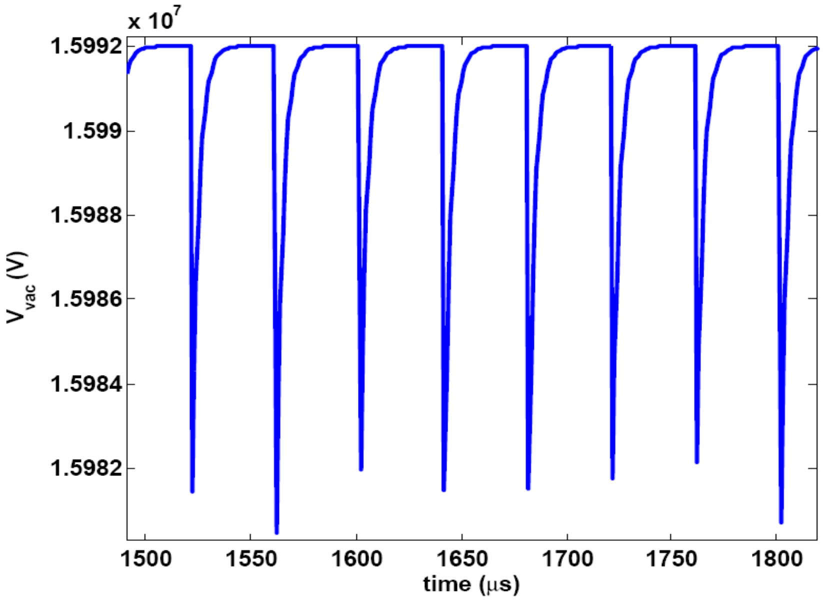

Figure 3.11: Simulated beam loading for a cavity with Q_L=3·10^7 driven in cw-mode. The bunch charge is about 2.5 nC including a bunch-to-bunch charge jitter of 5%. The beam loading induced voltage drop varies with the charge and arrival time jitter of the electron bunches. The field recovers after each bunch, as a control system compensates these losses.

Effect of detuning: Beam energy modulation

To show by means of simulation what influence the microphonics may have on the electron beam stability the calculations shown in Figure 3.12 represent a case with high detuning of σ_f = 10.8 Hz. The feedback gain is 200 and the loaded quality factor 4.1·10^7. The sinusoidal detuning (derived from a scaled measurement) is visible in the bunch-to-bunch energy fluctuations with time and the relative energy error is 1.2·10^{-3}. This is already a factor of two above the permissable cavity jitter derived in Section 2.5.

3.4 Field stability versus bandwidth

It has been shown in Section 2.5.1, that the low time jitter requires a low microphonics detuning or a low phase error in the individual cavities. While correlated energy chirps may be partly compressed by the bunch compressor, the uncorrelated errors (with respect to correlation of bunch energy against time) have to be suppressed by a high gain RF feedback to minimize the final time jitter. But the RF feedback may be limited in performance by measurement noise and it requires additional RF power. Hence, a better option is to limit or reduce the main error source, namely microphonics. This will be pursued in the following work.

A different approach would be to reduce the effect of detuning by increasing the RF bandwidth of the resonant mode. This is possible by increasing the coupling strength, i.e. the external and thus loaded quality factor Q_L (See Equation 3.27). In the same way for a given detuning one would decrease the phase error as $\sigma_\Phi = \arctan(\sigma_f/f_{1/2})$.

A limitation to this procedure is given by the amount of power needed to drive the cavity CW at a given beam loading and detuning of the cavity. Equation 3.48 displays the

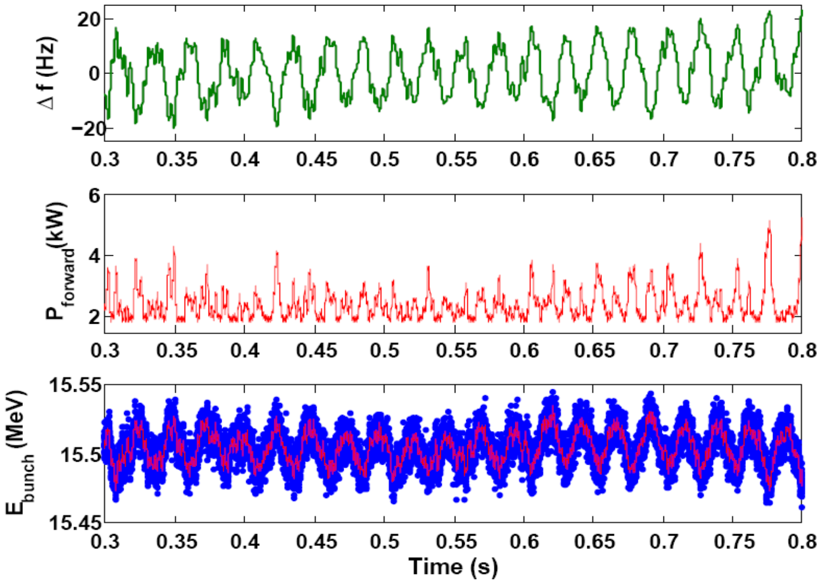

Figure 3.12: Detuning, forward power and induced bunch-to-bunch energy modulation (the red line shows an averaged value to emphasize the sinusoidal energy modulation) for σ_f = 10.8 Hz at Q_L=4.1·10^7 with an LLRF feedback gain of 200 and V_{cav} = 15.5 MV/m.

dependance of the required forward power to maintain a constant field [23].

$$P_{\text{f}} = \frac{V_{\text{cav}}^2}{4\left(\frac{r}{Q}\right)Q_{\text{L}}} \cdot \left(\left(1 + \frac{\left(\frac{r}{Q}\right)Q_{\text{L}}I_{\text{b}}}{V_{\text{cav}}}\cos(\Phi_{\text{b}})\right)^2 + \left(\left(\frac{\Delta f}{f_{1/2}}\right) + \frac{\left(\frac{r}{Q}\right)Q_{\text{L}}I_{\text{b}}}{V_{\text{cav}}}\sin(\Phi_{\text{b}})\right)^2\right) \tag{3.48}$$

For a machine with low beam loading the needed power merely evolves with the detuning over the half-bandwidth squared, so that for a small bandwidth significant power overhead is required by the RF control process to compensate detuning. Figure 3.13 shows the forward power as a function of the loaded quality factor (or bandwidth of the resonance) for different amount of peak detuning and a beam current of 75 μA. The optimized Q_{L} for an assumed peak detuning of 20 Hz would be $\simeq$ 3.2·10^7.

The amount one can reduce Q_{L} to improve the field stability is limited by the amount of power, which has to be supplied by the klystron and constantly transmitted by all waveguide components and the input coupler. Figure 3.14 shows the result of simulated phase stability and thus energy jitter of a cavity for different loaded quality factors and detuning levels, where the latter are typical rms detuning levels as obtained by measurements in Section 5.1.2. The gain of phase accuracy by lowering the quality factor is very low when regarding the increase of the needed power. A more than doubling of the RF power from 2.4 kW at Q_L=3·10^7 to 5.85 kW at Q_L=1·10^7 just reduces the phase error by $\sim$ 16%. That is because the other errors limit the achievable phase accuracy. Comparing the curves for the different detuning levels, it is more effective to reduce this error source externally.

As will be shown in Chapter 5 peak detuning events of 20 Hz may occur. Thus the design quality factor of the BESSY-FEL linac of 3·10^7 seems to be a good compromise

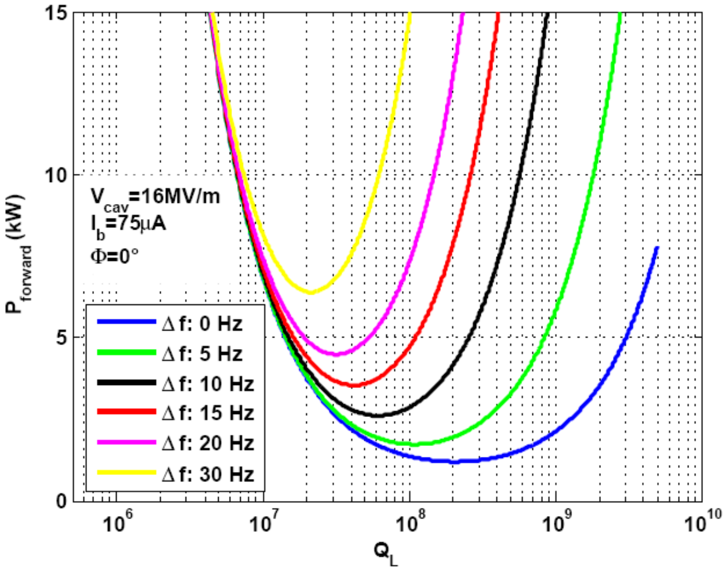

Figure 3.13: Forward RF power as a function of loaded quality factor $Q_{\rm L}$.

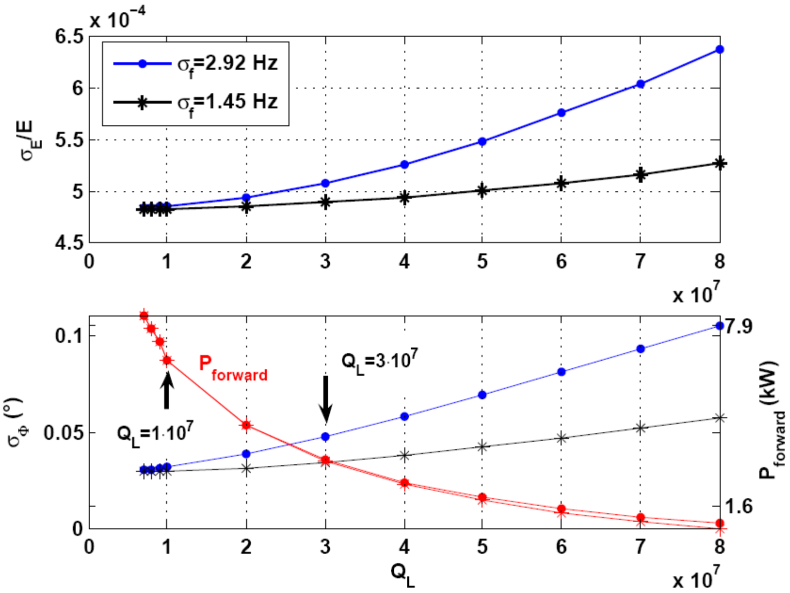

Figure 3.14: Dependence of energy jitter of a single cavity for different loaded quality factors at a given detuning (upper plot). The lower plot shows the phase stability and needed forward power as a function of the loaded quality factor.

between power consumption and achievable field stability. In the following work, this value will be used mainly for all stability considerations.

3.5 Linac calculations

To gain an estimate for the bunch-to-bunch beam stability delivered by the driver linac for the FEL process, the single cavity model has been expanded to the whole BESSY-FEL linac

Table 3.1: Main parameters of the linac simulation.

Parameter	**Value**	**Unit**
Accelerating field (L1, L2, L3)	16.3, 16.7, 15.9	MV/m
Loaded quality factor	$3 \cdot 10^7 \pm 10$	%
Beam accelerating phase (L1, L2, L3)	13, 5, 0	degrees
R_{56}, T_{566} BC1	-10.5, 16.4	cm
R_{56}, T_{566} BC2	-11.16, 124.04	cm
Bunch charge	2.5	nC
Energy jitter of photoinjector RMS	20	keV
Time jitter of photoinjector laser RMS	250	fs
Integrated time jitter of the RF system (LO) RMS	70	fs
LLRF feedback gain (L1, L2, L3)	250, 200, 100	-

as in Figure 2.7.

The model includes timing and energy jitter from the photo-injector as well as time jitter which follows the photo-injector due to velocity bunching in drift spaces up to the first booster cavity (see Appendix A). Furthermore the linearizing effects on the longitudinal phase space distribution of the 3^{rd} harmonic cavity are calculated. With the off-crest acceleration of the first cavities the bunch distribution is compressed at the first bunch compressor. Following another section of cavities with a slight off-crest acceleration, the second bunch compressor stage and the arc alter further the energy and time jitter of the beam. All error sources for the individual cavities are included. Table 3.1 summarizes the main parameters of the linac.

The beam related errors as time jitter and charge fluctuations are correlated errors along the linac such that no statistical suppression by $\sqrt{N_{cav}}$ is given. Furthermore the phase noise of the master oscillator is distributed by the reference system and modulates the phase of all cavities. The phase deviation seen by the bunch is nearly constant for all cavities as the total passage time of the linac is around 1 μs. Therefore the phase noise of the reference system is also a correlated error source.

As this work concentrates on characterizing the main error source in CW operation, microphonics, the simulations concentrated mostly on the two possible cases of correlated or totally uncorrelated microphonics between two or several cavities. A correlation along the whole linac seems very unlikely, because each cavity has its individual detuning spectrum as will be shown in Chapter 5. Nevertheless some spectra are very similar, that mounting of mechanically similar cavities in one module may result in intra-module correlated detuning. These two cases have been evaluated.

To determine the maximum allowable level of the detuning, the longitudinal phase space has been scanned according to two parameters of the acceleration process:

- A mean rms detuning level for all cavities between 1-12 Hz. The microphonics detuning is either totally uncorrelated or correlated for the cavities of one module.

- Electron beam timing jitter due to photo-injector laser jitter and increased time and energy spread by the non-relativistic acceleration effects.

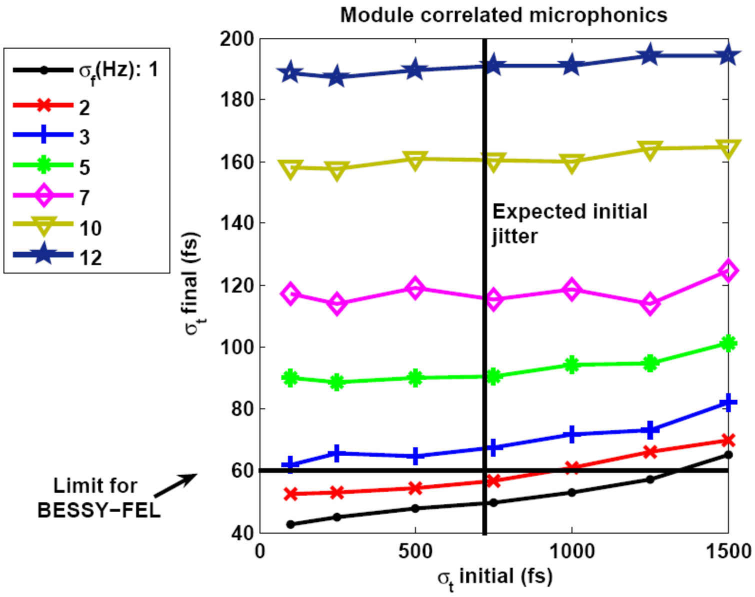

Figure 3.15: Final timing jitter of the electron beam against the initial jitter given by the gun and booster section of the linac. Each curve represents a different detuning level of the cavities. In this case the microphonics are correlated for cavities of one module. The black line denotes the maximum tolerance for the FEL.

These calculations assume quite low tolerable values for the other most influencing error sources. The initial energy spread of the gun is within the values measured at PITZ. Calculations given in Appendix A also resulted in values between 20-35 keV depending on the photo-injectors RF phase stability. The phase error integrated time jitter of 70 fs is within reach of present reference systems with near future systems expected to perform even better. The beam's charge jitter and timing jitter due to the cathode laser of 5% and 250 fs are achievable by modern laser systems [37].

Simulation results

Figures 3.15 and 3.16 show the final time jitter at the linac exit for different rms detuning values for the correlated and uncorrelated case, respectively. In the correlated case the uncompensated detuning level should not exceed 2 Hz rms to limit the time jitter to 60 fs, otherwise one has to compensate the fast mechanical oscillations. The case of uncorrelated microphonics allows an uncompensated detuning of 5 Hz rms assuming a maximum initial time jitter of $\sigma_t \leq 1250$ fs before the first bunch compression.

The energy jitter at the end of the linac depends mainly on the initial timing jitter for moderate microphonics. Even after bunch compression of this distribution, this still results in correlated acceleration phase errors, which thus influence mainly the gained energy. The relative energy jitter shows no significant difference between the two cases of detuning investigated here, the results being given in Table 3.2. If a relative energy jitter of $2.5{\cdot}10^{-4}$ is not good enough at $\sigma_{t,initial}$=1 ps, then it can only be further reduced by minimizing the time jitter before the first bunch compressor.

It is shown in Appendix A, that this jitter is to be expected to be between 600-700 fs. At 600 fs initial jitter, the time jitter at the linac exceeds 60 fs for detuning values above 2

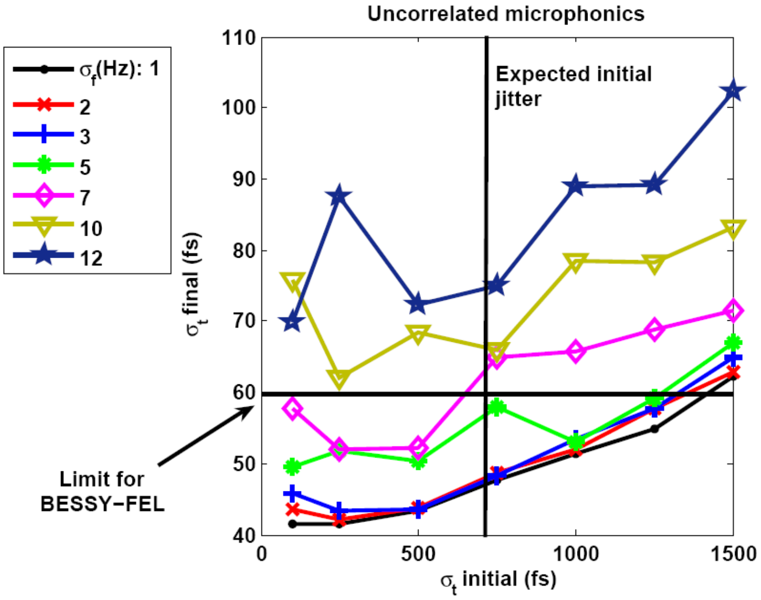

Figure 3.16: Timing jitter at the linac exit versus the initial timing jitter of the beam due to gun and booster section related acceleration errors. Here the microphonics of each cavity were assumed to be uncorrelated. The black line shows the maximum allowance for the BESSY-FEL.

Table 3.2: Relative energy jitter at the linac exit for different starting time jitter $\sigma_{t,initial}$. It is independent of the detuning levels between 1-12 Hz as the energy jitter is mainly given by the energy chirp. Here $f_{1/2}$=21.7 Hz, charge jitter =5%.

$\sigma_{t,initial}(fs)$	σ_E/E
100	$5.2 \cdot 10^{-5}$
250	$2.8 \cdot 10^{-5}$
500	$1.3 \cdot 10^{-4}$
750	$1.9 \cdot 10^{-4}$
1000	$2.5 \cdot 10^{-4}$
1250	$3.1 \cdot 10^{-4}$
1500	$3.7 \cdot 10^{-4}$

Hz (module correlated case). This is consistent with the error budget calculations shown in Section 2.5.1.

The simulations have shown, that for a bandwidth optimized for beam loading and power consumption there are stringent field-stability requirements for the single cavity. They correspond to a low detuning level on the one hand or display the need for a high gain RF field control.

To ensure, that the maximum beam jitter is not exceeded in a linac such as the BESSY-FEL, one has to consider compensation schemes to lower the detuning. Hence one has to measure and characterize the microphonics under accelerator-like conditions as well as the fast tuning systems, which will be used for detuning compensation. The results, obtained at the test facility introduced in the next chapter, serve as a basis for the development of a compensation strategy for the detuning.

Chapter 4

The cavity measurement setup

In the following, the test facility for superconducting cavities and the TESLA-type cavities themselves will be introduced. All measurements presented in this work have been performed at the HoBiCaT test facility under cryogenic conditions.

4.1 TESLA technology for the BESSY-FEL

Superconducting TESLA technology has been adopted for the BESSY FEL. Originally, this was developed for a project now known as the International Linear Collider, a 30 km long electron-positron collider[38][39]. TESLA technology is also planned for the XFEL project[40]. At 500 GeV and 20 GeV, respectively, the cryogenic load is prohibitively large and hence pulsed operation must be employed. Because of the moderate 2.3 GeV beam energy of the BESSY FEL, CW operation is an option. This is also the case for numerous other FEL and ERL projects that have been proposed, e.g. the Cornell ERL [41], the 4GLS energy-recovery-linac (ERL) project[42] and the Arc-en-ciel project [43]. The TESLA technology has been chosen for the BESSY-FEL, as it is as well mature and its reliability has been demonstrated at FLASH. However, its performance in CW operation has to be demonstrated at field levels between 15-20 MV/m.

The TESLA cavity

The TESLA cavity, depicted in Figure 4.1, is a structure of nine weakly coupled cells made from pure niobium, which becomes superconducting at 9.2 K. At 1.8 K, the envisaged helium bath temperature for cavity operation, intrinsic quality factors of the order 10^{10} are achieved. The accompanying low power loss in the walls due to residual ohmic resistance compared to normal conducting cavities allow for CW operation at high field levels. This not only allows a flexible choice of the beam bunch pattern, but is the main reason for the improved field stability.

The low power losses also allow the use of low-frequency, large aperture structures, that reduces interaction of the conducting walls with the beam (wakefields). The negligible power losses* in the cavity walls allow the transfer of almost all the RF power to the particle beam.

---

*These losses, although small, are at 1.8 Kelvin.

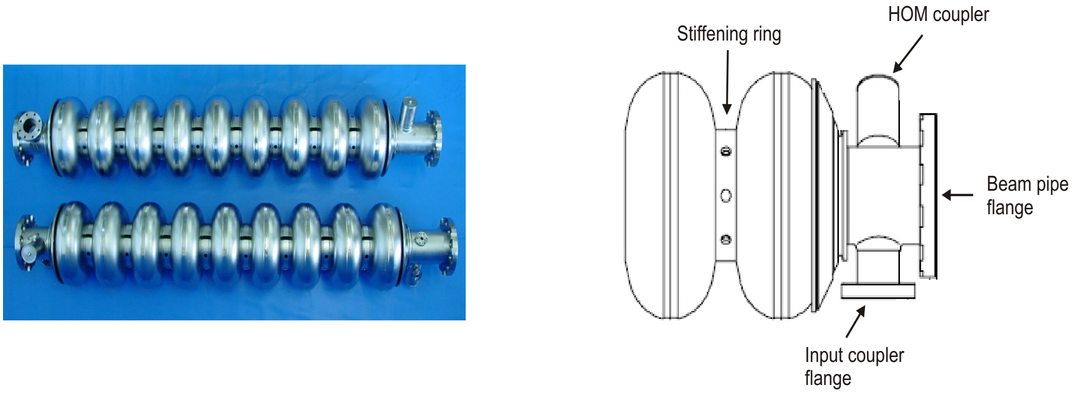

Figure 4.1: Left: Picture of two nine-cell niobium TESLA cavity before welding into their helium vessel. Coupler ports for higher-order-mode couplers and the input coupler are visible. Right: End-cell section of the TESLA cavity with beam pipe flange and openings for the input coupler antenna and higher-order-mode couplers. Between two cells mechanical stiffening rings are attached to make the cavity more rigid.

Table 4.1: Main parameters characterizing the nine-cell TESLA cavity.

Cavity parameter	**Value**
Accelerating mode	TM_{010} (π-mode)
Frequency	1.30 GHz
Intrinsic Quality factor (Q_0)	$1.3{\cdot}10^{10}$
Temperature of Helium bath	1.8 K
Accelerating length	1.038 m
Shunt impedance $\frac{r}{Q}$	1040 Ω
Peak electric field/accelerating field	2
Accelerating field	16.3 MV/m

The cavity has three flanges at its beam pipe to connect the fundamental power coupler and special higher-order mode (HOM) antennas to damp these unwanted modes. In between two cavity cells there are stiffening rings installed. They were mainly designed to lower the field pressure of the electric field component near the iris for the pulsed mode of operation. The cavity is thus less susceptible to the time-varying field-induced Lorentz-force detuning.

Figure 4.2 shows a drawing of a TESLA cavity installed in its cryogenic vessel or cryo-unit. On the input coupler side the cavity is directly welded to the helium vessel, but on the opposite side via a flexible bellow. This allows a tuning system to change the length of the cavity and hence its frequency.

The generated heat is conducted through the chimney to the two-phase line.

A cavity is powered by a klystron or IOT via coaxial input coupler. The coupling defines the bandwidth of the RF resonance; for the BESSY-FEL values around 40 Hz are used (Q_L of order 10^7). The main operational parameters of the TESLA cavity for the BESSY-FEL are summarized in Table 4.1.

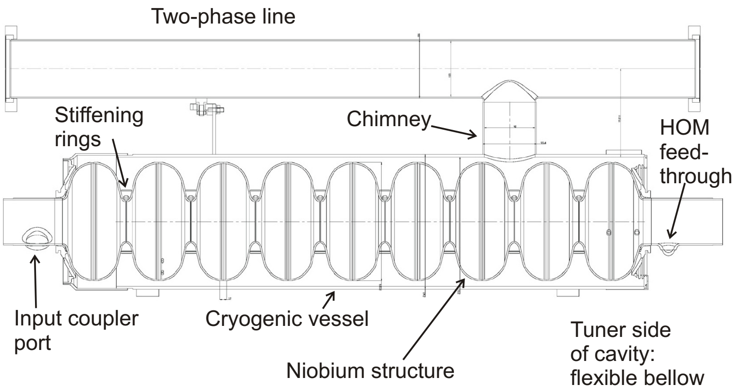

Figure 4.2: Sketch showing the TESLA cavity installed in its cryo-unit. The cavity tuner will be installed on the right side, where the cavity is connected via a flexible bellow with the stiff cryogenic vessel to allow a longitudinal deformation.

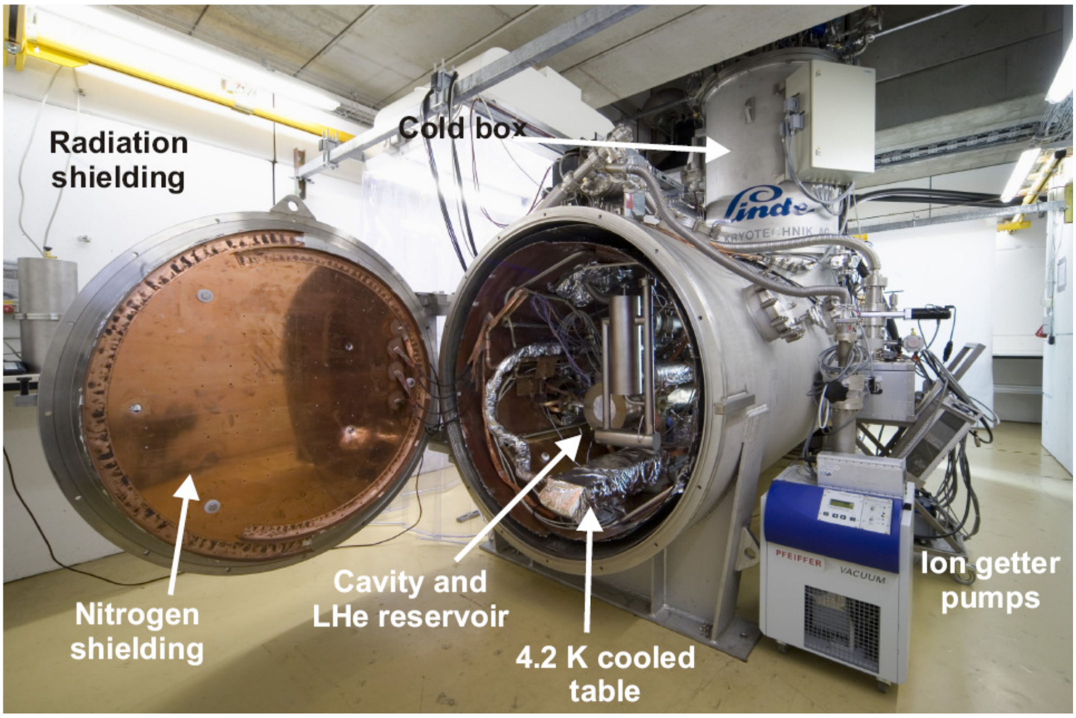

Figure 4.3: Fisheye view of the HoBiCaT test cryostat for superconducting cavities from the coupler side of the first cavity.

4.2 The HoBiCaT test facility

To study the adaptation of the TESLA technology for CW based linacs a test facility has been setup at BESSY. HoBiCaT stands for Horizontal Bi-Cavity Test-facility and is designed to address the following issues [44] [45]:

- CW measurement of the achievable intrinsic quality factor Q_0 with all ancillary devices like e.g. input and HOM couplers mounted as a function of RF field amplitude and helium bath temperature. This information is needed to optimize the bath temperature and to dimension the cryogenic plant of the BESSY-FEL.
- Measure the attainable pressure stability of the helium bath at the expected dynamic heat loss of 15-20 W per cavity. Redimension of the two-phase-line to handle the increased CW heat load.
- Analyze the present noise sources like microphonics to determine the amount of cavity detuning in CW operation.
- Measure the gain limit for RF feedback control and therefore the achievable cavity field stability.
- Characterization of different tuning schemes like the Saclay I and Saclay II tuner [46] to find the optimal system. The tuner systems, which have been characterized at HoBiCaT are presented in Chapter 6.
- Find methods to include fast (e.g. piezo based) tuning schemes into the coarse tuner of a cavity to actively damp or suppress microphonics detuning.

The HoBiCaT facility allows for cavity testing in an environment resembling a cryo-module while permitting rapid access to implement changes. As can be seen in Figures 4.3 and 4.4 the test facility consists of a cylindrical vacuum vessel. Inside the tank is a table which can be cooled to 4.2 K. Up to two cavities can be installed on sliding supports. Furthermore the vessel is equipped with thermal radiation shielding cooled to 80 K. The cavity is assembled with its ancillary devices —the input coupler, the mechanical tuning system, the pick-up antenna to measure the RF mode and higher-order-mode couplers located at each end of the cavity's beam pipe. The two-phase-line, supplying the cavity with superfluid helium, is equipped with helium level and pressure sensors, to control the liquid helium level and pressure to a stability of at least 100 μbar. The cryogenic system has been designed to handle a total heat load of 80 W at 1.8 K (16 mbar). The bath temperature can be varied between 1.5-2.2 K.

The RF power from the klystron or IOT is fed via a 3" coaxial cable to the RF waveguide, which incorporates the circulator with a load, the three-stub-tuner [47] and the warm part of the input coupler. By changing the position of the stubs of the three-stub-tuner the phase of the standing wave can be changed in such a way, that the coupling to the cavity is changed. A coupling range of a factor of ten is achieved. In combination with the variable antenna the external quality factor of the cavity can be varied in a range of $2.5 \cdot 10^7$-$1 \cdot 10^{10}$ (bandwidths: 26-0.07 Hz). In the framework of this thesis there were three different power sources installed. A solid state amplifiers delivering 400 W. The klystron and IOT provide 10 and 17 kW, respectively.

4.3 RF detuning measurements

One of the main tasks of this work is to analyze the cavity detuning to find means to control the field amplitude to the desired level. As described in Section 3.2 a cavity responds with

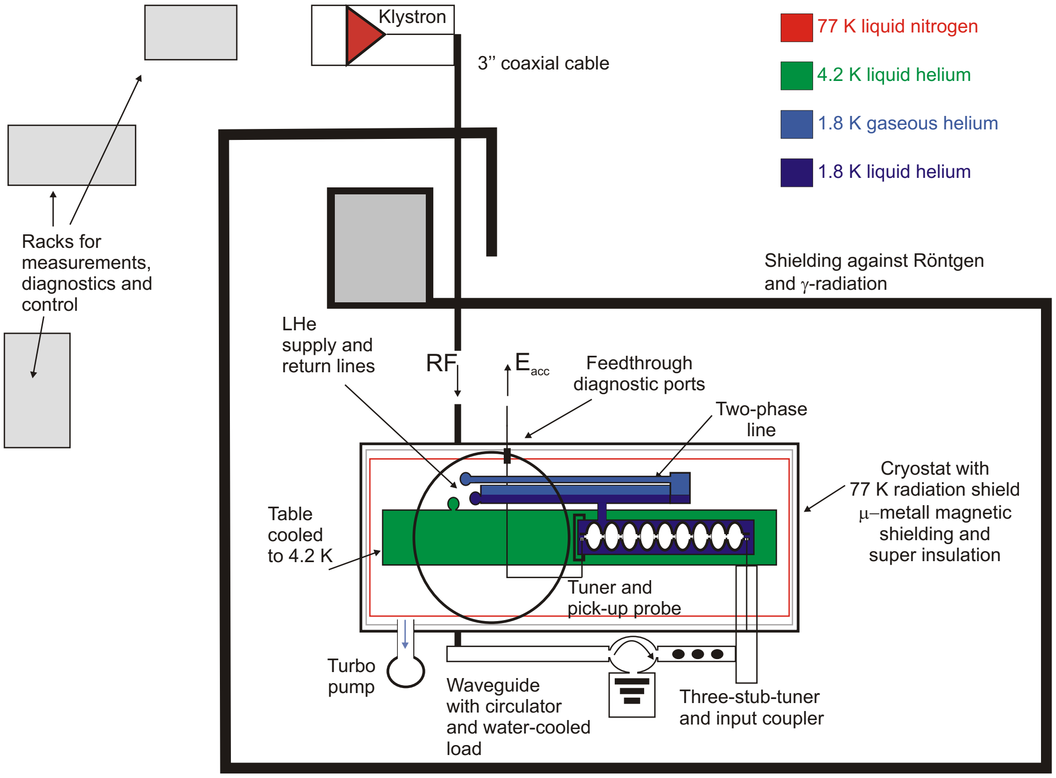

Figure 4.4: Overview of the HoBiCaT test facility from above. Shown is all cabling related to the RF measurement, colors indicate lines with liquid helium or nitrogen supply. Two cavities can be installed in HoBiCaT simultaneously.

a phase shift Φ if excited by an RF forward wave which is shifted in frequency from its resonant mode by

$$\tan(\Phi) = 2Q_{\mathrm{L}}\frac{\Delta f}{f_0}. \tag{4.1}$$

Any kind of time dependent detuning thus results in a phase modulation of the resonant mode. For a measurement of this effect we chose to down-convert this sideband modulation of the carrier frequency to DC-kHz, where cavity detuning is to be expected. Understanding the characteristics and response of such a measurement system thus is critical for the detuning measurement and RF control in general.

4.3.1 Principle of an RF mixer

The mathematical equivalent of down-conversion is a multiplication of the RF signal with a low noise reference signal to generate an intermediate signal. This preserves the amplitude and phase information of the original RF signal. For the usage in a low level RF control system, see [12], the mixing results in an intermediate frequency chosen such to optimize sampling of the cavity field vector envelope (usually several MHz). This is important to resolve the field amplitude variations due to beam loading at bunch repetition rates as high as e.g. 1 MHz [38].

For the detuning measurement here, the reference frequency is the same as the RF signal to only preserve the phase error in the detuning frequency bandwidth of several kHz.

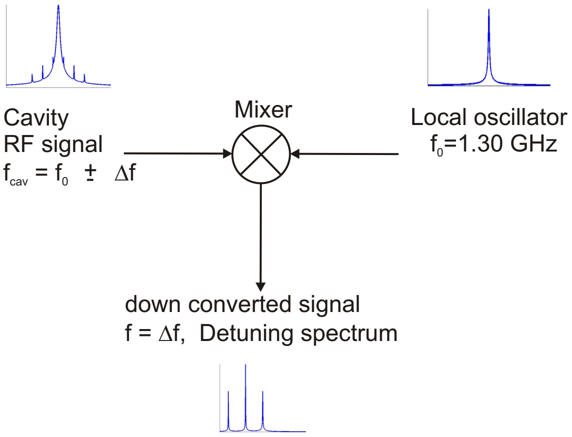

Figure 4.5: This scheme explains the principal of an RF mixer as a cavity phase detector. Dynamic detuning modulated on the RF carrier frequency of the cavity's TM_{010} mode is down converted to the carrier sideband frequency range.

The general setup for this measurement method is outlined in Figure 4.5. Assuming sinusoidal input signals for the RF (V_{RF}) and reference or local oscillator (LO, V_{LO})

$$V_{\mathrm{RF}}(t) = \hat{V}_{\mathrm{RF}} \cdot \sin(\omega_{\mathrm{RF}} t + \Phi_{\mathrm{RF}}), \qquad V_{\mathrm{LO}}(t) = \hat{V}_{\mathrm{LO}} \cdot \sin(\omega_{\mathrm{LO}} t + \Phi_{\mathrm{LO}}) \tag{4.2}$$

the intermediate output signal is given by the multiplication of the input signals

$$\begin{aligned} V_{\mathrm{IF}} = \frac{1}{2}\hat{V}_{\mathrm{RF}}\hat{V}_{\mathrm{LO}} \{&\cos\left[(\omega_{\mathrm{RF}} - \omega_{\mathrm{LO}}) + (\Phi_{\mathrm{RF}} - \Phi_{\mathrm{LO}})\right] \\ &- \cos\left[(\omega_{\mathrm{RF}} + \omega_{\mathrm{LO}}) + (\Phi_{\mathrm{RF}} + \Phi_{\mathrm{LO}})\right]\} . \end{aligned} \tag{4.3}$$

To only measure the cavity phase response generated by the detuning the high frequency components of the IF signal have to be removed by a low pass filter. In this case this would be far out of the range of any sampling device, but is done to remove high frequency measurement noise, spurious sideband lines of the reference source and to avoid aliasing due to under-sampling. The detuning information is given by the phase of the RF signal Φ_{RF}. To only obtain this component the reference source is tuned to the resonant frequency of the cavity ($\omega_{\mathrm{LO}} = \omega_{\mathrm{RF}}$). After lowpass filtering the phase error signal is given by

$$\begin{aligned} V_{\mathrm{IF}} &\approx \frac{1}{2}\hat{V}_{\mathrm{RF}}\hat{V}_{\mathrm{LO}} \cos(\Delta\Phi) \\ \Delta\Phi &= \Phi_{\mathrm{RF}} - \Phi_{\mathrm{LO}}, \Phi_{\mathrm{LO}} \simeq 0 \end{aligned} \tag{4.4}$$

For an accurate measurement it is therefore necessary to not only filter higher frequency components but also to use a very stable reference source. The integrated phase noise should be as low as possible, at least lower than the accuracy to be characterized. At an RF bandwidth of 20 Hz a resolution of the detuning down to 0.1 Hz would require phase noise less than 0.28° at 1.30 GHz. Also all amplitude modulations have to be removed from the measured data, as it is obvious by Equation 4.3, because they cannot be distinguished from the modulations given by the phase variation.

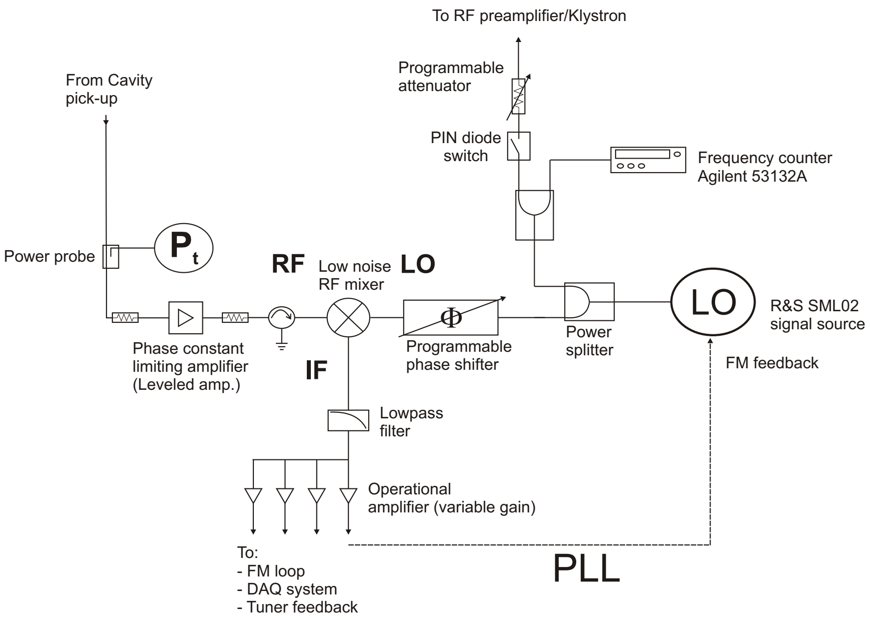

Figure 4.6: RF measurement setup at HoBiCaT. The system is optimized to measure the cavity detuning by determining the phase shift between the cavity and the RF source by using a low noise mixer (mini-circuits ZEM-4300) as a phase detector. Measurements have been performed both open and closed loop.

Measurement setup

The detailed RF setup used at HoBiCaT is shown in Figure 4.6. The phase of the local reference oscillator (LO) can be matched by a programmable phase shifter. A constant LO signal is maintained at the mixer. To vary the cavity input power a variable attenuator is employed before the input to the klystron.

The RF signal from the cavity pick-up antenna is amplified by a phase constant limiting amplifier. This suppresses all amplitude modulations of the cavity field, only preserving the phase information. The IF signal after the mixer is filtered by a lowpass filter, which can be programmed to different low pass settings. The resulting phase error signal is split and can be amplified by low noise operational amplifiers for different purposes.

For cavity testing and detuning measurements the RF measurement system can be used in different modes:

Mode 1 - open loop: The cavity is driven open loop directly by the local reference source. Any change of the cavity resonance frequency due to detuning effects are measured by the phase stable measurement setup. This mode has mainly been used to characterize the cavity detuning as explained in Chapter 5.

Mode 2 - phase locked loop: The phase-locked-loop (PLL) is closed by feeding the phase error signal back to the signal source which runs in frequency modulation mode (FM). The feedback gain set at this device (input voltage → frequency deviation) determines the loop bandwidth. The signal source thus follows the drifting frequency of the cavity within that bandwidth. This mode of operation has been used for high power and/or pulsed cavity operation and to characterize the tuning systems described in Chapter

6.

In principle this mode also can be used to measure the cavity detuning by multiplying the measured signal with the feedback gain to obtain the cavity detuning directly. But it has been shown, that the signal source in closed loop modes impresses a change in the PLL's transfer function. This low pass behavior suppresses lower frequency components of the spectrum more efficiently than higher spectral components. A solution would have been to increase the PLL gain and bandwidth, but as the detuning signals are very low, one will loose measurement accuracy and degrade the signal to noise ratio.

Mode 3 - tuner mode: One signal path of the phase error signal has been used to implement a piezo-based tuning feedback/feedforward system (labeled ”Tuner feedback” in Figure 4.6). This will be presented in Chapter 7.

Mode 4 - pulsed mode: A digital TTL signal controls a PIN diode switching the RF power to the klystron to run the cavity in pulsed mode. The switching time is of the order of 2-4 μs being 3 orders of magnitude faster than the smallest cavity time constant to be expected for the given coupling range. The rise time of the control signal is less than 30 ns.

For online monitoring or further digital signal processing and data analysis the IF-signal can be sampled and digitized by two independent systems. For data acquisition a data logging system with 16 bit ADCs and a sampling rate of up to 200 kHz of National Instruments was used.

For deterministic ADC/DAC control, as it is required for piezo-based detuning compensation (see Chapter 7), a National Instruments realtime$^{\mathrm{TM}}$controller has been used processing data with a 16 bit ADC board. This system is in use for prototyping and the characterization of possible controller schemes concerning microphonics detuning and has a potential latency of the order of 500 μs. At a later stage the source code of the feedback and/or feedforward algorithms will be transferred to more sophisticated DSP solutions, like FPGA's (field programmable gate array [48]) or Power PC's.

4.3.2 Measurement accuracy and calibration

The accuracy of this measurement method depends on the phase or frequency and amplitude stability of each subcomponent. Deviations with time would modulate the detuning signal and alter the measured spectrum.

Mixer behavior

The deviation of the mixer response from the ideal must be determined. After mixing, lowpass filtering and amplification the measured IF signal is proportional to the phase shift between the cavity and the incident RF wave of the local reference oscillator:

$$\Delta\Phi \propto \Delta V_{\mathrm{IF}}.$$

This value has to be calibrated in order to calculate the associated detuning. Equation 4.5 gives the relationship between cavity phase error and the associated detuning and the

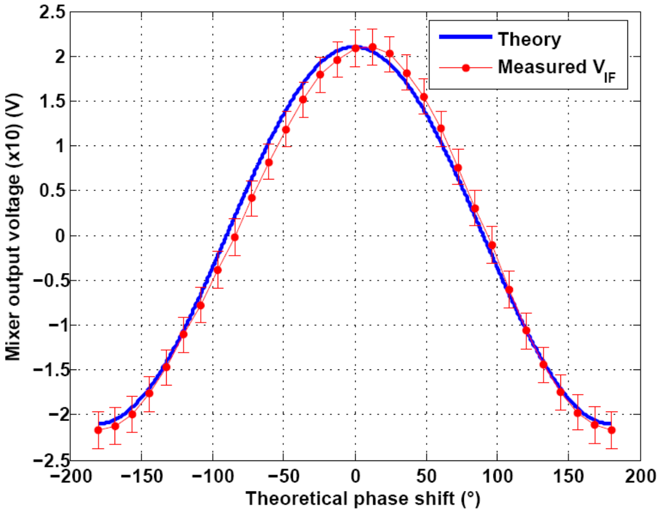

Figure 4.7: Measured and expected phase shift (Equation 4.3) response of the RF mixer for calibration purpose. The signal has been directly measured at the V_{IF} output port without any further amplification or signal conditioning. The error of the abscissa due to inaccuracies of setting the phase shifter is of the order of 0.16° (Determined by network analyzer).

parameters to be determined for calibration issues:

$$\Delta f = \frac{f_0}{2Q_{\mathrm{L}}} \cdot \tan\left[\arcsin\left(\frac{V_{\mathrm{IF}}}{V_0}\right)\right]. \tag{4.5}$$

V_0 is the voltage related to a phase shift of $\frac{\pi}{2}$. Furthermore the loaded quality factor and the mean frequency of the cavity mode have to be measured. This phase calibration has been done by varying the phase between two phase-locked signal generators representing the signals at the mixer inputs (Figure 4.7). The obtained curve resembles the theoretical mixer response within the measurement accuracy. Here the phase shifter could been set by software to an accuracy of 0.16°. Furthermore, the phase shift is not perfectly linear with respect to the control voltage to steer the shifter. To check this calibration during operation the frequency of the cavity has been shifted by tuning with the piezo tuner to obtain the phase response given in Figure 4.8. Alternatively the frequency of the local oscillator has been shifted vs the cavity passband mode to obtain the same phase deviation. This method proved to be useful as it also reflects the half bandwidth of the cavity where a phase shift of $\frac{\pi}{4}$ occurs to crosscheck the loaded quality factor measurement. The value from the field decay measurement and the quality factor obtained from fitting a resonance curve to the measured phase response of the tuning curve agree within 7%. More importantly the calibration of $V_0 \sim \Phi = \frac{\pi}{2}$ remained within 5% of the previously determined value for days of operation.

Characterization of the reference source and the leveled amplifier

All subcomponents have been analyzed with respect to their phase stability. The following error sources have been investigated:

- The integrated phase noise of the reference oscillator R&S SML02 adds up to a total

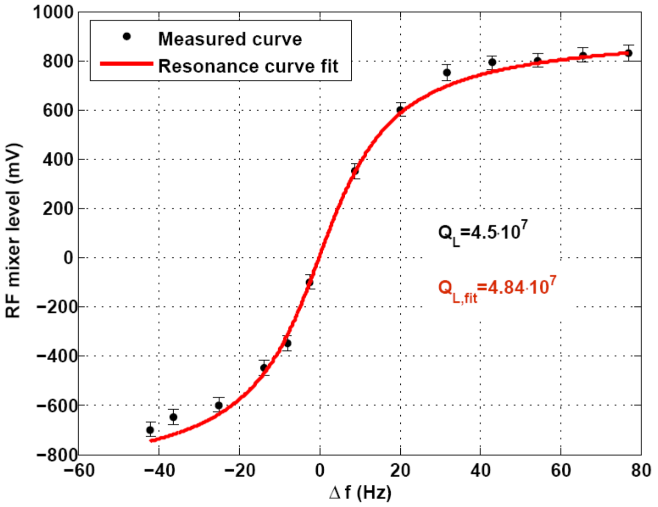

Figure 4.8: Phase response of a cavity detuned with piezo at Q_{L}=4.5·10^7 (black circles). The blue curve represents a fit of a resonance curve to the measured data resulting in Q_{L}=4.84·10^7. The difference is due to measurement errors of the tuning curve and the loaded quality factor.

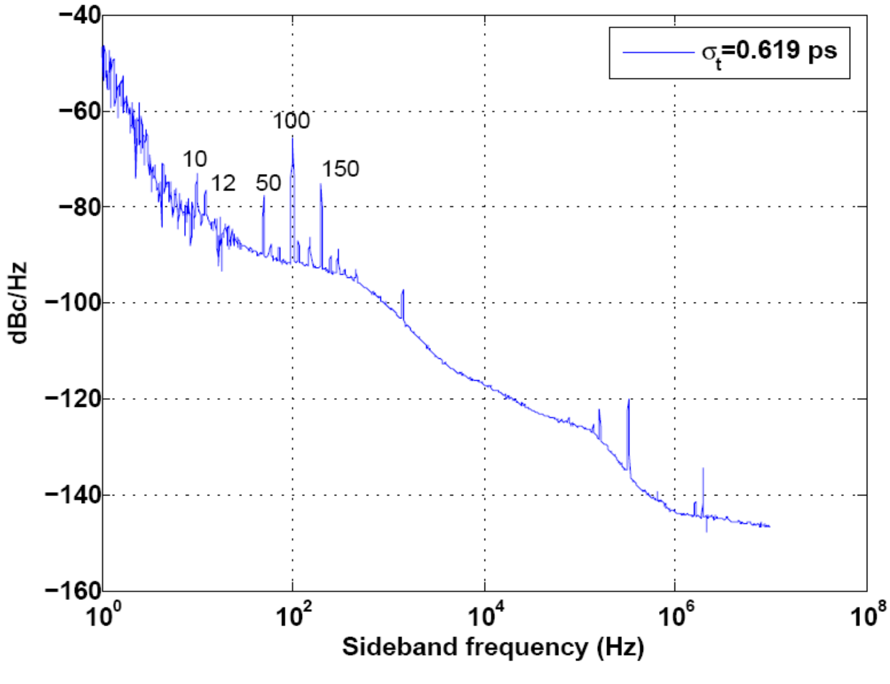

Figure 4.9: Single sideband (SSB) phase noise of the reference RF oscillator used at HoBiCaT. The integrated time jitter relates to f_0=1.30 GHz and a f_{mod} range from 1-10$^{\cdot 6}$ Hz for the double-sideband contribution. Spurious emissions occur at 50 Hz and higher harmonics and at 10 and 12 Hz.

timing jitter of

$$\sigma_{\mathrm{t}} = \frac{1}{2\pi \cdot f_0}\sqrt{\int_0^{f_m} \frac{(\Delta\theta_{\mathrm{rad}}^2)}{B} \cdot df} = 619\mathrm{fs} \tag{4.6}$$

(B measurement bandwidth, f_0 the carrier frequency,f_m sideband modulating frequency and θ_{rad} the corresponding phase noise amplitude in radian) for the double sideband (DSB) phasenoise from 1 Hz-10 MHz. This sideband noise at 1.3 GHz results in an effective phase jitter of 0.29° rms. The phase noise has been measured with a R&S FSUP spectrum analyzer with optimized resolution bandwidth (Figure 4.9).

- The phase of the phase constant limiting amplifier depends on the phase stability at constant input level (σ_{phase}) and also its variation with non-constant input level (σ_{level}). They add up to $\sigma_\phi = \sqrt{\sigma_{level}^2 + \sigma_{phase}^2}$ =0.024° rms ($\hat{=}$51 fs). These values have been determined with a network analyzer by measuring the phase deviation over time at a constant frequency and for varying RF level. For the latter at each measurement point the average has been taken over a time of 30 s.
- The reproducibility of setting the coupling and thus the loaded quality factor is given within an relative uncertainty of ± 0.1. This may be regarded as an systematic error.

These errors affect mainly the voltage at the mixer V_{IF} and the calibration value V_0. They can be assumed to be independent in a statistic sense. Thus, adding quadratically following Gauss law of error propagation
$\Delta y = \sqrt{\sum_{i=1}^{n} \left(\frac{\partial y}{\partial x_{\mathrm{i}}}\right)^2 \cdot \Delta x_{\mathrm{i}}^2}$ one receives for the total relative measurement error:

$$\frac{\Delta\left(\Delta f\right)}{\sigma_{f\mathrm{rms}}} = \sqrt{\left[\left(V_0^2 \Delta V\right)^2 + \left(\frac{V \Delta V_0}{V_0^2}\right)^2\right] \cdot \frac{\left(V_0^2 - V^2\right)^{\frac{4}{3}}}{\left\{\tan\left[\arcsin\left(\frac{V}{V_0}\right)\right]\right\}^2}} \tag{4.7}$$

Depending on the input levels to the mixer the relative measurement error of the detuning or the phase depends on the mean phase. For a typical detuning of 1.5 Hz rms the relative error is about 20%. This is valid for all measured detuning values presented in the following chapters.

Chapter 5

Microphonics in HoBiCaT

5.1 Introduction

The mechanical deformation of a cavity results in a shift of its actual resonance frequency. The cavity system responds with a reduction of the field amplitude and a phase shift of the field. The two main error sources for static and dynamic mechanical deformation of the cavity body have thus been measured and characterized at the cavity test facility HoBiCaT. On the one hand this gives an understanding for the feasibility of the required cavity performance for the BESSY-FEL's driver linac. On the other hand these data have been used to develop schemes to counteract and suppress detuning.

What follows is a characterization of the detuning observed in HoBiCaT. After identifying the main contributions to the detuning, long-term measurements of the variation with time of the obtained microphonics spectra, have been performed.

5.1.1 Sources of microphonics

The narrow bandwidth of 40.3 Hz will make the cavity very susceptible to any kind of mechanical deformation shifting the resonance. A change of the cavity sizes of about 1 nm results in a detuning of about ~ 0.3 Hz [27]. The potential microphonics sources are displayed in Figure 5.1.

External vibrations caused by heavy machinery like the pumps for the liquid helium system or vacuum pumps may be transmitted through the supply lines, the beam pipe or the ground. Depending on the process behind this noise source, it may be a sinusoidal kind of oscillation with a limited bandwidth, but also random broadband noise may be transmitted.

Beside these, ground motion may be transferred to the cavity system. All these external noise sources are partly filtered by the transfer medium. For the purpose of damping, special passively working supports below the pumps or flexible bellows between any pipe connecting vacuum pumps with the cryostat are installed.

Another noise source is given by the helium cooling system for the superconducting operation of the cavities. Pressure variation in the cryogenic system itself or changes of the liquid helium level in the two-phase line changes the forces on the cavity walls. Furthermore in high power operation, boiling may occur in the superfluid helium, that also may transfer vibrations to the cavity body.

As will be introduced later, the pressure of the cavity field will induce forces on the thin-walled cavity cells (see Section 5.3). If a variation of the field level with time occurs, e.g.

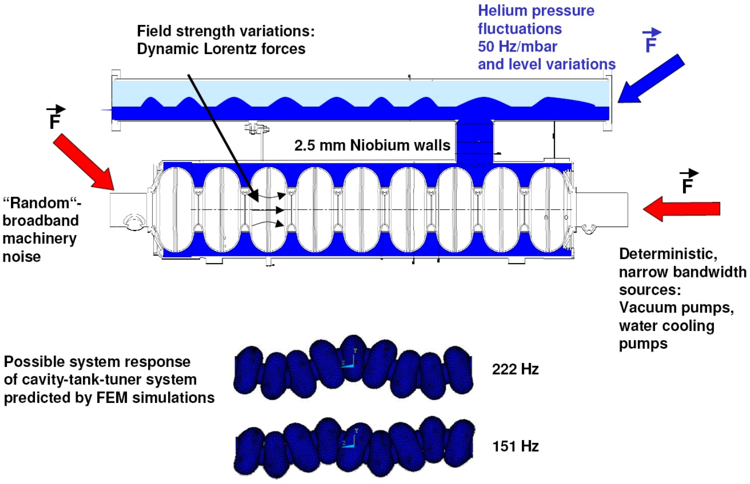

Figure 5.1: Scheme showing a technical drawing of a TESLA cavity welded in its cryo-unit. Possible detuning sources due to external vibrations or liquid helium level changes (microphonics) as well as the system response to external excitation are shown.

induced by strong microphonics, the field pressure will also become a time-varying quantity and will lead to additional dynamic detuning.

It has been shown by finite element simulations [49], that mechanical eigenmodes of the cavity-cryo-unit-tuner system may be excited by these external forces. The mechanics of the TESLA cavity have been optimized for pulsed operation to be more rigid against strongly varying Lorentz forces. Therefore the TESLA cavity is equipped with stiffening rings [38]. These may also reduce longitudinal and transverse movement of the cavity with respect to vibrations transmitted by the environment, but they are not optimized from this viewpoint.

For a measurement of the detuning it had to be considered, how the cavity-tuner mechanics may respond to these external noise source. It could be shown, that the mechanical eigenmodes play a major role in the total detuning spectrum (see Section 5.2.1). Nevertheless there is no direct means to measure the transfer function between the external oscillations and the cavity detuning. The cavity frequency itself is the most sensitive sensor for all mechanical movements.

5.1.2 Aim of the measurements

The results presented here were used to develop, test and characterize piezo based fast tuning systems to suppress the impact of mechanical detuning. The nature of microphonics and the characteristics of the tuner-cavity-system restrict the options for feedback or other control algorithms to achieve a stable and robust detuning compensation. CW microphonics detuning has been measured and characterized to:

- Determine the severity of this effect by measuring the rms detuning and spectra. Later, the results will be used for cavity and linac simulations to determine the expected field stability and thus beam jitter.

- Determine the components of the microphonics spectrum with respect to there contribution to the total detuning.
- Identify possible sources of microphonics detuning to find general methods for active or passive means of compensation.
- Analyze the measured data to check if the measured microphonics spectra are:
  - Time invariant, i.e. are their changes in frequency or amplitudes of the spectral components?
  - Driven by random noisy sources or by deterministic narrow bandwidth oscillations?
  - Find correlations between detuning and other system parameters like pressure of the liquid helium bath.

  This information is important for the design of compensation schemes.
- Perform long-term measurements to find the maximum peak-to-peak detuning, which can be expected for CW machine operation. The occurrence of these detuning events will determine the peak RF power that must be installed to maintain the field. If not enough power is available peak events can give rise to ponderomotive instabilities which lead to a total loss of the resonant condition. This will be explained in more detail in Appendix B.

5.2 Measurements with the phase detector

All results shown here have been measured at a helium bath temperature of 1.8 K, which most probably will be the operational temperature of the future FEL linac.

To cover the expected frequency range of sub-Hertz to kHz the detuning data sets have first been sampled at a high rate of up to 20 kHz. It was shown, that above several hundred Hertz up to one kHz only high frequency noise dominates the spectrum. These components represent the phase noise contributions of the RF measurement system, of which the main part is due to phase noise characteristics of the local oscillator as described in Figure 4.9.

To characterize the microphonics detuning the phase error signal from the RF mixer has thus been sampled between 1 and 2.5 kHz and filtered by an analog lowpass filter (3 dB cutoff frequency of 3 kHz) taking data sets as large as 400 ks. This means, that the measured frequency range includes slow drifts of the cavity resonance due to changes in the helium pressure as well as mechanical oscillations in the audio frequency range.

So far, two different TESLA cavity units have been characterized. One cavity, referred to as BESSY01, has been equipped with two different mechanical tuners to study their impact on the detuning spectrum. They are described in more detail in the tuner related Chapter 6. The measurements presented here were taken in open loop configuration to avoid artifacts of the PLL feedback loop. This means, that the spectra and standard deviations are filtered by the cavity field bandwidth:

$$\omega_{1/2} = \frac{\omega_0}{2Q_\mathrm{L}}.$$

A typical time domain data set is given by Figure 5.2. It shows some slow drifts of the open loop detuning over about tens seconds. Zooming into the data set reveals a faster

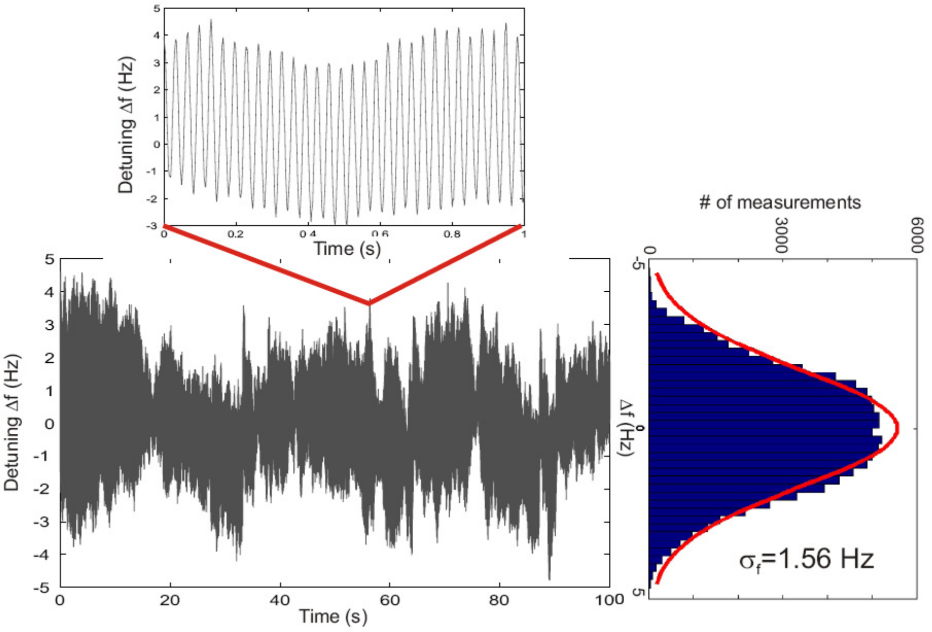

Figure 5.2: Typical time domain detuning data. A zoom into the data reveals a faster oscillation between 30-40 Hertz (upper insert).

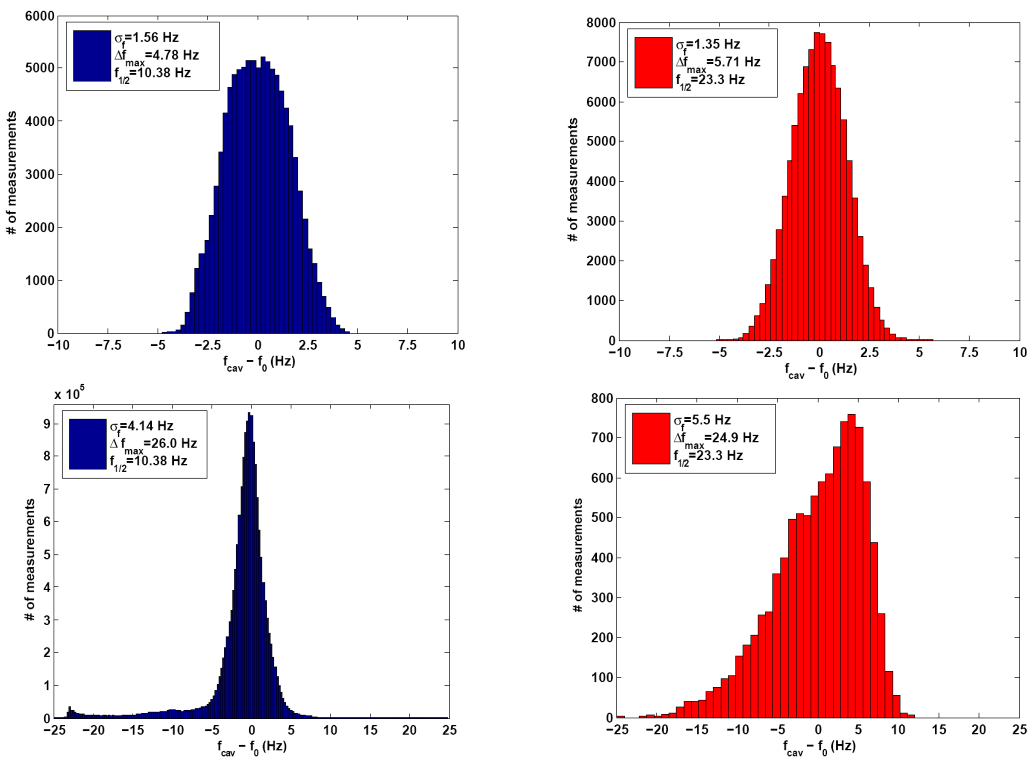

Figure 5.3: Typical open loop microphonics detuning measurements for the BESSY 01 cavity (right) at Q_{L}=2.7·10^7 and the DESY S33 cavity at Q_{L}=6.3·10^7.

oscillation at about 30 Hz. A measure for cavity stability is given by the rms value of the data. Representative data of microphonics are shown in Figure 5.3.

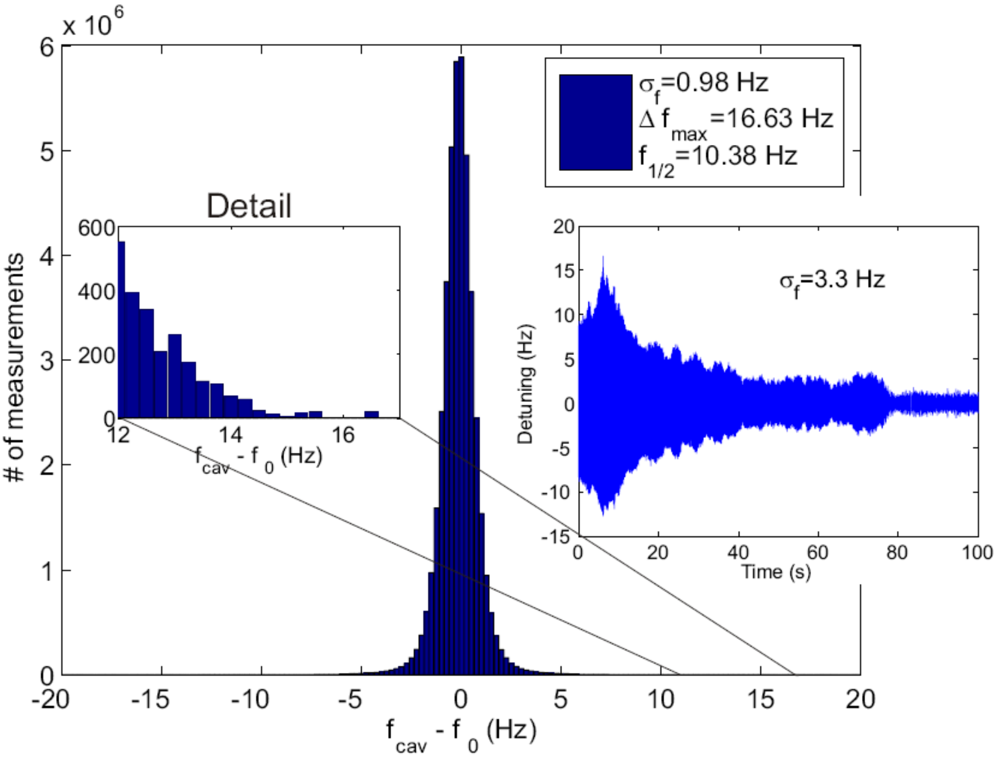

Figure 5.4: Long-term microphonics measurement with the Saclay II tuner installed on the BESSY 02 cavity. The rms detuning is about 1 Hz rms. But excited resonances lead to a peak detuning of 16-17 standard deviations for several of tens of seconds every 1-2 hours. The time signal of the peak event is displayed in the inserted plot on the right. The insert on the left shows a zoom to the detuning distribution for strong positive detuning values.

The open loop results yielded near Gaussian distributions with standard deviations ranging from 1.35 - 5.5 Hz. The lower right plot shows an example where a strong drift in the pressure of the liquid helium bath led to a slow shift of the carrier frequency thus shifting the whole distribution. This happened on a time scale of tens of seconds. During such an occurrence maximum detuning of up to 26 Hz could be observed.

Referring to Equation 3.48 this would mean for the BESSY-FEL an increase of the needed power from 3.5 kW up to 7.1 kW. A further offset of 10 Hz would lead to a power of 10 kW, which is already in the saturation regime of the klystron.

Long-term observations

The lower left plot shows open loop detuning data of the DESY S-33 cavity taken over a period of more than 4.5 hours to observe how often large excursions occur. During the measurement the liquid helium pressure was very constant (σ_P=25 μbar) and very slow drifts below 0.01 Hz were compensated by the tuning system.

The rms value of 4.1 Hz lies within the values obtained during shorter measurements ranging from 30 to several 100 seconds. Taking these data as being representative for a long-term stability of CW cavity operation the relative frequency of events with a detuning greater than the cavity half-bandwidth $f_{1/2}$ is in the range of 4 %.

To measure how often large excursions occur a measurement with the same settings over

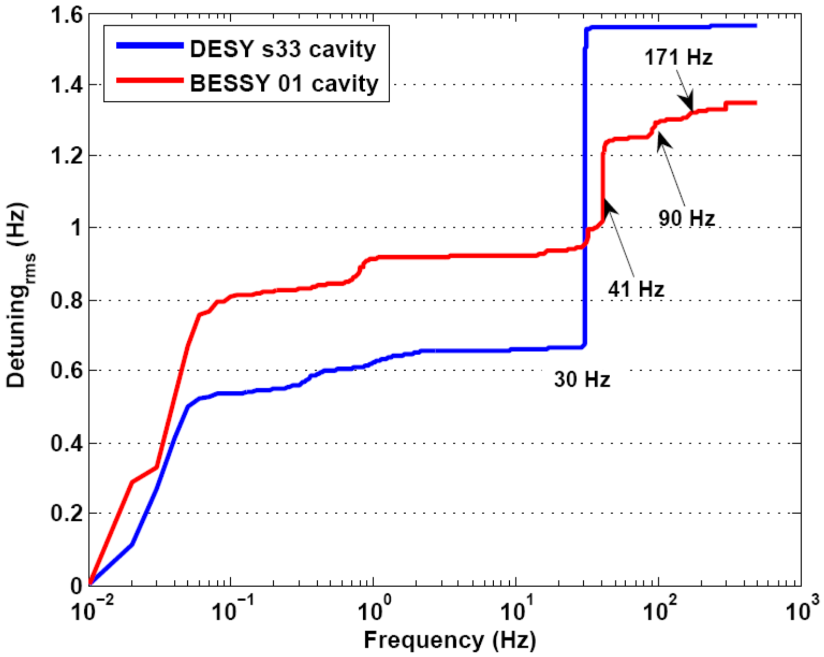

Figure 5.5: Integrated microphonics spectrum at $Q_{\mathrm{L}}=4 \cdot 10^7$. The main contribution of the microphonics come from low frequencies below 1 Hz already summing to about 50 % of the total detuning. The installed tuner system is the Saclay I tuner.

a period of 14 hours has been performed. This time, the BESSY 01 cavity with the Saclay II tuner installed has been characterized. The loaded quality factor was $2.9{\cdot}10^7$. Comparing data sets of 100 seconds in length the whole data set was saved, when a new peak detuning event happened. Therefore, the cause of this event could be analyzed later.

Figure 5.4 shows the detuning result. At that time the helium pressure had been stabilized down to 17 μbar due to changes in the helium pump control of the gas return pipe. Thus the rms detuning was only about 1 Hz rms. But nevertheless, peak deviations of up to 16-17 standard deviations occurred. The inset in Figure 5.4 shows the detuning time signal of the peak event. It shows an excitation and decay of what has been analyzed as a mechanical resonance (see Section 5.2.1). The increased excitation of the eigenmode, which is constantly present in the spectrum, lasts for 10-40 seconds. The incidence of such a high detuning event is about 5-10 times per 12 hour period. Several such measurements have been done and showed similar results. Another case of an extreme detuning event is given by increased, sinusoidal-like oscillations in the helium bath. An example is later given in Figure 5.13. Although these events occur rarely, they may trip a decay of the cavity field.

Detuning spectrum

Given in Figure 5.5 is the integrated spectrum of two typical detuning measurements for the two cavities , given by the summation of:

$$\Delta f_{\mathrm{rms}}(f_{\mathrm{mod\ n}}) = \frac{\sqrt{\sum_{i=1}^{n} |(FFT[\Delta f(t)])_{\mathrm{i}}|^2}}{\sqrt{2}}. \tag{5.1}$$

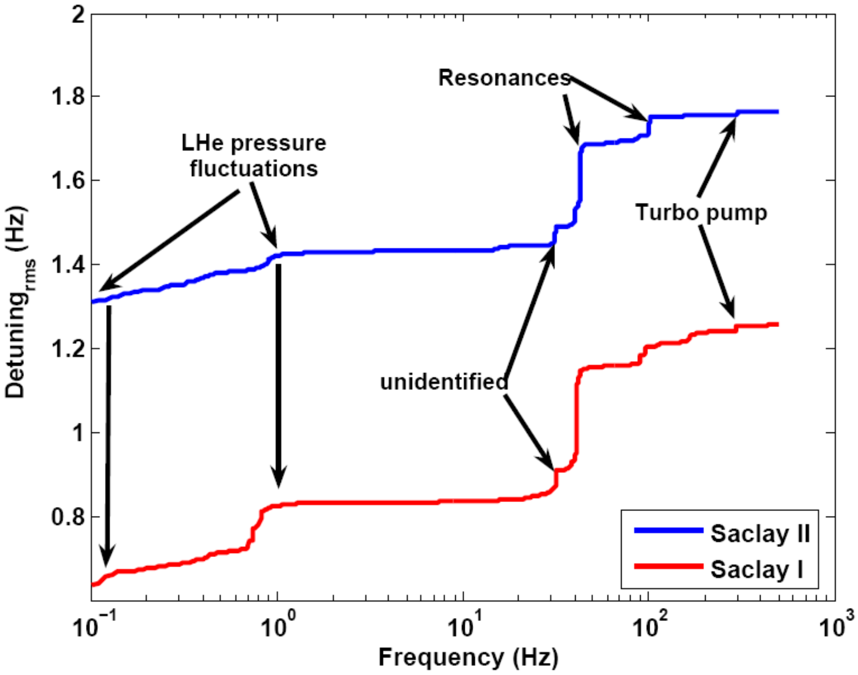

Figure 5.6: Integrated microphonics spectra of the same cavity equipped with two different tuning systems. It can be seen, that the spectral components are nearly independent of the tuner type. It can be further seen, that the contribution by the turbo pump is filtered by the cavity lowpass characteristic.

The result is divided by $\sqrt{2}$ to obtain the rms amplitude of the sinusoidal component. This illustrates which spectral component adds most to the overall shift of the resonance frequency with time. It is obvious, that a significant fraction of detuning is caused by low frequency modulations below 1 Hz. A second component dominating the spectrum are lines at 30 Hz (DESY S33) and 41 Hz for the BESSY 01 cavity.

To identify the sources for this detuning possible contributors have been switched off to observe for changes in the spectrum. Constantly present sources are the turbo pump at 300 Hz and cooling water pumps with a very weak contribution at 14-16 Hz. Furthermore distinctive peaks occur at 41, 90 and 171 for the BESSY 01 cavity, the DESY S33 only features the 30 Hz line. The latter are mechanical resonances of the cavity-tank-tuner system as shown later in the transfer function measurement (see Section 6.2.3).

The BESSY01 cavity has been tested with two different tuner systems installed to measure their impact on the detuning. Results are shown in Figure 5.6. Except for the different detuning due to different helium pressure variations the spectrum appears to be independent of the tuner type. Both spectra show lines generated by the constant single frequency error source at 300 Hz of the turbo, but also contributions identified as mechanical resonances are identical. This suggests, that at least the lower mechanical resonances are caused by the nine-cell structure of the cavity+helium tank itself and not the tuner. A further analysis of the resonant behavior of the mechanical structure will be given in Chapter 6.

5.2.1 Analysis of the detuning

To use the information obtained from the detuning data to develop a control scheme counteracting this error source one has to understand the nature of this effect in more detail:

- The spectrum appears to be only dependent on the installed cavity, but are the amplitudes of these components time invariant?
- If the amplitudes of the spectral components are not time invariant, is this kind of amplitude modulation of stochastic or deterministic, sinusoidal nature?
- Is there a way to separate detuning induced by broadband background noise from detuning driven by constant, single frequency oscillations?

It will be shown, that there are three different kinds of detuning sources dominating the microphonics spectrum:

1. Constant single frequency external sources which are transferred by the beam pipe and the supports of the cryo-unit.
2. Random pressure fluctuations of the liquid helium bath. Sometimes sinusoidal oscillations occur at low frequencies below 1 Hz.
3. Excited mechanical resonances of the cavity-tuner system, which are driven by broadband random background noise and are always present in the spectrum. The detuning amplitude may vary significantly with time.

Wavelet analysis of the microphonics spectrum

The technique of Wavelet analysis [50] was used to resolve changes in the detuning spectrum with time. In contrast to a windowed Fourier analysis a decomposition of the detuning time signal into time-frequency space by Wavelets allows one to determine the dominant modes and their variation with time with a better resolution. Beyond this feature a windowed discrete Fourier transformation alters the obtained results by frequency components of the windowing function [51]. Another advantage of the Wavelet method is, that an orthogonal basis set of finite Wavelet functions instead of infinite sine and cosine functions can be chosen, where the Wavelet basis functions are localized in the time and frequency domain. This improves the ability to detect sharp spikes in the time domain and thus sudden changes in the frequency spectrum.

For the microphonic detuning data analysis it has been useful for a qualitative and a quantitative analysis of the spectral uniformity with time. The variations of spectral detuning components with time set the boundary conditions for the tuner based controller.

Microphonics data showing a strong change of the detuning amplitude with time have been analyzed by Morlet Wavelets [52] as they are a good compromise between frequency and time resolution. Figure 5.7 is a typical representation of a detuning Wavelet spectrum measured with the BESSY01. The data exhibit a strong variation of the detuning power with time for the mechanical resonance. Especially the BESSY01 cavity reveals more than one resonance which appear within seconds and less and are damped down again. This is especially visible between 0.8 s$\leq$t$\leq$1.4 s. The amount of change in the detuning amplitude at the first resonance and the time scale on which this effect happens are given in Figure

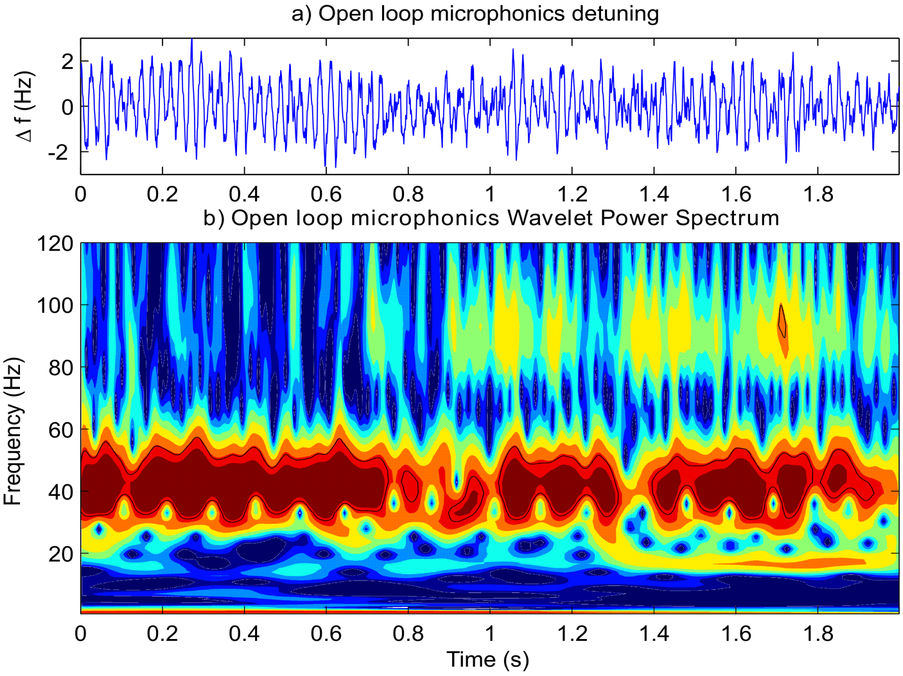

Figure 5.7: Open loop microphonics detuning measurements for the BESSY 01 cavity at Q_{L}=2.7·10^7. The upper plot shows the time data and below the time-frequency map with the color representing the detuning spectral power content. The analysis is based on Morlet Wavelets scaling the frequencies from 0.45 Hz to 486 Hz (Here only shown up to 120 Hz). Strong changes of the detuning amplitude mainly occur at the mechanical eigenmodes.

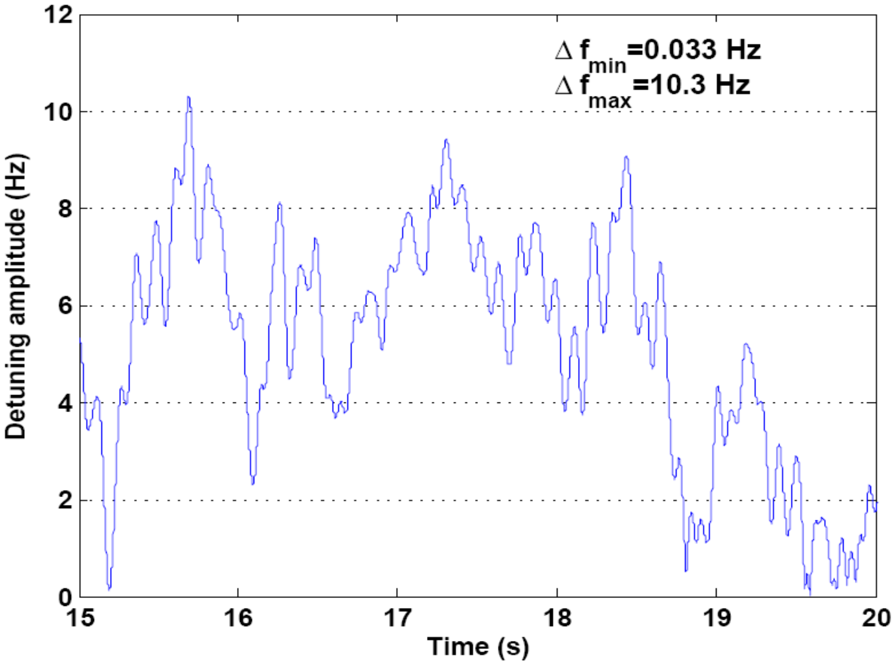

Figure 5.8: Time-frequency analysis of detuning data taken with the BESSY01 cavity with a Q_L=3·10^7 zoomed to the 41 Hz resonance (bandwidth of 1.8 Hz). The plot shows the detuning amplitude with time from a transformation with Morlet Wavelets.

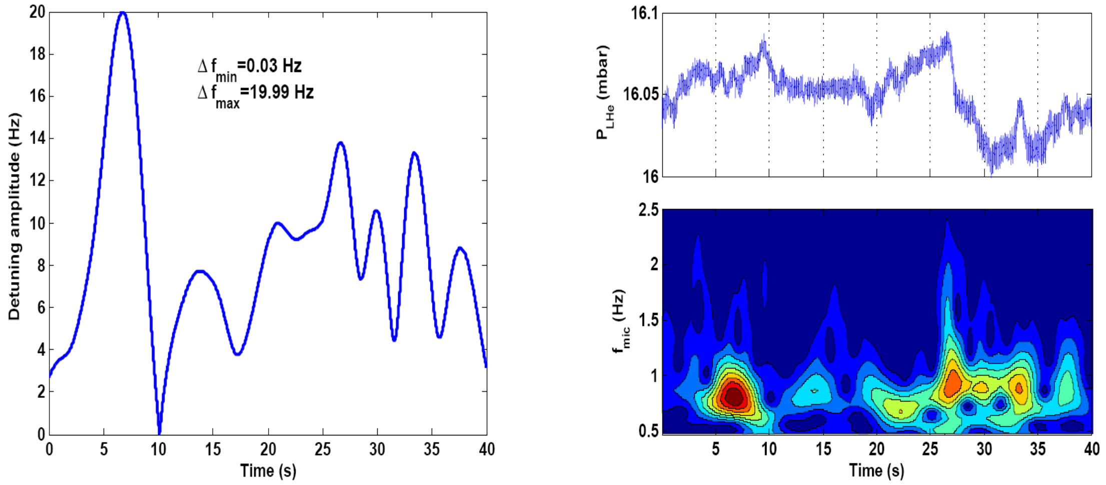

Figure 5.9: Wavelet analysis of the detuning due to pressure variations in the liquid helium bath. The 0.8 Hz line varies on the order of seconds in a stochastic way with peak detuning amplitudes ranging from practically zero to 20 Hz (left plot). The right contour plot emphasizes the stochastic nature of this contribution. The upper right plot depicts the corresponding helium pressure signal. Steep slopes of the pressure are sometimes related to short RF detuning responses at 0.8 Hz.

5.8. The plot is a cut to the resonance related detuning amplitude data in a bandwidth of 1.8 Hz. Analyzing the detuning shows a maximal variation of the level between 0.03 and 10.3 Hz on a time scale of $\sim$ 100 ms. The mean value is around 4 Hz showing, that this resonance is always present in the Fourier spectrum of a measurement. Any kind of controlling mechanism has to keep pace with the time scale on which the amplitude changes. This will be shown later in Chapter 7.

The frequency scaling of the Wavelet transform has been chosen to achieve a good resolution for the lower frequencies of the spectrum. This allows for a detailed interpretation of the helium pressure induced variation of the RF phase. A zoom to the lower frequency range of the time-frequency map of the detuning signal is displayed in Figure 5.9. Already in this short data section of about 40 s (400k samples) it can be seen, that for several seconds strong detuning at 0.8 Hz may occur. These pressure induced fluctuations appear randomly. For comparison in the upper right plot the variation of the pressure sensor signal is shown. Steep changes of the helium pressure are sometimes correlated with high detuning amplitudes at 0.8 Hz in the RF signal. Causes or system parameters triggering such an event have not be found so far, but are likely related to the control of the helium pump system [14]. The random nature complicates the controller design. From the point of view of designing countermeasures for this effect it has to be considered as of purely stochastic nature.

Autocorrelation of microphonics data

The detuning distributions varied from Gaussian, sinusoidal to multi-Gaussian distributions and a combination of those. The integrated spectra and time-frequency analysis showed, that this can be explained by a combination of the low frequency detuning shifts and some strongly excited lines between 30-100 Hz.

The nature of microphonics detuning can be better understood if one analyzes the char-

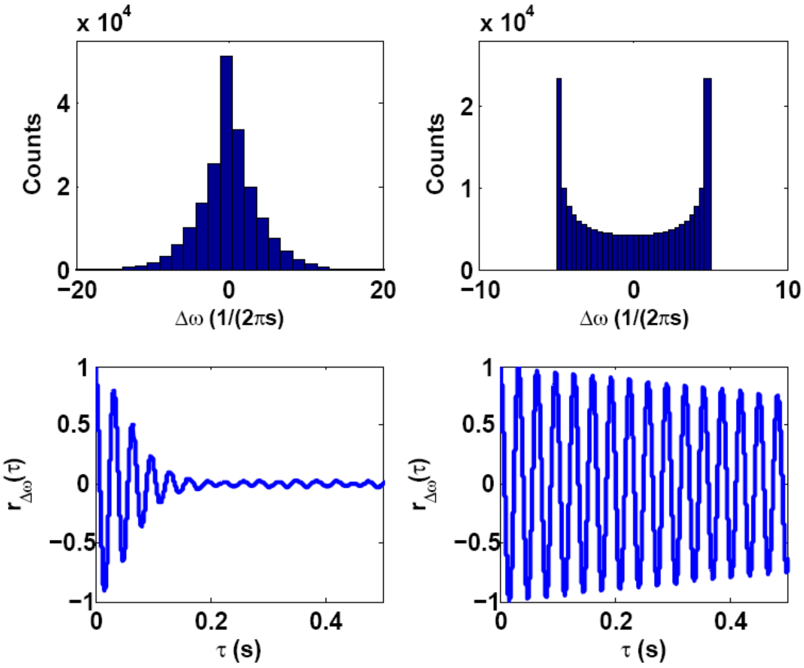

Figure 5.10: Bottom: Normalized autocorrelation of a damped harmonic oscillator driven by a sinusoidal signal (right) and white broadband noise (left). When driven by noise the envelope of the autocorrelation function decays with the time constant of the harmonic oscillator. The upper plot shows the corresponding distribution of the detuning.

acter of the noise sources driving the detuning. This is of special interest for the time varying detuning of the mechanical eigenmode. Useful information about the nature of these processes can be obtained by calculating the autocorrelation function of the detuning signal [53]. The autocorrelation is given by:

$$R_\mathrm{x}(\tau) = \langle x(t) \cdot x(t+\tau) \rangle = \lim_{T\to\infty} \frac{1}{T} \int_0^T x(t) \cdot x(t+\tau) dt \tag{5.2}$$

The autocorrelation depicts the correlation of a measured sample with samples shifted by a given time lag of $n \cdot T_\mathrm{sample}$. A signal of total stochastic behavior would have a maximum for a lag of zero and very low values for all following time lags. In Figure 5.10 (right plots) there is shown the simulated autocorrelation response of a harmonic oscillator of the time domain form given by:

$$\Delta\ddot{\omega}_\mathrm{n} + \frac{2}{\tau_\mathrm{n}} \Delta\dot{\omega}_\mathrm{n} + \Omega_\mathrm{n}^2 \Delta\omega_\mathrm{n} = n(t) \tag{5.3}$$

with $n(t)$ being the inhomogeneous driving term of this second order system, τ_n the damping time and Ω_n the mode's frequency. In the case of a deterministic sinusoidal driving term the system starts to oscillate with a constant amplitude and the frequency of $n(t)$. The normalized autocorrelation reflects this characteristic:

$$r_{\Delta\omega}(\tau) = \frac{R_{\Delta\omega}(\tau)}{R_{\Delta\omega}(0)} = \cos(\omega_{drive} \cdot \tau) \tag{5.4}$$

Note, that the amplitude of the function has a slightly decaying envelope. This is due to the fact, that the sine wave of the simulation is finite in length.

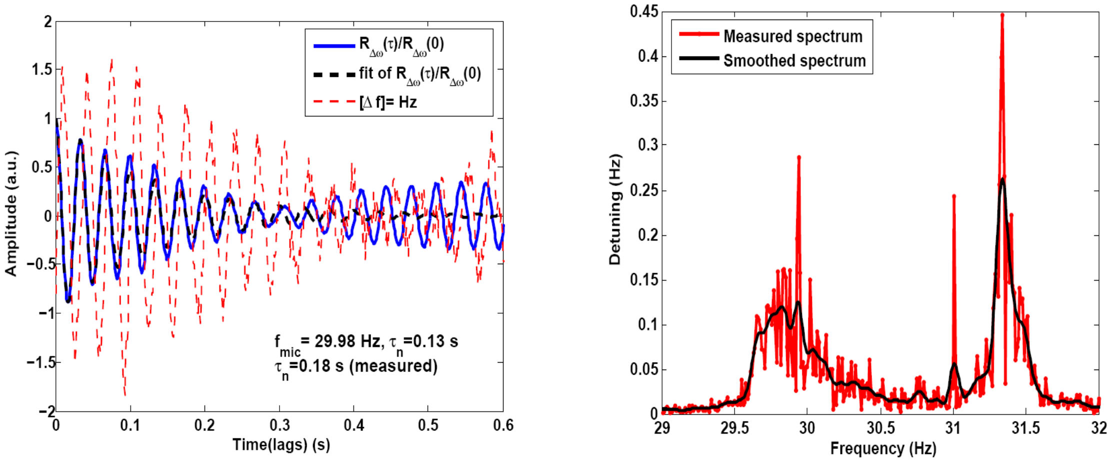

Figure 5.11: Autocorrelation function of measured microphonics detuning. In this case a 30 Hz mechanical resonance has been excited by an external noise-like source (band-limited), the autocorrelation function decays with the mode's time constant (Left plot). The right plot shows a zoom of the corresponding detuning spectrum. It can be seen, that the 30 Hz oscillation splits into two adjacent contributions at 29.9 and 31.3 Hz.

If the case of broadband non-stationary noise occurs, there is a chance of a resonant excitation of this second order system. Consequently the autocorrelation results in a damped cosine response oscillating with the mode's frequency Ω_n with the time constant of the envelope being the decay time τ_n:

$$r_{\Delta\omega}(\tau) = \cos(\Omega_n \cdot \tau) \cdot e^{-\left|\frac{\tau}{\tau_n}\right|} \tag{5.5}$$

Hence, modes excited by broadband and narrow-band noise have drastically different autocorrelations which can be used to distinguish between the two.

The autocorrelation function of measured microphonics detuning given in Figure 5.11 shows to some degree the exponential decay of a damped harmonic oscillator driven by broadband noise. The expected evolution of the curve has been fitted by Equation 5.5 resulting in a decay time of τ_n=0.13 s (τ_n and Ω_n as fit parameters). This differs by 27% from the measured value, which has been directly determined from the calculated autocorrelation of the detuning. This deviation between fit and measurement may be explained by two effects. First of all, when measuring the spectrum with a resolution better than 0.1 Hz, one can clearly resolve two close-by peaks at 29.9 and 31.3 Hz. It will be shown later (Chapter 6), that they belong to two polarization modes of a transverse mechanical eigenmode of the cavity.

Summarizing this means, that the driving process of the lowest strong excited lines (30 Hz, 41 Hz) is a stochastic process and may be regarded as noise. Furthermore these lines are excited second order systems. But as the structure of these resonances in the frequency domain is quite complex, as will be shown, the autocorrelation method is not suitable to derive the exact properties of the modes such as decay time τ_n. The measurement of the tuner transfer function will show an excitation of this mode with a decay time of $\approx$ 0.1 s (see Section 6.2.3). Nevertheless, the autocorrelation gives a qualitative understanding of the properties of the external noise sources driving the detuning. Also, at least the order of magnitude of the mechanical parameters can be determined.

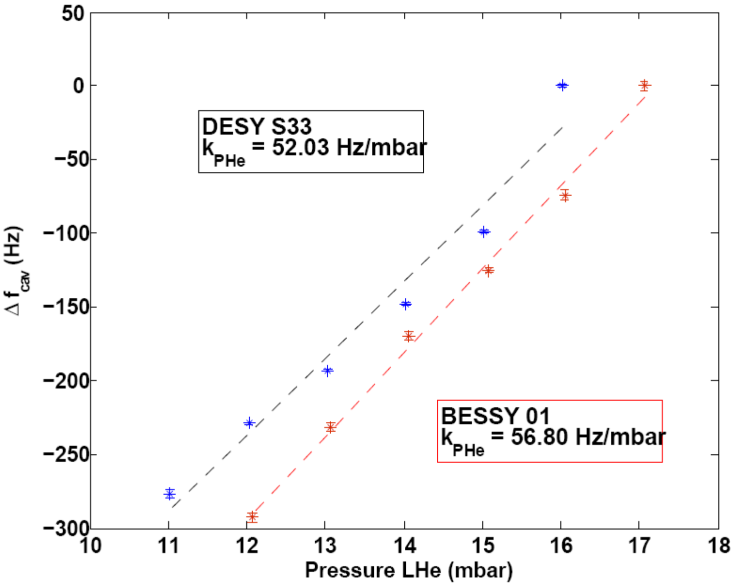

Figure 5.12: Dependance of the cavity frequency on the liquid helium pressure.

Summing up, this property of the detuning rules out any pure feedforward approach for the fast tuning controller, simply because this error source is non-constant with time. Any controller, if it is a feedback or feedforward system, has to adapt to these changes.

Liquid helium pressure stability

A large part of the total detuning is given by low frequency drifts and oscillations especially for very narrow-band cavities with a loaded $Q_{\mathrm{L}} > 1 \cdot 10^8$. They are mainly caused by pressure fluctuations in the two-phase He-line. Also, the level of liquid helium is controlled in the two phase line to a specified set point. Any deviation in this level leads to a change of the forces induced by the column of fluid above the cavity walls.

Due to the shape of a cavity cell, differences in the material's stiffness and due to the stiffening rings at the iris sections of the cavity, the cavity deformation does not respond uniformly to the pressure acting isotropically on the cavity. A change of the cavity shape at the equator because of inwards acting forces leads to an increase of the resonance frequency [12]. This is shown in Figure 5.12, where an increase in the static pressure increases the resonance frequency. The acquired value of $\approx$ 55 Hz/mbar leaves room for a further optimization of the cryo-unit to decrease this coefficient and demonstrated the need for a very stable cryogenic system. The measured values at around $\sim$ 55 Hz/mbar are about a factor of 2.5 larger than given in [54]. The usual measured pressure variations were between 16-25 μbar rms, which would generate a detuning of $\leq$ 1.4 Hz. But sometimes strong pressure variations with four times the usual amplitude and at frequencies of 0.4 or 0.8 Hz occurred. An example for such a strong event is given in Figure 5.13. Pressure fluctuations at 0.43 Hz led to a rms detuning of 5 Hz for modulating frequencies below 1 Hz. The equivalent pressure stability was 94 μbar rms and $\simeq$ 300 μbar peak-to-peak, yielding a quasi dynamic detuning of 53 Hz/mbar at 0.43 Hz. In such a case the total rms detuning exceeds the cavity bandwidth of 10.4 Hz more than doubling the required rms power to maintain the cavity field. Even though this event is reasonable rare, one has to ensure, that this RF power can

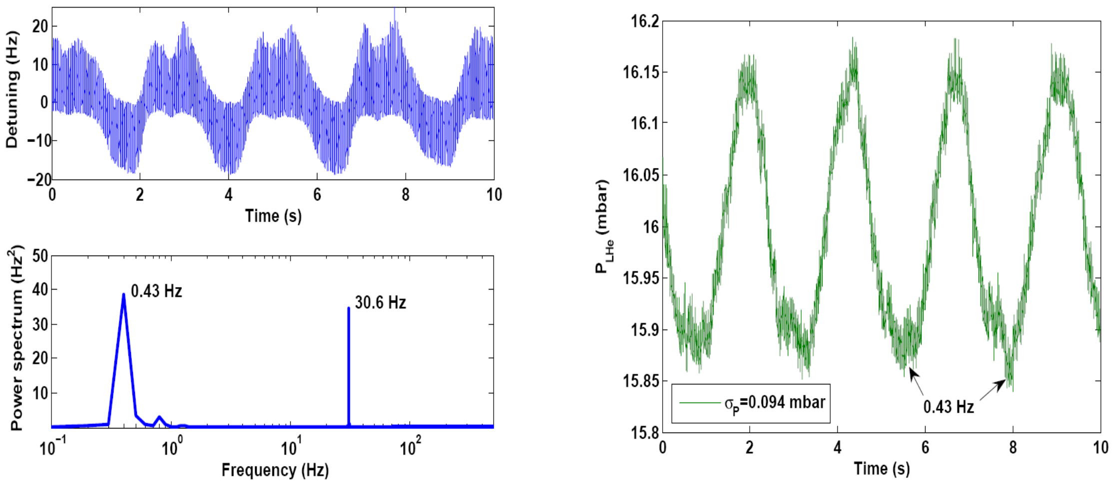

Figure 5.13: Open loop microphonics detuning measurements showing a case where very strong pressure fluctuations of the helium bath occurred. The left plots depicts the detuning signal with time (upper left) and below the corresponding Fourier spectrum is shown. The right plot displays the signal of the pressure sensor showing the same 0.43 Hz oscillation visible in the RF detuning. The rms detuning σ_f was 7.9 Hz at a bandwidth of 20.8 Hz.

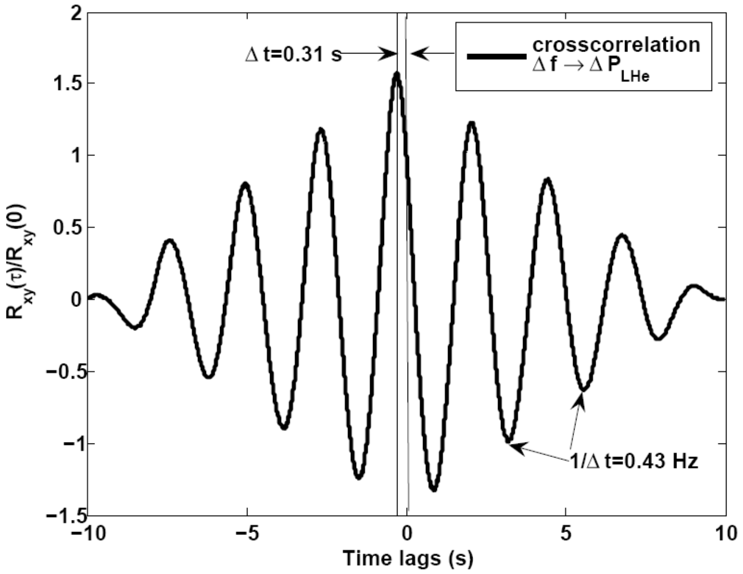

Figure 5.14: Cross-correlation between the helium pressure sensor signal and the RF detuning showing a peak at a time lag of 310 ms. This corresponds to the integration time of the pressure sensor. The observed periodicity is related to pressure fluctuations at 0.43 Hz.

be supplied by the klystron during operation.

The strong correlation between pressure changes and cavity detuning can be proven by calculating the cross-correlation between the phase error signal and the pressure signal. In Figure 5.14 there is given the normalized cross-correlation between the two signals, which were normalized themselves in advance. The data sets are the same than in Figure 5.13. The maximum correlation is given at a time lag of 310 ms between both signals, which is the integration time of the pressure sensor and thus is a measurement artifact. The

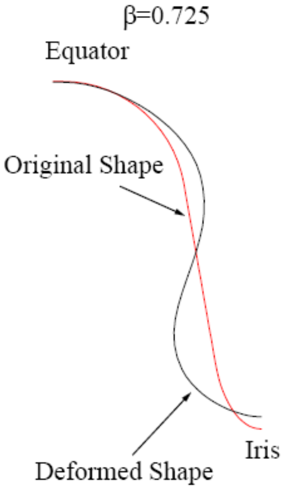

Figure 5.15: Deformation of a $\beta = 0.725$ cavity for the J-Parc project at 30 MV/m (exaggerated by a factor of). Usually a detuning of 1 Hz corresponds to a deformation of the order $\simeq$ 1-3 nm depending on the stiffness of the material.

periodicity reflects the 0.43 Hz pressure and detuning oscillation. The cause of these pressure fluctuations are not understood so far. It may be due to helium gas plugs in the helium supply line from the liquefaction plant or even thermo-acoustic waves in the two phase line.

5.3 Lorentz-Force detuning

Besides microphonics the second effect contributing to cavity detuning is due to the Lorentz forces acting on the cavity walls by the RF field itself (radiation pressure). The magnetic field exerts an outward force $\propto \frac{1}{2}\mu_0 H^2$ and the electric field an inward pulling force $\propto \frac{1}{2}\varepsilon_0 E^2$ [25] resulting in a total pressure of:

$$P_{\text{rad}} = \frac{1}{4}\left(\mu_0|\vec{H}|^2 - \varepsilon_0|\vec{E}|^2\right). \tag{5.6}$$

The radiation pressure effects a change of the resonators volume by ΔV causing a shift of the resonance frequency of the according excited RF mode given by Slater's formula [55]:

$$\frac{\delta\omega}{\omega} = -\frac{\int_{\Delta V}\left(\mu_0|\vec{H}_0|^2 - \varepsilon|\vec{E}_0|^2\right)dV}{\int_V\left(\mu_0|\vec{H}_0|^2 + \varepsilon|\vec{E}_0|^2\right)dV} \tag{5.7}$$

where $\vec{H}_0$ and $\vec{E}_0$ are the unperturbed field values and the denominator is the stored energy in the resonator.

Figure 5.15 shows the theoretical deformation of a $\beta = v/c$=0.725 elliptical cavity half-cell of the J-Parc project at 30 MV/m [56]. Similar to a TESLA cavity the strong electric field next to the cavity iris contracts the cell while the high magnetic fields at the equator lead to an outward deformation. Both effects add up to a negative change of the resonance frequency.

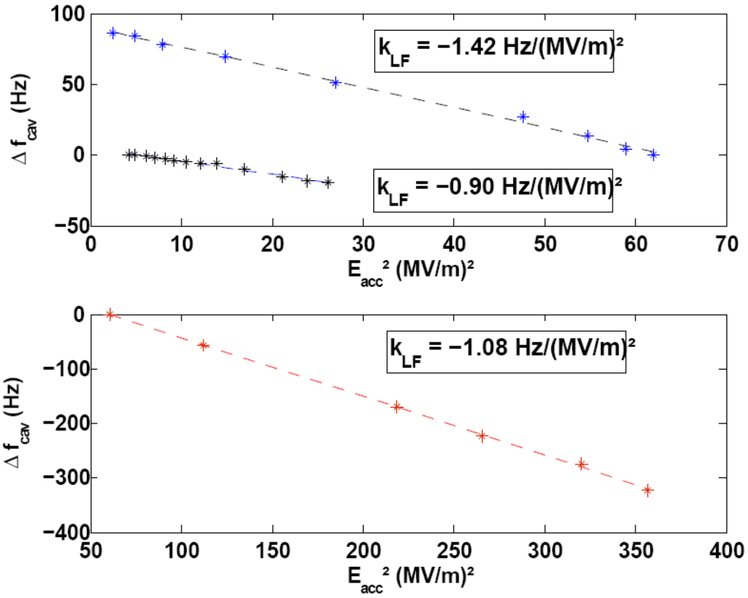

Figure 5.16: Static Lorentz force detuning measured for the BESSY01 and DESY S-33 (red stars, Saclay I) cavities. The BESSY01 cavity achieves a stiffer response with the Saclay II tuner (black stars, top) than with the Saclay I design (blue stars).

5.3.1 Static detuning

The static detuning for TESLA cavities has been measured with the PLL in closed loop mode by changing the accelerating field level and measuring the resonance frequency in equilibrium. The measured Lorentz-force detuning coefficients k_{LF} of 0.9-1.41 Hz/(MV/m)^2 (see Figure 5.16) lie well within the range given by [12] or [57] for a nine cell cavity equipped with stiffening rings. It appears, that the Saclay II tuner improves stiffness of the system (less Lorentz-force detuning). This has been proven, as the lowest coefficient has been measured with the Saclay I design by increasing the pre-load and thus stiffness as much as possible (black curve of Figure 5.16).

This also agrees with the observation, that the microphonics are reduced, when the Saclay II tuner is mounted. This will be discussed further in Chapter 6.

For CW operation the static value is in that respect of importance to determine the pre-detuning to operate the cavity at a certain field level. It also represents the total coupling strength of all mechanical eigenmodes.

5.3.2 Dynamic Lorentz force detuning

Even with RF feedback, during CW cavity operation the field amplitude will fluctuate slightly due to the various noise sources. Hence the Lorentz forces acting on the cavity have to be considered as a time varying quantity. Usually the low level RF system will keep the field amplitude within strict boundaries, but it has to be understood how far even small field modulations around the steady state can disturb the phase stability of the cavity field. This is especially true when the RF source is at its saturation limit when a runaway situation can ensue. The latter is often referred to as ponderomotive effects in cavity operation [53]. An example measurement and a simulation of this effect is given in Appendix B.

The mechanical properties of the cavity determine how much the changing forces may couple to eigenmodes of the nine-cell structure thus exciting unwanted oscillations. Simulations of [36] and measurements with pulsed cavities at the TESLA test facility (TTF) have shown [58], that the Lorentz force detuning dynamics is most likely described by a second order system of parallel acting modes as described in Section 3.2.

From a theoretical view, the mechanical system can be described by a vibrating string model and eigenmodes can be calculated by a modal analysis of this system. The derivation of this model can be found in [36], [59] and [60]. As shown by [61], this model can be transferred into a set of ordinary differential equations for the cavity mechanical eigenmodes $\Delta\omega_{m,i}$ as given by the following equations 5.8:

$$\Delta\ddot{\omega}_{cav,i}(t) + 2\xi\omega_{m,i}\cdot\Delta\dot{\omega}_{cav,i}(t) + \omega_{m,i}^2\cdot\Delta\omega_{cav,i} = -k_{LF,i}2\pi\omega_{m,i}^2 E_{acc}^2(t) \tag{5.8}$$

$$\Delta\omega_{cav}(t) = \sum_i \Delta\omega_{cav,i}(t). \tag{5.9}$$

The damping constant ξ_i, the eigenmode frequency $\omega_{m,i}$ and finally the coupling constant $k_{LF,i}$ of the i^{th} mode to the field modulation $E_{acc}^2(t)$ have to be determined experimentally. The contribution of each eigenmode detuning $\Delta\omega_{cav,i}$ adds up to the total time varying detuning. For very slow changes in the field amplitude the detuning is directly proportional to the measured Lorentz force detuning constant k_{LF} as given by $\Delta f_{cav} = -k_{LF}\cdot E_{acc}^2$. This means, that the static Lorentz force detuning constant can be understood as the DC component summing over all modes contributing to the detuning.

Measurement principle

The best way to determine the mechanical parameters of the model describing the mechanical Lorentz force response is to measure the response to a sinusoidal modulation of the Lorentz force detuning (transfer function). This will result in a steady state response at each modulation frequency, such that a complete Bode plot in frequency domain of this mechanism is obtained

Setup

An overview of the modified measurement setup is shown in Figure 5.17. To derive the exact mechanical parameters, the measurement results have to be decoupled from any filtering effect by the cavity (half-)bandwidth $\omega_{1/2}$. Hence, the PLL is locked to the cavity frequency (closed loop mode). The measured phase (i.e. detuning) response will bear a transfer function which is not altered by the cavity transfer function itself given a sufficient PLL gain.

The RF setup has been slightly changed to allow an amplitude modulation of the forward power resulting in a field amplitude modulated around a mean offset value.

To account for the quadratic proportionality of the detuning to the field level a operational amplifier-based electrical circuit [62] adapts the modulation signal from the lock-in amplifier. This is mandatory to create a clean amplitude modulation at the RF mixer of the forward power after the signal source. Thus the square root of the amplitude modulated signal is delivered to the mixer, which is thus a sinusoidal modulation of the power. The amplitude modulation of the forward power is given by $P_{\text{forward}} = P_0(1+\epsilon\sin(\omega_{\text{mod}}t))$. As $P_{\text{forward}} \propto E_{\text{acc}}^2$ the modulation index ϵ has to be chosen $\ll$1 to avoid the excitation of higher harmonics.

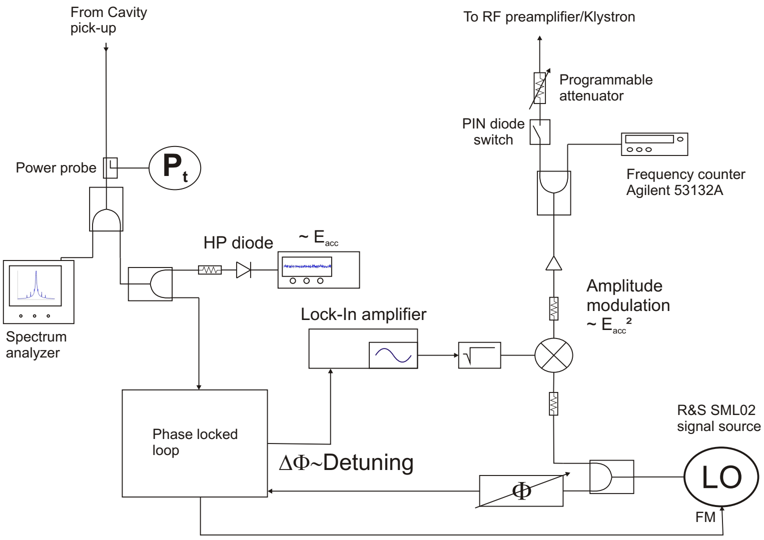

Figure 5.17: Modified measurement setup for the dynamic Lorentz force response of a TESLA cavity. The transfer function between Lorentz force modulation proportional to E_{acc}^2 and RF detuning has been taken with a lock-in amplifier using its internal sinusoidal reference output as the modulation source. The amplitude modulation of the forward RF signal is achieved with an RF mixer used as an up-converter. The field level has been tracked with a detector diode, the total system is run in closed loop mode.

This has been checked beforehand by locking on the higher harmonics of the modulation signal.

The phase or detuning response is measured by a lock-in amplifier [63] (It also delivers the harmonic excitation signal for modulating the forward power). In principal the lock-in amplifier performs a Fourier analysis of the incoming signal by sweeping a given frequency range, splitting the signal in its in-phase and in-quadrature components and mixing these I and Q components with its internal reference. This is just the decomposition into the Fourier components. The acquired transfer function thus shows the amplitude and phase response of the cavity to the Lorentz-force in frequency domain.

In the case of a second order system driven by an external force the steady state response is given by the particular solution of the differential equation [64] as can be shown by using the method of variation of constants. For an external modulation shifted from the mechanical eigenmode the amplitude response for $t \longrightarrow \infty$ is given by:

$$\Delta\omega_{cav,i} = \frac{-k_i E_{acc}^2 \epsilon \omega_{m,i}^2}{\sqrt{1 + tan^2(\Phi)}} \cdot \sin\omega_{mod} t + \Phi \tag{5.10}$$

with $\tan(\Phi) = Q_{m,i} \frac{(\omega_{m,i}^2 - \omega_{mod}^2)}{\omega_{m,i}\omega_{mod}}$ and $\epsilon = 2\frac{E_{mod}}{E_{acc}}$. To keep track of the real field oscillations in the cavity the transmitted Power (P_{trans}) has been measured in advance with this setup. Effectively this is a measurement of the (residual) filtering function of the cavity. This transfer function $P_{trans}(\omega_{mod})$ has been used to scale the detuning amplitude transfer function $\Delta\omega_{cav}(\omega_{mod})$ in relation to the real field amplitude variation. This showed to be necessary as the PLL gain had to be limited to achieve still a good measurement resolution.

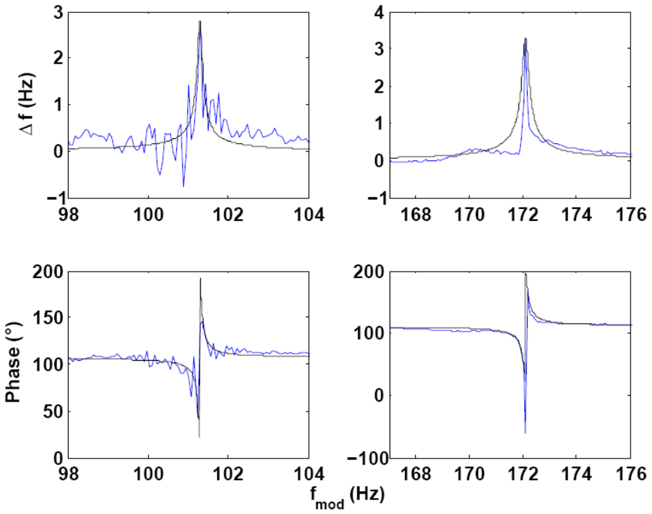

Figure 5.18: Dynamic Lorentz-force-detuning transfer function around two mechanical eigenmodes of the cavity. The black curves show the fitted Lorentz curve like distributions of the resonances. The measurement was done at about 4.2 MV/m and at a $Q_{\mathrm{L}} = 3.9 \cdot 10^7$.

Table 5.1: Parameters of the first five mechanical modes coupling to Lorentz force variations with the BESSY 01 cavity, Saclay II tuner.

Parameter	**1st mode**	**2nd mode**	**3rd mode**	**4th mode**	**5th mode**
$\omega_{m,i}(Hz)$	42.72	101.3	172.09	232.0	281.8
$Q_{m,i}$	30.5	848.4	705.3	23.2	108.4
k_i (Hz/(MV/m)^2)	0.0105	0.0108	0.0126	0.0098	0.0084

Typical results

For two identified mechanical modes at 101.3 and 172.1 Hz, which are quite isolated from neighboring eigenmodes, scans with an improved resolution of the frequency sweep have been performed. Their amplitude and phase responses are displayed in Figure 5.18. To obtain the parameters like the mechanical quality factor Q_m the theoretical response has been fitted to the data. It is obvious, that the Lorentz curve alone does not explain the measured data in all details. Both peaks show an asymmetric distribution around resonance. Furthermore especially the measurement at around 100 Hz exhibits a rising slope of the amplitude curve.

To measure the complete transfer function to obtain a description of all modes contributing to the overall detuning one would have to measure the systems response up to several kHz, as there are many longitudinal modes of the cavity body [36]. The response of these higher modes at lower frequency alter also the amplitude and phase response of the lower mechanical eigenmodes. Unfortunately due to the limited coupling range in the lower limit it is not possible to drive the cavity at a loaded quality factor low enough, that it would not alter the transfer function in the high frequency regime too much. This can partly be negated by the PLL, but only with a very high gain thus limiting the sensitivity of the setup.

Nevertheless, modes up to 280 Hz have been measured and their parameters are given in Table 5.1. The values of the coupling constant k_i are of the same order of magnitude as given

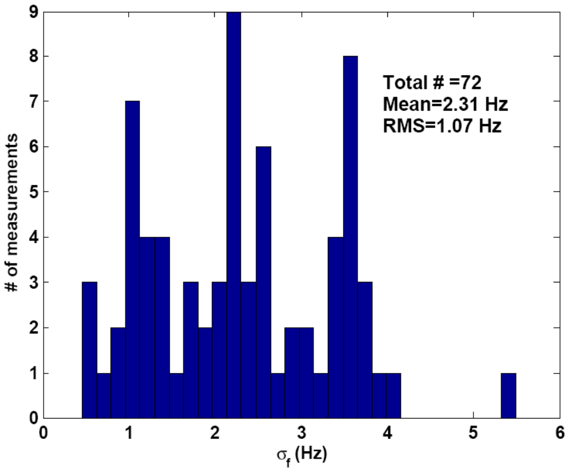

Figure 5.19: A histogram showing the rms detuning values of all open loop microphonics measurements taken at HoBiCaT including two cavities equipped with two different kind of tuning systems. The loaded quality factor was around $3{\cdot}10^7$

.

in simulations by [36]. The sum $\sum k_i$ of these modes is $\simeq$0.5 Hz/(MV/m)^2. The difference to the static value of 0.9 Hz/(MV/m)^2 is possibly given by the modes beyond the measurement range. The mechanical quality factors obtained are similar to the ones, which can be excited by the fast piezo tuner (Section 6.2.3). But as the forces acting on the cavity are different in their direction and distribution the shape and parameters of the modes are different in most cases. To obtain a deeper insight into the dynamics of the mechanical cavity system this measurement should be done at higher field levels with a small modulation index, but a modulation amplitude which is at least 1 MV/m for the frequency range of interest.

5.4 Conclusion: Cavity statistics at HoBiCaT

Summarizing all microphonics detuning measurements recorded at HoBiCaT one can derive some expected mean rms detuning for CW operation. A histogram showing all detuning data taken and adding up to more than 16 hours of measurements is displayed in Figure 5.19. The measurements were mostly recorded in open loop configuration with the cavity bandwidth $f_{1/2}$ around 21 Hz. One sigma of the distributed rms detuning values covers the range of 1.2-3.4 Hz.

The open loop error without any RF control would thus be 3.2°-8.9° for the loaded quality factor of $3{\cdot}10^7$. This corresponds to required feedback gains of 160-450 to achieve phase stabilities of 0.02°. As it is not clear, if it is possible to run cavities at such a high feedback gain (450) in a stable and efficient way, a fast tuner compensating the microphonics is desirable.

The peak detuning events at HoBiCaT exceeded values as high as 26 Hz and sometimes excursion to 17 standard deviations have been observed. To maintain strict field control during these events, a significant RF power overhead must be available.

Table 5.2 gives an overview of the most prominent lines in the different detuning spectra. In the usual case where there is no peak event related to strongly excited eigenmodes or increased pressure fluctuations most detuning results from slow pressure fluctuations. In

Table 5.2: Most prominent peaks in the detuning spectrum of all tested cavities

Cavity	**Tuner**	**Excited resonances (Hz)**	**External contributions (Hz)**
BESSY01	Saclay II	41, 100, 174	30, 300
DESY S-33	Saclay I	31	300

general this is a random effect. The specific lines in the spectra are related to the lowest mechanical eigenmode of the cavity-tuner system. The amplitude may vary stochastically with time. Some other lines can be identified with known external error sources, but their overall contribution to the rms detuning is negligible, primarily because of the small cavity bandwidth. But it is important to construct the cavity-tuner-system such, that the mechanical resonances are far away from these given sources.

One should take into account, that the microphonics detuning at a real linear accelerator facility could be somewhat more than shown here. Mechanical oscillations may couple between cavities of one cryo-module and there may be more ancillary equipment transferring acoustic noise to the cavities. Microphonics measurements taken at TTF [12] resulted in detuning ranging from 4-9 Hz rms. This is up to 100 % more than observed here. Nevertheless one should consider, that due to the pulsed operation these increased values could be explained by remnants of decaying mechanical eigenmodes.

Similar research with respect to CW detuning sources have been done at the Jefferson Laboratory for the SNS, RIA and CEBAF projects [65] [66]. The devices under test are five to seven cell elliptical cavities similar to the TESLA shape. The rms detuning values are between 2-6 Hz, similar to the results obtained in this work.

Given the differences in the obtained spectra of each cavity implies, that a microphonics compensation scheme has to be flexible with respect to changes in any system parameter (including the mechanical transfer function and the spectrum of the external noise sources). Therefore, it is indispensable to characterize each cavity after installation into the linac to program and adapt the individual control parameters of the algorithms.

Chapter 6

Piezo based fast cavity tuning systems

A full characterization of the detuning error sources at HoBiCaT has been presented in the previous chapter. The mean rms microphonics detuning level of 2.3 Hz would relate to a cavity phase stability of 0.03° at Q_L=$3{\cdot}10^7$ assuming an LLRF feedback gain of 200 can be realized. This amount of phase stability exceeds the limit for stable FEL operation (Section 2.5.1) even if other error sources do not exist. Moreover, the incidence of peak detuning events have to be considered as without control they may lead to unstable behavior which can trip the interlock. Therefore, it appears necessary to implement an active compensation system to reduce microphonic detuning.

In principle every accelerating cavity is equipped with a tuning system to match the resonance frequency to the desired accelerator operating frequency, 1.3 GHz in the case of the TESLA cavities. Here, the cavity tuning systems cover a broad tuning range of about 300-500 kHz, broad enough to compensate for cavity manufacturing tolerances and changes during cooldown. In the tuning systems for TESLA cavities fast, piezo-based, supplementary tuners can be integrated.

In the following, the tuning systems tested with the TESLA cavities are characterized especially with respect to their fast tuning capabilities. The goal is then to use this information to design a controller, that can compensate the dynamic detuning. Hence knowledge of the dynamic properties of the cavity-tuner system is of paramount importance.

6.1 Tuning systems for TESLA-type cavities

Several tuners have been developed for the TESLA system (Table 6.1 by [67]). The working principle is always given by deforming the cavity in such a way, that the change of the cavity volume leads to a shift of the resonance frequency. Only these Saclay type tuners developed at CEA-Saclay [46] have been tested at HoBiCaT so far.

6.1.1 The Saclay I and II tuning systems

Figure 6.1 shows pictures of the two tuning systems installed on the cavity opposite to the coupler end. The lower picture row gives a closer view of the piezo holding systems of the tuners. The working principal of the tuning systems can be explained by the simplified overview of Figure 6.2. The movement of a spindle is transferred by a lever system (Saclay

Table 6.1: Tuner types for TESLA cavities. Table of [67] extended with parameters measured at HoBiCaT.

Parameter	**CEA-Saclay I**	**CEA-Saclay II**
Coarse range [kHz]	±360	±250
Coarse resolution [Hz]	<1	<1
Fast system	Piezo	Piezo
Fast range [kHz]	0.5-0.7	1.0
Tuning direction	Tensile & compression	
Position of fast actuator	4 K, vacuum	
Position of motor	4 K, vacuum	
Position of tuner	End of cavity	

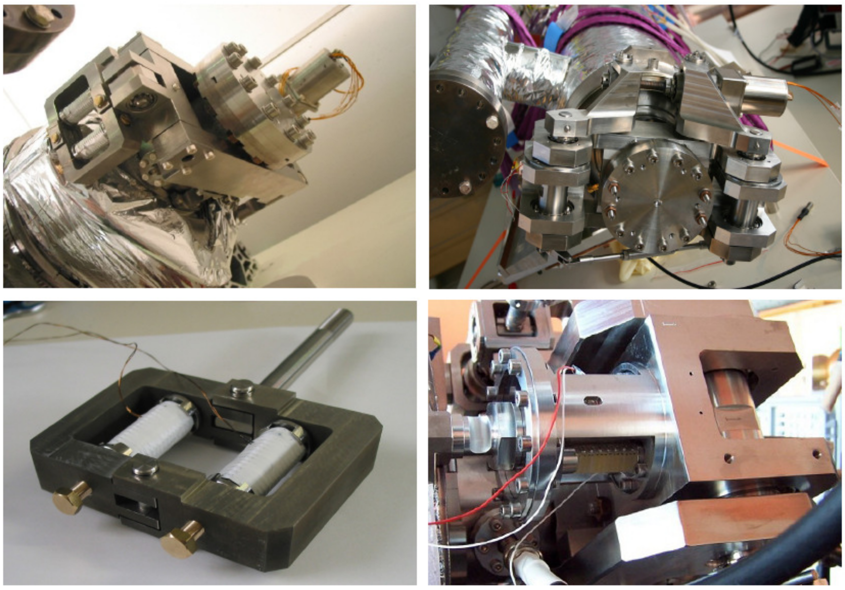

Figure 6.1: Saclay tuning systems for TESLA cavities. The upper row shows pictures of the Saclay I tuner (left) and Saclay II tuner mounted to the cryo-unit of a cavity. The lower pictures display the piezo holder frame of the Saclay I tuner with a two piezo design (left) and the two piezo design of the Saclay II tuner housing the piezos inside the cylindrical metal box.

I) or the excentric of the Saclay II tuner to the cavity's beam pipe flange. The force on the flange directly converts into a change of the cavity length.

The pre-load on the piezo elements is determined by the stiffness of the overall setup. For the Saclay I system it is given by the stiffness of the holder frame itself, the position of the screws fixing the piezos into their position and to some extend on the forces between cavity and tuner. The Saclay II tuner increases the pre-load onto the piezo elements by the tuning itself. The pre-load defines how well the fast tuning part couples to the cavity, thus influencing the response time of the fast tuner. Any loose parts or friction in the system will lower the resolution of the tuner and lead to an increased phase lag, complicating microphonics control. In the following the tuning systems will be called tuner type I and II.

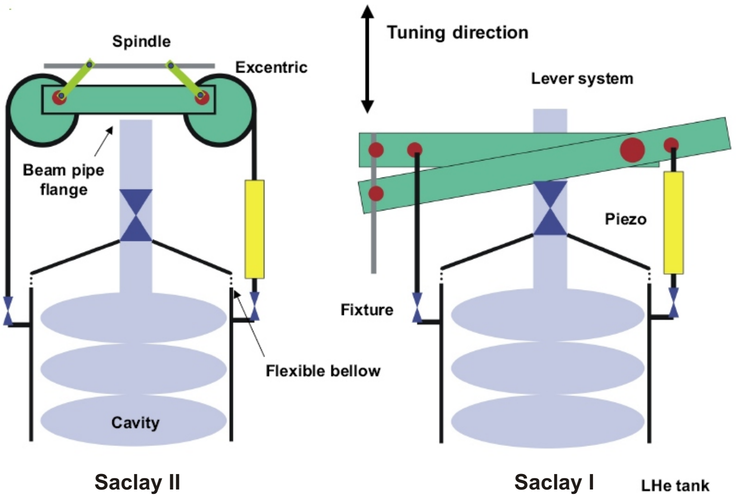

Figure 6.2: This scheme displays the working principle of both Saclay tuning designs. While both systems are based on transferring the rotation of a stepper motor via a spindle to a cavity deformation, the displacement is created by a lever system for the Saclay I tuner and an excentric rod for the Saclay II system.

6.1.2 The piezo tuner

The fast tuning part has to fulfill several functions to be used in the accelerators cryogenic environment:

- Achieve a displacement of several μm in a cryogenic environment from ≤ 2 K to 20 K. This corresponds to a tuning range of several hundred Hertz.
- Work against a stiff and massive system corresponding to a blocking force of several kN
- Work in a radioactive environment in case of beam loss or field emission in a cavity
- A sub-Hertz resolution of should be achieved related to a nm step width. This is of importance to counteract very low microphonics amplitudes.
- Few mechanical resonances in the range of microphonics detuning
- A fast response time (small group delay) to avoid too much phase lag in the control loop

The piezo tuner frame for the type I tuner is based on a DESY design to compensate the Lorentz force induced detuning during an RF pulse [68]. The original version was tested in HoBiCaT, but it soon became clear that it was not stiff enough [69]. Hence the thickness of the frame was doubled. To prevent transverse stress on the piezo elements the holders of both tuning designs use conical supports and spherical heads for the parts keeping the piezos in their frames. Additional fixtures connecting between the tuning frames and the cryo-unit also compensate for unwanted transverse motion of the fast tuner.

Table 6.2 gives an overview of the piezo stacks used for both tuning systems. The type II tuner features two low voltage Noliac$^{\text{TM}}$piezos. For the type I piezo holder high voltage

Table 6.2: Piezo stack parameters

Parameter	**Piezomechanik™**	**Noliac™**
Open loop travel [μm at 300 K]	40	42
Driving voltage [V]	0 to -1000	-10 to 150
Push/Pull force [N]	12500/2000	-
Blocking force [kN]	11.6	6.3
Capacitance [nF at 300K]	360	5700
Unloaded resonance frequency [kHz]	8.0	66.0
Stiffness [N/μm]	290	150
Resolution [nm]*	0.2	-

piezos from Piezomechanik™were used. They offer the advantage of an even bigger stiffness and blocking force. There are concerns, that the high voltage may lead to sparkovers should a helium leakage occur in the isolation vacuum. But referring to Paschen's law [70] the maximum potential of 1 kV would only lead to a breakdown at helium pressure above 0.39 mbar at 1 mm gap distance. One can assume, the cryomodule will not be operated should such a large helium leak occur.

6.2 Characterizing the tuning system

For the design of a fast tuner controller it is of importance to first fully characterize the effect how forces produced by the fast and the coarse tuner affect the cavity mechanics. This has to be understood for the frequency range of interest where microphonics detuning or even Lorentz force induced variations (refer to Section 5.3) may occur.

The amount of microphonics and the minimum level which can be compensated for is limited by the tuner's resolution. Beyond this for a given frequency it has to be determined how the tuner-cavity system responds in amplitude and phase when excited by a constant oscillating amplitude (transfer functions, mechanical resonances). Furthermore this leads to the question, if these values change when system parameters change (e.g. helium pressure, Lorentz force pressure, pre-detuning).

6.2.1 The coarse tuners

The PLL setup was used to record the tuning curve of the tuning systems. The stepper motor was driven by a number of steps and in parallel the cavity frequency was recorded with a frequency counter (see Figure 4.6). For the type II design the total tuning range is more than 500 kHz leaving enough overhead for pre-detuning variations during installation of the tuner and different deforming of the individual cavities during the cool-down process. The tuner's stiffness changed in the course of the measurement. It changed from 0.08 Hz/step to 0.1 Hz/step.

---

[*] This is a theoretical value only since the resolution of the piezo is also influenced by the supporting mechanics.

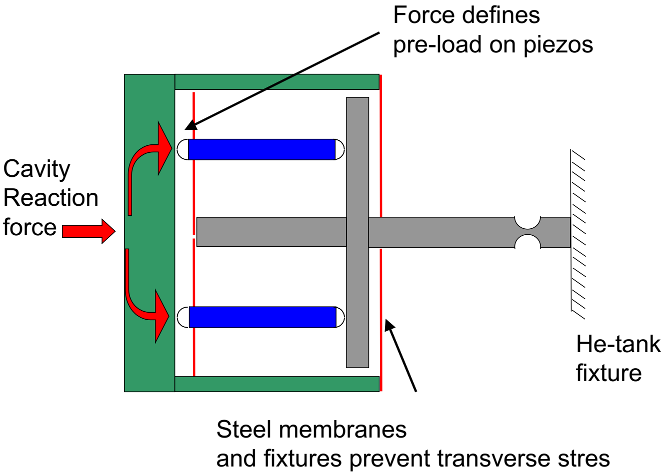

Figure 6.3: Scheme of the piezo holder of the type II tuning system.

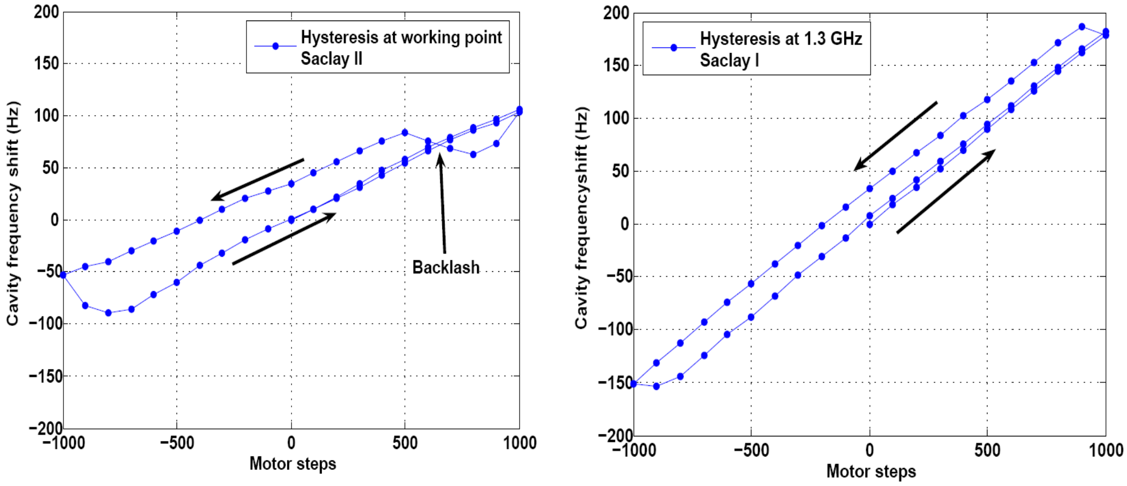

Figure 6.4: Measured motor tuner hysteresis of the type II tuner at the working point position of the tuner stepping by 100 steps ($\simeq$ 1 Hz). A hysteresis remanence of up to 50 Hz detuning has been measured. At the upper end of the curve a backlash happened (left curve). For the type I tuner the remanence is only about 30 Hz.

The type I design has a constant stiffness with respect to coarse tuning over the whole frequency range. The range is roughly 50 % increased compared to the type II tuner.

The coarse tuner is meant to keep the cavity's resonance frequency in a fixed position negating any slow drifts. To check for the linearity of the tuner for small drift amplitudes, the tuner has been moved 1000 steps (in steps of 100) in forward direction and back to its initial position. This is given by the fact, that total drifts of the RF eigenfrequency over a period of 24 hours of not more than 100 Hz have been measured.

The left plot of Figure 6.4 presents a typical motor tuning curve of the type II tuner at the above defined working point. It can be seen, that the curve features a hysteresis with a

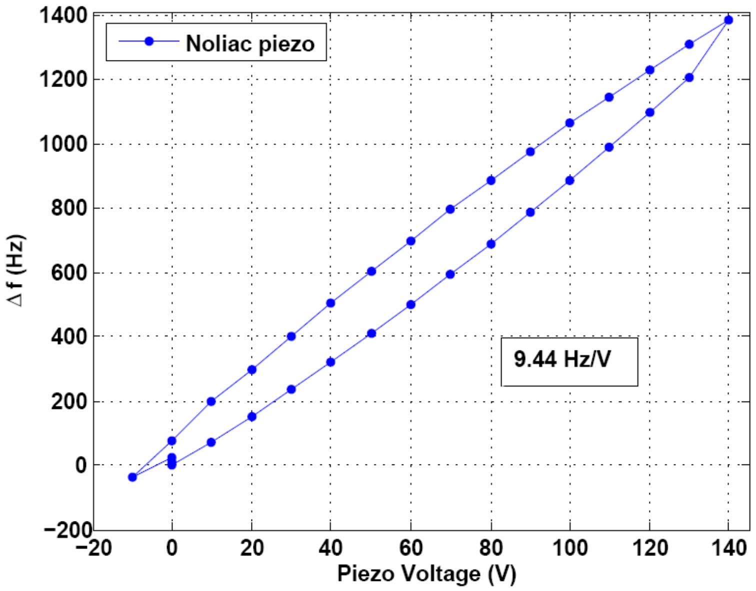

Figure 6.5: Total tuning range and hysteresis of a Noliac piezo at $\simeq$ 6-8 K installed in the tuning system type II.

maximum deviation or remanence detuning of 50 Hz, much more than the 1 Hz measurement error. Furthermore, at the end of this curve some backlash occurs (non-linear effect), where a movement of the motor does not affect any cavity tuning. To check, if this is a general effect of the tuner, this measurement has been done at various tuning positions. But it showed, that the backlash is a singular effect at the working region between 1.3004-1.3005 GHz. Still the hysteresis was shown to be independent of the tuner position. The type I design features a smaller remanence of $\sim$ 30 Hz and little backlash was observed (Right plot of Figure 6.4).

This means for the operation of the cavity, that it may be coarse tuned to an accuracy of ± 30-50 Hz by the motor tuner. But smaller drifts, even if they are slow, have to be compensated by the fast system. Even if microphonics compensation is not needed, each cavity will need a piezo tuner for fine tuning in the presence of slow drifts exceeding a few Hz.

6.2.2 DC characteristics of the piezo tuner

Piezo elements made of ferroelectric materials exhibit a hysteresis behavior like their magnetic counterparts [71]. During compensation of microphonics detuning the piezo will be driven bipolar with respect to some DC reference level, which reflects the position of the mean RF frequency or more accurately the residual phase. It had to be tested how much piezo-hysteresis would affect the tuner resolution and if there was a minimum microphonics level that can be compensated for.

The hysteresis and total tuning range of the Noliac$^{\mathrm{TM}}$piezos is given in Figure 6.5. The scheme of the piezo holder of the type II tuning system is given in Figure (by [72]). The piezo can cover a range of 1.4 kHz at 9.4 Hz/V. The maximum static Lorentz force detuning measured at HoBiCaT would be $\leq$ 400 Hz for 16.5 MV/m (k_{LF}=1.41 Hz/(MV/m)^2), long-term slow drifts have been of the order of 100 Hz. In the worst case this would still leave a

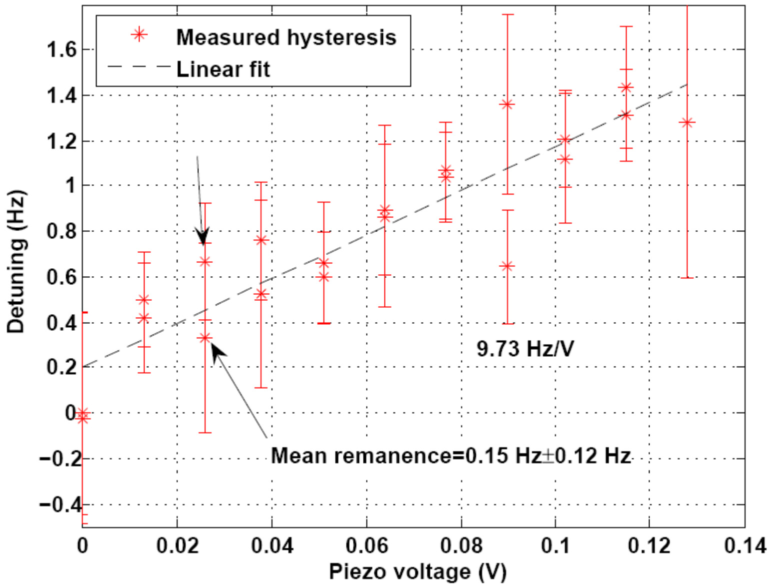

Figure 6.6: Piezo hysteresis for small tuning ranges needed for microphonics compensation. This hysteresis shows the limits with respect to the tuner's resolution.

tuning range of several hundred Hertz for microphonics compensation, much more than ever observed in any peak event.

Resolution of the fast tuner

As the microphonics detuning may only be a few Hertz or at least the individual spectral components of the detuning may be low, it is important to understand the resolution of the fast tuning system. In principal it is possible that the total detuning is made up of several lines each with very small detuning amplitudes, yet adding up to a significant total contribution. The fast tuner must be able to resolve these individual lines for a compensation scheme to work.

Theoretically the piezo alone can be driven in steps of 0.2 nm which would transform to 0.06 Hz cavity detuning. But in operation the tuner will experience movements around a steady state value in both directions and the complete mechanics will affect the resolution. How does the piezo hysteresis in this low level regime affect the tuning process and how big is the play in the tuner mechanics?

An answer is given by the measurement shown in Figure 6.6, where the hysteresis over a range of only a few Hz was recorded. The slope of the total range of 1.4 Hz is 9.73 Hz/V. This is only a 3.1 % deviation from the slope of the total tuning range in Figure 6.5. This measurement has been performed by measuring the detuning signal for 1 s after driving the piezo to the next DC level. To avoid any perturbations from a step like response the first 10 % of the samples have been removed from the data set. By taking the mean and checking the data with respect to slow drifts the DC detuning was derived. The theoretical step size was 0.12 Hz.

Independent of the hysteresis the slope between two steps is not always well defined. This means, that a change of the piezo voltage does not affect any cavity deformation. A probable interpretation is, that there is play in the tuner mechanics leaving a threshold under which

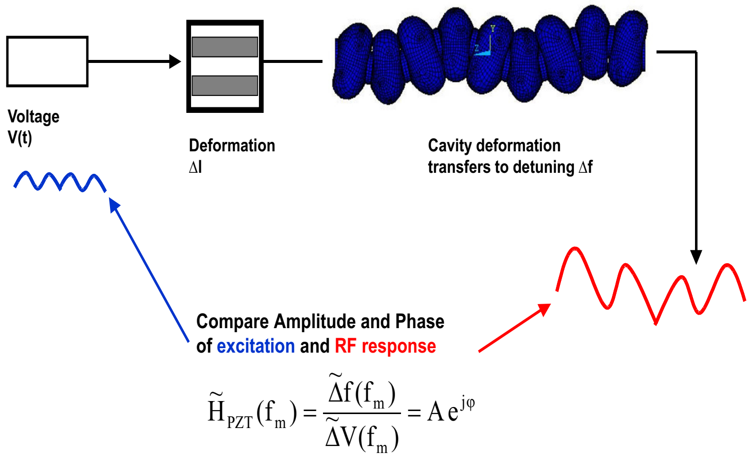

Figure 6.7: Principle of transfer function measurement between an harmonically excited piezo and the cavity response. This response is given by a detuning amplitude and a phase shift between piezo driving signal and detuning signal.

the action of the piezo is completely damped by this effect. The resolution of about 0.15 Hz has been determined by taking the mean of the difference in detuning for all voltage data points. Thus one can expect detuning compensation to only be effective down to 0.2 Hz, something that was confirmed by later measurements. This measurement represents more an estimate for the resolution because of the big measurement error. It is given by the quadratic sum of the microphonics detuning during the measurement and the general measurement error of the RF setup (Section 4.3.2).

6.2.3 The transfer function: Mechanical properties of the cavity-piezo-tuner system

Already the coupling between time varying sinusoidal field amplitudes and the cavity detuning due to Lorentz forces represents a transfer function or Bode plot of the cavity mechanical system (Section 5.3). For piezo-based microphonics detuning control it is of great importance to measure the transfer function between the piezo drive signal and the cavity deformation. Mechanical resonances will add phase shift that will lead to unstable feedback control. Hence, the coupling of piezo movements to these modes have to be quantified.

A scheme given in Figure 6.7 explains the way a transfer function measurement is to be understood. By a harmonic, mostly sinusoidal, excitation of the piezo the response of the cavity system is measured in detuning amplitude and phase lag between piezo driving signal and detuning signal. Sweeping through the frequency range of interest a Bode plot of the system can be derived.

The results are essential to derive a stable controller algorithm of the fast tuning based microphonics compensation. Especially at resonances the change of the phase is very steep, which has to be considered by the controller to remain within the stable boundary conditions.

The transfer functions presented here have all been taken in closed loop mode driving the piezo by the lock-in amplifiers internal sinusoidal reference. Most preferably the transfer function should be taken for the design loaded quality factor of the cavities for the FEL linac. As the narrow bandwidth of the cavity alters the transfer function the PLL gain has to be chosen quite high (50 kHz/V).

The gain is given by the conversion of the phase error $\Delta\Phi$ between the RF forward wave and the actual RF mode in the cavity into a corresponding voltage at the mixer. This voltage is a measure for the gain of the phase error ($[K_{mixer}]$ =V/rad). This signal is further amplified (by K_{amp}, see below) and fed to the frequency modulation port of the RF source, which converts the voltage to a shift of the (angular) frequency ($[K_{FM}]$ =rad/(V·s)). In total this gives:

$$\Delta\Phi \xrightarrow{K_{mixer}} \Delta V$$

$$\Delta V \xrightarrow{K_{FM}} \Delta\omega$$

$$K_{PLL} = K_{mixer} \cdot K_{amp} \cdot K_{FM}$$

Increasing the gain too much would reduce the resolution of the setup. For example given K_{mixer}=1.5 V/$\frac{\pi}{2}$ after amplification and K_{FM}=2.0 kHz·2π , the resolution would be 20 μV/Hz. The resolution of the lock-in amplifier is 2 μV at a bandwidth of 1.0 kHz and an ADC resolution of 18 bit (signed integer). A further increase of the gain is not desirable as the resolution of this measurement should be within the resolution of the piezo tuner to resolve the transfer function down to this resolution. This is important to implement it into a controller.

Transfer functions of the tuner systems

The electro-mechanical transfer functions measured with the different tuning systems are displayed in Figures 6.8-6.9. All measurements have been taken at 1.8 K.

Independently of the system all transfer functions have a similar structure of the modes. There is always a low frequency mode between 30-40 Hz, whose frequency seems to depend on the cavity. Furthermore a set of eigenmodes can be found at 150-170 Hz. Usually between 200-300 Hz there is a group of modes which have the largest amplitude response towards an external excitation. This may be due to the nine cell structure of the cavity. The position of the first eigenmodes up to 170 Hz is similar. The transfer functions are quite complex and contain more than 15 mechanical modes.

It is obvious, that most curves do not exhibit the typical Lorentz distribution as expected for a single-mode second order linear system. Many peaks in the amplitude plots have an asymmetric distribution with regard to their maximum. This is due to fact, that the mechanical eigenmodes coupling to the piezo excitation act in a parallel way. In a mathematical sense this means, that in the frequency or Laplace domain the individual modes are adding up. An example for two "idealized" second order systems in frequency domain is shown in Figure 6.10. Due to the summing of the two modes the curvature is altered and gets an asymmetric shape. This also means, that the bandwidth and thus the damping factor or quality factor of the mode cannot be derived by finding the full-width-half-maximum of the curve. Furthermore there are negative peaks in the transfer function or anti-resonances. The first resonance of each tuner shows a combination of a resonance-anti-resonance pair (Figure 6.11). This negative detuning with respect to the constant detuning level is given by eigenmodes responding with negative detuning to cavity shortening and vice-versa [73].

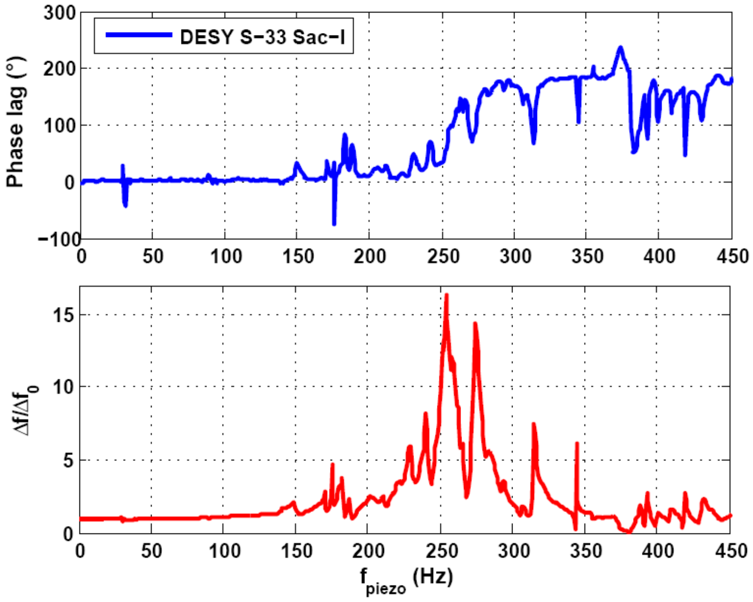

Figure 6.8: Transfer function between harmonic piezo excitation and cavity RF response for the Saclay I tuner. The upper plot shows the phase lag response while the lower one exhibits the amplitude response.

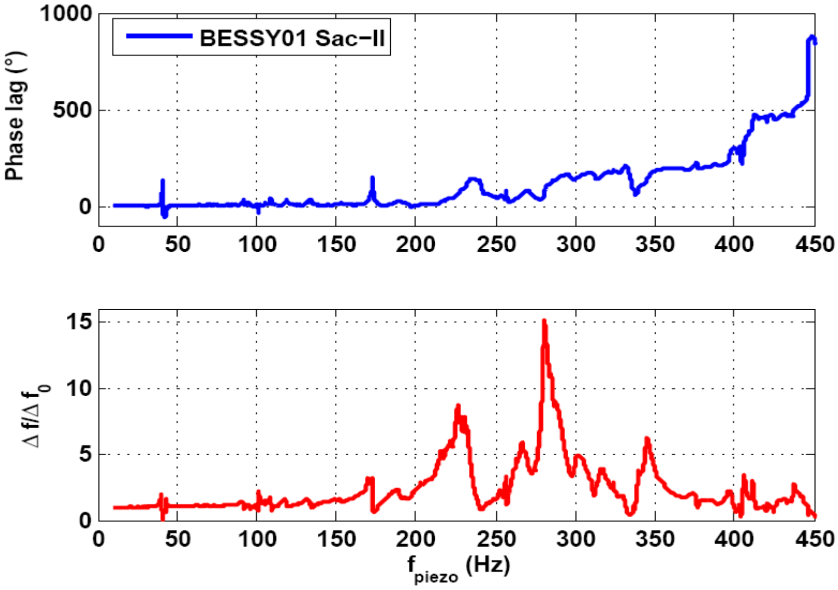

Figure 6.9: Transfer function between harmonic piezo excitation and cavity RF response for the Saclay II tuner. The upper plot shows the phase lag response while the lower one exhibits the amplitude response.

In the case of the first mode, always present in the different microphonics spectra, this may be a mode with two polarizations in the transverse direction. Finite-element simulations of e.g. [36] and [74] showed, that the cavity under the given assumed boundary conditions may start to oscillate in longitudinal or transverse directions. The transverse modes often are oscillations of the whole nine-cell structure, where the cell deformation itself and thus the detuning is lower compared to longitudinal modes. That would explain the negative

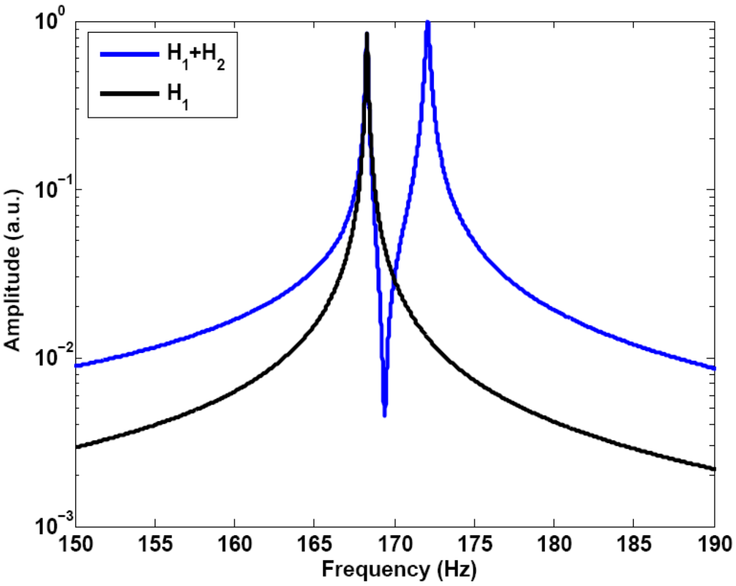

Figure 6.10: The black curve shows the Lorentz distribution of a second order system in frequency domain. Adding a second nearby system to the first alters the shape of the Lorentz curve in an asymmetric way.

resonances.

It can be seen, that especially for the type II tuner the structure of the modes contributing to microphonics, which is referred as being the first excited mechanical eigenmode, is very complex (Figure 6.11). There is at least a sum of two resonance-antiresonance pairs contributing to this mode ensemble. The type I tuner mounted to the same cavity also has the first mode at the same frequency. But in that case it only consists of one resonance-antiresonance pair.

Group delay

The part of the phase response which is not governed by eigenmodes shows a significant slope. It is a measure for the time lag between piezo excitation and response of the cavity field detuning. This group delay sets a limit for the frequency range where the tuner still could react fast enough. In principle all systems may compensate frequencies which are far above the highest microphonics contribution measured for the cavities. But the phase lag due to the group delay reduces the phase margin of a controller. Hence, a minimum delay is favorable. The group delay is between 0.1-0.2 ms for both tuning systems.

Transfer function stability

Finally it should be mentioned, that the transfer function was measured under different circumstances to check for changes due to different boundary conditions. These may be defined by the liquid helium pressure, position on the tuning curve (pre-load) and changes, that may occur when the tuner is disassembled and remounted between tests.

Several transfer functions taken at different tuner positions did not show any significant change. Also measurements taken with a warm-up and cool-down phase of the HoBiCaT cryostat in between look very similar. More obvious deviations have been observed due

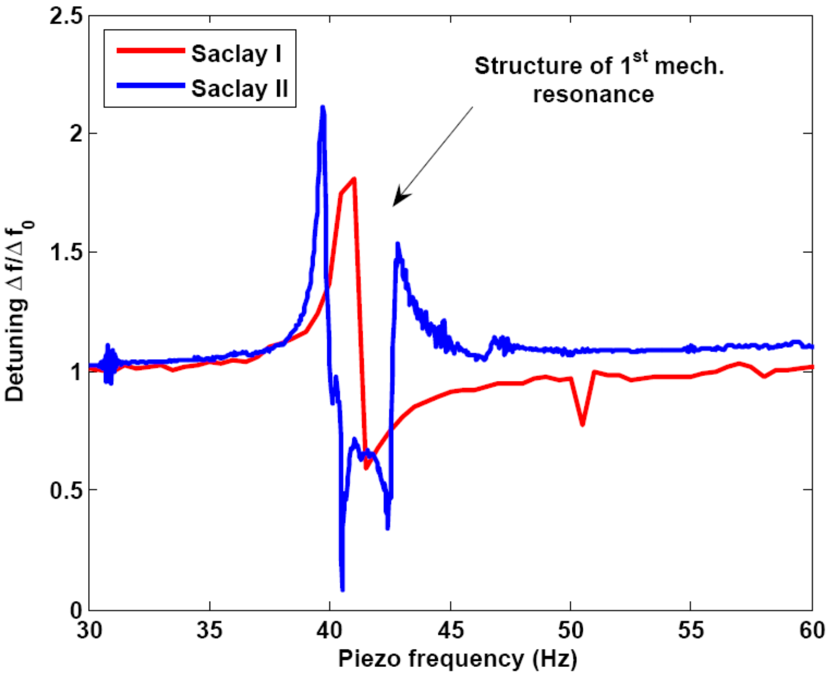

Figure 6.11: Comparison of the transfer functions of the type I and II tuner mounted to the same cavity in the range of 10-120 Hz. The general structure of the transfer function seems to be given by the cavity, but the tuner alters the peak shapes and amplitudes.

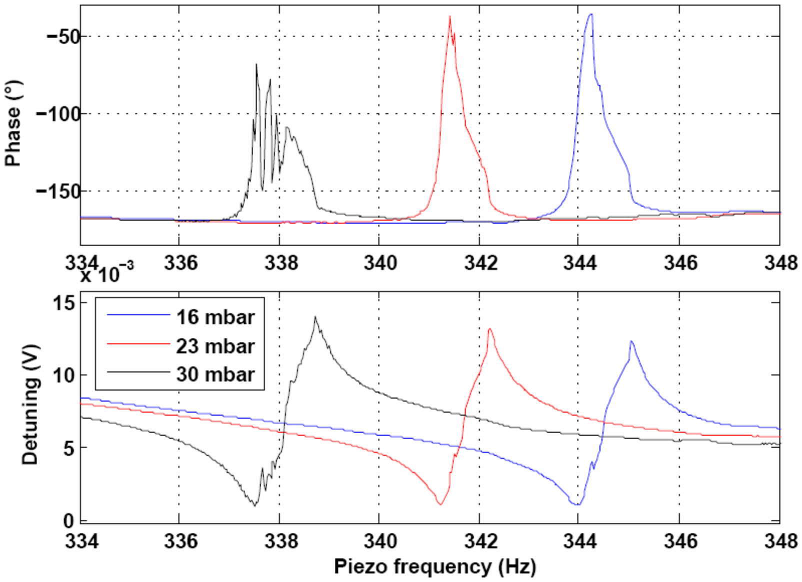

Figure 6.12: Zoom to a part of the transfer function where a shift of a resonance occurs due to a change in the helium bath pressure.

to a change of the liquid helium bath pressure. The helium defines an environment with isotropically distributed forces acting on the cavity. Figure 6.12 represents a mode which is shifted due to the change in the pressure. In total most modes seem to keep their position, amplitude and even phase response. But then a few others even vanish at higher pressures. The mechanical modes which are of interest for tuning control and in the range

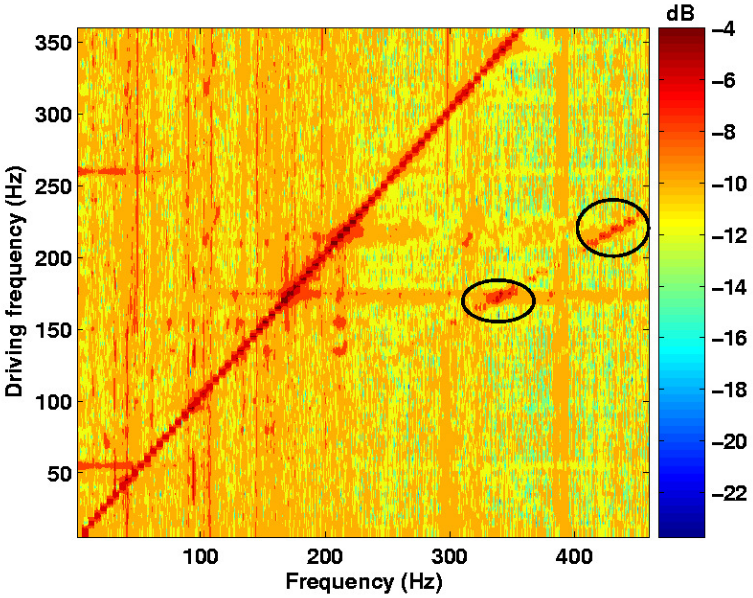

Figure 6.13: Frequency map of a piezo-to-RF transfer function. Vertical lines represent microphonics contributions present in all spectra at each measured piezo excitation frequency (ordinate). The microphonics background has been subtracted to emphasize the piezo action. Black circles show parts where higher harmonics occur due to non-linear excitation of the tuner. The vertical line represents the transfer function like given e.g. in 6.8.

of the microphonics detuning remained constant and are independent of the external helium pressure.

Frequency map: Higher harmonic excitation and non-linearities

To further analyze the fast tuner for a controller application, it has to be checked if there are non-linear behaviors. Any coupling between different modes by the tuner or excitation of higher harmonics would complicate a controller design. This has been done by measuring a 3-d transfer function.

As the lock-in amplifier only allows to lock to the driving frequency or higher harmonics a different method has been implemented to measure a frequency map. This contains for each driving frequency the whole response spectrum derived from the detuning signal. The principle of this measurement is the same as that of the lock-in method. The only difference is given by the fact, that all filtering and Fourier analysis is done by software after sampling the driving signal and the corresponding detuning for 10 seconds for each frequency step. The resultant frequency map of the type I tuner is given in Figure 6.13.

To emphasize the characteristics caused by the piezo action the mean microphonics background of all measurements has been subtracted. The ordinate displays the piezo driving frequency while the abscissa represents the resultant detuning spectrum. The strong diagonal line represent the measured transfer function. The regions marked by black circles show where higher harmonics of the piezo-tuning system occur due to non-linear behavior of the tuner. This non-linearity of the tuning system may be observed in operation when very high detuning levels have to be compensated. All signal generators and amplifiers in the signal path have been checked and ruled out as a source of this effect. It seems to be caused by the piezo-tuner-system itself. Any other non-linearity or coupling between different mechanical modes have not been measured. In general this measurement showed, that too high piezo amplitudes may result in excitation of higher harmonics. Higher mechanical resonances which are nearby may be excited due to the higher harmonic content. For the microphonics levels to be considered, it is very unlikely, that this effect will ever be observed.

Modeling of the transfer function

Summarizing the previous results one can assume, that the response at a given frequency is the linear combination of a finite number of mechanical eigenmodes. The global curve is convolved by the low-pass behavior due to the group delay. Also modes beyond the high frequency limit of the measurement will contribute to the transfer function. In principal one can try to develop a model of the transfer function, which may serve as a reference or even as an integral part of the detuning compensation. A model similar to the second order Lorentz force description can be used to describe the coupling between piezo action and cavity detuning [73] [75].

The time domain equations are composed of the same terms than in Equation 5.8 by just replacing the coupling coefficients $k_{LF,i}$ by $k_{p,k}$ which is given in Hz/V. Thus a time domain model is given by:

$$\Delta\ddot{\omega}_{cav,k}(t) + 2\xi\omega_{m,k} \cdot \Delta\dot{\omega}_{cav,k}(t) + \omega_{m,k}^2 \cdot \Delta\omega_{cav,k} = \pm k_{p,k} 2\pi\omega_{m,k}^2 V_{Piezo}(t) \qquad (6.1)$$

$$\Delta\omega_{cav}(t) = \sum_k \Delta\omega_{cav,k}(t) \qquad (6.2)$$

The transfer function represents the steady state solution of the second order system in the frequency domain. The total transfer function of the system incorporates the following terms in the Laplace domain:

- The individual modes given by the following transfer function:

  $$H_k(s) = \frac{\omega_k^2 M_k}{s^2 + 2\xi_k\omega_k s + \omega_k^2} \qquad (6.3)$$

  with $\xi_k = 2\omega_{1/2,k}/\omega_k = 0.5/Q_{m,k}$ and M_k is given by the steady state solution of the second order system as $\pm 2\xi_k \Delta f_k$. Δf_k is the measured amplitude response of the transfer function.

- The global phase slope due to the group delay of the acoustic wave in the tuner medium:

  $$H_{delay}(s) = \exp(-T_{delay} \cdot s) \qquad (6.4)$$

  T_{delay} is the measured group delay.

- To account for the lower frequency and DC contribution of modes beyond the measurement range a low-pass transfer function may be added:

  $$H_0(s) = \frac{M_0}{\tau s + 1}, \qquad (6.5)$$

  where $1/\tau$ relates to the cut-off frequency of the total measurement setup and is around 1.0 kHz.

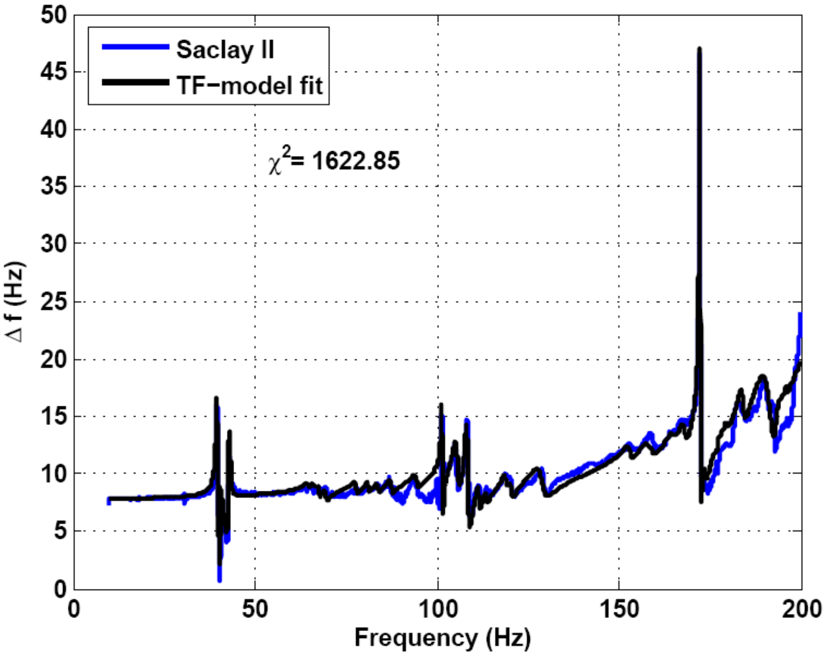

Figure 6.14: Fit of the model given by Equation 6.6 to the type II tuner transfer function in the subrange of 10-200 Hz. The measured transfer function is given by the blue curve by 16000 data points.

The total transfer function model thus is given by Equation 6.6:

$$H(s) = \left(H_0(s) + \sum_{k=1}^{N} H_k(s) \right) \cdot H_{delay}(s) \tag{6.6}$$

It is possible to fit the Equation 6.3 to an isolated mode whose curvature is not too much altered by a neighboring resonance. Using these results one can start a global fitting routine by minimizing the differences between model and measured transfer function. So far it has proven difficult to implement an automated fitting routine. First of all, the detuning with respect to the piezo driving voltage given by the coupling constant $k_{p,i}$ may be of both signs. Following an automated routine has to detect in a reliable way all negative and positive detuning peaks and the search algorithm has to rule out changes of signs in the slope of the transfer function caused by noise.

An example of a fit of the model given by Equation 6.6 to a subrange of the type II tuner transfer function is shown in Figure 6.14. 40 second order modes have been used in that range to achieve this result. Four modes behave like an antiresonance with a negative sign of the coupling coefficient $k_{p,k}$ resulting in a negative detuning response. Most of the modes to reconstruct the transfer function have very low amplitudes thus do not show up in any microphonics spectrum. Nevertheless to achieve a good reconstruction all of them have to be taken into account as they alter the total phase response and the shape of neighboring modes. Furthermore the rising edge of modes at frequencies beyond the given range change the slope of the total curve. For this range between 10-200 Hz this means to have a parameter space of 120+3 parameters (Δf_k,$f_{m,k}$,$Q_{m,k}$ per mode and τ, T_{delay}, M_0) to be optimized for fitting.

Appendix C provides a table including all fitting parameters. It is desirable to reduce

Table 6.3: Parameters of the most dominant mechanical modes of the type II and type I tuner (fit result) in the range of 10-220 Hz

Type II			**Type I**		
Δf **(Hz)**	f_m **(Hz)**	$f_{1/2}$**(Hz)**	Δf **(Hz)**	f_m **(Hz)**	$f_{1/2}$**(Hz)**
13.16	39.61	0.2	8.6	30.7	0.15
8.3	40.2	0.085	-1.35	30.885	0.6
-7.12	40.66	0.2	5.0	167.0	1.0
-9.6	42.8	0.3	6.3	173.4	1.0
3.34	43.2	0.5	35.5	175.76	0.11
7.3	101.35	0.125	16.0	175.85	0.04
4.7	101.58	0.1	23	175.97	0.03
4.85	105.54	0.75	-7.5	176.3	0.3
9.2	108.3	0.45	5.0	178.9	0.5
40.33	172.23	0.12	21.5	187.3	2.2
6.62	191.0	2.6	-8.0	189.3	0.6
40.54	213.25	0.6	25.5	209.8	4.0
55.06	226.3	8.0	65	237.0	8.0

Global parameters	
Group delay T_d=196μs	T_d=115μs
Cutoff time constant τ=0.1 ms	τ=0.1 ms
DC detuning M_0=2.8 Hz	M_0=3.0 Hz

this parameter space. Thus there is still need to check if a reduced order system is good enough to represent the physics of the cavity-tuner system. Even if this is not possible, one should be able to implement the measurement as a lookup table into a controller design.

An overview of the main resonances and their mechanical quality factor is given in Table 6.3. To compare the main tuner designs with respect to their complexity also a fit to the type I tuner transfer function has been done in the same frequency range. It features a similar structure with the low frequency mode and a high peak around 170 Hz. But fewer modes contribute to the total transfer function. That is underscored by the fact, that only half the number of modes were needed to perform this fit in comparison to the type II curve. Not surprisingly, the cavity in this tuner configuration had a simpler microphonics spectrum.

6.2.4 Summary: Evaluating tuner performance for CW operation

A summarizing overview of the tuner performances including both the motor and piezo tuning is given in Table 6.4. Preferable properties are marked in green.

The Saclay I design with the improved piezo tuner version has the following assets and drawbacks:

- A high stiffness which can be directly influenced by changes at the piezo tuner frame. This resulted in the smallest group delay (0.115 ms) and accompanying a smaller static Lorentz force detuning (1.08 Hz/(MV/m)^2).

- To fit a model to the transfer function in the range between 10-200 Hz 21 mechanical modes have been used. The transfer function is less complex than that of the Saclay II design.
- Because of the less complex transfer function the microphonics spectrum shows only one dominant line by an excited eigenmode.
- A major drawback is given by the design itself. When driving the coarse tuner the lever system pulls on the frame. As a result the pre-load of the piezos decreases which diminishes the fast tuning performance. This may be compensated for by increasing the pre-load on the piezos directly at the frame with the adjustment screws. But this can only be achieved by a significant reduction of the tuning range. To compensate for the loss of pre-load by the tuner-cavity system the pre-load by the frame can be increased.
- The piezo resolution has not been characterized properly for the Saclay I piezo tuner. But in the compensation measurements it showed a better performance than the Saclay II design when compensating small detuning amplitudes.

The Saclay II design features the following attributes:

- The major advantage of this design is an increase of the piezo's pre-load when tuning to the desired frequency by the coarse system. There has to be a proper pre-tuning during tuner assembly to obtain the working point with the maximum tuner stiffness at the desired frequency of 1.30 GHz for linac operation.
- The cavity in combination with this tuner achieved the lowest Lorentz force detuning constant (k_{LF}=0.9 Hz/(MV/m)^2) of all tuner-cavity combinations. Still, the group delay was higher than that of the Saclay I design.
- Though the position of the modes seems to depend on the cavity, the Saclay II design appears to complicate the structure of the first mode.

In principal both tuning systems achieved a similar performance with respect to their fast tuning capabilities. A design like the Saclay II tuner with a very simple, stiff piezo frame as given in the Saclay I design would be the optimum. In contrast to the given setup this would allow a direct action of the piezo forces on the cavity and the piezo resolution may be improved.

But nevertheless as the microphonics spectrum and general mechanical mode characteristic of the cavity-tuner system mainly depends on the cavity, there is still a need to investigate the mechanical cavity design for improvements of passive suppression of microphonics. The installed stiffening rings of the TTF cavity design have been developed to minimize the Lorentz force detuning of a pulsed machine. A change in that design has already been proposed by [74]. The measurements here underscore the importance of such changes. It would be preferable to stiffen the cavity to shift the first resonances to higher frequencies without loosing tuning capabilities.

According to mechanical finite element simulations of [74] it can be achieved by adding Titanium tubes between the Helium vessel and the stiffening rings. The first mode would be shifted from $\simeq$33.6 Hz to 130.5 Hz. Although, this is a field which should be examined in more depth to find a CW optimized TESLA cavity design.

Table 6.4: Coarse and fast tuning properties of the tested Saclay I and Saclay II cavity tuning system. The *italic type* marks preferable properties of the tuner.

Tuning parameter	**Saclay I**	**Saclay II**
Coarse resolution	0.176 Hz/step	0.09 Hz/step
Coarse tuning range	*750* kHz	500 kHz
Spindle movement	40 mm	40 mm
Coarse max. remanence	*30* Hz	55 Hz
Backlash observed	*No*	Yes
Piezo type	0-1000 V	0-150 V
Fast tuning range	700 Hz	*1420* Hz
Tuning coefficient	0.7 Hz/V	9.8 Hz/V
Max. piezo remanence	100 Hz	200 Hz
Resolution [Hz]	$\leq$ *0.2*	0.2
Maximum cavity response	∼x16	x*15*
Group delay	*115* μs	200 μs
Lowest resonance (30 or 41 Hz)	*single pair*	double pair structure
Stiffness while coarse tuning	decreasing	*increasing*

Chapter 7

Compensating microphonics detuning and impact on beam stability

To achieve the desired phase and amplitude stability for the first linac sections before the bunch compression a detuning compensation system is highly desirable. As has been shown in Chapter 3 a feedback gain of the LLRF system of 200-250 may control a cavity of the design bandwidth of $3{\cdot}10^7$ to within 0.02°. The efficiency of this controller will however be limited by any measurement noise of the reference and RF front-end system. A perfect controller aiming for a phase stability of σ_Φ=0.02° would allow a maximum detuning of $\leq$1.5 Hz rms, as:

$$\sigma_{f,max} \leq f_{1/2} \tan(\sigma_\Phi). \tag{7.1}$$

The detuning measurements have shown, that the general rms value may be above this value. Factoring in other noise sources that reduce the stability and the gain of the LLRF control would further reduce that detuning limit. Even for very stable cavities it may occur several times during a day of operation, that excited resonances or instabilities in the helium plant lead to bigger rms detuning values of several Hertz. Thus, the availability of detuning compensation is desirable, perhaps even mandatory, to ensure the necessary linac stability.

In the following, a fast controller based on the piezo tuner characterized before has been developed. It will be shown, that microphonics compensation is achievable at HoBiCaT.

7.1 Potential feedback and feedforward concepts

In recent years feedforward compensation of Lorentz force detuning using piezo actuators has been successfully demonstrated with pulsed TESLA cavities [58][75]. There are also some preliminary results with other elliptical cavity types demonstrating compensation of microphonics in CW mode, but the demands are quite different for the BESSY-FEL.

A system to compensate constant (known) narrow-band sources was successful at reducing the detuning from 60 Hz to 10 Hz[76]. However, this system cannot deal with mechanical resonances and changes in the excitation. Furthermore the permissible detuning was more than ten times than the limit for the BESSY-FEL.

The transfer characteristic between piezo and RF detuning prohibits the use of a classic PID feedback scheme and more complex, ”intelligent” controllers must be used. The mechanical resonances are the major source for instabilities and are nearly constantly present in the detuning spectra (Chapter 5).

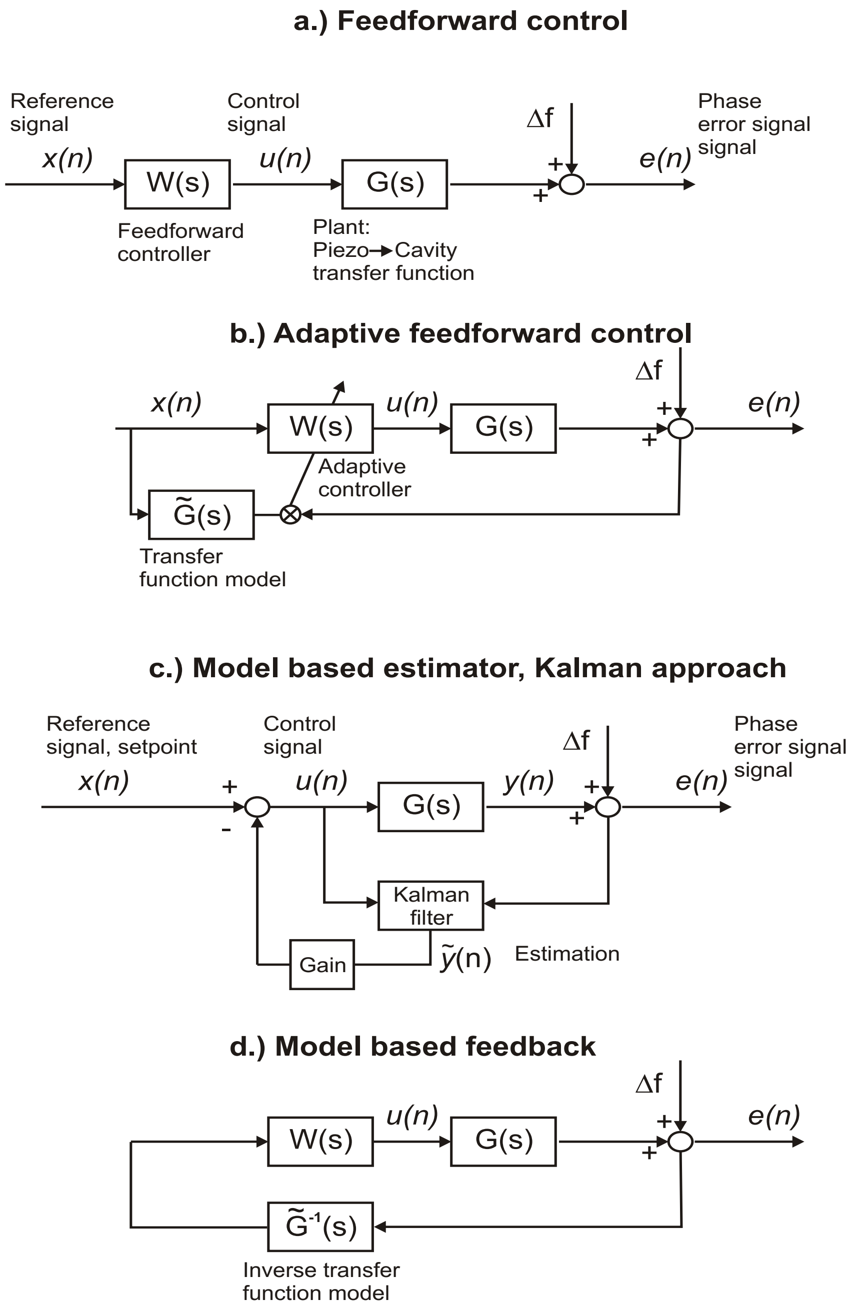

a.) Feedforward control

b.) Adaptive feedforward control

c.) Model based estimator, Kalman approach

d.) Model based feedback

Figure 7.1: Possible feedforward and feedback schemes for a piezo based microphonics detuning control. While the feedback systems given by c.) and d.) are based on a mathematical model of the piezo to RF detuning transfer function, a look-up table would be sufficient for the feedforward approaches (a.) and b.). W(s) denotes the controller transfer function while G(s) is the piezo-to-RF detuning transfer function of the cavity-tuner system.

Methods which can be adapted to CW cavity technology have partly been developed in the field of active noise control (ANC)[77]. The applications range from designing countermeasures to noise created by airplanes, stabilizing sensors in satellites or canceling acoustic sound in a noisy environment.

The general strategies for a controller can be divided into two different classes given by feedback and feedforward schemes. Figure 7.1 shows an overview of the possible controller solutions. Subfigure a.) and b.) present feedforward solutions while c.) and d.) show feedback concepts. The following general statements with respect to fast detuning control can be made:

a .) A simple feedforward design alters a reference signal in such a way, that the response of the plant (given by the piezo to RF detuning transfer function) being detuned by microphonics is minimized. The reference signal has to be given by some previously recorded microphonics sample. There is no other signal available which can be used as a reference. This setup needs a good characterization of the transfer function and the error sources causing the microphonics. The system will become unstable if the noise sources change in time regarding their amplitude or phase. Finally any changes in the system parameters represented by the transfer function may lead to further instabilities, as the feedforward is tuned to a fixed transfer function setting.

b .) A more stable operation can be achieved by adapting the feedforward controller with the current state of the system to be controlled. In the case of the cavity it is done by feedback of the phase error signal. It represents the current detuning, which is a combination of piezo movement and external noise acting on the cavity. A reference signal is altered by the controller in such a way, that the signal created on the piezo acts phase shifted by π to the external detuning source. Any residual error between the compensation and the detuning causes a phase error signal at the RF mixer. The amount of error defines how much the controller transfer function is changed to achieve minimum detuning.
This approach can cope with changes in the external error sources and within certain boundaries accepts variations of the transfer function. This concept has been chosen for the controller implemented at HoBiCaT.

c .) A promising strategy is given by a class of controllers which estimates the system response to any kind of input. A well known concept is given by the Kalman filter [78]. The Kalman filter incorporates a model of the cavity-tuner system and estimates its response by measuring the input to the controller piezo and the cavity detuning response. Any additional noise is filtered by the algorithm giving a good representation of the expected cavity behavior. The estimated state by the filter algorithm can be used to implement a state feedback controller [29]. In simulation the functionality of the Kalman filter has been shown. But as the cavity-tuner system consists of more than 20 modes, the Kalman approach would take too much computing power for a DSP or FPGA implementation.

d .) The feedback design in a similar way proposed by [73] alters the measured microphonics detuning or phase error signal by the inverted piezo to RF detuning transfer function. Thus the control signal incorporates the phase and amplitude information of the mechanical modes shifted by π. The controller block transfer function given by W(s) is used to set the gain at each frequency to a value, which guarantees a stable performance. The combination of the inverted model, the controller and the transfer function of the tuner-cavity system should result in a stable system. To achieve this, a precise measurement of the transfer function is mandatory and the model should give

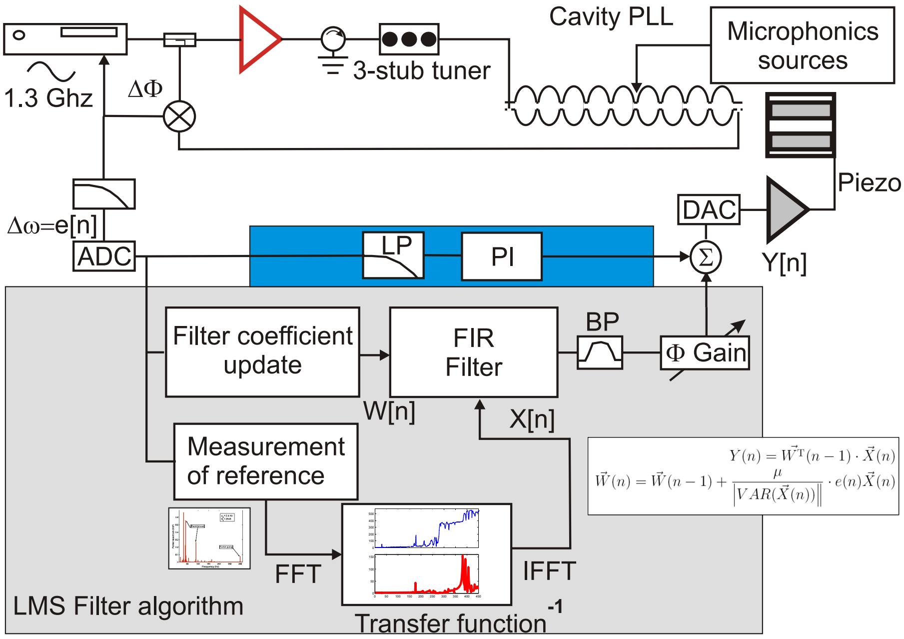

Figure 7.2: The complete microphonics detuning compensation scheme given by a feedback (blue) and an adaptive feedforward signal path (grey).

a good fit to the measurement. But there is no adaptation to changes of the system represented by the transfer function. To achieve more robustness one can decrease the feedback gains but will thus increase the residual error.

7.1.1 The piezo controller setup

To address the combination of microphonics due to stochastic detuning by LHe pressure fluctuations and time-varying lines due to mechanical eigenmodes a combined approach of PI control and adaptive feedforward has been chosen. Figure 7.2 gives an overview of the compensation scheme implemented on a National Instruments PXI realtime$^{\mathrm{TM}}$controller connected to a 16 bit ADC/DAC board (see Section 4.3).

After analog-to-digital conversion the phase error signal from the RF mixer is split into two pathes. The first signal path is used for feedback control of the low frequency part of the spectrum. A first order Chebychev type lowpass filter with a very low cutoff frequency between 1-20 Hz is employed to avoid excitation of the first mechanical resonance. The signal is processed by a proportional-integral control scheme to compensate for detuning mainly caused by pressure fluctuations. The integral part is kept quite small to achieve an elimination of the steady state error due to proportional control without producing to much overshoot.

The second signal path is used as the update signal of the adaptive feedforward controller. A previously measured record of the microphonics over several seconds acts as the reference signal for this adaptive algorithm. The reference signal is changed by a FIR (finite-impulse response) filter [79] in such a way, that the resulting deformation at the piezo-tuner reduces the external detuning. The filter's coefficients are updated every time step of the discrete algorithm by minimizing the error signal with the least-mean-square method (LMS) [80]. The individual signal paths and their performance with respect to detuning compensation will be discussed in the next sections.

Most measurements presented here were done with the type I tuner as demonstrated the better fast tuning capabilities. Tuner type II results are explicitly pointed out in the text. Further results with the type I tuner can be found in [69], [81] and [82].

7.2 Feedback control

The PI control path has to reduce the influence of randomly occurring helium pressure fluctuations without exciting mechanical modes of the cavity. The total open loop transfer function from an input signal to the controller to the output cavity detuning is given by the lowpass filter, the PI controller, the piezo to RF detuning transfer function and the lowpass filtering effect of the cavity.

The lowpass filter can be described in Laplace frequency domain by

$$H_{filt} = \frac{\omega_c}{(s+\omega_c)^n} \tag{7.2}$$

with ω_c the cutoff frequency and n the order of the filter.

The proportional-integral controller is given by the feedback gain K_{FB} and the integration time constant T_i. As the subsystems represented by the individual transfer functions are linear-time-invariant consecutively acting systems, the total system is given by their product in frequency domain. The resulting transfer function is invariant against a permutation of its subcomponents. Therefore all gains and attenuations in this feedback path may be summarized by K_{FB} [35]. K_{FB} includes the digital feedback gain, a variable attenuation parameter in the feedback path, the conversion from phase error voltage to detuning and the piezo amplifier gain:

$$H_{PI} = \frac{1}{T_i \cdot s} + K_{\mathrm{FB}}. \tag{7.3}$$

The latency of the digital system has been measured by comparing a pulsed signal with the delayed signal due to the digital signal processing. It is given by 0.5 ms, basically caused by the sampling at the ADC's. The latency or group delay of a signal from the piezo to cavity detuning is already included in the transfer function. The digital time delay is represented in Laplace domain by

$$H_{delay} = e^{-T_d \cdot s}. \tag{7.4}$$

On resonance the real and imaginary part of the cavity transfer function are given by lowpass like behavior [12]. For frequencies $|s| \gg \omega_{1/2}$ the amplitude of the cavity transfer function rolls off by 20 dB per decade (see Equation 3.31): $|H_{cav,11}| \propto \frac{1}{\omega}$.

$$H_{cav,11}, H_{cav,22} = \frac{\omega_{1/2}}{s+\omega_{1/2}}. \tag{7.5}$$

The total transfer function is thus given by the product of the subcomponents:

$$H_{\Delta f_{drive} \rightarrow \Delta f_{cav}} = H_{filt} \cdot H_{PI} \cdot H_{delay} \cdot H_{Piezo \rightarrow \Delta f} \cdot H_{cav}. \tag{7.6}$$

It is sufficient to do the stability analysis in continuous Laplace domain. A time discrete description in the so called z-domain [83] is only mandatory if the sampling frequency will lead to aliasing effects. The sampling frequency used here has been between 2.0-3.0 kHz thus

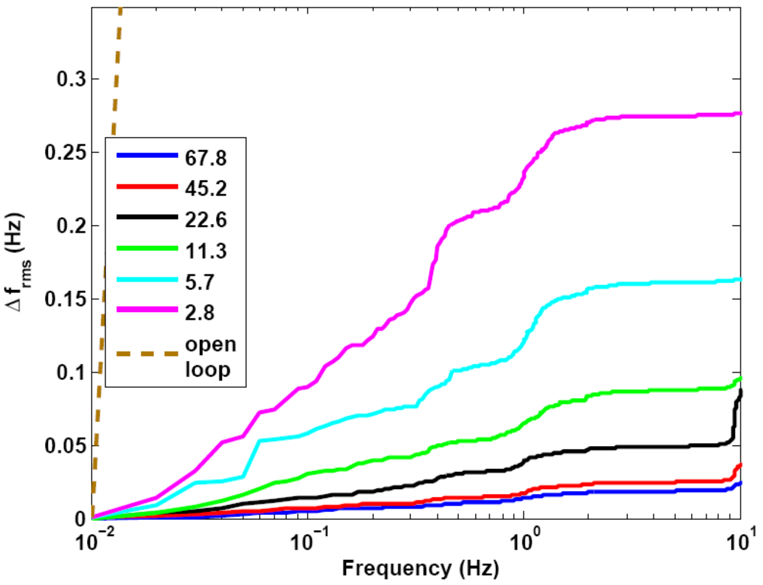

Figure 7.3: Integrated low frequency microphonics spectra for different feedback gains K_{FB} of the PI-controller signal path. All parameters are given in table 7.1.

Table 7.1: Parameters of the feedback path

Feedback parameter	**Value**
Proportional gain K_{FB}	2.8, 5.7, 11.3 22.6, 45.2, 67.8
Integration time (s)	1.2
Sampling frequency (Hz)	2.0 k
Lowpass 3dB cutoff frequency (Hz)	1.4
Piezo gain at 1.8 K (Hz/V)	9.8±0.8
Cavity bandwidth (Hz)	21.7

limiting the frequency range according to Shannons sampling theorem to 1.0-1.5 kHz. This covers the frequency range given by the observed microphonics and the appendant transfer function.

Feedback measurements

The performance of the feedback path has been tested first by locking the RF resonance frequency by pure piezo operation. The LMS path has been turned off and the cavity PLL was in open loop mode. The filter cutoff frequency, order and the parameters of the PI controller were adjusted to maintain lock by compensating for slow frequency detuning with the piezo alone. Starting from this point the values were changed primarily to find the limits where the system becomes unstable. Secondly it has been quantified how much the feedback may excite the first resonance at around 30 Hz. The result of this approach is shown in Figure 7.3. It shows the integrated spectra for different digital and thus piezo feedback gains up to detuning frequencies of 10 Hz. Table 7.1 summarizes the parameters of this measurement.

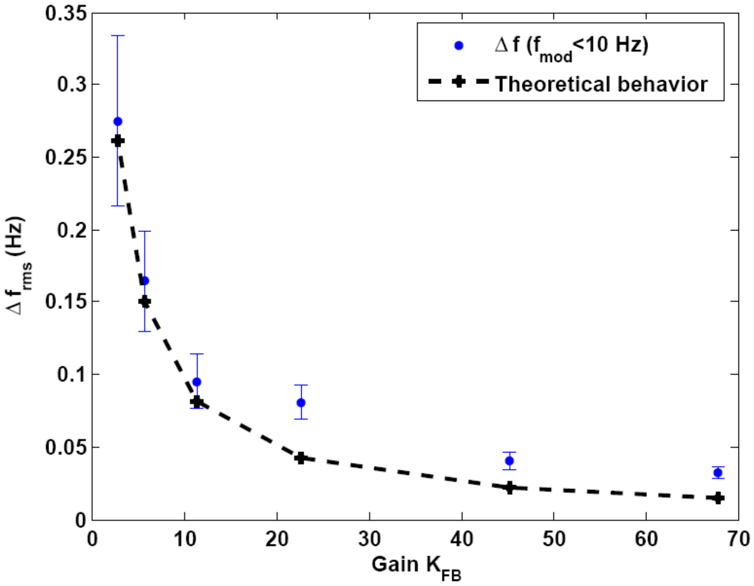

Figure 7.4: Residual detuning error (up to 10 Hz mod. frequency) vs. the feedback gain. The results follow the theoretical prediction given by the dashed black line.

The open loop low frequency detuning $\Delta f_{f_{mod}<10\mathrm{Hz}}$ has been around 1 Hz varying from measurement to measurement by up to 0.2 Hz. The compensation of the LHe pressure induced detuning follows as expected the residual steady state error of a proportional controller $\Delta f_{res} = \frac{1}{1+K_{\mathrm{FB}}}$ as can be seen in Figure 7.4. The influence of the integral part, which should decrease the residual error to zero, is limited due to the rather long integration time constant T_I which is related to the integrative gain K_I by $K_I = 1/(T_I s)$.

A comparison between the achieved detuning compensation and the theoretically expected value is displayed in figure 7.4. The error bar is given by the 0.2 Hz uncertainty of the open loop detuning scaled by the feedback gain and the measurement error of the HoBiCaT RF system (see Subsection 4.3.2). Down to the gain of 11.3 the measured residual summed rms detuning below 10.0 Hz follows the expected behavior of the controller. For higher gains there is still a further reduction, but there seems to be a superimposition of a saturation effect. This happens at $\Delta f_{res} \simeq$0.1 Hz rms. It can be understood by the limited piezo resolution of 0.2 Hz observed in Section 6.2.

An increase in feedback gain appears to be desirable as it directly reduces the low frequency detuning. But this will increase the overall bandwidth of the system and can give rise to an excitation of the nearby first resonance. Also the phase change is very steep at the resonance, so that the phase margin for stability is small. The total phase of the controller may reach its 180° point where the system starts to be unstable for gains $K_{\mathrm{FB}} > 1$. Also the first resonance is nearly always present in the spectrum of the error signal. A controller increasing the bandwidth above the first resonance will, depending on the phase relation between external noise and controller output, at least add partly to the existing spectral component. It has been shown, that gains above 22.6 increased the probability of a resonant excitation of the first mode significantly. As the excitation of this mode is still a process driven by random noise (see Section 5.2.1), it could not be quantified how much the increased gain increases the probability for excitation. But all measurements at higher gains featured an increase of the first resonance detuning contribution.

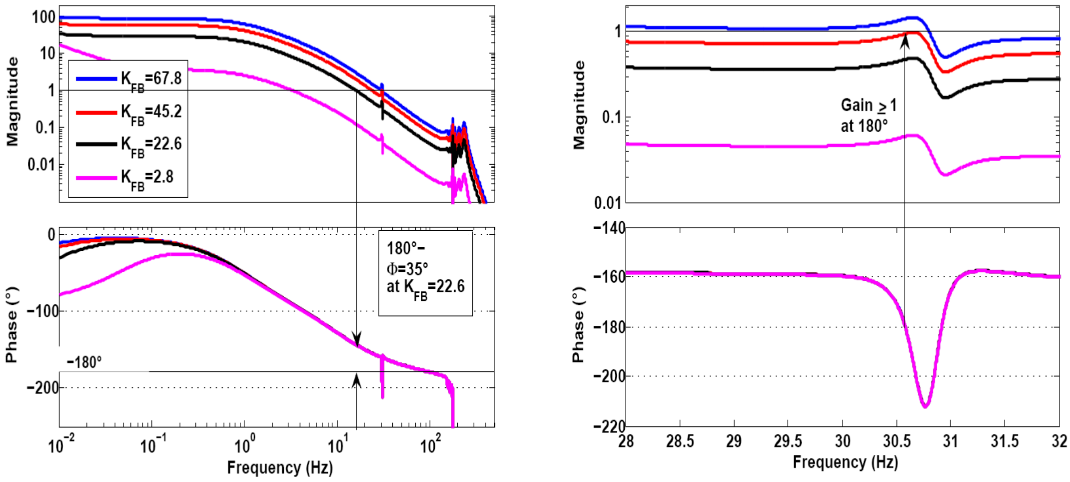

Figure 7.5: Bode plots of the piezo→RF transfer function, the transfer function for different feedback gains of the PI path including lowpass filtering because of the cavity bandwidth and the transfer function of the maximum P gain without cavity part. The right plot depicts a zoom to the first mechanical resonance at 30 Hz to explain the stability limit of the gain.

To account for this, a higher gain could be compensated for with a higher order filter, which has a steeper response in amplitude. But following any change in the filter an immediate instability of the total loop happened. This can be further investigated by the Bode plot of the total transfer function given by Equation 7.6. For four different feedback gains of 2.8, 22.6, 45.2 and 67.8 the Bode plots of the total transfer function are shown in Figure 7.5. Regarding the first mechanical eigenmode each transfer function crosses the 180° at that position. The gain margin of a control loop is defined by the gain where the closed loop feedback system would become unstable. This happens at the frequency where the transfer function crosses the unity amplification given by the 0 dB (magnitude=1) line at a phase lag of 180°. According to parameter optimization rules by Ziegler and Nichols [35] a stable closed loop operation is given by choosing half the maximum feedback gain. The transfer functions for gains of 67.8 and 45.2 already have 0 dB gain or even more at the first resonance. The black curve representing K_{FB}=22.6 thus fulfills the stability criterion and has a -7.0 dB damping of the first resonance. The phase margin at the 0 dB line is 35°.

For future measurements including the feedforward path of the controller this gain has been kept as a stable solution. But one must consider, that this system has to work in parallel with a LLRF control system. The high LLRF gain needed for the BESSY-FEL application also increases the closed loop bandwidth of the cavity-LLRF controller system. It has to be tested how this may affect the feedback transfer function of the piezo tuner, when the LLRF system provides the error signal for the piezo controller.

7.3 LMS–based adaptive feedforward control

The feedforward path aims to minimize the phase error signal with respect to dominant lines in the microphonics spectrum. Mainly the first mechanical resonance of the cavity-tuner system has to be suppressed.

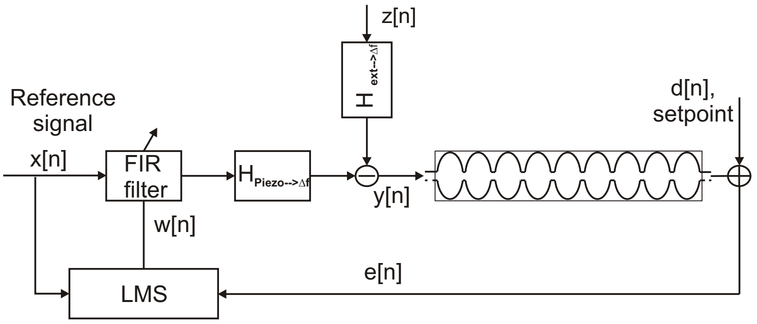

Figure 7.6: The least-mean-square filter algorithm applied to cavity detuning compensation. The reference signal x_n is altered by FIR filter coefficients w_n such, that the output signal y_n negates external detuning sources at the cavity to achieve a zero error signal e_n with respect to a desired set point d_n. The filter is updated according to the least-mean-square outcome.

7.3.1 LMS-Theory

The idea of the filtered least-mean-square feedforward algorithm is to find a set of filter coefficients which leads to a minimum of the measured phase error signal when a reference signal is passed through the filter. Figure 7.6 displays the least-mean-square filter algorithm in detail. In the following the parameter n refers to a discrete time step $n \cdot T_{sample}$. The size of all given vectors is thus a measure for the number of samples or filter taps to be used for the calculations. A reference signal $\vec{x}_n$ is altered by a finite-impulse-response filter (FIR) such, that the resulting signal to the piezo ideally negates the external microphonics noise.

The microphonic detuning is a convolution of the external noise by some unknown transfer function $H_{ext\to\Delta f}$ between the noise itself and the resulting cavity detuning. It is not possible to measure this function between external forces from all directions in space and the detuning. The transfer function $H_{Piezo\to\Delta f}$ from piezo movement to cavity detuning has been well characterized (Section 6.2.3) and may be included in the controller. The reference signal (vector) $\vec{x}_n$ should reflect the nature of the measured error sources to achieve a fast convergence of the filter coefficients $\vec{w}_n$ of the FIR filter. The final residual error is compared to a set point or reference variable, which is in general zero. The final error e_n is fed back to the least-mean-square filter coefficient update algorithm to adapt the filter coefficients to the actual system parameters.

In a mathematical sense this is an optimization problem of the filter parameters with respect to a given detuning. A given set of filter coefficients will result in a specific residual detuning composed of external noise source and piezo action on the cavity. The filter coefficients span a space of corresponding to values e_n with the dimension depending on the number of filter components chosen. The task of the least-mean-square algorithm is to find a filter setting which represents the minimum of this distribution. In an ideal world the FIR filter would represent the inverted piezo-to-RF transfer function.

The numerical method behind the LMS algorithm is the method of the steepest descent[84].

The final detuning error at time step n is given by

$$e_n = y_n - d_n, \tag{7.7}$$

while the set point d_n equals zero the total detuning y_n is given by the sum of the external detuning z_n and the action of the piezo $\vec{w}_n^{\mathrm{T}} \cdot \vec{x}_n$:

$$y_n = H_{ext\rightarrow\Delta f}(t) z_n - H_{Piezo\rightarrow\Delta f}(t) \vec{w}_n^{\mathrm{T}} \cdot \vec{x}_n \tag{7.8}$$

To find an update rule for the filter coefficient vector $\vec{w}_n$ the Taylor expansion of e_n with respect to $\vec{w}_n$ up to the linear term is derived. The assumption is, that there exists a set of filter coefficients $\vec{w}_{opt}$ where a absolute minimum of the absolute error signal distribution is located in the plain spanned by the $\vec{w}_n$ components*.

$$e_n(\vec{w}_{opt}) = e_n(\vec{w}_n) + (\vec{w}_{opt} - \vec{w}_n)\nabla e_n(\vec{w}_n) \tag{7.9}$$

Assuming a small change in the coefficients between two steps and a non-zero gradient of the detuning e_n towards the minimum the equation simplifies to

$$0 \overset{!}{=} e_n(\vec{w}_n) + (\vec{w}_{opt} - \vec{w}_n)\nabla e_n(\vec{w}_n) \tag{7.10}$$

The absolute minimum $\vec{w}_{opt}$ by approximation may be replaced with the final step of the algorithm $\vec{w}_{n+1}$, thus one obtains a linear relationship for the difference of two consecutive sets of filter coefficients:

$$e_n(\vec{w}_n) = -(\vec{w}_{n+1} - \vec{w}_n)\nabla e_n(\vec{w}_n) \tag{7.11}$$

A solution of such a difference equation is given by

$$\vec{w}_{n+1} = \vec{w}_n - \alpha \nabla e_n \tag{7.12}$$

Introducing this solution in 7.11 α is $\alpha = \frac{e_n(\vec{w}_n)}{(\nabla e_n)^2}$. Including the definition of e_n in 7.11 the final update rule is given by

$$\begin{aligned} \vec{w}_{n+1} &= \vec{w}_n - \frac{\left(H_{ext\rightarrow\Delta f} z_n - H_{Piezo\rightarrow\Delta f} \vec{w}_n^T \cdot \vec{x}_n\right) \nabla e_n}{(\nabla e_n)^2} && (7.13) \\ &= \vec{w}_n - \frac{e_n \vec{x}_n}{\vec{x}_n^T \cdot \vec{x}_n} && (7.14) \end{aligned}$$

The change of the filter coefficients follows the steepest gradient of the error signal, the sign of the detuning determines the direction of change of the $\vec{w}_n$'s elements.

At this point the least-mean-square rule has an update gain of 1 or the gain is defined by the inverse norm of the reference signal

$$\frac{1}{\vec{x}_n^T \cdot \vec{x}_n}, \tag{7.15}$$

which is often referred to as signal strength. Figure 7.7 visualizes the algorithm for a case of two filter coefficients. The filter is changed by following the steepest gradient of the error

---

*Note, that ∇e_n is a differentiation of e_n with respect to w_n.

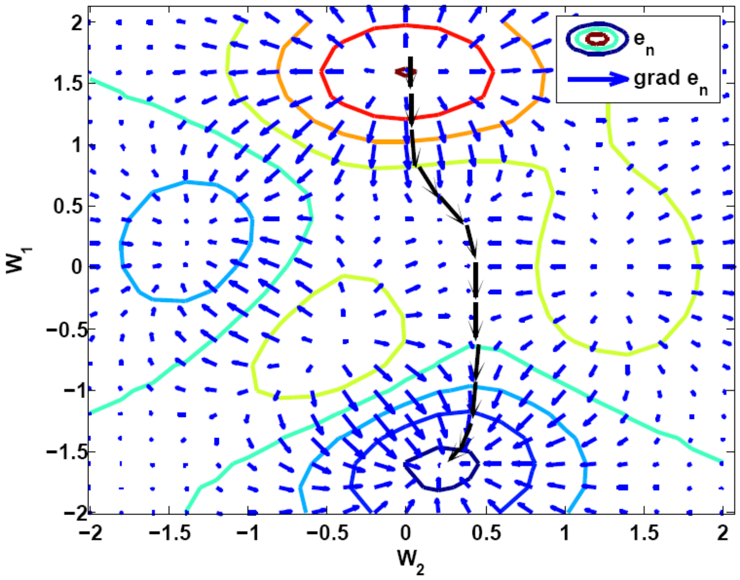

Figure 7.7: Contour plot to illustrate the method of the steepest descent. The choice of the filter coefficients W_1 and W_2 define the amount of microphonics e_n in the orthogonal direction of the plane. The deepest decent algorithm converges given a correct choice of parameters (indicated by the black arrows) to the (local) minimum of the distribution.

signal distribution which is defined by the filter coefficient themselves. According to the derived Equation 7.14 this is a possible solution. But in a real cavity-tuner environment the external noise sources are changing with time, even changing system parameters may affect the piezo to RF detuning transfer function. As it will be not possible to update the reference signal continuously the algorithm may not converge to a stable solution towards the local minimum of the residual error signal. To account for this uncertainty the update gain α according to [77] and [85]should be chosen smaller than 1.

This has also been observed experimentally. To start the feedforward process, as the stable filter solution is unknown in the beginning, the filter coefficients are initialized to zero. It has been observed during attempts to control the microphonics by this algorithm, that a very low update gain $\alpha \ll 1$ kept the filter within stable boundaries, such that the total effect on the detuning was very small. When the gain had been chosen too high the system started to oscillate and amplified the mechanical resonance instead of damping its effect on the cavity detuning.

Furthermore the denominator of the second term of equation 7.14 represents the variance of the reference signal distributed around zero mean value. In the case the microphonics detuning and thus the reference signal should become very low, the update gain as a product of the update coefficient α and the inverse of the variance of the reference signal may grow beyond all boundaries. To account for this effect, the experimentally proven instability, and to make the feedforward method more robust, two parameters have been included. The update gain is varied by an additional gain value now denoted as μ and the denominator is expanded by a small constant β.

The final feedforward filter algorithm is thus given by:

$$y_n = H_{ext \to \Delta f} z_n - H_{Piezo \to \Delta f} \vec{w}_n^T \cdot \vec{x}_n \tag{7.16}$$

$$e_n = y_n - d_n \tag{7.17}$$

$$\vec{w}_{n+1} = \vec{w}_n - \mu \frac{e_n \vec{x}_n}{\beta + \vec{x}_n^T \cdot \vec{x}_n} \tag{7.18}$$

In the derivation of the feedforward algorithm the piezo to RF detuning transfer function has not been explicitly named. In the real system the output of the filter $\vec{w}_n^T \cdot \vec{x}_n$ is altered by the transfer function, such that the detuning counteracting the microphonics is given by

$$y_n = H_{ext \to \Delta f} z_n - (\vec{w}_n^T \cdot \vec{x}_n) H_{Piezo \to \Delta f}. \tag{7.19}$$

In the real system the filter always reflects partly the inverse of the transfer function by adapting the filter gain and phase according to the distribution of the mechanical resonances.

7.3.2 Implementation of the feedforward controller

The controller has been implemented on the realtime system described in Section 4.3.1. The parameters of the feedforward path are summarized in Table 7.2. A sampling frequency of the phase error and reference signal of 2.0 kHz was shown to be sufficient to control microphonics up to 300 Hz.

The phase error or detuning signal is continuously sampled for the PI controller and to adapt the FIR transfer function. The reference signal is recorded every minute and optionally deconvolved with the piezo-to-RF detuning transfer function, which is implemented in a look-up table. This transforms the detuning from the cavity to the tuner side. In theory such a deconvolved signal shifted by π in phase should approximately interfere deconstructively with the microphonics acting on the cavity after passing the FIR filter and the piezo to RF transfer function. The experiments showed, that still some fine tuning in amplitude and phase of the feedforward signal was needed to start compensation. Especially microphonics at the first mechanical resonance were found to be very sensitive to the settings of the controller parameters.

It is also possible to create a sinusoidal reference signal or a linear combination of several frequencies with individual phases. Included is a variable gain allowing for a change of the peak-to-peak amplitude. The obtained signal $\vec{x}_n$ is played continuously and the last n_{taps} samples are used for the feedforward signal processing, where n_{taps} is the number of filter weights or coefficients.

The filtered signal is further filtered by a narrow 5^{th} order bandpass filter of Butterworth type with a pass-band of 20 Hz around the resonance. Preliminary results with feedforward detuning compensation [69] showed an excitation of a neighboring mode, which was not present in the uncontrolled case. A reduction of the 41 Hz mode resulted in an increase of the next mechanical mode at 94 Hz. This problem is eliminated by the Butterworth filter. Phase offsets in the total transfer function of the feedforward path can be compensated for with an additional programmed phase shifter. Finally the feedforward signal is added to the PI controller signal and fed to the piezo amplifier.

Table 7.2: Typical parameters of the feedforward path

Feedforward parameter	**Value**
Reference $\vec{x}_n$ ($\mathrm{Hz}_{\text{peak-peak}}$)	0.05-0.2
Number of filter taps	400
Update gain μ	0.2-1
β	0.05-0.1
Sampling frequency (Hz)	2.0&4.0 k
# samples for reference signal	2000
ADC/DAC resolution (Bit)	16
Theoretical input resolution (Δf (mHz))	0.2
Theoretical output resolution (mHz)	1.2
Cavity bandwidth (Hz)	10.8-21.7

7.4 A combined controller: Achieved results

A successful microphonics detuning compensation using a combination of feedback and feedforward methods has been performed at HoBiCaT. All measurements have been performed at 1.8 K. The microphonics detuning was measured in open loop mode beforehand to have a reference for validating the achieved level of control. For the feedforward compensation both methods for generating a reference signal $\vec{x}$ (measurement and artificial $\sin(\omega t)$ generation of $\vec{x}$) have been tested. In some cases the artificial signal created by the software itself achieved a more stable and effective performance than using recorded microphonics detuning samples. This has been done by varying the signal's parameters as amplitude and phase (the frequency is determined by the microphonics to be damped) until an effective compensation is achieved.

Figure 7.8 shows an example of adaptive feedforward compensation of the first mechanical resonance. The achieved peak-to-peak compensation is about a factor of six. The rms detuning has been reduced from 1.70 Hz to 0.45 Hz. In this case the reference signal was created by software and adapted by hand in amplitude and phase until the algorithm started to converge to a stable solution achieving minimum residual detuning at that frequency. Here the low-frequency PI controller was turned off and there are still slow pressure fluctuations present in the signal.

Once stable settings are found and assuming that the external detuning sources are only slightly changing with time, it was tried to measure how fast the LMS based controller reaches its steady state error. For testing, a higher resonance at 176 Hz was excited by an external piezo frame installed on the cavity support in HoBiCaT. First the parameters for convergence were determined by manual adjustment. Then the controller, including the feedback part, was switched off and after a few seconds on again. To measure the settling time of the controller, the envelope of the detuning data was determined and lowpass filtered to remove high frequency noise. The resulting distribution was fitted with a Fermi-Dirac-like distribution (Figure 7.9). The FWHM value of the derivative with time is a measure for the switching or convergence time of the algorithm. In this case about 1.0±0.2 s has been determined. This is at least the time a system needs to settle when during operation a reinitialization has to be performed.

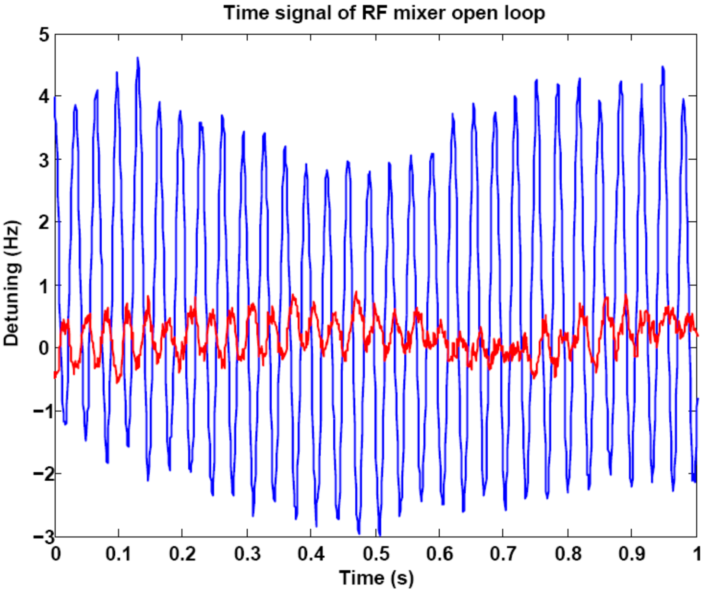

Figure 7.8: Example of microphonics detuning reduction at the first mechanical resonance using the adaptive feedforward filter algorithm. For comparison the blue line denotes a measurement without controller.

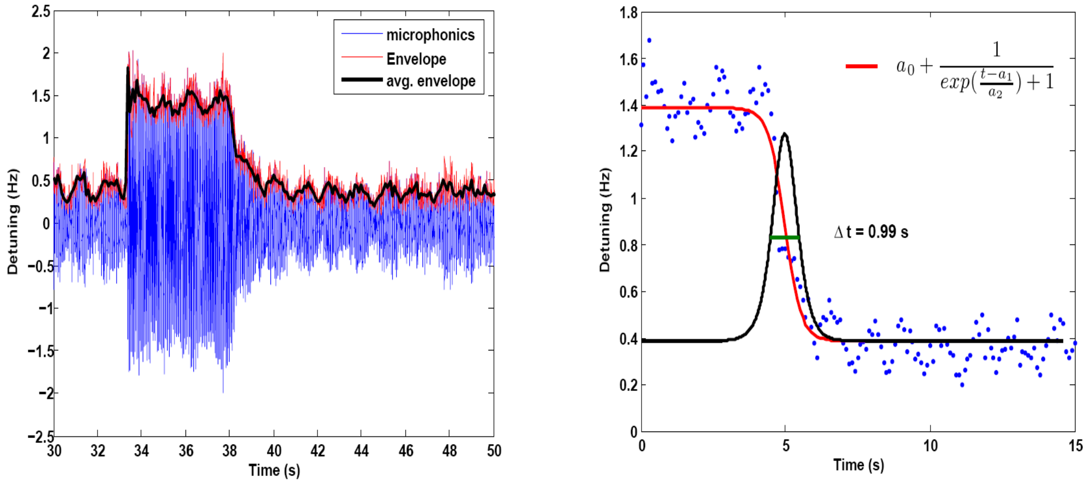

Figure 7.9: The left plot shows the response of an excited resonance at 176 Hz. After switching the controller off and on again the envelope of the detuning data have been determined and filtered (red and black curve). To determine the switching time of the controller a Fermi-Dirac distribution has been fitted to the data of the averaged envelope, calculating the time from the derivative of the fitting result(right plot, derivative given by black curve).

7.4.1 Compensation of measured microphonics at 1.8 Kelvin

Figure 7.10-7.12 give an overview of detuning compensation. The loaded quality factor was adjusted to $6.4 \cdot 10^7$ corresponding to a half bandwidth of 10 Hz. The microphonics spectrum in the open loop case (blue curve) shows a typical composition of low frequency pressure variations and the excited first mechanical eigenmode. Smaller contributions are due to the turbo pump and other external sources like water supply pumps. The rms detuning was

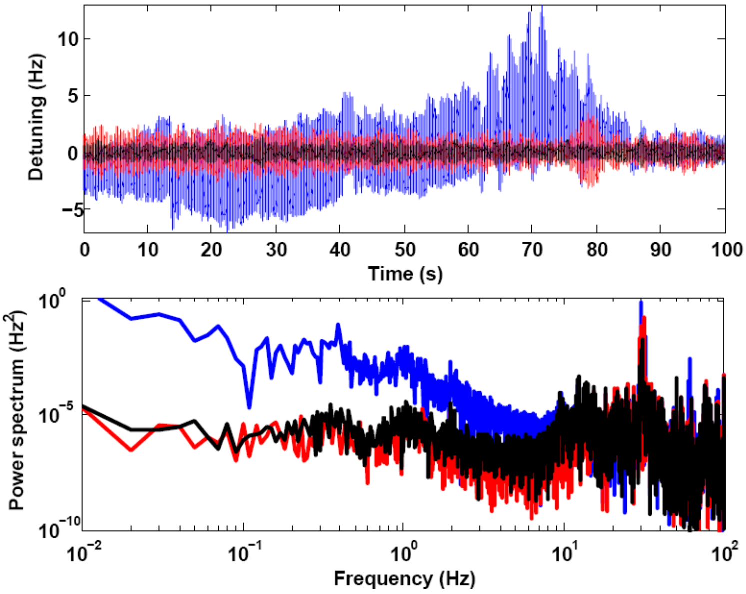

Figure 7.10: Time domain detuning data in open loop mode (blue curve), PI controller (red curve) and combined feedback and feedforward control (black curve). The lower plot shows the corresponding Fourier spectra for each case. The measurements were done at 1.8 K and Q_L=6.4·10^7.

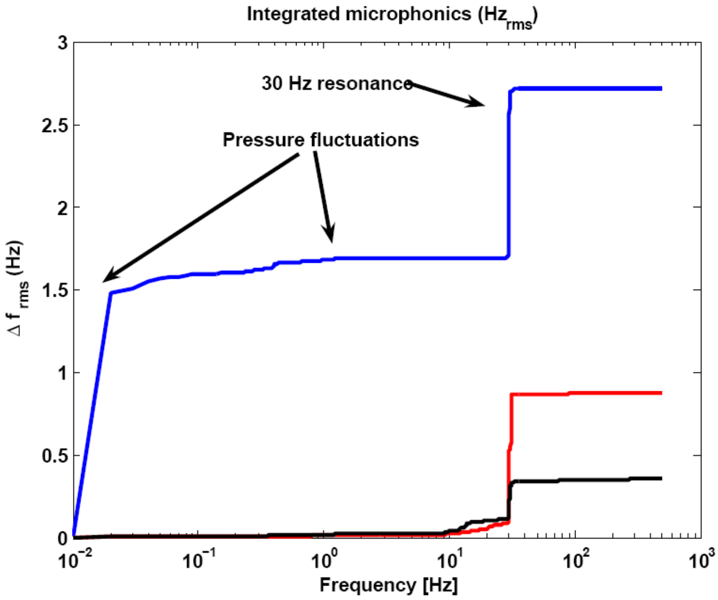

Figure 7.11: Integrated detuning spectra of open loop detuning (blue curve), feedback controlled detuning (red curve) and residual detuning with feedback and feedforward compensation (black curve).

around 2.5 Hz with a peak value of 12.5 Hz.

For the compensation tests no further control loop like the phase-locked-loop or a LLRF controller has been used to lock the RF resonance. After activating the feedback path of the controller the low frequency regime $\leq$ 10 Hz is reduced by a factor of 15.5 to 0.1 Hz rms detuning (red curve, gain K_{FB}=22.6). The residual phase error is equivalent to an rms

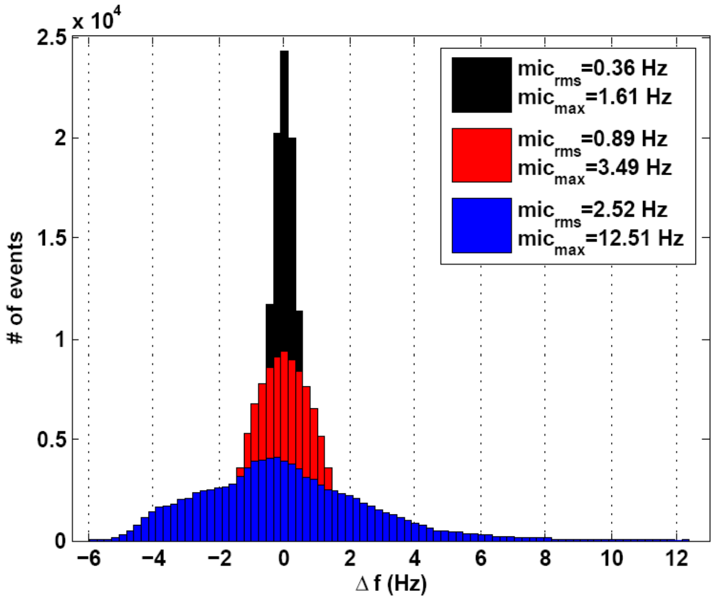

Figure 7.12: Open loop (blue), PI controlled (red) and PI+FF controlled detuning distributions (black).

detuning of ∼0.9 Hz, which is mainly caused by the eigenmode. The time signal shows a variation of the peak-to-peak detuning envelope by a factor of 4 over a sub-second time scale (compare to Figure 5.8). The feedforward path has to quickly adapt to these detuning amplitude fluctuations.

After stabilization of the feedback path a measured reference signal has been fed to the FIR filter, whose coefficients have been initialized to zero. After finding the correct value for the update gain μ the feedforward system quickly converged. The mechanical resonance contribution was suppressed by a factor of 3.3 leaving a total residual rms detuning error of 0.36 Hz (black curve), which is close to the tuner resolution of 0.2 Hz. The peak detuning of 1.61 Hz is well below the half bandwidth of the cavity. In total the rms and peak detuning have been reduced by a factor of seven. Given the implementation of an additional LLRF with feedback gain of 200, the phase error would be reduced from 0.07° to 0.01°—well within the limit acceptable for the BESSY-FEL.

Limitation by tuner resolution

Similar results were obtained with the type II tuner. An example result is presented in Figure 7.13. In this case the uncompensated microphonics already were very low. Usually measured values taken in intervals of about 100 seconds showed an rms detuning between 0.5-1.0 Hz. As for the experiments with the type I tuner system it was here possible to reduce the pressure induced detuning by the feedback controller from $\simeq$ 1 Hz rms to $\simeq$0.1 Hz rms. The residual detuning components at higher frequencies only incorporated amplitudes of about 0.1-0.3 Hz close to the limit of the tuner resolution. Hence the first mechanical resonance was artificially excited by an external device, which is the case in Figure 7.13. Below the supporting structure of the table carrying the cavities a low frequency loudspeaker was attached to the outside flange. It was driven by a low frequency amplifier modulating the signal with a standard function generator. The first eigenmode was thus excited to 3.6 Hz.

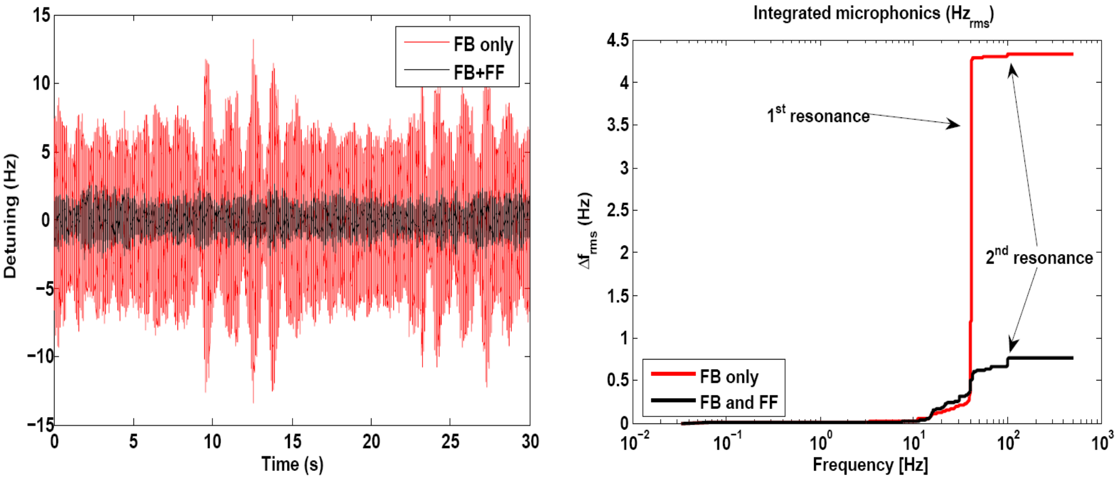

Figure 7.13: Time domain detuning and integrated detuning spectra with feedback control only (red curve) and combined feedback and feedforward control of the type II tuner.

This time the feedforward algorithm was used by creating a reference signal $\vec{x}$ by software resembling the measured microphonics detuning. The update gain μ, the peak-to-peak amplitude of the reference signal and the phase of the controller signal was changed until convergence has been reached. The first resonance, actually being composed of two peaks in the spectrum, has been damped by a factor of eight. The total detuning of 4.3 Hz rms has been decreased to a final detuning of 0.8 Hz rms. Peak detuning events have been decreased by a factor of four.

But the final detuning components again show the limit of the tuner. The spectral components of the residual microphonics acting on the cavity have detuning amplitudes below 0.3 Hz. As this is near the assumed piezo and measurement resolution, the total limit for the given microphonics at HoBiCaT showed to be 0.4-0.8 Hz rms (equivalent to $\sigma_\Phi = 2.1°$ at $Q_L = 3 \cdot 10^7$).

Control of multiple microphonics sources

Although most measured cavity detuning only showed one dominant detuning component at the first mechanical resonance, it has to be shown, that several higher frequency microphonics sources may be compensated by this scheme simultaneously. This experiment has been done with a cavity showing more than one major contribution to the overall detuning at frequencies between 20-50 Hz. The microphonics was quite low, about 1.0 Hz rms.

The result is displayed in Figure 7.14. The time signal of the uncompensated case with only the feedback controller compensating the pressure fluctuations exhibit the typical beat behavior for an interference of two nearby frequencies. To achieve feedforward control a reference signal was created by incorporating the piezo to RF detuning transfer function information and individual Bessel-type bandpass filters for each signal at these frequencies. The total feedforward compensation achieved an additional factor of two for the detuning reduction by lowering a 31 Hz[†] and the first resonance contribution at 41 Hz. Some part of the compensation achieved was negated by excitation of a higher harmonic of the 31 Hz line.

[†] The 31 Hz line seems not to be a mechanical resonance of this cavity, —it cannot be excited by the piezo tuner.

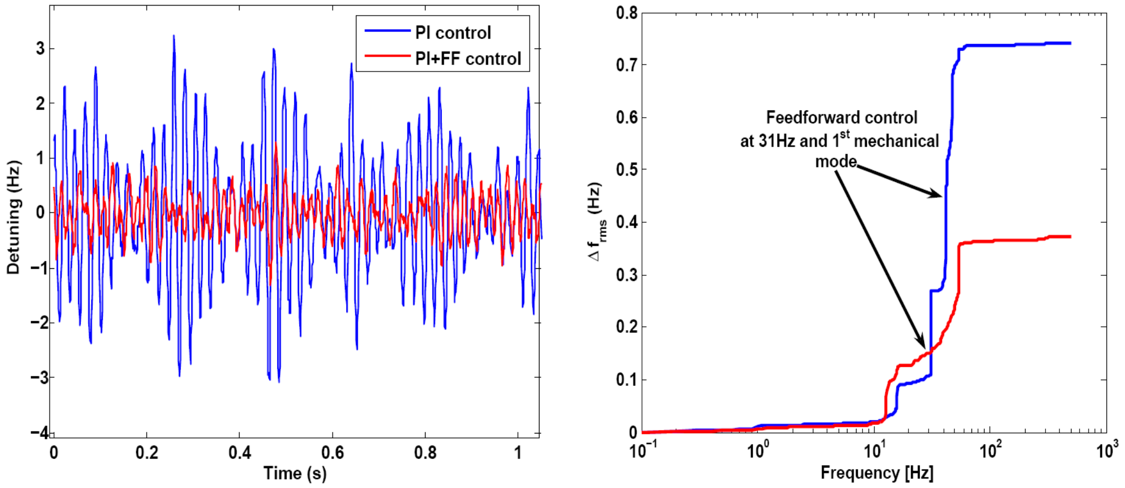

Figure 7.14: Feedforward control with the type I tuner controlling two spectral contributions in parallel. Disturbances at 31 Hz and the first mechanical mode at 41 Hz are controlled by one least-mean-square based process. The very low microphonics of 0.74 Hz has been reduced to 0.37 Hz. On the left time domain data, on the right integrated detuning spectra, the red curves are with activated feedforward control.

Table 7.3: Achieved phase stability and theoretical phase stability if a future LLRF system with gain 200 is included. In the first three rows Q_L was $6.4{\cdot}10^7$, in the last two rows $4{\cdot}10^7$. The third row shows a result where high pressure variations occurred.

Open loop: $\sigma_{f,res}$ (Hz)	Closed loop:$\sigma_{f,res}$ (Hz)	σ_Φ(°)	$\sigma_{\Phi,theo}$(°), K_P=200
1.7	0.45	2.52	0.013
2.52	0.36	2.01	0.01
3.8	1.7	9.43	0.05
5.3	0.8	2.82	0.014
0.74	0.37	1.32	0.007

This harmonic at 62 Hz has a detuning amplitude of 0.1 Hz. The residual detuning values in the spectrum hint at a better resolution of the tuner being even below 0.1 Hz (the Saclay I tuner was installed with maximum allowable pre-load on the piezos).

Table 7.3 summarizes the outcome of the examples of measurements presented in this section.

7.4.2 Stability and robustness of the controller

The controller is so far realized as a proof of principle experiment, which still has to be implemented as a reliable system equipped with enough diagnostic tools to ensure stable and automatic longterm operation. Another issue that remains to be studied is whether both controllers, the piezo tuning and the future LLRF system interfere with each other or exhibit any kind of undesired crosstalk.

While the feedback path alone already showed stable operation over several hours, the feedforward algorithm only ran for several hundred seconds.

An example of a set of converged filter coefficients of the FIR filter recorded during a

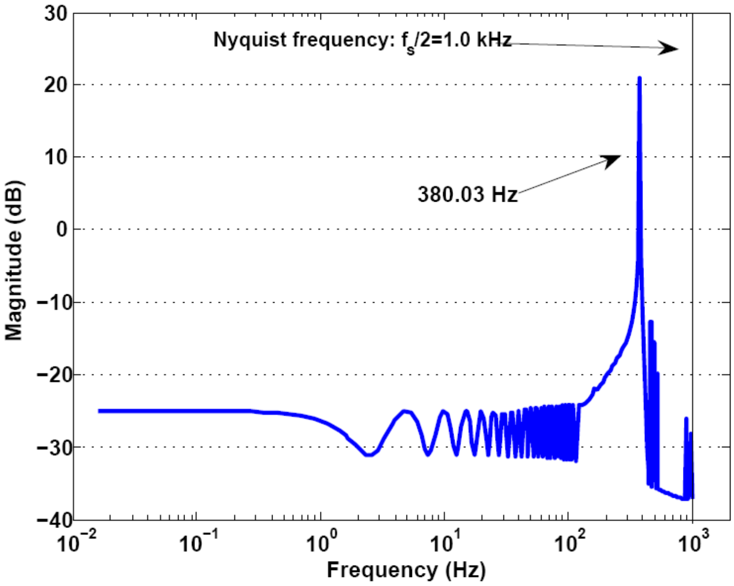

Figure 7.15: Bode plot of the final filter configuration of a 100 s long detuning compensation measurement. In this case a resonance at 380 Hz has been suppressed.

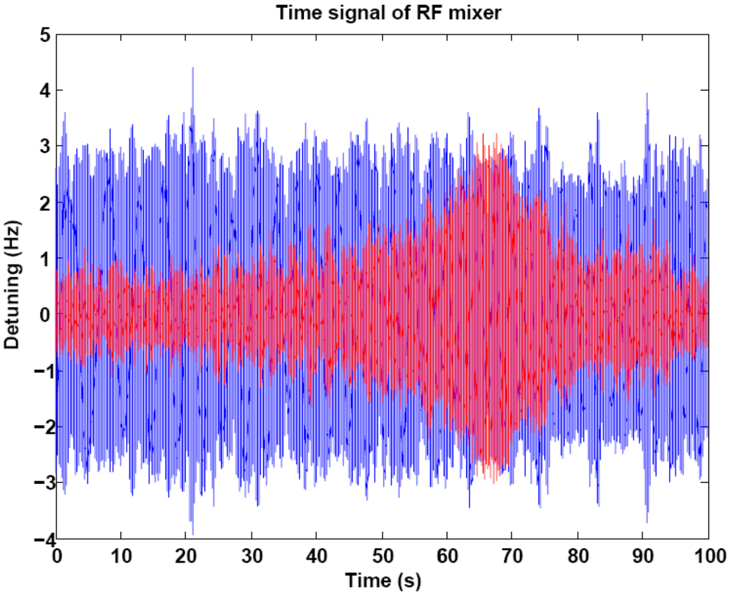

Figure 7.16: Microphonics detuning compensation using the feedback path of the controller only (blue curve). The red curve shows the additional application of the adaptive feedforward path. The algorithm nearly diverges after 67 seconds. The LMS parameters like μ and $\vec{x}_n$ have been kept constant.

measurement with stable controller operation is shown in Figure 7.15. Here, a resonance had been excited at 380 Hz with the external loudspeaker which then was compensated by the feedforward scheme. The resulting filter transfer function resembles a bandpass filter with a narrow bandwidth around the compensated resonance. All other frequencies are significantly damped. To achieve such a filter with that frequency resolution 400 filter coefficients are needed given the sampling frequency of 2 kHz. But even after converging to a stable filter configuration the algorithm still may diverge leading to unstable behavior, if the system parameter change in future.

To illustrate this point, Figure 7.16 displays detuning compensation with feedback only (blue curve) as a reference and with additional adaptive feedforward applied to the piezo tuner. The compensation remained stable at a constant residual detuning of about 2 Hz peak-to-peak for a period of 30 seconds. But then the error signal increases up to the level of the uncompensated case. The system remains for some time in this unstable regime, then the algorithm converges again to a new set of filter coefficients related to a local minimum of the error signal. The reference signal remained unchanged during the data acquisition. The algorithm nearly diverged, as a change of the external noise exciting the resonance resulted in a different state of the mechanical system. This state had been outside the convergence radius of the adaptive feedforward for the given update gain μ and the constant reference signal $\vec{x}$. Unfortunately this range of convergence cannot be measured by experimental means for the cavity system because the excitation spectrum varies with time and in principle the external transfer function is unknown (mechanical expiation → RF detuning). Future experiments with artificial noise, dominating the "natural" background, e.g. by another piezo, may be used to determine the radius of convergence.

To achieve more reliable and stable operation periodic recording and updating of the reference signal is mandatory. This procedure should incorporate some decision rule based on the measured residual microphonics to trigger an update.

This requirement obtained by the experiment is also to be found in modern signal processing theory. The stability of the LMS algorithm is realized as long as the update gain α or in our case $\mu \cdot \alpha$ obeys the following boundaries [86]:

$$0 < \mu\alpha < \frac{1}{\lambda_{max}} \tag{7.20}$$

whereas λ_{max} is the maximum value expectation value of the quadratic mean value of a signal, in this case of the reference signal $\vec{x}_n$. For the adaptive feedforward control of a superconducting cavity this means, that an update of the reference signal about every second is needed to keep μ within the margin of stable operation, as μ is a function of $\vec{x} \cdot \vec{x}^T$. If the reference signal is obtained by processing it with the measured or modeled piezo-to-RF detuning transfer function, a maximum deviation of less than 90° is allowed in phase between the real and modeled transfer function at each frequency [87]. Otherwise an amplification instead of damping of the detuning will happen.

There is still room left for a further optimization of this routine. For example one can trade-off accuracy and performance against stability by introducing a leakage term δ in the filter update equation 7.18, which then becomes:

$$\vec{w}_{n+1} = (1 - \mu\delta)\,\vec{w}_n - \mu\frac{e_n\vec{x}_n}{\beta + \vec{x}_n^T \cdot \vec{x}_n} \tag{7.21}$$

A high δ term would result in a more stable system at the cost of larger residual detuning errors. The meaning of the term is, that with time the influence of the filter goes to zero, if the residual error e_n remains very low for a longer time.

Another possibility could be observing the variation of the FIR filter coefficients with time. Figure 7.17 displays the 400^{th} filter coefficient with time over a measurement range of 2.1 seconds. In the case of stable control the variation of the filter values changes slowly

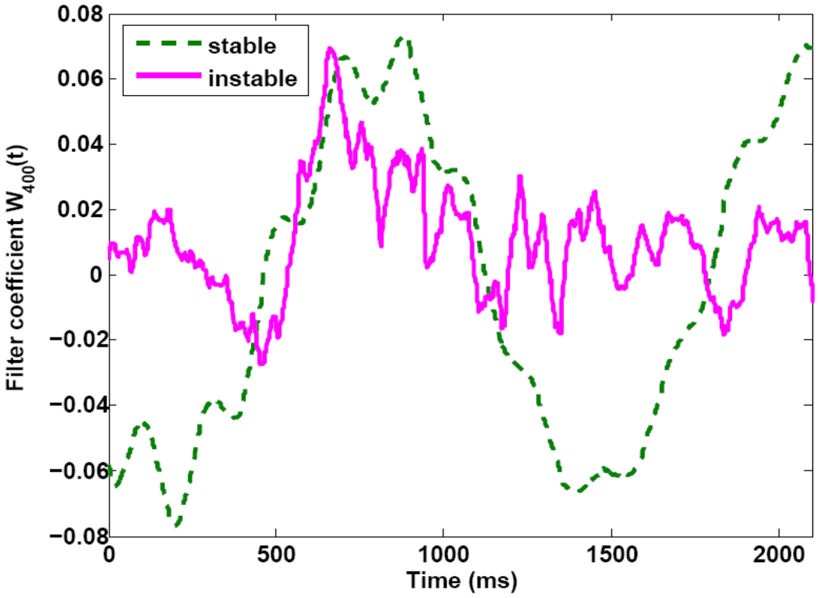

Figure 7.17: Evolution of the last filter coefficient $w_n(400)$ with time during feedforward detuning compensation. The dashed line represents a case where the compensation achieved a detuning reduction. For the magenta case no compensation was achieved.

with time, following the changes in the detuning amplitudes. The unstable case (magenta line) represents a system without convergence. It features a less smooth change with time. A parallel observation and ruling of the residual detuning error and the evolution of the filter with time or the derivative of the coefficients with time may serve as a basis to decide to update the reference signal.

7.5 Impact of detuning control on cavity operation

Returning to the cavity simulations in Section 3.3 and including the compensation result allows one to estimate the potential impact of such a system on the beam stability of the BESSY-FEL.

The model given in Chapter 3 has been expanded by a simplified version of the measured piezo-to-RF detuning transfer function. Further, the least-mean-square based adaptive feedforward algorithm has been included featuring the same parameters as found during the measurements. Also the parameters of the dynamic Lorentz force detuning second order model have been updated with the results taken at the HoBiCaT test facility.

The question to be answered by the following simulations is how the two systems of LLRF control and mechanical microphonics detuning control will perform simultaneously and what ultimate field stability one might expect. Thereby the LLRF system measures and controls the cavity's amplitude and phase (or I and Q component of the field) and provides the adaptive feedforward with the detuning information.

In principal the transfer function between the external forces acting on the cavity and the microphonics detuning is unknown. The only information between externally imposed mechanical deformation and resulting RF resonance shift is given for the longitudinal piezo movement and the Lorentz forces acting on the cavity cells. To create an external noise

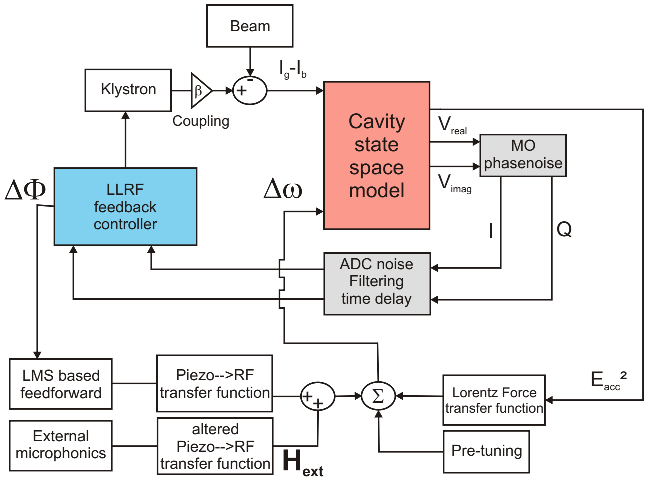

Figure 7.18: Simulation scheme with included measured transfer functions, microphonics excitation and least-mean-square based feedforward algorithm.

signal the measured microphonics detuning has been deconvolved by the piezo to RF detuning transfer function and fed back to the detuning $\Delta\omega$ of the cavity state space model by convolving it with an altered transfer function. This should reflect the situation, that the transfer function between outer world and cavity is different than between piezo and cavity.

The varied transfer function has been derived from the original piezo-to-RF by varying the parameters for the individual mode's coupling $k_{p,k}$, the damping coefficient ξ_k and the mode's amplitude M_k by a random Gaussian distributed factor Δ_{par} of 10% referring to one sigma. For example:

$$\tilde{\xi}_k = \xi_k \cdot (1 + \Delta_{par})\,.$$

An overview of the changed simulation scheme as compared to Figure 3.8 is sketched in Figure 7.18.

The phase error signal from the LLRF controller is used like in the real system as the reference signal for the adaptive LMS based feedforward system and as well as the update signal of the FIR filter. It is reduced by the LLRF system gain as $1/(1{+}K_P)$ (ideal situation). The critical parameters like update gain μ, sampling rate and total system gain of the piezo tuner system are chosen as determined in the measurements. The mechanical model of the cavity and accompanying microphonics spectrum are related to the type II tuner results with the BESSY01 cavity. The piezo to RF detuning transfer function incorporates the main 20 mechanical modes of the spectrum up to 450 Hz. The dynamic Lorentz force detuning model includes the three dominant modes characterized at HoBiCaT[‡].

For the RF control section the phase noise of the local oscillator has been taken from a measured spectrum and scaled to an integrated time jitter of 70 fs, which is feasible by present signal sources. Table 7.4 gives an overview of the cavity parameters and assumed error sources for the single cavity simulation.

[‡] Three modes provided by the measurements at HoBiCaT, the remaining nine are from measurements at DESY [68]

Table 7.4: Parameters for the cavity simulations including a combination of LLRF control and piezo based adaptive feedforward, representing a cavity after bunch compression.

Parameter	**Value**
Microphonics σ_f (Hz)	5.2
Feedforward sampling frequency (Hz)	2.0k
Reference samples $\vec{x}_n$	4.0k
Number of filter taps	400
Phase noise $\sigma_{\Phi,noise}$ LO (°)	0.036
Amplitude noise (1 σ) (‰) LO	1.9
Klystron noise (‰)	5.0
Beam current (mA)	2.5
Beam charge jitter (%)	5
Beam time jitter (fs)	250
# Lorentz force modes	12
k_{LF} (Hz/(MV/m)^2)	1.0
# Mechanical modes piezo→RF	20 (DC-450 Hz)
Q_L	$4{\cdot}10^7$
$f_{1/2}$ (Hz)	16.3
V_{cav} (MV/m)	16.0
Acceleration phase Φ_b (°)	0.0
Feedback gain K_P (LLRF)	25-2000
Klystron avail. power (kW)	13.0
LLRF time delay (μs)	1.0
Simulation time constant T_{sample} (s)	$1{\cdot}10^{-6}$

7.5.1 Cavity stability

Figures 7.19 and 7.20 show an example of the simulation result for an LLRF feedback gain of 200. The microphonics detuning without compensation was 5.2 Hz rms. This value was chosen as it is the maximum rms detuning measured at HoBiCaT (see Section 5.4) and to simulate this worst case scenario. The adaptive feedforward algorithm of the piezo tuner converged after 0.8 seconds of the simulated period using the phase and thus detuning information from the LLRF algorithm. Even though the present system has a fair amount of phase noise a reduction of a factor of three of the detuning has been achieved (Figure 7.20). The controlled phase signal of the cavity $\Phi(t)$ shows features of the residual detuning in its spectrum as well as contributions from the slower phase noise components (1-10 Hz).

The achieved accuracies are a relative energy jitter of σ_E/E=$1.9{\cdot}10^{-4}$ at an rms phase error of σ_Φ=0.03°. The mean forward power P_f was 2.0±0.15 kW.

To examine how the variation of the LLRF feedback gain changes the performance of the piezo-based tuning and which value results in an optimum for the cavity operation a scan of the gain has been performed in simulation. Figure 7.21 displays the resulting detuning and cavity phase. The red curve shows the residual rms phase error after the adaptive

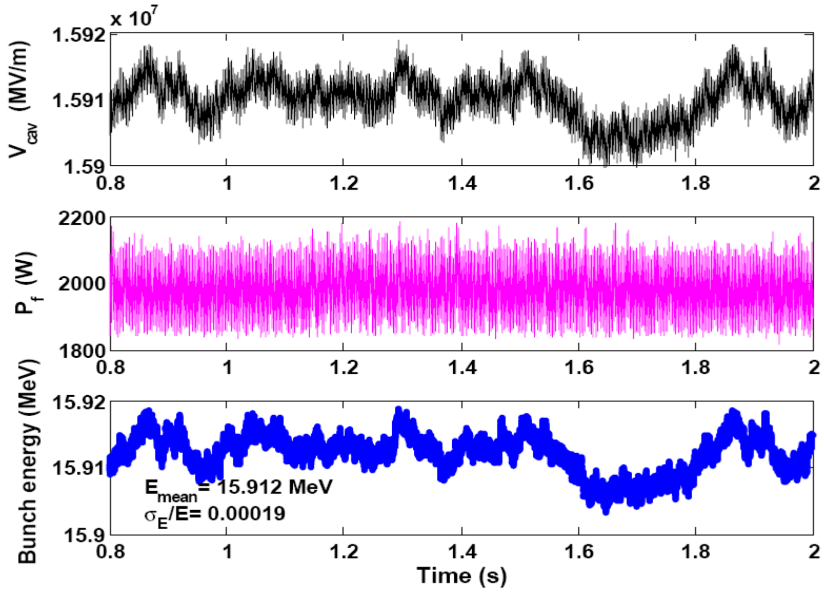

Figure 7.19: Cavity field amplitude, forward power of the klystron and energy of the electron bunches after the adaptive piezo based feedforward has converged.

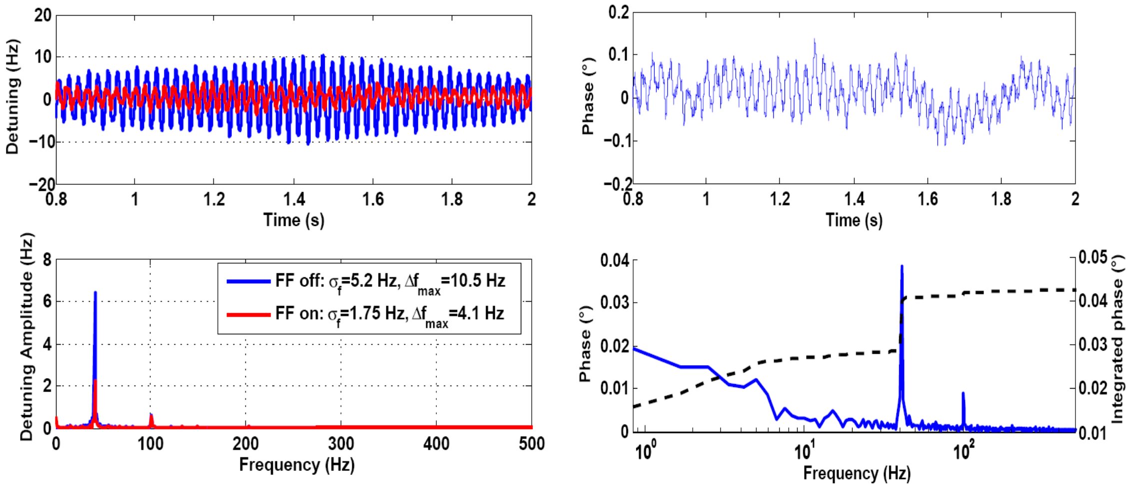

Figure 7.20: A comparison of the simulated external detuning acting on the cavity with and without adaptive feedforward. In simulation the feedforward detuning reduction has been a factor of 3. The LLRF feedback gain is 200, all given error sources were included (left plot). The right plot shows the time signal and spectrum of the phase signal during feedforward piezo control. The phase spectrum shows features of the detuning but also phase noise induced by other components (frequency<10 Hz).

feedforward piezo tuning converged for maximum possible compensation under the given starting conditions. The curve shows a local minimum at a LLRF gain of 200. At K_P=300 there is another shallow local maximum, thereafter for higher gains the resulting phase error remains constant with rising gain. This is more obvious by comparing it with the expected phase error given by the black curve, which is given by

$$\sigma_{\Phi_{theo}} = \frac{\sigma_\Phi}{1 + K_P}. \tag{7.22}$$

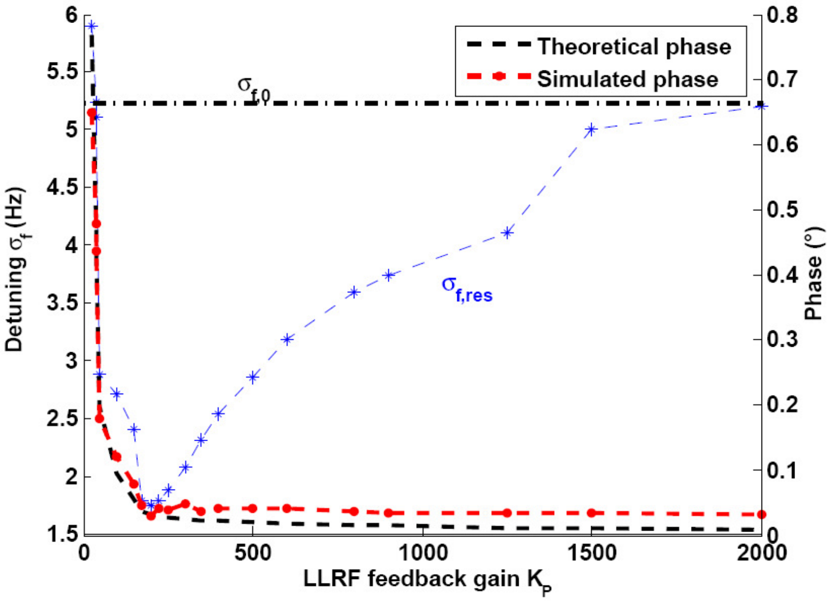

Figure 7.21: Residual detuning (blue curve) and phase error (red curve) of a cavity detuned by 5.2 Hz rms (black dash-pointed line) with piezo compensation and phase noise plotted against LLRF proportional feedback gain. The black curve shows the theoretical expected phase error with perfect LLRF control.

It is also noticeable, that the residual detuning has a local minimum at K_P=200 and rises for lower and higher LLRF gain values. This happened even though the error signal for the LMS feedforward algorithm has been scaled according to the LLRF feedback gain to obtain a phase error signal of constant magnitude. This is important, as otherwise this would directly change the update gain μ of the algorithm reducing the margin of stable operation.

Analyzing the data with respect to phase error and the different detuning sources the minimum may be explained by the following. For a higher gain the detuning itself is compensated by the LLRF control system by increasing the RF power and correcting for phase errors, thus leaving a residual error signal which is dominated by phase noise contribution. The higher the feedback gain, the less detuning information content is given for the tuner to achieve stable controller settings. This results in a detuning level which is given by the total external microphonics for the highest gain value.

For lower feedback gains another unwanted coupling between the cavity's mechanical behavior and the RF system happened. Due to the small gain the residual amplitude error of the cavity is significant and these deviations with time coupled to the Lorentz force detuning of the cavity. This increases the detuning above the open loop detuning level $\sigma_{f,0}$ in extreme cases. Peak-to-peak Lorentz-force detuning levels of up to 5 Hz have been excited. This additional time varying detuning has not been considered by the reference signal of the adaptive feedforward, as it is based on a signal recorded prior to the event. This is an example of a ponderomotive effect as discussed in Appendix B.

Summarizing the following demands have to be fulfilled for a control system of a CW driven cavity:

- The noise of the reference system has to be kept to a minimum as it reduces the effectiveness of the LLRF controller and the piezo tuning control.

- Any change in the control parameters of the RF system have to be considered to update the piezo control.
- Each cavity including the total tuner setup has to be characterized individually by its transfer function before a piezo controller can be established. The same holds true for the microphonics.
- The resolution of the piezo tuning system should be further improved.
- Should noise limit the performance there are two possible solutions to improve the tuner performance:
    - It has to be tested whether a force measurement sensor, like a second independent piezo sensor, would deliver a signal reflecting the actual cavity detuning
    - For the slower tuner control algorithm a Kalman state estimator may be implemented. This may extract the cavity's phase and detuning information from the noisy measurement signal. This should improve the pure detuning control.

The main result of these simulations is, that a stable parallel operation of the LLRF controller and the piezo-based adaptive feedforward appears possible. But to optimize the performance the two systems cannot be operated independently.

7.5.2 Summary

The achieved level of detuning control by the combined feedback and feedforward method pushed the residual detuning considerably below the maximum level for stable FEL operation. The mean level of compensation reached around 0.5 Hz rms. To achieve the desired phase stability of the first linac section (between 0.016-0.02°, see Section 2.5.1), a LLRF feedback gain of 66-80 would suffice.

For the operation of the BESSY-FEL linac these results were included into the linac simulations. The mean residual detuning level of 0.5 Hz rms has been included into the simulations with a standard deviation of 0.3 Hz (here microphonics are uncorrelated) accounting for different microphonics detuning level and variations in the effectiveness of the piezo controllers. Even with starting condition of a quite high time jitter of 1-1.2 ps the time and relative energy jitter of the beam remain below 56 fs and $2.5 \cdot 10^{-4}$, respectively.

For the future facility it may be sufficient to equip the first 48 cavities before bunch compression with a fast compensation system. Nevertheless regarding the tuning of the cavities in general to compensate for slow drifts of the resonance frequency, a fine tuning system will probably be needed for all cavities (see Section 6.2).

Chapter 8

Summary and future perspectives

For the BESSY-FEL based on the seeded high-gain-harmonic-generation principle the linear accelerator has to deliver a very stable electron beam with respect to bunch-to-bunch time jitter and energy deviation. Critical for a low beam jitter is the stabilization of the cavity field to $1{\cdot}10^{-4}$ relative amplitude error and about $0.02°$ phase error. This is especially important in the linac sections before the bunch compressors.

Because the design foresees a loaded quality factor around $3{\cdot}10^{7}$, the resulting narrow bandwidth makes the cavity RF resonance very susceptible to any kind of detuning effect. It is thus vital to understand the nature of the microphonics. To develop compensation schemes to reduce the impact of microphonics the characterization of the mechanical and RF cavity system is necessary.

This thesis addressed the characterization and testing of TESLA-type cavities at the HoBiCaT test facility under conditions similar to those expected in the BESSY-FEL. The main error sources for the field stability with respect to amplitude and phase have been determined. Microphonic detuning was at the level of 1-5 Hz RMS. For open loop operation this corresponds to 2.6-13 degrees phase error. A tool to simulate the cavity behavior was developed, which incorporated the measured noise sources. This was used to simulate the performance of the individual cavities as well as the expected beam stability for the entire BESSY-FEL. The required field stability of $0.02°$ and 0.01% for efficient lasing were determined with these simulations.

In parallel, TESLA cavity units including their frequency tuning systems were characterized. Several mechanical tuner designs with fast piezo-based tuners were tested. The knowledge of the microphonics and the piezo-to-RF detuning transfer function laid the groundwork to develop methods to suppress the effect of microphonics on the cavity field stability. Compensation results of up to a factor of seven were achieved reducing the detuning to about 0.4 Hz rms.

Including the controller, the measured microphonics and the cavity mechanics into the cavity model showed, that in simulation the fast tuning system successfully reduced the total detuning at least by a factor of four in agreement with measurements. The low-level RF control, acting in parallel, thus was shown to achieve a phase stability around $0.02°$, therefore meeting the linac requirements.

The main results can be summarized as:

- The main error source for the cavity field stability, the mechanical detuning, has been extensively characterized. The most probable detuning level in the HoBiCaT facility is between 1-3 Hz rms (but also reaching up to 5 Hz rms). Peak events up to 10-17 standard deviations occurred. The relative frequency of these events is about 8-10 times in 24 hours. They last about 10-20 seconds.

- An analysis of the microphonics data by time-frequency methods, as Wavelets, and autocorrelation of the signal revealed two main components of the detuning. Slow helium-pressure fluctuations occurred randomly and contain frequencies up to 1 Hz. The amplitude of these components vary with time and sometimes sinusoidal behavior may occur. Presumably they are of a thermo-acoustic nature, but their origin is not understood so far. The second main component is given by the first mechanical eigenmode of the cavity-tuner system. The position of this resonance is independent of the different tuners that were tested and presumably is a property of the cavity itself. This suggests that a change of the cavity design (stiffening rings) can improve the cavity response to external vibrations. An autocorrelation analysis of the resonance showed, that mainly broadband noise causes excitation of mechanical modes.

- Analysis of the steady-state response of the cavity to helium pressure and Lorentz force detuning due to the field level showed comparable results as obtained by the TESLA collaboration. The measured detuning of 55 Hz per mbar pressure change demonstrates the need for a very stable cryogenic facility. For the static Lorentz forces values between 0.9-1.4 Hz/(MV/m)^2 have been measured. It has been shown, that those values are also dependent on the overall stiffness of the tuning systems.

- The mechanical transfer function between a modulation of the piezo tuner and the cavity detuning shows many mechanical resonances. In principle, the positions of the primary modes are determined by the nine-cell cavity itself, but the type of tuner system impacts the structure of the resonances, which is more complex for the latter tuner. It is possible to model the transfer functions by a sum of second order systems, but the number of free parameters for the fitting procedure is still too large to be implemented in a cavity tuner controller.

- Measurements of the cavity's detuning response to an oscillating RF field (dynamic Lorentz-force detuning) show a similar eigenmode structure to that measured with the piezo tuner. Here, however, the distribution of forces acting on the cavity is different, and it is not surprising that the modes' characteristics are quite different. The measured LF-detuning transfer function was included in the cavity RF simulations. These demonstrated that LF detuning only contributes about 10% to the total cavity field error for CW operation and hence can largely be ignored. But at lower LLRF feedback gain, where large microphonics detuning peaks cause a change of the field amplitude a crosstalk of the microphonic detuning to the Lorentz force detuning might occur leading to a total increase of this error source. This has been shown with measurements at the ELBE accelerator and has also been reconstructed with the simulation tools (see Appendix B).

- Based on the mechanical features of the presently available tuners alone, it was not possible to identify the superior system. A good solution for the BESSY FEL would be the Saclay II tuner with a simpler piezo frame to minimize the complexity of the resonances in the transfer function.

The resolution limit of the fast tuners is about 0.1-0.2 Hz detuning, thus limiting the microphonics compensation of the dominant lines to this level. The limitation is possibly given by play in the mechanics. A good resolution is vital because some microphonics spectra may consist of many lines with amplitudes below this resolution limit whose sum still contributes significantly to the cavity detuning, thus increasing the phase field stability beyond the 0.02° limit.

- Both tuning systems showed a significant hysteresis of the coarse tuning with the stepper motor driven spindle and lever mechanics. Slow drifts of the order of the cavity bandwidth may therefore still have to be compensated by the piezo tuner.
- Based on the measured microphonics and tuner transfer functions, a detuning compensation scheme has been developed. A combination of adaptive feedforward FIR filter algorithm and low frequency feedback showed a successful compensation under varying conditions. The total detuning has been reduced by a factor ranging from 2-7. Sometimes the controller became unstable because of changes in the external noise sources. This showed, that a continuous update of the microphonics to be used as the feedforward reference signal is essential.

The cavity simulation tool has been expanded by the LMS based feedforward piezo controller including all transfer functions and error sources determined at the test facility. This demonstrated that the RF control loop and microphonic detuning compensation must be considered as a complete system, rather than separately. The results demonstrate that an optimal RF control gain exists at 200-300. Measurements must still be performed to verify these results with a real system. For a total cavity control system it has to be shown, that the LLRF and tuning system do not show any kind of undesired crosstalk or excite instabilities in the other control loop. For this reason a digital RF control system is under development [88].

For the operation of the BESSY-FEL linac these results are promising. The achieved level of detuning compensation achieves the set detuning limits, which have been derived by the cavity-linac modeling. Even with starting condition of a quite high time jitter of 1-1.2 ps the time and relative energy jitter of the beam remain below 56 fs and $2.5 \cdot 10^{-4}$, respectively.

These results are not only interesting for the application of the BESSY-FEL, but may be transferred to other projects, in particular, linacs with little beam loading such as ERLs like the Daresbury 4GLS [42] and Cornell ERL [41]. Similar to the BESSY FEL, these require field and phase stability in the range $1 \cdot 10^{-4}$ and 0.01°, respectively. The Cornell ERL project demands for a phase stability of 0.06° [89] at loaded quality factors as high as $2.6 \cdot 10^{7}$ or even higher [90].

8.1 Outlook

The limit for the microphonics control has been the measurement accuracy of the HoBiCaT RF system and the resolution of the fast tuning systems. The first problem may be solved by using ultra-stable RF reference sources with integrated phase noise in the 0.01 degree regime.

Furthermore it should be tested if the piezo tuner systems can be improved in resolution to adapt to low detuning amplitudes.

As the mechanical design of the cavities themselves determine the detuning and the microphonics spectrum, one can envisage a CW-optimized cavity whose mechanical resonances are far beyond the bandwidth so that detuning control above 1 Hz may be no longer necessary. To evaluate this approach, measurements with LLRF feedback controllers have to show, if higher mechanical resonances may contribute more to the overall detuning, when a high gain RF feedback system increases the total system bandwidth.

For the allowable level of detuning it is critical to know, if the microphonics may couple between cavities. This would lead to a phase error correlation along two or more cavities and thus increase the total timing jitter of the electron beam compared to the uncorrelated case. Such measurements will be performed with two cavities installed in HoBiCaT simultaneously, but should be expanded to the full eight cavity TESLA modules operating CW.

To aim at combining detuning and LLRF control, first extensive LLRF tests will have to show the achievable phase stability of CW cavities at high loaded quality factor. Following steps would be to design an integrated system of both, LLRF and detuning control. Furthermore, this system then has to demonstrate its Robustness under operational conditions adapting to changes in the total cavity system and long-term stability. Many decisions made so far by the experimenter have to be automated to allow stable operation even during exceptional events.

In summary the piezo based detuning control will likely be an essential part of a cavity control system to allow stable performance to the required precision. Likewise it will permit continuous operation even during the occurrence of high peak detuning events even if only moderate RF power is available (< 15 kW). This limits the capital investment for the RF system and reduces the thermal load on critical components such as the input couplers. Most importantly, it has been demonstrated that the cavity/tuner performance is sufficient to meet the stringent stability requirements of the BESSY FEL.

Appendix A

Timing jitter in the photoinjector and booster

In the following section the influence of the field stability in the photoinjector and booster RF cavities on the time jitter of the bunches before the first bunch compressor will be evaluated (scheme shown in Figure A.1). As is shown by the results of Section 3.5 it will also define the amount of uncorrelated error, i.e. detuning, a single cavity is allowed to experience to still fulfill the final jitter requirements at the linac exit.

Figure A.2 shows the electric field distribution of the accelerating mode inside the photoinjector RF cavity and a TESLA cavity. In the unperturbed case it experiences this peak field altered by the transit time dependent phase shift and gains the energy of the reference particle. For the following calculations of the expected timing jitter from bunch-to-bunch in the photo-injector cavity, a short drift space and the first accelerating cavity the following assumptions are made:

- The injection phase of the electron bunch depends on the injection time jitter due to the laser system and is given by 250 fs. This relates to a phase error $\sigma_{\Phi_{\mathrm{inj}}}$=$1.3{\cdot}10^9{\cdot}2\pi\cdot\sigma_{\mathrm{t,inj}}$=0.12 °.
- Uncorrelated amplitude and phase errors for the injector cavity and the first accelerating cavity have been assumed.
- The field and energy gain is calculated stepwise as there is no complete analytical expression for this problem. Therefore the accelerating gaps l_{acc} are divided into n_a sub-steps where the field is assumed constant and estimated by the Euler method
- The total time an electron needs to pass this section is around 6-7 ns. As the effects contributing to the field deviations in phase happen on a much slower time scale, the phase and amplitude errors are only determined once during the simulation.

For one electron bunch the calculation is as follows:
The starting field at the cathode is given by the chosen injection RF phase Φ_0, the phase error due to the Laser jitter $\sigma_{\Phi_{inj}}$, the general phase error σ_Φ of the RF, the field at the position z and the accompanying amplitude error σ_A:

$$V_{\mathrm{acc}}(t=0,z=0) = [E_{\mathrm{acc}}(0)\cdot(1+\sigma_A)]\cdot\cos(\Phi_0+\sigma_{\Phi_{\mathrm{inj}}}+\sigma_\Phi) \tag{A.1}$$

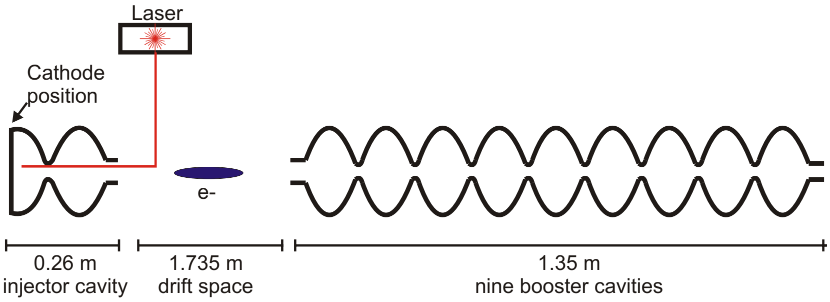

Figure A.1: Setup of the photo-injector cavity, the following drift space and one of the nine TESLA-type booster cavities.

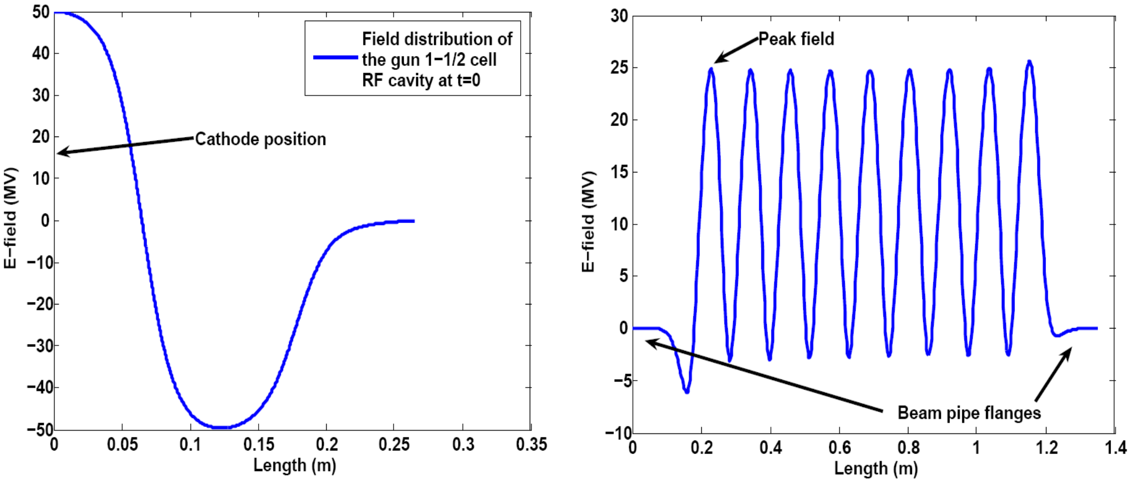

Figure A.2: E-field distribution in the 1-1/2 cell normal-conducting RF cavity of the photo-injector (left) and a nine-cell TESLA cavity of the booster section at t=0.

The gained energy of the first step is thus

$$E_n(t=0, z=0) = e \cdot V_{\text{acc}}(t=0, z=0) \cdot dz, \;\; dz = \frac{l_{\text{acc}}}{n_a} \tag{A.2}$$

In the relativistic notation of the Lorentz factor γ with $\beta = \frac{v}{c}$ the energy gain may be expressed by

$$\gamma = \frac{1}{\sqrt{1+\beta^2}} = 1 + \frac{E_n(t,z)}{m_0 c^2} \text{ with } m_0 \text{ is the electron rest mass.} \tag{A.3}$$

For the next step the new velocity $\beta = \sqrt{1 - \frac{1}{\gamma^2}}$ is calculated and the position along the z-axis is shifted by dz. For the phase with respect to the oscillating RF field $\omega_0 \cdot t$ the propagation in time is calculated as

$$t_{n+1} = \frac{dz}{\overline{\beta}} + t_n \tag{A.4}$$

Table A.1: Resulting time jitter for different phase errors of the injector and eight booster cavities. The laser-induced timing jitter is 250 fs for all cases.$\sigma_{A,inj}$=1 ‰, $\sigma_{A,cav}$=0.2 ‰. $\sigma_{t,initial}$ is the time jitter at the booster exit, but being the initial jitter for the linac.

$\sigma_{\Phi,inj}(^\circ)$	$\sigma_{\Phi,cav}(^\circ)$	$\sigma_{t,initial}$(fs)
0.1	0.02	488
0.3	0.02	608
0.5	0.02	798
0.8	0.02	1143
1.0	0.02	1427
0.3	0.15	645

where $\bar{\beta} = \frac{1}{2}(\beta_n + \beta_{n+1})$.

For different rms phase errors of the gun and booster cavity the resulting timing jitter of the electron bunches have been computed. The results are summarized in Table A.1. E.g. for the case of 0.8° phase error and 1 ‰ amplitude error in the injector cavity with 0.02° and $2 \cdot 10^{-4}$ in the following booster cavity the following results were obtained for the timing jitter:

- 944 fs after the injector
- 1113 fs after the 1.735 m drift section
- 1143 fs after the eight booster cavities

The final longitudinal phase space distribution (E_n, z) is later compressed by the bunch compressor (Equation 2.9). The maximum possible jitter compression is limited by the amount of time jitter $\sigma_{t,initial}$, the energy jitter after the first section and deviations in the correlated energy jitter or chirp $k = \delta E/\delta z$. To achieve a small time jitter at the linac exit, it is mainly important to have a stable RF control for the injector cavity. But any kind of cavity field error disturbs the design energy chirp for the bunch compression and thus increases the residual timing jitter. This can be directly deduced from Figure A.3 showing the evolution of the time and energy jitter along the RF cavities and the drift section.

Regarding the presently achievable field control of normal conducting RF photoinjector cavities of 0.3°[22] the expected time jitter after the booster is about 600-700 fs (see Table A.1).

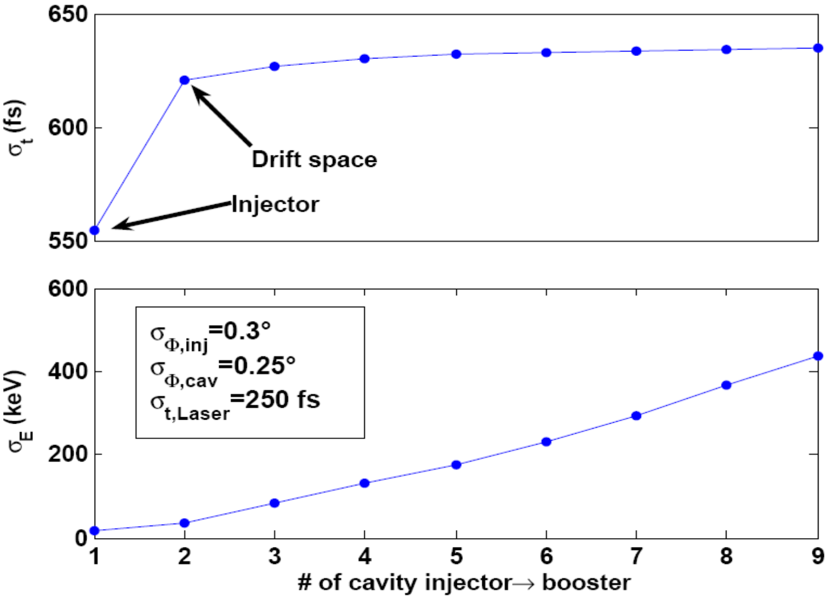

Figure A.3: Simulated evolution of injection time jitter (upper plot) and energy spread along the first Linac section including injector cavity, drift section and the first eight booster cavities. The Laser time jitter is 250 fs.

Appendix B

Ponderomotive effects

An occurrence most probably influencing the field stability in CW mode driven cavities is due to the coupling of the mechanical detuning to the time varying Lorentz forces. In combination with an RF feedback system in a generator driven setup with a fixed reference frequency, this coupling may lead to unwanted oscillations of the RF field level and phase [53] [91] —if significant RF power is available to compensate.

In principal two cases can occur and have been demonstrated by measurements taken at the linear accelerator of the radiation source ELBE [92]. Assuming a situation where the klystron is driven near its saturation regime positive or negative detuning from the resonance frequency may happen due to microphonics:

- For a positive frequency shift the field decays due to this detuning. Following the klystron saturates when the low level RF system tries to compensate the loss in field amplitude by increasing the needed forward power as given by Equation 3.48. Because no more RF power is available, the field drops. This leads to a further positive detuning, because the lower field level comes along with a reduced negative Lorentz force detuning offset. Even when the microphonics detuning event causing this should reduce, the field may now not recover. It is now too far away from the resonance, the klystron remains saturated and the field decays to a small value.

- For a negative shift from the resonance frequency an oscillatory instability can be observed. The induced perturbation by the microphonics will be compensated by the Lorentz force detuning as soon as the field starts to drop. The directionality of the ponderomotive effect is a result of the negative proportionality of the Lorentz force detuning.

At the ELBE linac it only was possible to measure the effect during an RF pulse of $\approx$ 50 ms. The ELBE cavity is a nine cell superconducting cavity with a TESLA shape. Figure B.1 reflects the ponderomotive effect for the two cases. The black curve shows the stable condition, driving the cavity at 11.5 MV/m at a loaded quality factor of $1.3 \cdot 10^7$ (Bandwidth 100 Hz). The maximum klystron power for this run had been reduced to 10 kW. The blue curve displays the obtained result for positive detuning because microphonics immediately saturate the klystron. The field never reaches its intended gradient and decays to a lower level of approximately 5 MV/m. In the case of negative detuning the expected oscillatory behavior has been measured (red curve). The time varying field level seems to excite a possible mechanical eigenmode of the cavity at 100 Hz. This may correspond to the mode shown in Figure 5.18.

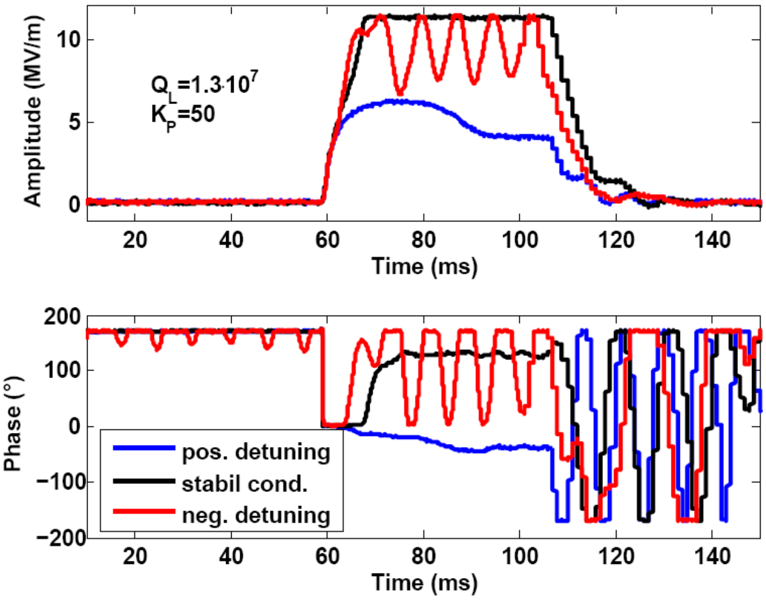

Figure B.1: Measurement of ponderomotive effects at the ELBE linac. A saturation of the klystron due to microphonics detuning leads to a decay (blue curve) or oscillation (red curve) of the field amplitude due to the Lorentz force detuning to the field level. Depending on the direction of the detuning offset from the resonance frequency the case of decay or oscillation may occur. As a reference measurement the stable case is given (black curve). The data have been sampled at a set point field level of 11.5 MV/m and a loaded quality factor of $1.3\cdot10^7$.

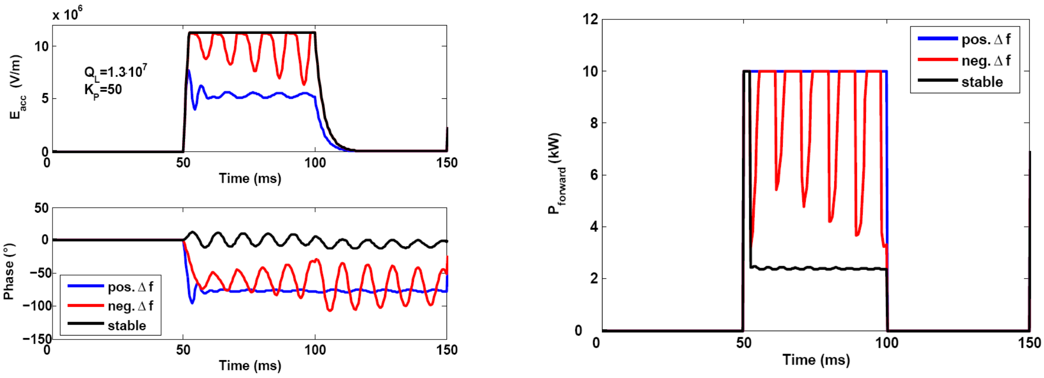

Figure B.2: Reconstruction of the measured ponderomotive effect at ELBE with the cavity simulation. As well as in Figure B.1 a positive detuning leads to a decay of the field amplitude (blue curve). Also an oscillatory instability can be seen when detuning the cavity in negative direction off resonance (red curve).

For both cases the microphonics at ELBE had not been strong enough to trigger this effect by its own. The cavity had to be detuned by 7 Hz for the positive and about 50 Hz for the negative case to bring the klystron close to saturation. In general the microphonics measurements taken at HoBiCaT so far show, that the case of klystron saturation will be a very uncommon effect. But nevertheless the long-term measurements revealed a peak detuning as high as 26 Hz or for another case a factor 12-17 of the usual rms value (see Section 5.2). So not only to improve the overall phase stability of the RF field but moreover to compensate for these peak events a fast tuning system is mandatory.

The ELBE measurements are finally also a good crosscheck for the cavity simulation model. Figure B.2 shows the simulated ponderomotive effect with the Matlab single cavity model. The ELBE parameters were incorporated in the calculations. An uncertainty was given by the mechanical model of the Lorentz force detuning, that the measured eigenmodes of the TESLA cavity of Table 5.1 had been used. For the modeling of the controller only the feedback gain of the ELBE amplitude-phase control system is known. Any kind of feedforward table or pre-detuning is not implemented in the same way as in the measurement. Nevertheless the simulation reconstructs the general behavior measured at ELBE in Figure B.1.

Appendix C

Fit parameter for the electro-mechanical transfer function

Table C.1: Fit parameter for the transfer function of the Saclay II tuner given in Figure 6.14 part 1

Δf_{det} **(Hz)**	f_k **(Hz)**	$f_{1/2}$ **(Hz)**
13.158	39.614	0.2
8.3	40.2	0.085
-7.12	40.6575	0.2
1	41.45	0.1
-9.6	42.8	0.3
3.34	43.2	0.5
0.50	64.6	0.4
0.7	66.3	0.85
1.2	67.6	0.5
1.2	69.5	0.5
1.1	77.8	0.6
1.0	81.2	0.5
1.0	83.8	0.5
1.3	87.5	0.6
1.3	94.5	0.8
0.2	100	0.18
7.3	101.35	0.125
4.7	101.58	0.1
4.85	105.54	0.75
9.2	108.3	0.45

Table C.2: Fit parameter for transfer function given in Figure 6.14 part 2

Δf_{det} **(Hz)**	f_k **(Hz)**	$f_{1/2}$ **(Hz)**
2.4	111.5	0.4
1.2	113.6	0.45
1.6	119	0.8
1.5	120.5	0.5
2.73	128.7	1.75
1.5	153.0	1.0
1.7	158.6	2
1.2	165.0	1.5
2.3	168.0	1
40.33	172.228	0.12
3.5	173.4	0.8
-1	177.05	0.075
1	179.8	0.6
3.3	184	0.8
6.62	191.0	2.6
-3.6	193	1
0.7	196.1	0.2
40.54	213.25	0.6
55.06	226.3	8

Table C.3: Fit parameter for the transfer function of the Saclay I tuner

Δf_{det} **(Hz)**	f_k **(Hz)**	$f_{1/2}$ **(Hz)**
8.6	30.7	0.15
-1.35	30.885	0.6
1.8	154.35	0.75
2.8	155.85	0.7
1.8	158.5	1.2
2.8	159.85	1.1
1.6	163.5	0.6
5.0	167.0	1.0
2.1	169.95	0.9
6.3	173.4	1.0
35.5	175.76	0.11
16	175.85	0.04
23	175.97	0.03
-7.5	176.3	0.3
5.0	178.9	0.5
21.5	187.3	2.2
-8.0	189.3	0.6
6.5	195.0	1.1
25.5	209.8	4
65	237.0	8.0

Danksagung

Zuallererst bedanke ich mich bei Herrn Prof. Jaeschke für die Möglichkeit bei BESSY meine Promotion anzufertigen, für die Bereitschaft diese Arbeit als Erstgutachter zu betreuen und für die Ermöglichung mehrerer Auslandsreisen, um meinen wissenschaftlichen Horizont zu erweitern.

Herrn Prof. Hermann Kolanoski und Herrn Prof. Shaukat Khan danke ich für die freundliche Übernahme der weiteren Gutachten.

Ganz besonders bedanken möchte ich mich bei Dr. Jens Knobloch, welcher diese Arbeit intensiv betreut hat, ein hervorragendes Arbeitsklima in der SRF Gruppe bei BESSY ermöglicht hat und bei vielen Fragestellungen und Problemen mit neuen Blickwinkeln und Ratschlägen weiterzuhelfen wusste. Mein Dank gilt weiterhin Dr. Oliver Kugeler, mit dem ich viele Meßschichten an HoBiCaT teilen durfte.

Des weiteren danke ich allen Mitarbeitern der SRF und HF Gruppe bei BESSY, sowie denjenigen, die beim Betrieb und Aufbau von HoBiCaT mitgearbeitet haben. Im einzelnen wären das Dr. Wolfgang Anders, Andre Frahm, Sascha Klauke, Dirk Pflückhahn, Stefan Rotterdam und Michael Schuster. Bezüglich des HF- Senderbetriebs geht mein Dank an Grzegorz Mielczarek, Andreas Heugel, Hans-Georg Hoberg und Thomas Westphal.

Bei technischen, programmier -und DSP-bezogenen Sachfragen waren oft die Mitarbeiter von ”15.8” eine große Hilfe. Ihnen gilt mein Dank. Hervorheben möchte ich da besonders Rainer Görgen, Ralph Lange und Klaus Ludwig.

Eine sehr gute Zusammenarbeit und Kollaboration hat sich mit den Kollegen von CEA-Saclay, Dr. Guillaume Devanz und Michel Luong, ergeben. Bei ihnen bedanke ich mich für die fruchtbaren Diskussionen und die freundliche zur Verfügungsstellung des Saclay-II Tuners.

Ferner bedanke ich mich bei allen Kollegen der FEL Projektgruppe, welche mehr oder minder zum Zustandekommen dieser Arbeit beigetragen haben. Besondere Erwähnung verdient hier mein Bürokollege, Dr. Michael Abo-Bakr, mit dem ich viele Diskussionen "über den Tellerrand" hinaus führte.

Abschließend möchte ich mich bei meinen Eltern bedanken, die mir das Physikstudium ermöglicht haben und dadurch diese Arbeit erst initiiert haben.

Mein besonderer Dank gilt Andrea für die kontinuierliche Unterstützung und den Blick auf das Leben außerhalb der Physik.

Bibliography

[1] D. Krämer, E. Jaeschke, and W. Eberhardt, editors. *The BESSY Soft X-ray Free Electron Laser.* BESSY, 1st edition, 2004. ISBN 3-9809534-0-8. URL `http://www.bessy.de/publicRelations/publications/files/TDR_WEB.pdf`.

[2] M. Abo-Bakr and *et al.* *Visions of Science, The BESSY SASE-FEL in Berlin Adlershof.* BESSY, Berlin-Adlershof, 1 edition, 2001. URL `http://www.bessy.de/publicRelations/publications/files/sc.pdf`.

[3] S. Eisebitt, J. Luening, W.F. Schlotter, M. Loergen, O. Hellwig, W. Eberhardt, and J. Stoehr. Lensless imaging of magnetic nanostructures by x-ray spectro-holography. *Nature*, 432(7019):885–888, December 2004.

[4] H. Wiedemann. *Particle accelerator physics I & II.* Springer Verlag, Berlin, 2 edition, 2003. ISBN 3-540-00672-9.

[5] K-.J. Kim and Z. Huang. Present status of x-ray FELs. In *AIP conference proceedings*, pages 185–202, 2001.

[6] L.-H. Yu and *et al.* High-gain harmonic-generation free-electron laser. *Science*, 11(289): 932–934, aug 2000.

[7] L.-H. Yu. Generation of intense uv radiation by subharmonically seeded single-pass free-electron lasers. *Phys. Rev. A*, 44:5178, 1991.

[8] B. Kuske, M. Abo-Bakr, and A. Meseck. Impact studies of bunch parameter variations on the performance of the BESSY HGHG FEL. In *Proc. of the 26th Free Electron Laser Conference, Trieste*, 2004.

[9] M. Abo-Bakr, M. v. Hartrott, J. Knobloch, B. Kuske, and A. Meseck. Start-to-end injector and linac tolerance studies for the BESSY-FEL. In *Proc. of the 26th Free Electron Laser Conference, Trieste*, 2004.

[10] D. Lipka. *Investigations about the longitudinal phase space at a photo injector for minimized emittance.* PhD thesis, Humboldt Universität Berlin, 2004.

[11] M. Borland. Design considerations for linac fel drivers . http:// filburt.lns.mit.edu/accelphy/XRayFEL/, 2002.

[12] T. Schilcher. *Vector sum control of pulsed accelerating fields in Lorentz force detuned superconducting cavities.* PhD thesis, Universität Hamburg, 1998.

[13] M. Liepe, S. Belomestnykh, J. Dobbins, R. Kaplan, and C. Strohman. A new digital control system for CESR-C and the Cornell ERL. In *Proc. of the 20th PAC, Portland, Oregon*, 2003.

[14] J.G. Weisend. *The Handbook Of Cryogenic Engineering.* CRC, 1 edition, 1998. ISBN 978-1560323327.

[15] B. Baklakov, T. Bolshakov, A. Chupyra, A. Erokhin, V. Parkhomchuk P. Lebedev, Sh. Singatulin, J. Lach, and V. Shiltsev. Ground vibration measurements for fermilab future collider projects. *Physical review special topics - accelerators and beams*, 1, 1998.

[16] H. Schlarp. Status of the laser based synchronization system at flash, 2006.

[17] P. Baudrenghien, G. Hagmann, J. C. Molendijk, R. Olsen, T. Rohlev, V. Rossi, D. Stellfeld, D. Valuch, and U. Wehrle. The LHC Low Level RF. In *Proc. of the 10th EPAC(2006), Edinburgh*, 2006.

[18] S.O. Cho, B.C. Lee, Y.U. Jeong, J. Yoo, and S.H. Park. Analysis of wakefield effects on the operation of an energy-recovering superconducting linear accelerator. *Journal of the Korean Physical Society*, 41(5):662–666, 2002.

[19] A. Novokhatski, M. Timm, and T. Weiland. Single bunch energy spread in the TESLA cryomodule. TESLA report 99–16, DESY, DESY, Notkestrasse 85, D-22607 Hamburg, 1999. URL `http://flash.desy.de/reports_publications/tesla_reports/tesla_reports_1999`. .

[20] M. Ferrario, A. Mosnier, L. Serafini, F. Tazzioli, and J.-M. Tessier. Multi-bunch energy spread induced by beam loading in a standing wave structure. TESLA report 95–06, DESY, DESY, Notkestrasse 85, D-22607 Hamburg, 1995. URL `http://flash.desy.de/reports_publications/tesla_reports/tesla_reports_1995`. .

[21] A. Mosnier and J.M. Tessier. Field stabilization study for TESLA. TESLA report 94–16, DESY, DESY, Notkestrasse 85, D-22607 Hamburg, 1994. URL `http://flash.desy.de/reports_publications/tesla_reports/tesla_reports_1994`. .

[22] E. Vogel, W. Koprek, and P. Pucyk. FPGA based RF field control at the photo cathode RF gun of the DESY vacuum ultraviolet free electron laser. In *Proc. of the 10th EPAC(2006), Edinburgh*, 2006.

[23] H. Padamsee, J. Knobloch, and T. Hays. *RF superconductivity for accelerators.* John Wiley & Sons, New York, 1 edition, 1998. ISBN 0471154326.

[24] J.D. Jackson. *Classical electrodynamics.* John Wiley & Sons, New York, 3 edition, 1999. ISBN 978-0471309321.

[25] W. R. Smythe. *Static and dynamic electricity.* McGraw-Hill Book Company, New York, 3 edition, 1986.

[26] E. Haebel. Couplers: Tutorial and update. *Particle Accelerators*, 40:141–159, 1992.

[27] J. Sekutowicz. Tutorial: Superconducting high β cavities. In *Proc. of the 13th SRF workshop(2007), Beijing*, 2007.

[28] M.L. Boas. *Mathematical methods in the physical sciences.* John Wiley & Sons, New York, 2 edition, 1983. ISBN 0-471-04409-1.

[29] J. Lunze. *Regelungstechnik 1&2, Mehrgrössensysteme, Digitale Regelung.* Springer-Verlag, Berlin, 2 edition, 2002. ISBN 3-540-43116-0.

[30] W.H. Press, S.A. Teukolsky, W.T. Vettering, and B.Flannery. *Numerical recipes in C++.* XXVIII, Cambridge University Press, Cambridge, 2 edition, 2002. ISBN 0-521-75033-4.

[31] P. Schuett and T. Weiland. Feasibility study of a HOM IOT for TESLA. In *Proc. of the 17th PAC(1997), Vancouver*, 1997.

[32] A. Heugel. Private communications, 2007.

[33] W.P. Robins. *Phase Noise in Signal Sources.* IEE Telecommunication series 9, London, revised edition edition, 1982.

[34] A. Neumann. Phase noise modeling for time domain cavity simulation. Internal report, BESSY, BESSY, Albert-Einstein-Strasse 15, D-12489 Berlin, 2005. .

[35] H. Lutz and W. Wendt. *Taschenbuch der Regelungstechnik.* Verlag Harri Deutsch, Frankfurt a.M., 4 edition, 2002. ISBN 3-8171-1668-3.

[36] G. Devanz, M. Luong, and A. Mosnier. Numerical simulations of dynamic Lorentz detuning of SC cavities. In *Proc. of the 8th EPAC(2002), Paris*, 2002.

[37] T. Quast. Private communications, 2004.

[38] R. Brinkmann, K. Floettmann, J. Roßbach, P. Schmueser, N. Walker, and H. Weise, editors. *TESLA technical design report, part II - The accelerator.* DESY, Hamburg, 1 edition, 2001. ISBN 3-935702-00-0.

[39] ILC collaboration. International linear collider project. http:// www. linearcollider.org/cms, 2007.

[40] M. Altarelli and *et al.*, editors. *The Technical Design Report of the European XFEL.* DESY-2006-097, Hamburg, 1st edition, 2006. ISBN 3-935702-17-5.

[41] G. H. Hoffstaetter, I.V. Bazarov, D. Bilderback, M. Billing, S. Gruner, M. Liepe, D. Sagan, C. Sinclair, R. Talman, and M. Tigner. ERL Upgrade of an Existing X-ray Facility: CHESS at CESR. In *Proc. of the 9thEPAC(2004), Lucerne*, 2004.

[42] 4GLS design group. 4gls conceptual design report. http:// www. 4gls.ac.uk/documents.htm#CDR, 2006.

[43] M. E. Couprie and *et al.* The Arc-en-Ciel FEL proposal. In *Proc. of the 28th FEL(2006), Berlin*, 2006.

[44] J. Knobloch, W. Anders, J. Borninkhof, S. Jung, M. Martin, A. Neumann, D. Pflueckhahn, and M. Schuster. Status of the HoBiCaT Superconducting Cavity Test Facility at BESSY. In *Proc. of the 9th EPAC(2004), Lucerne*, 2004.

[45] J. Knobloch, W. Anders, D. Pflueckhahn, and M. Schuster. HoBiCaT–A test facility for superconducting RF systems. In *Proc. of the 11th SRF workshop(2003), Travemuende*, 2003.

[46] P. Bosland and Bo Wu. Mechanical study of the Saclay piezo tuner PTS (Piezo Tuning System). TESLA report CARE-Note-2005-004-SRF, CEA-Saclay, Paris, 2005. .

[47] M. Huening. Selbstoptimierende parametersteuerung der hochfrequenz des supraleitenden linearbeschleunigers tesla test facility. Master's thesis, RWTH Aachen, 2000.

[48] Xilinx Inc. Xilinx website. http://www.xilinx.com, 2008.

[49] H. Gassot. Mechanical stability of the RF superconducting cavity. In *Proc. of the 8th EPAC(2002), Paris*, 2002.

[50] C. Torrence and G.P. Compo. A practical guide to wavelet analysis. *Bulletin of the American Meteorological Society*, 1998.

[51] M. Farge and *et al.* Wavelet transforms and their applications to turbulence. *Annu. Rev. Fluid Mech*, 24:395–457, 1992.

[52] J. Morlet and *et al.* Wave propagation and sampling theory-part i: Complex signal and scattering in multilayered media. *Geophysics*, 47(2):203–221, 1982.

[53] J. Delayen. Tutorial: Ponderomotive instabilities and microphonics. In *Proc. of the 12th SRF workshop(2005), Cornell*, 2005.

[54] M. Liepe. Regelung supraleitender resonatoren mit strahlbelastung am tesla-test-linearbeschleuniger. Master's thesis, Universität Hamburg, 1998.

[55] J.C. Slater. *Microwave electronics.* The Bell telephone laboratories series, Toronto, 6 edition, 1963.

[56] Y. Yamazaki and et al. *Accelerator Technical Design Report for J-PARC.* http://hadron.kek.jp/ accelerator/TDA/tdr2003/index2.html, Tsukuba, Ibaraki 305-0801 Japan, 1 edition, 2003.

[57] H. Gassot. *Etudes de la stabilité mécanique des cavités supraconductrices et de la méthode de rigidification par projection thermique de cuivr.* PhD thesis, Université Paris Sud Paris XI, 2001.

[58] M. Liepe, W.D. Moeller, and S.N. Simrock. Dynamic Lorentz Force Compensation with a fast piezoelectric tuner. In *Proc. of the 19th PAC(2001), Chicago*, 2001.

[59] N. Ouchi, E. Chishiro, C. Tsukishima, and K. Mukugi. Pulsed SC Proton Linacs. In *Proc. of the 20th LINAC(2000), Monterey, California*, 2000.

[60] M. Doleans and Sang ho Kim. Insights in the physics of the dynamic detuning in SRF cavities and its active compensation. In *Proc. of the 20th PAC(2003), Portland, Oregon*, 2003.

[61] M. Doleans. *Etudes dans les cavites supraconductrices elliptiques a beta-reduit.* PhD thesis, Universite Paris 7, 2003.

[62] D.T. Smith. A square root circuit to linearize feedback in temperature controllers. *Journal of Physics E: Scientific Instruments*, 5(6), 1972.

[63] M.L. Meade. *Lock-in amplifiers: principals and applications.* Peter Peregrinus Ltd., London UK, iee electrical measurement series 1 edition, 1983.

[64] W. Walter. *Gewoehnliche Differentialgleichungen.* Springer Verlag, Berlin, 6 edition, 1996. ISBN 3-540-59038-2.

[65] J.R. Delayen and G.K. Davis. Microphonics and Lorentz transfer function measurements on the SNS cryomodules. In *Proc. of the 11th SRF workshop(2003), Travemuende*, 2003.

[66] C. Hovater, J. Delayen, L. Merminga, T. Powers, and C. Reece. RF control requirements for the CEBAF energy upgrade cavities. In *Proc. of the 20th LINAC(2000), Monterey, California*, 2000.

[67] M. Liepe and S. Noguchi. Report on current status for ilc tuner development. Workgroup 5, Snowmass 2005, to be published, 2005.

[68] L. Lilje, S. Simrock, D. Kostin, and M. Fouaidy. Characteristics of a fast piezo-tuning mechanism for superconducting cavities. In *Proc. of the 8th EPAC(2002), Paris*, 2002.

[69] A. Neumann, W. Anders, S. Klauke, J. Knobloch, O Kugeler, and M. Schuster. Characterization of a piezo-based microphonics compensation system at HoBiCaT. In *Proc. of the 10th EPAC(2006), Edinburgh*, 2006.

[70] F. Paschen. Ueber die zum funkenübergang in luft, wasserstoff und kohlensaeure bei verschiedenen drücken erforderliche potentialdifferenz. *Wied. Annalen der Physik*, 37 (6):69–75, 1889.

[71] L. Bergmann, C. Schaefer, and W. Raith. *Lehrbuch der Experimentalphysik, Elektromagnetismus, Band 2.* Walter de Gruyter, Berlin, New York, 2 edition, 1999. ISBN 978-3110188981.

[72] G. Devanz and M. Luong. Lorentz force and microphonics compensation in tesla type cavities with the saclay ii tuner. BESSY FEL seminar, 2006.

[73] M. Luong, P. Bosland, G. Devanz, and E. Jacques. Analysis of microphonic disturbance and simulation for feedback compensation. In *Proc. of the 10th EPAC(2006), Edinburgh*, 2006.

[74] G. Bisoffi. Overview on the HoBiCaT measurement programme at BESSY. Internal report, INFN Legnaro, BESSY, Albert-Einstein-Strasse 15, D-12489 Berlin, 2003. .

[75] G. Devanz and *et al.* Compensation of Lorentz force detuning of a TTF 9-cell cavity with a new integrated piezo tuner. In *Proc. of the 10th EPAC(2006), Edinburgh*, 2006.

[76] T.H. Kandil, T.L. Grimm, W. Hartung, H. Khalil, J. Popielarski, J. Vincent, and R.C. York. Adaptive Feedforward Cancellation of Sinusoidal Disturbances in Superconducting RF Cavities. In *Proc. of the 22th LINAC(2004), Luebeck*, 2004.

[77] O. Tokhi, S. Veres, and editors. *Active sound and vibration control, theory and application.* IEE control engineering series 62, London, 1 edition, 2002. ISBN 3-9809534-0-8.

[78] R.E. Kalman. A new approach to linear filtering and prediction problems. *Transactions of the ASME-Journal of Basic Engineering*, 82(6):35–45, 1960.

[79] U. Meyer-Baese. *Digital signal processing with Field Programmable Gate Arrays.* Springer Verlag, Berlin, 2 edition, 2004. ISBN 3-540-21119-5.

[80] J. Stoer. *Numerische Mathematik 1&2.* Springer Verlag, Berlin, 8 edition, 1999. ISBN 3-540-66154-9.

[81] O. Kugeler, W. Anders, J. Knobloch, and A. Neumann. Microphonics measurements in a cw-driven TESLA-type cavity. In *Proc. of the 10th EPAC(2006), Edinburgh*, 2006.

[82] A. Neumann, W. Anders, J. Knobloch, and O. Kugeler. Microphonics in CW cavities and their compensation with fast tuners. In *Proc. of the 13th SRF workshop(2007), Beijing*, 2007.

[83] O. Foellinger. *Laplace-, Fourier- und z-Transformation.* Huethig Verlag, Heidelberg, 7 edition, 2000. ISBN 3-7785-2706-1.

[84] G. Engeln-Muellges and F. Reutter. *Numerische Mathematik fuer Ingenieure.* **B** ·**I** · Wissenschaftsverlag, Zuerich, 5 edition, 1987.

[85] G. Kubin. Computational intelligence. Lecture given during summer term 2005, 2005.

[86] K. Kroschel. *Statitische Informationstechnik.* Springer Verlag, Berlin, Heidelberg, 5 edition, 2004. ISBN 3-540-40237-3.

[87] W. Ren and P.R. Kumar. Adaptive active noise control: structures, algorithms and convergence analysis. *Proc. InterNoise89*, 82:435–441, 1989.

[88] A. Neumann, R. Goergen, J. Knobloch, and K. Ludwig. A digital fpga based low level rf control system for cw-driven tesla-type sc cavities. to be published, 2009.

[89] M. Liepe and S. Belomestnykh. RF parameter and field stability requirements for the Cornell ERL prototype. In *Proc. of the 20th PAC(2003), Portland, Oregon*, 2003.

[90] G. A. Krafft and L. Merminga. Rf specifications for erl, 2005.

[91] A. Neumann and J. Knobloch. RF control of the superconducting linac for the BESSY-FEL. In *Proc. of the 9th EPAC(2004), Luzern*, 2004.

[92] A. Büchner, F. Gabriel, E. Grosse, P. Michel, W. Seidel, and J. Voigtländer. The Elbe-project at Dresden-Rossendorf. In *Proc. of the 7th EPAC(2000), Vienna*, 2000.

List of Figures

1.1 Peak brilliance and peak power of the BESSY-FEL 2

2.1 Overview of HGHG process for one stage 6
2.2 Scheme of HGHG cascade 6
2.3 Electron bunch profile for the HGHG process 7
2.4 Electron bunch phase space at linac exit 9
2.5 Spectra of the low energy FEL for varying offset beam energies 9
2.6 Acceleration principle in a time varying RF field 10
2.7 The driver linac of the BESSY-FEL 11
2.8 Principle of bunch compression 12
2.9 Effect of bunch compression on longitudinal bunch-to-bunch phase space in simulations 13
2.10 Generic layout of an LLRF control system 14
2.11 Bunch energy jitter in dependance of cavity error sources 18
2.12 Bunch energy jitter in dependance of cavity detuning and RF feedback gain 19
2.13 Longitudinal phase space at linac exit for different detuning levels 20

3.1 Scheme of an adjustable power coupler 25
3.2 Passband modes of a TESLA cavity 26
3.3 The equivalent circuit representation of a nine cell cavity with magnetically coupled cells 27
3.4 Equivalent circuit model for a cavity connected via a coupler antenna to an RF power source and accelerating a particle beam 28
3.5 Amplitude and phase response of a cavity in frequency domain 30
3.6 Phasor representation of the RF field vector 31
3.7 Transient behavior of the cavity field components for several detuning values at constant forward power 33
3.8 Overview of the cavity modeling in Matlab-Simulink^{TM} 35
3.9 Measured IOT gain curve 35
3.10 Simulated Lorentz force detuning, microphonic detuning and phase of a high loaded Q cavity 37
3.11 Simulated beam loading effect 39
3.12 Simulated detuning, forward power and bunch-to-bunch energy modulation . 40
3.13 Forward power in dependance of loaded quality factor 41
3.14 Dependence of energy jitter of a single cavity for different loaded quality factors at a given detuning 41

3.15 Final timing jitter of the electron beam against the initial jitter given by the gun and booster section of the linac parameterized by correlated detuning . . 43
3.16 Final timing jitter of the electron beam against the initial jitter given by the gun and booster section of the linac parameterized by uncorrelated detuning 44

4.1 Picture of TESLA cavities and end-cell section 48
4.2 Technical drawing of a TESLA cavity and its cryo-unit 49
4.3 Fisheye view of the HoBiCaT test cryostat for superconducting cavities . . . 49
4.4 Overview of the HoBiCaT facility 51
4.5 Principle of RF phase detection by RF mixer 52
4.6 RF measurement setup at HoBiCaT 53
4.7 RF mixer calibration curve 55
4.8 Measured phase response of a detuned cavity 56
4.9 SSB phase noise of the reference RF oscillator 56

5.1 Overview of detuning sources 60
5.2 Time domain detuning data 62
5.3 Histograms of typical open loop microphonics detuning 62
5.4 Long-term microphonics measurement 63
5.5 Integrated microphonics detuning spectrum 64
5.6 Integrated microphonics spectra of the same cavity equipped with two different tuning systems 65
5.7 Wavelet time-frequency map of open loop microphonics detuning 67
5.8 Time-frequency analysis of detuning data zoomed to the 41 Hz resonance . . 67
5.9 Wavelet analysis of the detuning due to pressure variations in the liquid helium bath 68
5.10 Simulated autocorrelation function of the detuning 69
5.11 Autocorrelation function of measured microphonics detuning 70
5.12 Dependance of the cavity frequency on the liquid helium pressure 71
5.13 Microphonics detuning with strong helium pressure fluctuations 72
5.14 Cross-correlation of the microphonics detuning and helium pressure signal . . 72
5.15 Deformation of a $\beta = 0.725$ cavity for the J-Parc project at 30 MV/m 73
5.16 Measurement of static Lorentz force detuning 74
5.17 Modified measurement setup for the dynamic Lorentz force response of a TESLA cavity 76
5.18 Dynamic Lorentz-force-detuning transfer function around two mechanical eigenmodes of the cavity 77
5.19 Histogram showing the rms detuning values of all open loop microphonics measurements taken at HoBiCaT 78

6.1 Pictures of the Saclay tuning systems 82
6.2 Working principle of the tuning systems 83
6.3 Scheme of the piezo holder of the type II tuning system 85
6.4 Measured motor tuner hysteresis 85
6.5 Tuning range and hysteresis of a Noliac piezo 86
6.6 Piezo tuner resolution 87
6.7 Principle of transfer function measurement 88

6.8 Transfer function of the Saclay I tuner 90
6.9 Transfer function of the Saclay II tuner 90
6.10 Lorentz distribution of second order systems 91
6.11 Tuner transfer functions (type I and II) mounted to the same cavity 92
6.12 Influence of helium bath pressure on the transfer function 92
6.13 Frequency map of a piezo-to-RF transfer function 93
6.14 Fit to the type II tuner transfer function 95

7.1 Possible feedforward and feedback schemes for a piezo based microphonics detuning control 100
7.2 The complete microphonics detuning compensation scheme given by a feedback and an adaptive feedforward 102
7.3 Integrated low frequency microphonics spectra for different feedback gains . 104
7.4 Residual detuning error (up to 10 Hz mod. frequency) vs. the feedback gain 105
7.5 Bode plots of the piezo→RF transfer function, the transfer function for different feedback gains of the PI path including lowpass filtering because of the cavity bandwidth and the transfer function of the maximum P gain without cavity part 106
7.6 LMS filter algorithm scheme 107
7.7 Contour plot to illustrate the method of the steepest descent 109
7.8 Example of microphonics detuning reduction at the first mechanical resonance using the adaptive feedforward filter algorithm in time domain 112
7.9 Switching capability of the LMS algorithm 112
7.10 Time domain data of compensation results at 1.8 K 113
7.11 Integrated detuning spectra of compensation results at 1.8 K 113
7.12 Histogram distributions of compensation results at 1.8 K 114
7.13 Compensation results with the Saclay II tuner 115
7.14 Control of multiple microphonics sources 116
7.15 Bode plot of the final filter configuration for a control of the 380 Hz resonance 117
7.16 Example for divergence of the filter algorithm 117
7.17 Evolution of the last filter coefficient $w_n(400)$ with time during feedforward detuning compensation 119
7.18 Simulation scheme with included measured transfer functions, microphonics excitation and least-mean-square based feedforward algorithm 120
7.19 Cavity field amplitude, forward power of the klystron and energy of the electron bunches after the adaptive piezo based feedforward has converged . . . 122
7.20 A comparison of the simulated external detuning acting on the cavity with and without adaptive feedforward 122
7.21 Residual detuning and phase error of a cavity detuned by 5.2 Hz rms with piezo compensation and phase noise plotted against LLRF proportional feedback gain 123

A.1 Setup of the photo-injector cavity, the following drift space and one of the nine TESLA-type booster cavities 130
A.2 E-field distribution in the 1-1/2 cell normal-conducting RF cavity of the photo-injector and a nine-cell TESLA cavity of the booster section at t=0 130

A.3 Simulated evolution of injection time jitter and energy spread along the first Linac section including injector cavity, drift section and the first eight booster cavities 132

B.1 Measurement of ponderomotive effects at the ELBE linac 134
B.2 Reconstruction of the measured ponderomotive effect at ELBE with the cavity simulation 134

List of Tables

3.1 Main parameters of the linac simulation 42
3.2 Relative energy jitter at the linac exit for different starting time jitter 44

4.1 Main parameters characterizing the nine-cell TESLA cavity 48

5.1 Parameters of the first five mechanical modes coupling to Lorentz force variations 77
5.2 Most prominent peaks in the detuning spectrum of all tested cavities 79

6.1 Tuner types for TESLA cavities 82
6.2 Piezo stack parameters 84
6.3 Parameters of the most dominant mechanical modes of the type II and type I tuner (fit result) in the range of 10-220 Hz 96
6.4 Coarse and fast tuning properties of the tested Saclay I and Saclay II cavity tuning system 98

7.1 Parameters of the feedback path 104
7.2 Typical parameters of the feedforward path 111
7.3 Overview of obtained compensation results 116
7.4 Parameters for the cavity simulations including a combination of LLRF control and piezo based adaptive feedforward 121

A.1 Electron beam time jitter after injector and booster cavity 131

C.1 Fit parameter for the transfer function of the Saclay II tuner given in Figure 6.14 part 1 138
C.2 Fit parameter for transfer function given in Figure 6.14 part 2 139
C.3 Fit parameter for the transfer function of the Saclay I tuner 140

Selbständigkeitserklärung

Ich versichere, daß ich diese Arbeit selbständig verfaßt und keine anderen als die angegebenen Quellen und Hilfsmittel benutzt habe.

Berlin, den ________________________ ________________________
Axel Neumann